Design and optimisation of a novel magnetic detection scheme for encoded magnetic information carriers.
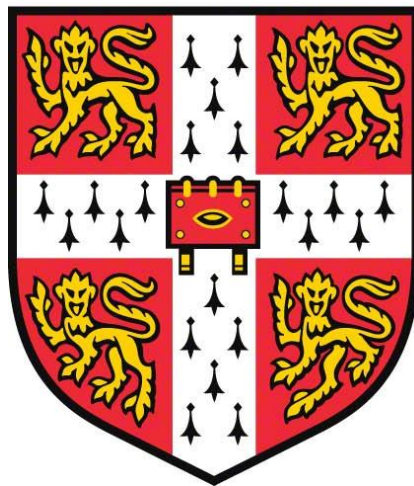
Jake David Zipfel

This dissertation is submitted for the degree of Doctor of Philosophy.

Department of Physics
University of Cambridge

Darwin College

July 2021

Declaration

This thesis is the result of my own work and includes nothing which is the outcome of work done in collaboration except as declared in the preface and specified in the text.

It is not substantially the same as any work that has already been submitted before for any degree or other qualification except as declared in the preface and specified in the text.

It does not exceed the prescribed word limit for the Physics Degree Committee.

Abstract

Previous work in the field has outlined a method to create micron-sized, tuneable encoded magnetic information carriers that can be redeposited through a liquid suspension. This thesis aims to build on this work, further characterising the information carriers and presenting a possible novel detection technique.

The magnetic information carriers in this work use synthetic antiferromagnetic (SAF) particles with perpendicular magnetic anisotropy (PMA), attenuating the coupling strength between the magnetic layers using a platinum interlayer. This provides a controllable magnetic parameter which is used as the basis for the magnetic encoding. These particles can be lifted off the substrate into a solution for redeposition onto a surface which provides a magnetic 'tag'. The particles are presented and characterised, including statistical distributions of switching events to better understand their detectable properties.

A novel detection scheme for these particles is then proposed using inductive sensing and a rotating permanent magnet as a drive field source. Device efficacy is evaluated using computational simulations, allowing for the optimisation of the parameter space before physical building. The efficacy of different input parameters is evaluated using a figure of merit – the number of possible channels the detector can measure. The simulations begin with an idealised model of the detector and particle set, with zero coercivity SAF particles and perfect alignment. The different methods that the detector can be used in are assessed, as well as exploring the possible input geometries.

Real-world constraints are later built into the model including the switching distributions of particles and the effects of misalignment. From these, the build constraints and electronic requirements of the system can be characterised. The detector is finally presented virtually through computer-aided design, which would be used to create a prototype model of the device.

"I can't wait 'til the day that you're pushing around my trolley at Asda"
Mr Thompson – Hellesdon High School

This one's for you, pal.

Acknowledgements

Firstly, I would like to thank Prof. Russell P Cowburn for his continuous support and guidance. It has been a pleasure to watch such an incredible mind work and to be a part of your team. I would also like to show my appreciation to Ingenia Holdings Ltd for funding this project.

Special thanks go to Dorothée Petit, who has been especially patient in reading this work over the past few months. I will always be thankful for your support, and for putting up with my regular Jake-isms. Your tolerance of my idiosyncratic thought processes is truly saintly, and I can only thank that you have the patience that comes with raising two toddlers!

Thank you to everyone at Cambridge who made the experience less alien. It has been a pleasure working with Pat, Paul and all of the Darwin College Library team, and I'm proud of how the facility has progressed over the past four years. Thank you to all of the demonstrating team, especially Richard King who has always been a superstar. Our walks/chats/runs/cricket have been a real therapy at times. Thanks to all at CUJC too – the tatami became a welcome (and much missed) break from the grind. And thanks to all those I lived with at Darwin, especially Jordan and Luke. The food/climbing/flaming nunchucks are always good memories!

The biggest thing that COVID screwed was being able to come in and work around an awesome group of people. Thanks to Mike, Emma and Holly for the lunchtime puzzles, and deep dives into random pond related queries. Thank you to Spence, Alex, Selma, Jung-Wei and especially Lucy for all your help in showing me the ropes. Dédalo – we lost a real gem after you graduated, and I still look at the words of encouragement you left for me when leaving! I am particularly thankful to Tarun and Jerry, who kept my head above water through the writing process. Thank you for always bringing home some perspective when I was classically beating myself up. Lastly, a big thanks go to everyone at stores and the workshops (Huw, Nigel, Kevin, Sean, etc.) who made tinkering, building, and solving equipment problems much more pleasant.

I wouldn't be in this situation without the unwavering support of my family. Thank you to both my parents for teaching me respect, hard work and kindness, and for inspiring my inquisitive nature to understand 'How things work'.

Finally, thank you to my Golda, who has put up with code/thesis Jake for too long. Thank you for always being the most kind, beautiful person, and for being with me every step.

Table of Contents

Acronyms and nomenclature

$\hat{A}$	Defines a unit vector, A
$\vec{A}$	Defines a vector, A
$\bar{A}$	Defines an average of A
$|A|$	Defines a magnitude of a vector $\vec{A}$
$\oint$	Integral over a closed surface
$\sum_{S}$	Sum of all elements over a surface S
$\begin{vmatrix} A_1 \\ A_2 \\ A_3 \end{vmatrix}$	Defines components of a vector $\vec{A}$
(a, b, c)	Dimensions of the magnet used in Akoun code
(x, y, z)	Cartesian base vectors
(ϕ, ρ, y)	Cylindrical base vectors
(R, ℓ)	Dimensions of the magnet used in the Caciagli model, with $(R, \ell) = (\mathrm{OD, L})/2$
α	Angle of external field to the anisotropy axis
α_G	Gilbert damping coefficient
β	Stable minimum of SW astroid
β'	Metastable minimum of SW astroid
γ	Gyromagnetic ratio
ε	Electromotive force (EMF)
ε_K	Kerr elipticity
ζ	Spin orbit constant
η	The figure of merit – number of possible channels for a detector
θ	Angle of magnetisation to the anisotropy axis
θ_F	$W_{0.3-0.7}$ times KRV

θ_M	Magnetisation angle in the XZ plane, defined from the z-axis
θ_n	Angle for a channel n that NSA = 0.5
θ_0	Halfway angle of a transition
θ_R	Kerr rotation angle
λ_F	Fermi wavelength
Λ	Oscillation period of RKKY function
μ	Permeability
μ_0	Permeability of free space
ρ_m	Equivalent bulk charge
σ	Standard deviation
σ_m	Equivalent surface charge
τ	Time constant
ϕ	Phase
ϕ_m	Scalar potential
Φ	Magnetic flux
χ	Membership function
ω	Frequency
ω_m	Angular velocity of a rotating magnet
a	Transition sharpness of a Boltzmann sigmoidal transition
A	Amplitude of an exponential decay
A_c	Adjustable coupling strength parameter
A_S	Area of a surface $\vec{S}$
A_1	Start value for a Boltzmann sigmoidal transition
A_2	End value of a Boltzmann sigmoidal transition

AC	Alternating current
AF	Anti-ferromagnetic
AFGM	Alternating field gradient magnetometry
AFM	Atomic force microscopy
AP	Anti-parallel
AMR	Anisotropic magnetoresistance
ΔB	Transition width
$B_\perp$	Field applied perpendicular to the sample plane
$B_\parallel$	Field applied parallel to the sample plane
$\vec{B}$	Magnetic field
B_{eq}	Equivalent B_n for a rotational transition
B_{Lin}	Equivalent linear field for a transition in a rotating field
B_{max}	Maximum field (usually for a plane at a distance from the drive magnet)
B_n	Channel field for a number n
B_0	Coupling field of the highest channel value
$\vec{B}_{sample}$	Field from the collection of magnetic particles
B_{set}	Set field (for rotational switching astroids)
B_{start}	Start field before rotation in a measurement
c	Centre of a Boltzmann sigmoidal transition
CAD	Computer aided design
CNC	Computer numerical code
d	Distance from the magnet centre to the sample plane, $= p + OD/2$.
d_p	Sample plane to coil separation
DC	Direct current

e	Electron charge
E	Energy density
$\vec{E}$	Electric field
EA	Easy axis
f	frequency
$f(x)$	A function f of x
F	Force
FFT	Fast Fourier transform
FM	Ferromagnetic
$G(r)$	Spatial sensitivity of an induction coil
GMR	Giant magnetoresistance
h	Normalised field
$h_\parallel$	Normalised field, parallel to the anisotropy axis
$h_\perp$	Normalised field, perpendicular to the anisotropy axis
$\hbar$	Planck's constant
H	Magnetic field
H_C	Coercivity
H_{eff}	Effective field
H_J	Coupling field
H_K	Hard axis saturation/anisotropy field
H_n	Switching event defined by transition n
H_{sat}	Saturation field
HA	Hard axis
HDMS	Hexamethyldisilane

$\mathcal{H}_{ij}$	Hamiltonian for the interaction between a magnetic layer spin and a conduction electron spin
I	Current
IC	Integrated circuit
ID	Inner diameter
IEC	Interlayer exchange coupling
IP	In-plane
IPA	Iso-propyl alcohol
J	Interlayer coupling strength
$J(R_{ij})$	Exchange integral
J_{bulk}	Bulk charge
J_{RKKY}	RKKY Coupling energy
J_s	Spontaneous polarisation
J_{surf}	Surface charge
k	Scale factor
K_A	Anisotropy energy
K_{eff}	Effective anisotropy
k_F	Fermi wavevector
K_i	Intrinsic anisotropy
K_S	Surface anisotropy
K_U	Uniaxial anisotropy energy
K_V	Volume anisotropy
KRV	Key ratio value
$\widehat{K}_{i,j}$	Demagnetisation Kernel

l	Solenoid length
ℓ	Length (of a cylindrical magnet)
L	Magnet length
LCP	Left circularly polarised
LLG	Landau Lifshitz Gilbert
$\vec{m}$	Magnetic moment
$m_\parallel$	Moment parallel to the sample plane
$m_\perp$	Moment perpendicular to the sample plane
m_e	Electron mass
m_{orb}	Orbital (d) moment
$\vec{M}$	Magnetisation
M_s	Saturation magnetisation
M_{eff}	Effective saturation magnetisation
MCA	Magnetocrystalline anisotropy
MOKE	Magneto-optical Kerr effect
MRAM	Magnetic random-access memory
MRI	Magnetic resonance imaging
MTJ	Magnetic tunnel junction
$\mathcal{N}$	Demagnetising tensor
n	Channel number
n_c	Number of charge carriers
N_{el}	Number of elements within a summation
NSA	Normalised Switched Area
OD	Outer diameter

OOP	Out of plane
p	Distance from the drive magnet to the sample plane
p_0	p value for the first channel B_0
P	Parallel
PCB	Printed circuit board
PMA	perpendicular magnetic anisotropy
PR	Photoresist
PVD	Physical vapour deposition
q	Charge
$\vec{r}$	Distance vector
$r_{\pm}$	Reflection coefficient of LCP (-) and RCP(+) light
R	Cylinder radius, in the Caciagli paper
R_{coil}	Detection coil radius
$\vec{R}_i$	Atomic positions
RCP	Right circularly polarised
RFID	Radio Frequency Identification
RKKY	Ruderman Kittel Kasuya Yoshida coupling
s_{rad}	Sample radius
$\vec{S}$	Surface
$\vec{s}$	Spins of conduction electrons
$\vec{S}_i$	Spins on atomic sites
SAF	Synthetic antiferromagnet
SLA	Stereo lithography
SLS	Selective laser sintering

SOI	Spin orbit interaction
SQUID	Superconducting quantum interference device
SRT	Spin reorientation transition
STT-MRAM	Spin transfer torque magnetic random access memory
t	Time
t_{CoFeB}	CoFeB layer thickness
t_d	Decay constant of an exponential decay
t_{Pt}	Platinum interlayer thickness
t_{SRT}	Spin reorientation transition thickness
T_c	Curie temperature
TMR	Tunnelling magnetoresistance
$\vec{u}$	A magnetisation of length $|M|$ aligned along $\hat{x}$
$\vec{v}$	A magnetisation of length $|M|$ aligned along $\hat{z}$
V	Volume
V_0	Atomic volume
V_H	Hall effect voltage
$\mathcal{V}_i$	Contact potential
VSM	Vibrating sample magnetometry
$W_{0.3-0.7}$	Transition width between NSA = 0.3 and 0.7, in terms of angle

Chapter 1.

Context

Project aims

Magnetic thin films have underpinned the digital revolution, with improvements in the areal density of magnetic memory allowing for much more powerful recording technology. This has only arisen due to the developments in perpendicular materials – where the magnetisation, which determines the state of the bit, lies out of the plane of the film [1]. In most magnetic systems, states are differentiated in a binary fashion, with a magnetic state in one direction providing an 'on', or 1 state, and a second magnetic state providing an 'off' or 0 state. In perpendicularly magnetised materials, the anisotropy values are generally much higher than those of in-plane materials, leading to much higher energy barriers and more stable magnetic states. Perpendicular recording technology is still at the forefront of magnetic memory research, with much focus on the applications. This is exemplified by the release of the first commercial STT-MRAM (Spin Transfer Torque – Magnetic Random Access Memory) chips by Everspin in 2016 [2], and an expansion to a 1 Gb unit in 2019 [3].

In addition to nanoscale (2D) magnetic material research for solid-state memory, there has been much focus on nanoparticle suspensions for biological applications. These usually consist of superparamagnetic iron-oxide nanoparticle suspensions, with single-particle sizes $\approx 10\ nm$ (all dimensions) [4]–[6]. These have many uses, including as contrast agents in MRI [7], [8], cancer therapeutics [9]–[12], targeted delivery, tumour detection [13], [14] and biological tagging [15], [16]. Biological tagging (using magnetic nanoparticles) consists of a magnetic particle that has been functionalised with ligands to combine with a particular biological marker. In current technologies, these are either filtered magnetically or combined with an optical/fluorescent marker to distinguish between different assays.

This project looks to bridge the two above fields, utilising encoded magnetic information in the form of magnetic microparticles that can be dispersed in a liquid suspension. The merging of both disciplines allows the creation of multiparticle liquid suspensions with the potential for use in track and trace applications as well as biological sensing.

We aim to be able to create a 'tag', a mix of binary 1s and 0s, which we can measure as an individual test result – similar to a barcode. We look to achieve this by fabricating Synthetic Anti-Ferromagnetic (SAF) microparticles with Perpendicular Magnetic Anisotropy (PMA). These consist of two nominally identical ferromagnetic layers that are antiferromagnetically coupled through a non-magnetic spacer layer. In the absence of an applied field, the magnetic layers orient in an antiparallel fashion (perpendicular to the plane), with a net zero moment. When in an applied field, these particles retain zero moment below the coupling field between the two layers, after which they align parallel to one another. The position of the transition between the antiparallel and parallel magnetisation states can be measured and is related to the indirect exchange coupling [17].

Critically, for a barcode style system to work, we require a tunable magnetic parameter. We achieve this through attenuation of the indirect exchange coupling. The presence/absence of a transition at a given coupling field gives rise to the 1/0 used in binary logic. The particles solutions can be combined, and when scanning in terms of an applied field, a barcode can be formed. The liquid suspension can then be applied to a surface to produce a tag. For the barcode to work, we require each channel field to be distinguishable from its near neighbours. The number of possible identifiers (combinations of particles forming an individual barcode) is proportional to the number of distinguishable channel fields. For this reason, we must look to maximise the number of distinguishable channel fields. A presence/absence detection method has 2^n different possible identifiers, where n is the number of available channels. This can be improved by using a volumetric detection scheme. Standard 1D optical barcodes (EAN) have 10^{11} possible identifiers, with many more possible with QR. The number of identifiers will provide a limit for the scalability of the solution.

Due to the large aspect ratio of the particles, they will tend to deposit with the magnetic easy axis perpendicular to the surface – and our sensor axis. As we plan to produce micron-scale particles, the information carriers will be effectively invisible, and difficult to locate for removal. An additional benefit of our proposed method is that balanced SAF particles – with nominally identical magnetic layers – should possess a net-zero moment and produce no magnetic field. This stops agglomeration in solution, allowing for easier application onto the tag surface.

This tagging method overcomes many of the current within the industry. Current optical technologies such as barcoding or QR coding are easily defaced or mimicked, and solid-state solutions such as RFID and BLE are susceptible to corruption by strong magnetic fields. By producing micron-scale information carriers our proposed tags are invisible to the naked eye and as such are

more difficult to tamper with. We propose to produce identifiers that have zero-remanant magnetisation, and as such are not susceptible to corruption of their remanant magnetic state.

The second half of this project involves the design and modelling of an appropriate detection scheme for these particles. We must consider that the reduction in lateral dimensions reduces the volume, and hence the magnetic moment of the particles. This leads to weaker signal strength, which must be considered in any detection scheme. The particles can be characterised using current laboratory devices, though these are large, static and expensive. We seek to have an industrially viable technology, ideally being low-cost, small/portable and usable with no prior experience.

In this thesis, we first look to validate that our encoded magnetic particles can be fabricated. We wish to characterise these using standard laboratory techniques. We next outline a potential detection scheme and test its viability using computational simulations and Computer-Aided Design (CAD).

[1] H. J. Richter and S. D. Harkness IV, "Media for magnetic recording beyond 100 Gbit/in.2," *MRS Bull.*, vol. 31, no. 5, pp. 384–388, 2006, doi: 10.1557/mrs2006.98.

[2] S. Bhatti, R. Sbiaa, A. Hirohata, H. Ohno, S. Fukami, and S. N. Piramanayagam, "Spintronics based random access memory: a review," *Materials Today*, vol. 20, no. 9. Elsevier B.V., pp. 530–548, Nov. 01, 2017, doi: 10.1016/j.mattod.2017.07.007.

[3] Everspin Technologies, "EMD4E001G | Everspin." https://www.everspin.com/family/emd4e001g?npath=3557 (accessed Jun. 17, 2021).

[4] I. Nurdin, M. R. Johan, I. I. Yaacob, B. C. Ang, and A. Andriyana, "Synthesis, characterisation and stability of superparamagnetic maghemite nanoparticle suspension," *Mater. Res. Innov.*, vol. 18, pp. S6-200-S6-203, Dec. 2014, doi: 10.1179/1432891714Z.0000000001017.

[5] J.-F. Berret, O. Sandre, and A. Mauger, "Size Distribution of Superparamagnetic Particles Determined by Magnetic Sedimentation," 2006.

[6] C. V. Yerin, "Particles size distribution in diluted magnetic fluids," *J. Magn. Magn. Mater.*, vol. 431, pp. 27–29, Jun. 2017, doi: 10.1016/j.jmmm.2016.09.122.

[7] R. Van Roosbroeck *et al.*, "Synthetic antiferromagnetic nanoparticles as potential contrast agents in MRI," *ACS Nano*, vol. 8, no. 3, pp. 2269–2278, Mar. 2014, doi: 10.1021/nn406158h.

[8] L. Peixoto *et al.*, "Magnetic nanostructures for emerging biomedical applications," *Applied Physics Reviews*, vol. 7, no. 1. American Institute of Physics Inc., p. 11310, Mar. 01, 2020, doi: 10.1063/1.5121702.

[9] R. Mansell *et al.*, "Magnetic particles with perpendicular anisotropy for mechanical cancer cell destruction OPEN," doi: 10.1038/s41598-017-04154-1.

[10] M. Goiriena-Goikoetxea *et al.*, "Disk-shaped magnetic particles for cancer therapy," *Applied Physics Reviews*, vol. 7, no. 1. American Institute of Physics Inc., p. 011306, Mar. 01, 2020, doi: 10.1063/1.5123716.

[11] R. Hergt, S. Dutz, R. Müller, and M. Zeisberger, "Magnetic particle hyperthermia: nanoparticle magnetism and materials development for cancer therapy," *J. Phys. Condens. Matter*, vol. 18, no. 38, pp. S2919–S2934, Sep. 2006, doi: 10.1088/0953-8984/18/38/S26.

[12] A. Jordan, R. Scholz, P. Wust, H. Fähling, and Roland Felix, "Magnetic fluid hyperthermia (MFH): Cancer treatment with AC magnetic field induced excitation of biocompatible superparamagnetic nanoparticles," *J. Magn. Magn. Mater.*, vol. 201, no. 1–3, pp. 413–419,

Jul. 1999, doi: 10.1016/S0304-8853(99)00088-8.

[13] G. G. Kenning *et al.*, "Detection of magnetically enhanced cancer tumors using SQUID magnetometry: A feasibility study," *Rev. Sci. Instrum.*, vol. 76, no. 1, p. 014303, Dec. 2005, doi: 10.1063/1.1834696.

[14] Endomag, "Magnetic Sentinel Lymph Node Biopsy." Accessed: Sep. 19, 2017. [Online]. Available: http://www.endomag.com/sites/default/files/documents/END0005 4pp Brochure_Single Pages.pdf.

[15] M. Colombo *et al.*, "Biological applications of magnetic nanoparticles," *Chem. Soc. Rev.*, vol. 41, no. 11, pp. 4306–4334, May 2012, doi: 10.1039/c2cs15337h.

[16] C. H. Yu, K. Y. Tam, C. C. H. Lo, and S. C. Tsang, "Functionalized silica coated magnetic nanoparticles with biological species for magnetic separation," in *IEEE Transactions on Magnetics*, Jun. 2007, vol. 43, no. 6, pp. 2436–2438, doi: 10.1109/TMAG.2007.894203.

[17] R. Lavrijsen, A. Feránndez-Pacheco, D. Petit, R. Mansell, J. H. Lee, and R. P. Cowburn, "Tuning the interlayer exchange coupling between single perpendicularly magnetized CoFeB layers," *Appl. Phys. Lett.*, vol. 100, no. 5, p. 052411, Jan. 2012, doi: 10.1063/1.3682103.

Chapter 2.

Literature review and theory

This chapter seeks to review the theory behind the magnetic information carriers as well as the techniques that are currently available to both activate and detect them. Our magnetic information is encoded into SAF microparticles of tuneable coupling strength, which turn 'on' and 'off' at distinct field values.

We begin with the magnetic theory behind our particle system. From this, we outline how particles are influenced by field and then how we obtain our desired properties. We achieve tuneable switching values via modulation of Ruderman Kittel Kasuya Yoshida (RKKY) coupling using attenuation spacer thickness and highly stable magnetic states with sharp switching through Perpendicular Magnetic Anisotropy (PMA). We consolidate these into one model, which can be used to characterise our information carriers.

Using the knowledge of the magnetic properties of our information carriers, we then analyse current detection methods to evaluate suitable technologies for measuring the changes between the 'on' and 'off' states. After this, we evaluate drive field mechanisms. Finally, we can outline a suitable detector geometry, as well as its limitations. This will provide the foundations for the modelling of our particle set for our chosen detector geometry.

2.1. Theory

Here we outline the physics needed in the production of our magnetic information carriers. We start by looking at the effect of a magnetic field on a macrospin through the Stoner-Wohlfarth model. Next, we characterise the physics underpinning our magnetic information carriers. We begin with how strong anisotropy is achieved out of the plane of the sample, moving onto antiferromagnetically coupled layers through indirect exchange. Finally, we combine these into one consolidated macrospin model that can be used to characterise our information carriers.

2.1.1. Stoner-Wohlfarth Model

Magnetic hysteresis can be calculated by minimising the energy of a system with respect to the applied field. The simplest analytical model that exhibits hysteresis is the model presented by Stoner and Wohlfarth [1].

The Stoner-Wohlfarth model assumes a single particle with uniform magnetisation. Therefore, we only need to consider the anisotropy and Zeeman energies [2].

The Stoner-Wohlfarth model assumes that the particle is elliptical with uniaxial anisotropy (which we define along the long axis of the ellipsoid). The particle is under the influence of an external field H at an angle α to the anisotropy axis and the magnetisation M is at an angle θ from the anisotropy axis, as seen in Fig 2.1. We can then minimise the energy to find the most favourable magnetisation angle. The energy density of the system is defined by:

$$E = K_A \sin^2(\theta) - \mu_0 M_S H cos(\alpha - \theta), \tag{2.1}$$

where the first term represents the anisotropy energy (uniaxial) and the second the Zeeman energy. Here, K_A is the uniaxial anisotropy, M_S the saturation magnetisation and μ_0 the permeability of free space.
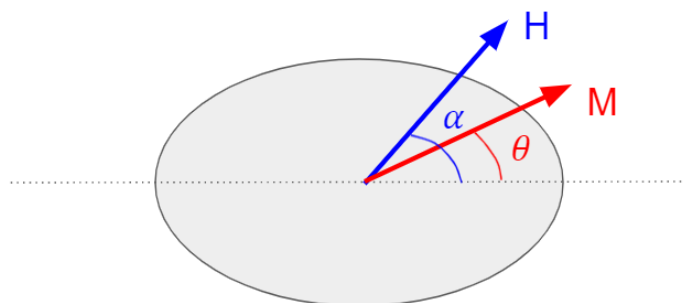
Fig 2.1 A schematic showing a Stoner particle and the definitions used in this section.

Hysteresis is seen when there are two solutions to the minimisation of E, (minima are found when $dE/d\theta = 0$ and $d^2E/d\theta^2 > 0$). Inflexions in $\frac{d^2E}{d\theta^2}$ indicate the transition between these two minima and characterise a switching event. It is easily noted that,

$$\frac{\delta E}{\delta \theta} = K_A \sin(2\theta) - \mu_0 M_S H sin(\alpha - \theta), \tag{2.2}$$

$$\frac{\delta^2 E}{\delta \theta^2} = 2K_A cos(2\theta) + \mu_0 M_S H cos(\alpha - \theta). \tag{2.3}$$

It is important to note the solutions at two particular field incidences – parallel and perpendicular to the anisotropy axis. Parallel to the anisotropy axis (where $\alpha = 0$), by expanding out the first double angle term, Equation 2.2 and Equation 2.3 become:

$$\frac{\delta E}{\delta \theta} = \sin(\theta)\left[2K_A \cos(\theta) + \mu_0 M_S H\right], \tag{2.4}$$

$$\frac{\delta^2 E}{\delta \theta^2} = 2K_A \cos(2\theta) + \mu_0 M_S H \cos(\theta). \tag{2.5}$$

Here, we wish to understand the angle with minimum energy, i.e. where:

$$\frac{\delta E}{\delta \theta} = \sin(\theta)\left[2K_A \cos(\theta) + \mu_0 M_S H\right] = 0, \tag{2.6}$$

$$\frac{\delta^2 E}{\delta \theta^2} = 2K_A \cos(2\theta) + \mu_0 M_S H \cos(\theta) > 0. \tag{2.7}$$

Equation 2.6 is satisfied in three situations: $\theta = 0$, $\theta = \pi$, $\cos(\theta) = -\frac{\mu_0 M_S H}{2K_A}$. In the situation where $\theta = 0$, Equation 2.7 has a solution if $H < -\frac{2K_A}{\mu_0 M_S}$. In the situation where $\theta = \pi$, Equation 2.7 has a solution if $H > +\frac{2K_A}{\mu_0 M_S}$. In the situation where $\cos(\theta) = -\frac{\mu_0 M_S H}{2K_A}$, Equation 2.7 has no real solutions, and cannot be an energy minimum. This shows that there are only two possible energy minima, corresponding to stable magnetisation states parallel/antiparallel to the anisotropy axis. Switching events occur between these two states, and are found when H equals the anisotropy field $H_K = \pm\frac{2K_A}{\mu_0 M_S}$. This yields square hysteresis loops with no bias. It should be noted that K_A includes both the uniaxial anisotropy K_U described earlier, but also the shape anisotropy that is apparent in all particles. Shape anisotropy arises due to the demagnetisation fields that are apparent within a particle. We can also describe the case of $\alpha = 0$ to have a coercivity H_C:

$$H_C = 2\left(\frac{K_U}{\mu_0 M_S}\right) + [(1 - 3\mathcal{N})/2]M_S, \tag{2.8}$$

with $\mathcal{N}$ describing the demagnetisation factor (which lies between 1 and 0, consistent with Brown's theorem) [3]. A second thing to note is that solutions to Equation 2.4 and Equation 2.5 have single solutions at $|H| > H_K$ giving $\theta = \pi$ at $H < -H_K$ and $\theta = 0$ at $H > +H_K$ but have two solutions for each value of $|H| < +H_K$. We then must consult the field history to establish the state of the system. This bifurcation of the energy minima is the basis for hysteresis in magnetic particles.

If we consider the second case, where the applied field is perpendicular to the anisotropy axis ($\alpha = \pi/2$) Equation 2.2 and Equation 2.3 become:

$$\cos(\theta)\,[2K_A \sin(\theta) - \mu_0 M_S H] = 0, \tag{2.9}$$

$$2K_A \cos(2\theta) + \mu_0 M_S H \sin(\theta) > 0. \tag{2.10}$$

Here, Equation 2.9 has solutions at $\theta = \pm\frac{\pi}{2}$ and $\sin(\theta) = \frac{\mu_0 M_S H}{2K_A}$. If $\theta = +\frac{\pi}{2}$, Equation 2.10 is satisfied when $H > +\frac{2K_A}{\mu_0 M_S}$, i.e., $H > +H_K$. If $\theta = -\frac{\pi}{2}$, Equation 2.10 is satisfied when $H < -\frac{2K_A}{\mu_0 M_S}$, i.e., $H < -H_K$. If $\sin(\theta) = \frac{\mu_0 M_S H}{2K_A}$, Equation 2.10 is satisfied within the region $|H| < \frac{\mu_0 M_S}{2K_A}$. This leads to a loop of three parts: negative saturation ($\theta = -\frac{\pi}{2}$) at $-H_K$, positive saturation ($\theta = \frac{\pi}{2}$) at $+H_K$, and a linear region between $-H_K < H \leq +H_K$, with $\theta = \sin^{-1}(\frac{\mu_0 M_S H}{2K_A})$. In this region, the component of M along the hard axis (the field direction) is equal to $(\mu_0 M_S^2/2K_A)H$. This description is typical of a paramagnet, with no hysteresis and saturating at H_K.

If we want to consider other values of θ, we consider the field in terms of parallel and perpendicular components (to the easy axis). If we also use the normalised field h where $h = H/H_K$, Equation 2.1 is transformed into:

$$E = K_A \sin^2(\theta) - 2K_A h_\parallel \cos(\theta) - 2K_A h_\perp \sin(\theta), \tag{2.11}$$

where $h_\parallel$ and $h_\perp$ are the components of h parallel and perpendicular to the anisotropy axis. Here, we look to understand where the equilibrium angles lie, i.e. $\frac{dE}{d\theta} = 0$. This is rearranged as:

$$1 = \frac{h_\perp}{\sin(\theta)} - \frac{h_\parallel}{\cos(\theta)}. \tag{2.12}$$

We wish to obtain information about the locations of switching events. Switching events occur at locations where the energy minima become unstable, i.e. where $\frac{dE}{d\theta} = 0 = \frac{d^2 E}{d\theta^2}$, giving:

$$0 = 2K_A[\cos(2\theta) + h_\parallel \cos(\theta) + h_\perp \sin(\theta)]. \tag{2.13}$$

Using these two parametric equations (Equation 2.12 and Equation 2.13) it is found that $h_\perp = \sin^3(\theta)$ and $h_\parallel = -\cos^3(\theta)$. Removing the theta dependence through $\sin^2 + \cos^2 = 1$, it is found that:

$$h_{\parallel}^{2/3} + h_{\perp}^{2/3} = 1. \qquad (2.14)$$

Equation 2.14 defines the boundaries of the Stoner-Wohlfarth astroid which defines the bifurcation of the free energy of the system. Outside the astroid there is a single energy minimum whereas inside, two minima exist. Travelling from the inside of the astroid to the outside, the boundary of the astroid defines the location of a switching event. Inside the astroid, no switch can take place – only a coherent rotation of magnetisation. The resulting astroid can be seen in Fig 2.2.

We can consider the magnetisation angle at all points by considering the gradient of the astroid:

$$\frac{dh_{\perp}}{dh_{\parallel}} = \frac{dh_{\perp}}{d\theta} \frac{d\theta}{dh_{\parallel}} = \tan(\theta). \qquad (2.15)$$

This shows that the magnetisation will always lie tangentially to the astroid for any given field. This construction is shown in Fig 2.2, and shows the existence of both minima present when inside the astroid –the stable minimum β and the metastable minimum β'.

Hysteresis loops can then be found by surveying the landscape of the energy minimum. By following the minimum energy path for a chosen function of h and θ. An example of how this might be constructed is given in Fig 2.3 from [4].
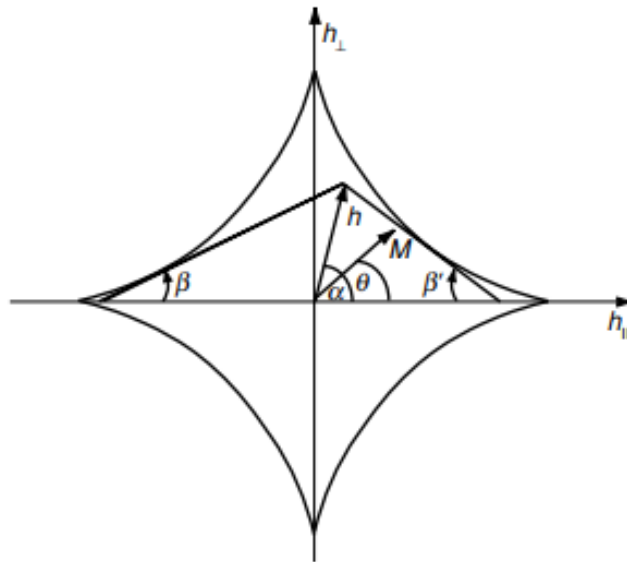
Fig 2.2 An ideal Stoner-Wohlfarth astroid. No switching event can take place within the astroid, only when crossing from the inside to the outside. The boundary of the astroid defines the point of bifurcation of the system's free energy [3]

Though the model was originally calculated for magnetic grains, in a thin film system where uniaxial anisotropy is present the Stoner-Wohlfarth model is considered an acceptable approximation if the demagnetising energy is considered [5].
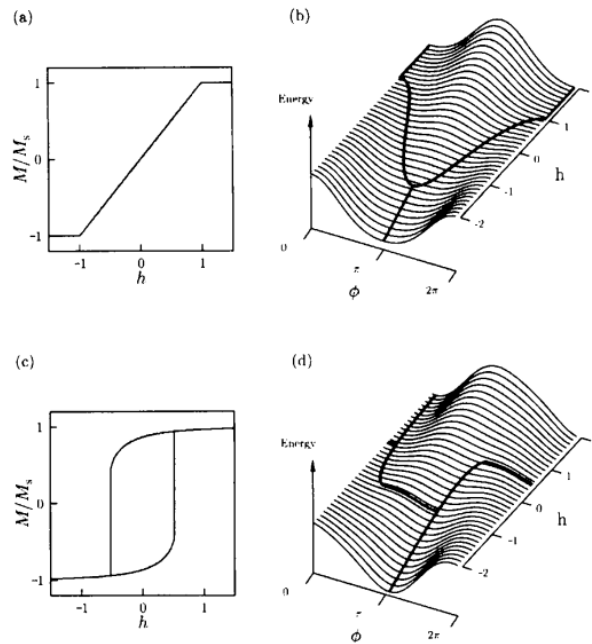
Fig 2.3 Demonstrations of hysteresis loops and energy minimisation landscapes for Stoner particles for (a,b), $\theta = 90°$ and (c,d), $\theta = 30°$. The hysteresis loop can be constructed for any field angle by taking the minimum energy path through the landscape. Note that this figure uses ϕ to denote magnetisation angle which is taken with respect to the field angle instead of the anisotropy axis. From [4]

2.1.2. Perpendicular Magnetic Anisotropy

It was noted earlier that the energy competition in thin-film systems could be described as a combination of the anisotropy and Zeeman energies of the system (amongst other energy contributions). The anisotropy determines how easy or hard it is to align the magnetisation of the material in a particular direction, with the easy axis offering the lowest energy configuration.

Atomic structure and its relationship with electron orbitals can create anisotropy within a material. Magnetocrystalline Anisotropy (MCA) is the difference in required energy to change a magnetic state when attempted along different directions within the material, reflecting the symmetry within the material. It has been theorised that the MCA in single crystals (cubic) arises due to the spin-orbit interaction (SOI) [6]. This couples the spin magnetic moment of an orbiting electron to the field it produces when orbiting the nucleus. This induces a small orbital momentum, which then couples to the crystal axes, coupling the electron spin to the crystal. This means that there is a strong correlation between the crystal axes, and the orientation of the orbitals (leading to magnetisation).

Perpendicular magnetic anisotropy (PMA) manifests due to the lowered symmetries at interfaces, the result being different terms for anisotropy for the surface layers in comparison to layers within the volume. It was first predicted by Néel in 1954 [7] and confirmed experimentally by Gradmann and Müller in 1968 [8], growing NiFe layers on Cu which possessed an easy axis of magnetisation

that is perpendicular to the film plane. They also observed an inverse relationship of the anisotropy magnitude with magnetic layer thickness. After further studies [9] it was found that the effective anisotropy observed could be separated into volume and surface terms:

$$K_{eff} = \frac{2K_S}{t} + K_V,$$

(2.16)

where t is the thickness of the magnetic layer. The assumption made here is that both the top and bottom surfaces of the film are identical. This expression shows a clear dependence on the proportion of surface atoms to bulk atoms. Plotting $K_{eff}t$ vs t allows us to evaluate both anisotropy terms, yielding $2K_S$ from the y-intercept and K_V from the gradient. It also shows for which thickness the effective anisotropy K_{eff} changes polarity – changing the easy anisotropy axis from out of plane (OOP) to in plane (IP). This thickness is termed the Spin-Reorientation Transition (SRT) thickness. An example of such a plot is given in Fig 2.4.
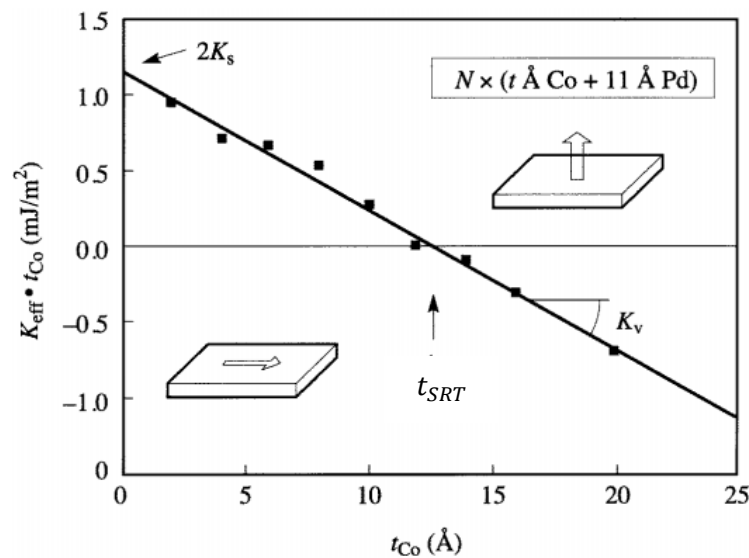
Fig 2.4 A schematic showing the relationship between effective anisotropy with magnetic layer thickness. K_S and K_V are shown. t_{SRT} is the SRT thickness, for which the system goes from in-plane to out-of-plane anisotropy. Note that for $K_{eff} < 0$ the sample has in-plane anisotropy, and perpendicular for $K_{eff} > 0$. From [9]

If we consider the angle-dependent section of the energy density (volume) for different field/magnetisation directions:

$$E = \left(K_i - \frac{\mu_0}{2}M_S^2\right)\sin^2(\theta) - \frac{1}{2}\mu_0 M_S H cos(\alpha - \theta).$$

(2.17)

We see that we have a competition between anisotropy (the first term – including magnetostatic energy) and Zeeman energy (the second term). Here α and θ are the angles of field and

magnetisation direction respectively defined from the film normal. The magnetostatic energy arises from the demagnetising field of the sample, which favours a magnetisation in the film plane. K_i contains all the intrinsic anisotropy contributions except shape anisotropy which is given by the second term $-\frac{\mu_0}{2} M_S^2$ [10]. The effective anisotropy K_{eff} is:

$$K_{eff} = K_i - \frac{\mu_0}{2} M_S^2. \tag{2.18}$$

We obtain K_{eff} from our samples by measuring the hard axis saturation field. Fig 2.5 demonstrates the situations where the hard axis saturation can be used, and how it should be handled. If $K_{eff} < 0$, the film is preferentially in-plane, and the hard axis saturation field (perpendicular to the plane) is given by $-2K_{eff}/\mu_0 M_S$. If $K_{eff} > 0$, the easy axis aligns out of the plane. If PMA is strong enough, the system can stabilise large scale domains and be fully remanent at zero fields. If this is the case, the hard axis saturation field is given by $2K_{eff}/\mu_0 M_S$. If the PMA is not dominant, as the field reduces the system forms a multi-domain state to minimise the magnetostatic energy. The system then requires a finite field to saturate for any field orientation. In this thesis, all our films have large PMA so the assumption that hard axis saturation equals $2K_{eff}/\mu_0 M_S$ is valid.
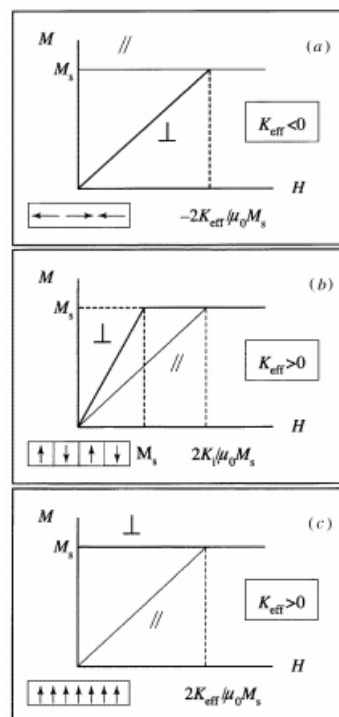
Fig 2.5 A schematic showing the effects of K_{eff} on the easy and hard axis MH measurements. (a) shows in-plane measurements, whereas (b) and (c) are out of the plane. Both (a) and (c) are for single-domain systems, with (b) depicting a multi-domain state. From [9]

Within this thesis, we use $Co_{20}Fe_{60}B_{20}$ as our thin magnetic layers. These systems exhibit strong PMA, which we further increase by utilising surrounding Pt layers to enhance the interfacial anisotropy. When a heavy metal/magnetic layer interface is present such as Pt/Co or Pd/Co, the 3d orbitals of the magnetic layer and the highly spin-polarized 5d orbitals of the heavy metal layer hybridise producing an increased d orbital moment m_{orb} compared to the magnetic layer on its own [11]. A linear relationship between $\vec{m}_{orb}$ and uniaxial PMA has been found in Co/Pt systems which suggests that it is an increase in $m_{orb}^{\perp}$ specifically, the magnetic orbital moment perpendicular to the plane [12]. This hybridization affects the spin-orbit constant ζ, which is directly related to the anisotropy (uniaxial) [13].

Though we use CoFeB/Pt which is amorphous, rather than Co/Pt which is crystalline, the hybridisation of the Co 3d and Pt 5d orbitals is still the main assumption for the large PMA observed at our interfaces. Other materials have been used in PMA systems [14], [15]. Substrate conditions also affect the strength of PMA [16].

2.1.3. Ruderman-Kittel-Kasuya-Yoshida (RKKY) coupling

Previously we have described the effects arising in single layer ultra-thin magnetic films. We also couple perpendicular layers with antiferromagnetic RKKY coupling. This is facilitated by a layer of Ruthenium sandwiched between the two ferromagnetic heterostructures. The thickness of Ru is chosen so that the RKKY coupling – which has an oscillatory dependence with the distance between magnetic layers – is antiferromagnetic. For nominally identical anti-ferromagnetic (AF) coupled magnetic bilayers, we can achieve a zero remanent state which inhibits agglomeration in solution. By careful control of the thickness of a thin Pt layer sandwiched between the magnetic layers and the Ru, the RKKY coupling strength can be attenuated. This leads to transitions of the magnetisation direction of the magnetic layers at differing applied fields, allowing channels of differing coupling strength to be distinguished from one another. The use of Pt to attenuate the RKKY coupling strength also yields a secondary benefit in an enhancement in the perpendicular magnetic anisotropy through hybridisation of the CoFeB (3d) and highly spin polarised Pt (5d) orbitals, as previously described.

Microscopic origin

RKKY is an indirect exchange coupling of two ferromagnetic layers sandwiched around a non-magnetic spacer layer. The original theory was put forward by Ruderman and Kittel who proposed that there existed a coupling of magnetic moments of magnetic nuclei with conduction electrons via the hyperfine interaction [17]. This was later expanded on by Kasuya and Yoshida who considered the effect of the conduction (s) electrons with the unoccupied inner shell electrons (d) within a

transition metal [18], [19]. This s-d interaction was an expansion on Zener's s-d model – which was purely phenomenological and did not include antiferromagnetism, originally interpreting the interaction purely to describe ferromagnetism [20].

In the RKKY interaction, spins $(\vec{S}_i)$ of the magnetic layer are located at sites defined by the atomic positions $(\vec{R}_i)$. These can interact with the conduction electrons within the spacer layer, inducing a spin polarisation which can propagate through the spacer and in turn couple with the spins on the second ferromagnetic layer – which the first is not contiguous with. Since the effects of this polarisation instigated in the first ferromagnetic layer impact the state of the second ferromagnetic layer with no direct coupling, the interaction is one of indirect exchange. This can then be evaluated as an interaction of two separate events – first the interaction between a ferromagnetic layer and the conduction electrons of the spacer layer and second the propagation of the polarisation through the non-magnetic layer. The first aspect manifests through the s-d mixing and hyperfine interaction [21], [22]. Bruno and Chappert tackled the second aspect by tackling the oscillatory interlayer exchange as an RKKY problem [23]. In the original RKKY approach, if the conduction elections are defined by spin $\vec{s}$ and positions $\vec{r}$ whilst the spins within the magnetic layer are defined by spin $\vec{S}_i$ and positions $\vec{R}_i$, the interaction between the magnetic layer spins and the conduction electrons is described by a contact potential $\mathcal{V}_i$

$$\mathcal{V}_i(\vec{r}, \vec{s}) = A_c \delta(\vec{r} - \vec{R}_i)\, \vec{s} \cdot \vec{S}_i, \tag{2.19}$$

where A_c defines an adjustable coupling strength parameter. This approximation has limitations and often yields incorrect phases for the coupling but yields accurate oscillation periods which is sufficient for Bruno's theory to build on accurately. Bruno's assumption accounts for the discreteness of the spacer layer. In their approach, the Hamiltonian for the interaction between a magnetic layer spin and a conduction electron spin is described by

$$\mathcal{H}_{ij} = J(\vec{R}_{ij}) \times \vec{S}_i \cdot \vec{s}_j, \tag{2.20}$$

In this, $J(\vec{R}_{ij})$ describes the exchange integral. When these are considered at large distances and considering the conduction electrons as a free electron gas with homogeneous density, the exchange integral for the free electron model yields:

$$J(\vec{R}) = \frac{4A_{ex}^2 m_e k_F^4}{(2\pi)^3 \hbar^2} F(2k_F R), \tag{2.21}$$

where A_{ex} is the intra-atomic exchange parameter, k_F the Fermi wavevector, m_e the mass of the electron and the decay function F defined as:

$$F(x) = \frac{x\cos(x) - \sin(x)}{x^4} \approx \frac{\cos(x)}{x^3}. \qquad (2.22)$$

This is the well-known decay characteristic of the RKKY interaction, with oscillation period $\Lambda = \lambda_F/2$ and an inverse cubic decay with respect to R. Here, λ_F is the Fermi wavelength. This shows damping of the exchange interaction as well as a dual-polarity, oscillating between ferro and anti-ferromagnetic coupling as a function of separation. If the approximation replaces ferromagnetic spins with two ferromagnetic layers with a continuous homogeneous spin density and selects one of the layers to act as a reference the interlayer coupling per unit area reduces to:

$$J_{1,2}(x) \approx -J_0 \frac{d^2}{x^2} \sin(2k_F x), \qquad (2.23)$$

with

$$J_0 = \left(\frac{A_{ex}}{V_0}\right)^2 S^2 \frac{m_e}{16\pi^2 \hbar^2}, \qquad (2.24)$$

where V_0 is the atomic volume and S the spin density. This interatomic coupling again has a period $\Lambda = \lambda_F/2$ but this has an inverse square dependence with x – the separation between the two ferromagnetic layers.

As we wish to obtain the strongest possible antiferromagnetic coupling between our two ferromagnetic layers, we select the smallest spacer distance that corresponds to an AF interlayer coupling peak. This scenario is shown in Fig 2.6.
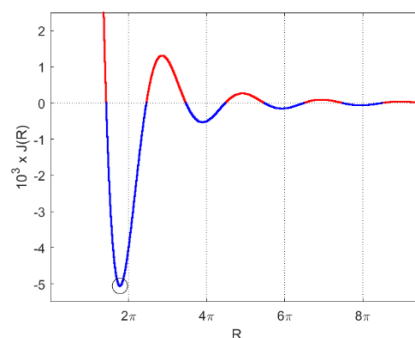
Fig 2.6 Schematic showing the oscillation and decay of interlayer coupling (Equation 2.22) as a function of separation. Anti-ferromagnetic coupling is denoted in blue, ferromagnetic-coupling in red. The strongest AF peak is indicated by the black circle and is the thickness aimed for throughout this work. In this plot, $2k_F R \rightarrow R$ for simplicity.

Phenomenological treatment

We consider the RKKY interaction to be an additional term in the equations for energy density. It is seen that the coupling energy density (per unit area) between two ferromagnetic layers with RKKY coupling has an angular dependence usually described by:

$$E_{RKKY}(\theta) = J_{RKKY}\cos(\theta_2 - \theta_1), \tag{2.25}$$

where J_{RKKY} [Jm^{-2}] is the interlayer coupling constant of the coupled film system and $\theta_{1,2}$ describe the angles of the magnetisation of each layer with respect to the easy axis of magnetisation [24].

If we assume both layers to be nominally identical, we may consider the energy density term as a mutual coupling field between the layers:

$$J_{RKKY} = \mu_0 H_J M_S t_{CoFeB}, \tag{2.26}$$

with H_J the coupling field, and t_{CoFeB} the thickness of the magnetic layers, respectively. The value of the coupling field can be extracted experimentally from minor loops. In a bilayer SAF, a minor loop is a switching of a single layer back and forth between its remanent and saturated states. Though we assume here that both magnetic layers are identical, in reality minor differences will be seen. This means that the first switching event occurs in the softer of the two magnetic layers.
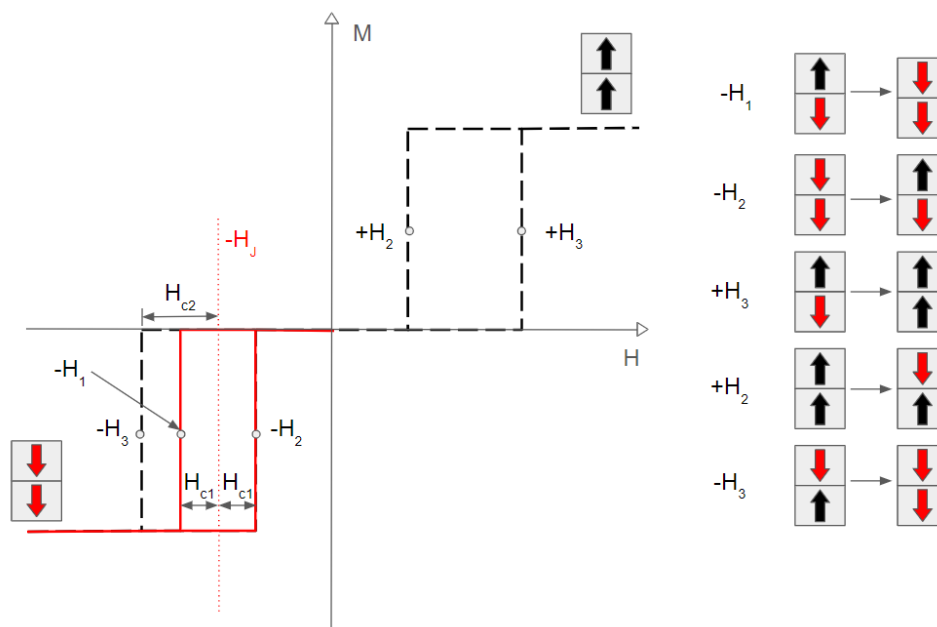
Fig 2.7 A schematic showing the nomenclature for each switch in a major (black) or minor (red) loop. In this figure, the field is applied along the easy axis – i.e. perpendicular to the film plane. M defines the magnetisation state of the system, and H the applied field. In this instance, it is assumed that the top layer is magnetically softer. Note that H_2 is the same for both major and minor loops, being the P-AP switch of the softer layer in both instances.

The coupling field is defined as the centre of the minor loop, calculated as the average of switching values for the parallel to anti-parallel (P-AP) and anti-parallel to parallel (AP-P) transitions. These are shown in Fig 2.7, with $H_J = \frac{1}{2}(H_1 + H_2)$. The switching fields for each transition are then defined as $H_{1,2} = H_J \pm H_{C1}$ with H_{C1} the coercivity of the easier layer $H_{C1} = \frac{1}{2}(H_2 - H_1)$. The coercivity of the harder magnetic layer can be deduced from the major loop. The coercivity in a major loop is equal to the sum of the coercivities from both magnetic layers. Thus $H_{C2} = H_3 - H_J$.

We will use these switching events to detect our information carriers. When $M = 0$, the system will be considered to be in its 'off', or 0 state. At $M = M_s$, the system will be considered in its 'on' or 1 state. By application of different fields, we can detect the presence/absence of particles with a particular switching field, giving a binary information output.

2.1.4. Consolidating exchange and anisotropy

Considering the energy as an areal density (as opposed to volume density), the magnetisation angle dependence is:

$$E = K_{eff,1}t_{CoFeB,1}\sin^2(\theta_1) + K_{eff,2}t_{CoFeB,2}\sin^2(\theta_2) +$$
$$\mu_0 M_S H t_{CoFeB,1}\cos(\alpha - \theta_1) + \mu_0 M_S H t_{CoFeB,2}\cos(\alpha - \theta_2) \quad (2.27)$$
$$+ J_{RKKY}\cos(\theta_2 - \theta_1),$$

where $t_{CoFeB,1,2}$, $K_{eff,1,2}$ and $\theta_{1,2}$ are the CoFeB thickness, effective anisotropy and magnetisation angle for each layer (1,2). In this thesis, bilayers of equal nominal magnetic layer thickness are produced and are assumed to have the same anisotropy $K_{eff,1} = K_{eff,2} = K_{eff}$, reducing the energy density to:

$$E = K_{eff}t_{CoFeB}[\sin^2(\theta_1) + \sin^2(\theta_2)]$$
$$+ \mu_0 M_S H t_{CoFeB}[\cos(\alpha - \theta_1) + \cos(\alpha - \theta_2)] \quad (2.28)$$
$$+ J_{RKKY}\cos(\theta_2 - \theta_1).$$

M_S can be found from easy axis measurements, though a subtle difference occurs for the measurement of the anisotropy coefficient. Whereas before we showed the effective anisotropy to be related to the hard axis saturation field, we must note that this was for a single layer. For hard axis saturation to occur in our AF PMA SAF, both the anisotropy field and the coupling field for both layers must be overcome, meaning that $H_{Sat} = H_K + 2H_J$. As described in section 2.1.2, $K_{eff} = \mu_0 M_S H_K / 2$. Since we can obtain values for saturation magnetisation, coupling field and anisotropy field from experiments, we can also calculate K_{eff}:

$$K_{eff} = \frac{1}{2}\mu_0 M_S \left(H_{sat} - 2H_J\right).$$

<div align="right">(2.29)</div>

The magnetisation angle in these systems is always a competition between effective anisotropy and RKKY coupling, exchange and Zeeman energies. Anisotropy makes it favourable for the spins to lay in a particular orientation and coupling favours parallel/antiparallel alignment. Fig 2.8 shows the expected loops for systems where a) anisotropy is the dominant energy contribution, b) the weaker contribution and c) a system with no anisotropy. We maintain high PMA, evidenced by strong spin-flip transitions (as in Fig 2.8a)). The key parameters defining their transitions are extracted from measurements.

Now that the theory underlying the behaviour of our magnetic information carriers is understood, we shall examine the current technologies available for both applying the driving field and sensing the changes between the 'on' and 'off' states. From this information, we can choose a suitable detection geometry for design and modelling.
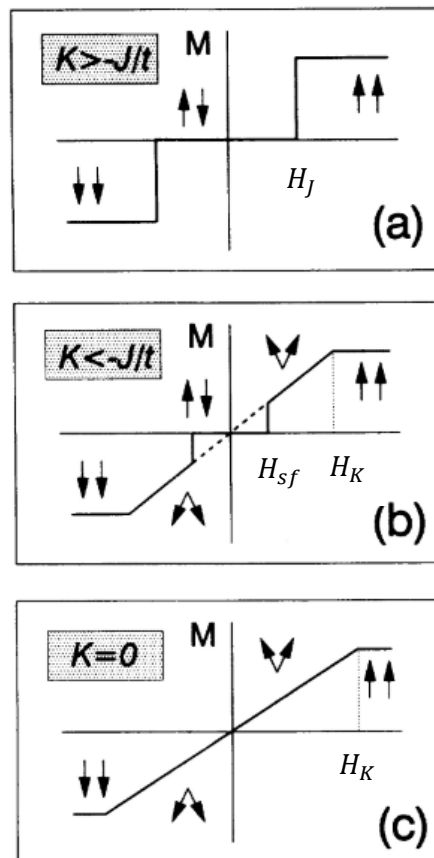
Fig 2.8 M-H curves for a nominally identical bilayer stack with different uniaxial anisotropies. In (a), anisotropy is the dominant energy contribution, (b) the weaker contribution and (c) has no anisotropy. From [25]. In this schematic, H_{sf} represents the field at which the spin flop transition occurs.

2.2. Current methods of detecting magnetic signals

2.2.1. Magnetoresistive

Magnetoresistive elements depend on the changes in the resistive properties of a material according to its magnetisation. This has developed from simple, spin-orbit scattering in single layers (Anisotropic Magnetoresistance (AMR)), to the revolutionary Giant Magnetoresistance (GMR) due to spin accumulation in multilayer magnetic stacks and onwards with Tunnelling Magnetoresistance (TMR) in Magnetic Tunnel junctions (MTJs). These effects have underpinned the progress in magnetic storage technology over the past half-century. AMR is measured by the effect of a field on the magnetisation direction of a uniaxial, IP material such as permalloy. The field is applied perpendicular to the easy axis, which acts to torque the magnetisation away from the easy axis. This changes the resistivity of the material, which is detected. The difference between parallel and perpendicular resistivities is no larger than 2-4%, limiting the sensitivity of these devices.

GMR improved this, with multilayer systems exhibiting over 50% changes in resistivity in the initial studies by Fert and Grunberg [26], [27], but up to 82% in more recent work [28]. In GMR systems, multilayer stacks of ferromagnetic and normal metals are used to create spin accumulation at the interfaces which further amplifies the change in resistances between parallel and perpendicular states. GMR sensors are often used in spin-valve structures. In this system, two ferromagnetic layers are present, where one layer's magnetisation is constrained (the fixed layer) and the other is free to interact with external fields (free layer). The free layer can then rotate relative to the fixed layer, and the resistivity of the sample indicates the applied field magnitude.

The most recent developments have been in TMR – a similar structure to a spin valve, but instead of a non-magnetic spacer layer, an insulating material is used. This means that any conduction must occur via tunnelling. These systems exhibit much higher differences in resistivity, though they are intrinsically noisier than GMR systems so require higher signal to noise ratios to be effective [29].

Magnetoresistive sensors can be used in high-frequency applications and have noise floors of 10 nT/√Hz (AMR/TMR) or 1 nT/√Hz (GMR) [3]. They have extremely small package sizes and are easily integrated with integrated circuits (ICs) for applications.

These sensors have proved fruitful in many areas, showing promise in magnetic memory (spin valves using GMR and MTJs using TMR [30]–[33]), cryogen free medical science devices (e.g. in magnetocardiography [34]–[36]), biological marker detection [37], [38], cheap consumer magnetic sensors (compasses, proximity sensing, magnetic switches, positional indicators [39]) and non-destructive evaluation (material testing and current testing [40]). Though these systems have the sensitivity to detect signals from micron-sized, nanometre thick magnetic particles (as proven by the

differentiation between grains in magnetic recording technology), they can only be used in small applied fields, no larger than the saturation value of the sensor. This also limits the upper bound for magnetic field sensing capabilities - generally of the order 1 mT.

2.2.2. Magneto-Optical

Magneto-optical sensing can provide information about the magnetisation state of a sample via the magneto-optical Kerr effect (MOKE). More information about the theory behind these systems is presented in section 3.1.2.2, but briefly, the interaction of polarised light with a magnetised moment causes a rotation in the polarisation angle of the light, which is detected. These measure changes in magnetisation angle, and only probe areas which interact with the incident light. This means that MOKE is localised and surface sensitive, limited to the penetration depth of the laser light (of the order of 25 [nm] for transition metals [41]).

MOKE requires precise optical alignment and optimisation, though as it measures differences in magnetic states it can be extremely sensitive locally – easily characterising a single microparticle. As optical measurements are sensitive to changes in magnetisation, a magneto-optical system could be used to detect the presence or absence of a particular magnetic property in the hysteresis loops of a sample – in our instance the switch at a particular switching field value. Due to the localised nature of the measurement, the laser would either have to scan across a sample to detect a collection of microparticles or be completed out of focus to enlarge the spot size. Optical instrumentation requires good vibration isolation, which must be considered in the design of devices.

2.2.3. Inductive

Inductive technologies emerge from Faraday's law of induction. A moving charge produces a magnetic field, this is Ampere's law. Faraday's law works on the inverse – a changing magnetic field will induce a voltage in a conductive material. This effect is increased by making the conductor path longer, generally through coiling. The voltage (ε) is then proportional to the rate of change of the magnetic flux (Φ) through the surface of the coil (S):

$$\varepsilon = \oint_S -\frac{\delta \Phi}{\delta t}. \tag{2.30}$$

As can be seen from Equation 2.30, a time variance is required to produce an EMF. This can either be achieved through the movement of the sample with respect to the coil, e.g. linear motion in an extraction magnetometer or rotation with respect to the coil, e.g. a rotating field magnetometer.

Due to this being dependent on the surface of the coils, the arrangement of the coils can be made to benefit the application. For example, gradiometer coil sets, consisting of two oppositely wound but otherwise identical coils, allow for the nulling of potential variations in a homogeneous applied field.

This idea is utilised in almost all flux-dependent techniques, with much work on the optimisation of coil-sets [42], [43]. Inductive coils can achieve sensitivities of $\sim 10^{-10}\ T$ [44].

Compared to new electronic sensors (Hall or magnetoresistive), inductive sensor units are generally much larger. However, their breadth of application is large and the sensor can be tailored to the system. As such, the application space is vast, from examining large undulator sets in particle accelerators [45] to actuator feedback in small reciprocating electric motors [46], [47].

However, on the downside, as the induction is driven by charge carriers, inductive technologies can be subject to thermal drifting. They are also highly calibration dependent. Due to their sensitivity to temporal changes in magnetic flux density, inductive technologies are highly spatially dependent and should be vibrationally isolated from any motion (usually external vibrations).

2.2.4. Hall effect sensors

Hall effect devices utilise the Lorentz force to measure magnetic fields. The simplest version of a Hall device is seen in Fig 2.9, showing the field, current and Hall voltage orthogonal to one another.
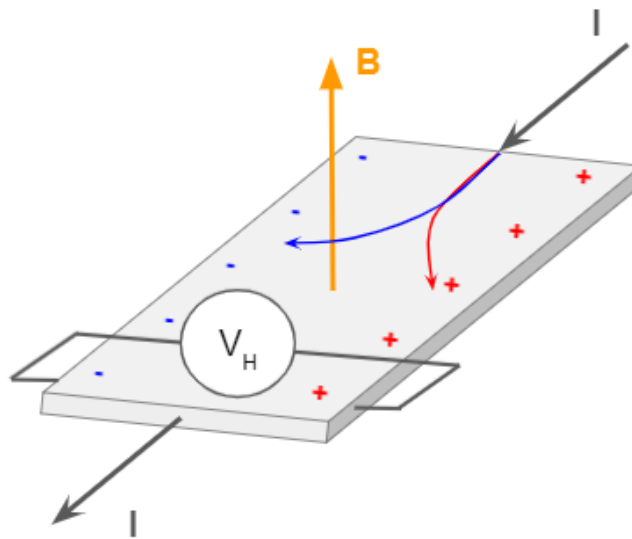
Fig 2.9 simple Hall geometry, with the current and applied field perpendicular to one another. A Hall voltage is produced in the direction orthogonal to both current and applied field.

In the presence of a magnetic field perpendicular to the direction of the current, the charge carriers are deflected by a Lorenz force towards the outer extents of the sample. This charge accumulates until the potential difference generated is equivalent to the motion of charge due to the Lorentz force. This means that a Hall sensor is only sensitive to a field perpendicular to the sensor. The generated potential difference is proportional to the inverse of the number of charge carriers in the system, and as such, semiconductors make great candidates for enhanced Hall effect devices. The voltage V_H is directly proportional to the applied field B, with:

$$V_H = \frac{BI}{n_c et},$$ (2.31)

where B is the applied field, I is the sensing current, n_c the charge carrier density, e the electron charge and t the thickness of the material.

Hall effect sensors occupy a wide application space due to their low cost and ease of measurement. They are great candidates in consumer electronics as magnetic switches [48], rotational sensors [49], proximity sensors (in conjunction with a permanent magnet) [48], accelerometers [50], flow rate sensing [51], [52], camshaft sensors [53], etc. They are also used in higher-level applications such as field confirmation from permanent magnet arrays (such as particle accelerators) [45], [54], 3D field mapping [55], [56], calibration of applied fields in laboratory instrumentation and feedback control [57]. Their small package size, ease of integration with ICs, simplicity and inexpensive nature cohere strongly with the project's requirements.

Although Hall sensors have many beneficial properties, there are also drawbacks. Firstly, they are limited to $\sim 0.1\ \mu T$ resolution [45]. This means that they are not suitable for dynamic measurement of fields from collections of SAF particles. Due to their reliance on electrical properties, they are susceptible to temperature drifts and ageing of the semiconductor leading to drifting of the dopants in the layer [58]. This means that these devices require periodic re-calibration.

2.2.5. Force

An applied magnetic induction B produces a force on a magnetic moment m equal to $F = \nabla(m \cdot B)$. Magnetic fields are usually applied using an electromagnet in a single direction(x), with a gradient in the perpendicular direction (z). This simplifies the force to $F_z = m(dB_x/dz)\hat{e}_z$. To achieve field gradients, tapered pole pieces or secondary coil sets are used. The force can be measured using a cantilever or piezoelectric module, providing a scalar measurement of the magnetic moment. The field can be oscillated with a frequency equal to the resonant frequency of the sample holder, allowing for larger signals. This allows for the detection of magnetic moments comparable to those of Vibrating Sample Magnetometry (VSM), which is of the order $10^{-10}\ \mathrm{Am^2}$ [59]–[61].

Examples of force measurements are the Faraday balance and Alternating Field Gradient Magnetometers (AFGM). These techniques are generally large and expensive. The force sensors must be mechanically isolated, usually by hanging the sense module using dampening springs. This also impacts the portability of the device.

2.3. Summary of detection techniques

Here we outline a summary of the detection techniques described above.

Method	Sensitivity	Detects	Advantages	Drawbacks
Magnetoresistive	10^{-9} T [29]	H	Measures changes, cheap, sensitive	Saturable at fields $\approx 1\ mT$
Magneto-optical	10^{-5} T [3]	M	Measures changes	Local, surface sensitive, large, sensitive to vibrations
Induction	10^{-10} T [44]	$\delta\Phi/\delta t$	Flexible, cheap	Spatially sensitive
Hall	10^{-7} T [45]	B	Cheap, linear, integrates with ICs	Low sensitivity – unable to measure magnetic particles
Force	$10^{-11} Am^2$ [59], [60]	m	Sensitive	Large, sensitive to vibrations, costly
VSM	$10^{-10}\ Am^2$ [61]	m	Sensitive	Large, sensitive to vibrations, costly
SQUID	$10^{-11}\ Am^2$ [62]	m	Sensitive	Requires cryogenics

Table 2.1 Summary table of magnetic sensing techniques outlined in section 2.2.

2.4. Magnetic field production methods

Magnetic fields can emanate from one of two sources: moving electric charges and magnetic materials. When considering electromagnetic problems, we often interchange between the two to make the problem easier to solve, e.g. the Coulombian and Ampèrian approximations in field calculations convert magnetic moment to equivalent current loops or surface charge, respectively.

In this section, we assess both field production methods, their benefits and drawbacks. From this, we evaluate which method shows the most promise and propose a geometry to be used within our detector.

2.4.1. Solenoidal field production

We first look at the production of a magnetic field from moving charges – or solenoidal field. Solenoids can be easily tailored to suit their application, with the field produced being proportional to the coil radius, current and number of turns. The field within a long enough solenoid of length l, is $H = IN/l$, often simplified to $H = nI$, with $n = N/l$ the number of turns per unit length. The magnitude of the field can be increased by placing a piece of soft magnetic material with high permeability within the core of the solenoid. The field is, increased in magnitude by the permeability μ. This benefit is limited – once the magnetic moment of the material is fully saturated, no additional

benefit is seen – but allows for an increase of up to μM_S. The field diverges from the edges of the core material, decreasing rapidly with distance to the surface of the core. This can be reduced by creating a circular yoke with a small discontinuity, or air gap. This allows for a closed flux path, concentrating the flux in a uniform region within the air gap. Most modern laboratory electromagnets use this geometry. The exposed edges of the core can be tapered to further concentrate the magnetic flux.

The magnitude and polarity of the field can be modulated using the input current. Since solenoidal fields are proportional to current, they are often limited by their resistive heating. Dissipative power is proportional to I^2, and overheating can cause disintegration of cable dielectrics and short-circuiting of the system. For large systems, this is improved by using water cooling, but this increases the size of the device and inhibits its portability. Heating can be reduced by increasing the diameter of the cables. Again, this adds to the spatial cost.

Electromagnetic field production is also limited to static or low-frequency applications at high fields. At higher frequencies, the changing current polarity causes eddy currents in the conductors opposing the direction of the field. This provides a limit on the field sweep rate and maximum field at a particular frequency. Care should also be taken as the inductance of the coil scales with the number of turns. The time constant (τ) of an LR circuit is $\tau = L/R$, with L the inductance and R the resistance. This means that an increase in the number of turns N will increase the inductance and also the time constant of the coil, reducing its responsiveness. For this reason, the field is generally changed gradually, limiting high field, high-frequency application.

2.4.2. Permanent magnets

Alternatively, ferromagnets can be used to create magnetic fields. In these systems, highly coercive, or magnetically 'hard', materials can be actuated to create a changing field, or combined to superpose fields for particular purposes – e.g. to increase the homogeneity. These systems require no energy (other than in physical actuation) and can be used for both uniform and non-uniform field applications. There is no time variance unless actuated, and coercivities of up to 1.64 T have been produced [63]. For applications that require a large field sweep rate, permanent magnets provide a good option as they are only limited by actuation speed and are not limited by self-inductance.

The magnitude of magnetic fields from permanent magnets is dependent on their spontaneous polarisation J_S, a term more commonly used in engineering with the relationship $J_S = \mu_0 M_S$, where M_S is the saturation magnetisation. There have been large developments in the field in the previous century, with the development of material science and the ability to overcome shape constraints with the discovery of magneto-crystalline anisotropy [64]. This is evidenced by the increase in energy

per unit volume (BH, Jm^{-3}), doubling every ~12 years over the course of the 20th century [65]. The market is now dominated by neodymium iron boron (commonly $Nd_2Fe_{14}B$) magnets, which can easily have fields $> 1\ T$ near the surface of the materials, with spontaneous magnetisation values of $J_s > 1.5\ T$ ($M_S = 1.28 \times 10^6\ Am^{-1}$) [66].

In permanent magnets, the anisotropy field values are considerably higher than the spontaneous polarisation. This means that the magnetisation is virtually unaffected by other fields in an assembly – two perpendicular $SmCo_5$ blocks with perpendicular easy axes in full contact will deviate by less than one degree [67]. This effective magnetic transparency (non-interaction) means that flux from multiple sources superposes linearly and allows for combinatory assemblies. Permanent magnets possess a non-uniform field profile. By combining magnets in ring structures such as Halbach arrays [3, 68-69] uniform fields can be obtained within the airgap.

Until only a decade ago, it was believed permanent magnets could altogether replace electromagnetic sources for some applications, with much interest in the field [66], [67]. The recent findings on the scarcity of rare-earth elements have been a serious limitation to this, but the benefits are undeniable for small applications. For instance, if we consider a small disk-shaped magnet of 8 mm diameter, 2 mm thickness and $J_s = 1$ T, a coil with the same diameter would require 2000 A turns. This is not physically achievable. This system will also not suffer from electrical losses or corresponding frequency limits.

Our drive field also must be compatible with the sensing technique. For example, gradiometer coils rely on subtraction of the drive field to detect the smaller signals from a sample, requiring both coils to be under the influence of the same drive field magnitude. The measurement resolution can be limited by this. Permanent magnets have been shown to be effective replacements to electromagnets in inductive systems such as VSM, with comparable resolution and greatly decreased spatial requirements [68], [69]. This makes a device more portable, which aligns with our detector requirements.

However, there are limitations to using the field from permanent magnets. Though the magnetic properties are incredibly stable, they can still be altered by application of a magnetic field greater than the anisotropy field of the magnet. The Curie temperature of $Nd_2Fe_{14}B$ is $T_c = 588\ K$, meaning they are also not suitable for extreme temperature applications [66]. Some permanent magnets, such as NdFeB, are also susceptible to corrosion along grain boundaries, which can limit their applications. This corrosion can change the magnetic state of the material, and cause it to become brittle.

Though fields from permanent magnets are stable, they can be time-varying if the magnet is actuated. This can lead to a large eddy current generation in conducting material near the drive magnet. This may produce reductions in drive field value and could also cause spurious detection signals. This can be minimised by using insulating or laminated materials but should be considered in an effective measurement system.

2.5. Proposed detector technique and geometry

There are a multitude of techniques available to detect magnetic signals, though we must consider which would be most suitable for our application. Our information carriers will be differentiated by their switching fields. Particles are in one of two states, with an 'on' state above the switching field and an 'off' state below. Therefore, our sensor must be able to operate under a potentially large applied field without saturating, eliminating sensitive and cheap technologies such as magnetoresistive sensors.

We must also consider the requirement for a compact, easy to use and inexpensive device. For this reason, apparatus such as force technologies are unsuitable. MOKE is insensitive to applied fields and would provide the sensitivity needed to measure the switching of single microparticles but only in focused mode, rendering the technology impractical for detecting the switching of a large collection of randomly located particles.

Inductive technologies have the benefit of flexibility, with the possibility to nullify the background signal from applied fields. The sensor element is extremely inexpensive, though they will require large and costlier apparatus such as lock-in amplifiers to enhance the signal to a measurable value. Inductive sensors require a temporal change in magnetic flux – which will arise during the switching event from zero net moment to saturation. To achieve this, we must either search for a discontinuity in the voltage from an AC applied field or apply DC fields of a fixed value and oscillate the sample (as in VSM). The latter would be difficult to achieve as it would limit our application space to objects that must be insensitive to the oscillations. For this reason, inductive technologies with AC drive fields would be best suited to our application.

Initially, to increase the number of available channels, we need to have a large range of coupling fields. To maximise this range, we require high maximum coupling fields, with an initial estimate of 0-0.5 T. This is the highest coupling field that is reliably achieved in our group. This field can be achieved with a permanent magnet.

As we will see in Chapter 4, our information carriers are largely insensitive to magnetic field components in the sample plane. A cylindrical rotating permanent magnet can therefore be used to provide a sinusoidal out of plane field component.

The downside to AC fields is eddy current production. When looking to measure inductively, any conductive material from the sensor assembly could produce spurious signals in our detector. These will have the same frequency as the drive field and will not be simple to filter using lock-in techniques. For this reason, we minimise their effects by using an assembly made of as little conductive material as possible.

In this setup, we can differentiate between channels in a presence/absence technique, with variation in AC drive field amplitude controlled by the magnet-sample distance. This will have to be controlled extremely accurately due to the fast decay of field strength with increasing distance. If the technique proves sensitive, we may also expand this to not only measure the presence/absence of a particular switching event but also the volumetric quantity of particles within a specific channel, allowing for many more combinations of digital identifiers.

To ensure nullification of the drive field, we will place coils at equal distances on either side of the drive magnet. Due to the symmetry of the system, the field should be equal at both points – though due to the fast decay of field strength, the positioning of both coils will need to be extremely accurate. A PID feedback system may be used to minimise the effect of position inaccuracies in real-time. This would minimise the sinusoidal background that is present in the detection coil voltage as a result of coil misalignment. The sample can be placed in direct contact with one of the coils in the pair, keeping their separation within the micrometre scale. When the switching field is reached, the change in magnetic state has a concomitant change in the magnetic particle's field. This is incredibly small due to its small magnetic volume, so having the smallest separation gives us the best chance of detection.

We will seek to design and computationally optimise a detector consisting of inductive sensors and an AC permanent magnet drive field as described in the previous paragraphs. The computational simulation will test the limits of both our detector and our particles, allowing for a faster and more cost-effective build process.

In the next chapter, we outline the experimental methods used to develop and characterise our information carriers as well as the methods employed in the computational optimisation.

[1]   E. C. Stoner and E. P. Wohlfarth, "A mechanism of magnetic hysteresis in heterogeneous alloys," *Philos. Trans. R. Soc. London. Ser. A, Math. Phys. Sci.*, vol. 240, no. 826, pp. 599–642, May 1948, doi: 10.1098/rsta.1948.0007.

[2]   A. Aharoni, *Introduction to the theory of ferromagnetism*. Oxford University Press, 2000.

[3]   J. M. D. Coey, *Magnetism and Magnetic Materials*. Cambridge: Cambridge University Press, 2010.

[4]   S. Blundell, *Magnetism in condensed matter*. Oxford University Press, 2001.

[5]   C. Tannous and J. Gieraltowski, "The Stoner-Wohlfarth model of ferromagnetism," *Eur. J. Phys.*, vol. 29, no. 3, pp. 475–487, May 2008, doi: 10.1088/0143-0807/29/3/008.

[6]   J. H. Van Vleck, "On the anisotropy of cubic ferromagnetic crystals," *Phys. Rev.*, vol. 52, no. 11, pp. 1178–1198, Dec. 1937, doi: 10.1103/PhysRev.52.1178.

[7]   L. Néel, "Anisotropie magnétique superficielle et surstructures d'orientation," *J. Phys. le Radium*, vol. 15, no. 4, pp. 225–239, Apr. 1954, doi: 10.1051/jphysrad:01954001504022500.

[8]   U. Gradmann and J. Müller, "Flat Ferromagnetic, Epitaxial 48Ni/52Fe(111) Films of few Atomic Layers," *Phys. status solidi*, vol. 27, no. 1, pp. 313–324, Jan. 1968, doi: 10.1002/pssb.19680270133.

[9]   M. T. Johnson, J. H. Bloemen, J. A. Den Broeder, and J. J. De Vries, "Magnetic anisotropy in metallic multilayers,", *Rep. Prog. Phys.,* vol 59, 1409, IOP Publishing, 1996. doi: 10.1088/0034-4885/59/11/002.

[10]   C. A. F. Vaz, J. A. C. Bland, and G. Lauhoff, "Magnetism in ultrathin film structures," *Reports Prog. Phys.*, vol. 71, no. 5, p. 056501, May 2008, doi: 10.1088/0034-4885/71/5/056501.

[11]   D. Weller, H. Brändle, and C. Chappert, "Relationship between Kerr effect and perpendicular magnetic anisotropy in Co1-xPtx and Co1-xPdx alloys," *J. Magn. Magn. Mater.*, vol. 121, no. 1–3, pp. 461–470, Mar. 1993, doi: 10.1016/0304-8853(93)91246-4.

[12]   D. Weller, Y. Wu, M. G. Samant, B. D. Hermsmeier, and C. Chappert, "Orbital magnetic moments of Co in multilayers with perpendicular magnetic anisotropy", Phys. Rev. B, vol. 49, pp. 12888-12896, 1994.

[13]   P. Bruno, "Physical origins and theoretical models of magnetic anisotropy," in *Ferienkurse des Forschungszentrums Jülich*, KFA Jülich, 1993, pp. 24.1-24.27.

[14] C. S. S P Parkin, N. More, and K. P. Roche, "PHYSICAL REVIEW LETTERS Oscillations in Exchange Coupling and Magnetoresistance in Metallic Superlattice Structures," 1990.

[15] M. D. Stiles, "Interlayer exchange coupling," *J. Magn. Magn. Mater.*, vol. 200, no. 1–3, pp. 322–337, Oct. 1999, doi: 10.1016/S0304-8853(99)00334-0.

[16] D. Weller, H. Brändle, G. Gorman, C. J. Lin, and H. Notarys, "Magnetic and magneto-optical properties of cobalt-platinum alloys with perpendicular magnetic anisotropy," *Appl. Phys. Lett.*, vol. 61, no. 22, pp. 2726–2728, Nov. 1992, doi: 10.1063/1.108074.

[17] M. A. Ruderman and C. Kittel, "Indirect exchange coupling of nuclear magnetic moments by conduction electrons," *Phys. Rev.*, vol. 96, no. 1, pp. 99–102, Oct. 1954, doi: 10.1103/PhysRev.96.99.

[18] T. Kasuya, "A Theory of Metallic Ferro- and Antiferromagnetism on Zener's Model," *Prog. Theor. Phys.*, vol. 16, no. 1, pp. 45–57, Jul. 1956, doi: 10.1143/ptp.16.45.

[19] K. Yosida, "Magnetic properties of Cu-Mn alloys," *Phys. Rev.*, vol. 106, no. 5, pp. 893–898, Jun. 1957, doi: 10.1103/PhysRev.106.893.

[20] C. Zener, "Interaction between the d-shells in the transition metals. II. Ferromagnetic compounds of manganese with Perovskite structure," *Phys. Rev.*, vol. 82, no. 3, pp. 403–405, May 1951, doi: 10.1103/PhysRev.82.403.

[21] Y. Wang, P. M. Levy, and J. L. Fry, "Interlayer Magnetic Coupling in Fe/Cr Multilayered Structures,",Phys. Rev. Lett., vol. 65, pp. 2732-2735, 1990.

[22] C. Lacroix and J. P. Gavigan, "Interlayer coupling in magnetic multilayers: analogy to superexchange processes in insulators," *J. Magn. Magn. Mater.*, vol. 93, no. C, pp. 413–417, Feb. 1991, doi: 10.1016/0304-8853(91)90372-H.

[23] P. Bruno and C. Chappert, "Ruderman-Kittel theory of oscillatory interlayer exchange coupling," 1992.

[24] P. Bruno, "Theory of interlayer exchange interactions in magnetic multilayers," *J. Phys. Condens. Matter*, vol. 11, no. 48, pp. 9403–9419, Jul. 1999, doi: 10.1088/0953-8984/11/48/305.

[25] P. J. H. Bloemen, H. W. Van Kesteren, H. J. M. Swagten, and W. J. M. De Jonge, "Oscillatory interlayer exchange coupling in Co/Ru multilayers and bilayers," *Phys. Rev. B*, vol. 50, no. 18, pp. 13505–13514, Nov. 1994, doi: 10.1103/PhysRevB.50.13505.

[26]   M. N. Baibich *et al.*, "Giant magnetoresistance of (001)Fe/(001)Cr magnetic superlattices," *Phys. Rev. Lett.*, vol. 61, no. 21, pp. 2472–2475, Nov. 1988, doi: 10.1103/PhysRevLett.61.2472.

[27]   G. Binasch, P. Grünberg, F. Saurenbach, and W. Zinn, "Enhanced magnetoresistance in layered magnetic structures with antiferromagnetic interlayer exchange," *Phys. Rev. B*, vol. 39, no. 7, pp. 4828–4830, Mar. 1989, doi: 10.1103/PhysRevB.39.4828.

[28]   A. Hirohata *et al.*, "Review on spintronics: Principles and device applications," *Journal of Magnetism and Magnetic Materials*, vol. 509. Elsevier B.V., p. 166711, Sep. 01, 2020, doi: 10.1016/j.jmmm.2020.166711.

[29]   F. . Freitas, P. P.; Ferreira, R.; Cardoso, S.; Cardoso, "Magnetoresistive sensors," *J. Phys. Condens. Matter*, vol. 19, p. 165221, 2007, doi: 10.1088/0953-8984/19/16/165221.

[30]   A. Fert and F. N. Van Dau, "Spintronics, from giant magnetoresistance to magnetic skyrmions and topological insulators," *Comptes Rendus Physique*, vol. 20, no. 7–8. Elsevier Masson SAS, pp. 817–831, Nov. 01, 2019, doi: 10.1016/j.crhy.2019.05.020.

[31]   S. Ikegawa, F. B. Mancoff, J. Janesky, and S. Aggarwal, "Magnetoresistive Random Access Memory: Present and Future," *IEEE Trans. Electron Devices*, vol. 67, no. 4, pp. 1407–1419, Apr. 2020, doi: 10.1109/TED.2020.2965403.

[32]   D. Apalkov, B. Dieny, and J. M. Slaughter, "Magnetoresistive Random Access Memory: Magnetoresistive random access memory (MRAM) and particularly spin-transfer-torque MRAM is a nonvolatile memory with very high endurance and scalability. It is based on an array of magnetic tunnel junctions with magn," *Proc. IEEE*, vol. 104, no. 10, pp. 1796–1830, Oct. 2016, doi: 10.1109/JPROC.2016.2590142.

[33]   S. Bhatti, R. Sbiaa, A. Hirohata, H. Ohno, S. Fukami, and S. N. Piramanayagam, "Spintronics based random access memory: a review," *Materials Today*, vol. 20, no. 9. Elsevier B.V., pp. 530–548, Nov. 01, 2017, doi: 10.1016/j.mattod.2017.07.007.

[34]   M. Pannetier-Lecoeur, L. Parkkonen, N. Sergeeva-Chollet, H. Polovy, C. Fermon, and C. Fowley, "Magnetocardiography with sensors based on giant magnetoresistance," *Appl. Phys. Lett.*, vol. 98, no. 15, p. 153705, Apr. 2011, doi: 10.1063/1.3575591.

[35]   Y. Ono, A. Ishiyama, N. Kasai, and K. Chinone, "Development of biomagnetic measurement system for mice with high spatial resolution," *Appl. Phys. Lett.*, vol. 85, no. 2, p. 332, Jul. 2004, doi: 10.1063/1.1772517.

[36] Y. J. Kim, I. Savukov, and S. Newman, "Magnetocardiography with a 16-channel fiber-coupled single-cell Rb optically pumped magnetometer," *Appl. Phys. Lett*, vol. 114, p. 143702, 2019, doi: 10.1063/1.5094339.

[37] T. Klein *et al.*, "Development of a multiplexed giant magnetoresistive biosensor array prototype to quantify ovarian cancer biomarkers," *Biosens. Bioelectron.*, vol. 126, pp. 301–307, Feb. 2019, doi: 10.1016/j.bios.2018.10.046.

[38] T. Klein *et al.*, "Comparative analysis of several GMR strip sensor configurations for biological applications," *Sensors Actuators, A Phys.*, vol. 216, pp. 349–354, Sep. 2014, doi: 10.1016/j.sna.2014.05.033.

[39] L. Jogschies *et al.*, "Recent Developments of Magnetoresistive Sensors for Industrial Applications," *Sensors*, vol. 15, no. 11, pp. 28665–28689, Nov. 2015, doi: 10.3390/s151128665.

[40] D. Rifai, A. N. Abdalla, K. Ali, and R. Razali, "Giant Magnetoresistance Sensors: A Review on Structures and Non-Destructive Eddy Current Testing Applications," 2016, doi: 10.3390/s16030298.

[41] S. Pathak and M. Sharma, "Polar magneto-optical Kerr effect instrument for 1-dimensional magnetic nanostructures," *J. Appl. Phys.*, vol. 115, no. 4, p. 1243, Jan. 2014, doi: 10.1063/1.4862908.

[42] A. Zieba and S. Foner, "Detection coil, sensitivity function, and sample geometry effects for vibrating sample magnetometers," *Rev. Sci. Instrum.*, vol. 53, p. 1344, 1982, doi: 10.1063/1.1137182.

[43] X. Xu, A. Sun, X. Jin, H. Fan, and X. Yao, "Method for calculating the induced voltage in a vibrating sample magnetometer detection coil system," *Rev. Sci. Instrum.*, vol. 67, no. 11, pp. 3914–3923, Jun. 1996, doi: 10.1063/1.1147292.

[44] S. Tumanski, "Induction coil sensors—a review," *Meas. Sci. Technol*, vol. 18, pp. 31–46, 2007, doi: 10.1088/0957-0233/18/3/R01.

[45] L. Bottura and K. N. Henrichsen, "FIELD MEASUREMENTS.", CAS - CERN Accelerator School : Superconductivity and Cryogenics for Accelerators and Detectors, pp.118-148, 2002, DOI: 10.5170/CERN-2004-008.118

[46] D. Howe, "Magnetic actuators," *Sensors Actuators, A Phys.*, vol. 81, no. 1, pp. 268–274, Apr. 2000, doi: 10.1016/S0924-4247(99)00174-0.

[47]   S. M. Jang and S. S. Jeong, "Armature reaction effect and inductance of moving coil linear oscillatory actuator with unbalanced magnetic circuit," in *IEEE Transactions on Magnetics*, 2001, vol. 37, no. 4 I, pp. 2847–2850, doi: 10.1109/20.951325.

[48]   G. Pepka, "Position and level sensing using Hall-effect sensing technology," *Sens. Rev.*, vol. 27, no. 1, pp. 29–34, 2007, doi: 10.1108/02602280710723442.

[49]   Honeywell, "MICRO SWITCH Sensing and Control HALL EFFECT SENSING AND APPLICATION," 2018. Accessed: Mar. 04, 2020. [Online]. Available: https://sensing.honeywell.com/hallbook.pdf.

[50]   T. Korhonen, "Three-dimensional Hall effect accelerometer for recording head movements of freely moving laboratory animals," *Physiol. Behav.*, vol. 49, no. 3, pp. 651–652, Mar. 1991, doi: 10.1016/0031-9384(91)90295-Y.

[51]   E. A. Ponce, S. B. Leeb, and P. A. Lindahl, "Know the Flow: Non-Contact Magnetic Flow Rate Sensing for Water Meters," *IEEE Sens. J.*, vol. 21, no. 1, pp. 802–811, Jan. 2021, doi: 10.1109/JSEN.2020.3014843.

[52]   R. Sood, M. Kaur, and H. Lenka, "Design and Development of Automatic Water Flowmeter DESIGN AND DEVELOPMENT OF AUTOMATIC WATER FLOW METER," *Int. J. Comput. Sci. Eng. Appl.*, vol. 3, no. 3, 2013, doi: 10.5121/ijcsea.2013.3306.

[53]   M. Motz, D. Draxelmayr, T. Werth, and E. Katzmaier, "A programmable Hall sensor for camshaft applications," in *Proceedings of IEEE Sensors*, 2004, vol. 3, pp. 1438–1441, doi: 10.1109/icsens.2004.1426456.

[54]   P. Keller, "Technologies for Precision Magnetic Field Mapping." Accessed: Mar. 02, 2020. [Online]. Available: www.metrolab.com.

[55]   M. Blagojevic and D. Mancic, "The system for magnetic field mapping based on the integrated 3D Hall sensor," Jan. 2017, doi: 10.1109/TELFOR.2016.7818852.

[56]   J. Pascal, N. Weber, J. Felblinger, and O. Julien, "Magnetic gradient mapping of a 3T MRI scanner using a modular array of novel three-axis Hall sensors," *ISMRM 2018*, 2018. https://archive.ismrm.org/2018/1759.html (accessed Jun. 15, 2021).

[57]   H. Zijilstra, *Experimental Methods in Magnetism: Measurement of magnetic quantities - H. Zijlstra - Google Books*. North-Holland Pub. Co., 1967.

[58]   S. Sanfilippo, "Hall probes: physics and application to magnetometry 'What I do teaches me what I am looking for,'" arXiv:1103.1271, 2009.

[59]   P. J. Flanders, "An alternating-gradient magnetometer (invited)," *J. Appl. Phys.*, vol. 63, no. 8, pp. 3940–3945, Jun. 1988, doi: 10.1063/1.340582.

[60]   G. A. Gibson and S. Schultz, "A high-sensitivity alternating-gradient magnetometer for use in quantifying magnetic force microscopy," *J. Appl. Phys.*, vol. 69, no. 8, pp. 5880–5882, Aug. 1991, doi: 10.1063/1.347855.

[61]   B. C. Dodrill, "The Performance of the Model 7400 VSM: Sensitivity."

[62]   M. Buchner, K. Höfler, B. Henne, V. Ney, and A. Ney, "Tutorial: Basic principles, limits of detection, and pitfalls of highly sensitive SQUID magnetometry for nanomagnetism and spintronics ARTICLES YOU MAY BE INTERESTED IN," *J. Appl. Phys*, vol. 124, p. 161101, 2018, doi: 10.1063/1.5045299.

[63]   T. Song, X. Tang, W. Yin, R. Chen, and A. Yan, "Coercivity enhancement of hot-pressed magnet prepared by HDDR Nd-Fe-B powders using Pr-Cu eutectic alloys diffusion," *J. Magn. Magn. Mater.*, vol. 471, pp. 105–109, Feb. 2019, doi: 10.1016/j.jmmm.2018.09.079.

[64]   R. Skomski and J. M. D. Coey, "Magnetic anisotropy - How much is enough for a permanent magnet?," *Scr. Mater.*, vol. 112, pp. 3–8, Feb. 2016, doi: 10.1016/j.scriptamat.2015.09.021.

[65]   W. Matizamhuka, "The impact of magnetic materials in renewable energy-related technologies in the 21st century industrial revolution: The case of South Africa," *Advances in Materials Science and Engineering*, vol. 2018. Hindawi Limited, 2018, doi: 10.1155/2018/3149412.

[66]   J. M. D. Coey, "Perspective and Prospects for Rare Earth Permanent Magnets," *Engineering*, vol. 6, no. 2. Elsevier Ltd, pp. 119–131, Feb. 01, 2020, doi: 10.1016/j.eng.2018.11.034.

[67]   J. M. D. Coey, "Permanent magnet applications," *Journal of Magnetism and Magnetic Materials*, vol. 248, no. 3. Elsevier, pp. 441–456, Aug. 01, 2002, doi: 10.1016/S0304-8853(02)00335-9.

[68]   O. Cugat, R. Byrne, J. McCaulay, and J. M. D. Coey, "A compact vibrating-sample magnetometer with variable permanent magnet flux source," *Rev. Sci. Instrum.*, vol. 65, no. 11, pp. 3570–3573, Nov. 1994, doi: 10.1063/1.1144538.

[69] P. Stamenov and J. M. D. Coey, "Vector vibrating-sample magnetometer with permanent magnet flux source," *J. Appl. Phys.*, vol. 99, no. 8, p. 08D912, Apr. 2006, doi: 10.1063/1.2170595.

Chapter 3.

Methods

In this chapter, we outline the experimental and numerical techniques that have been applied in this work. We begin with the experimental, outlining the instrumentation required to produce and characterise magnetic micro-particles. An outline of sputter deposition processes and optical lithography describes the production with characterisation completed using magneto-optical and vibrating sample techniques. In addition to the experimental techniques, the foundations for the theoretical modelling of magnetic microparticles are also presented.

3.1. Experimental methods

In this section, we outline the experimental methods used, which is primarily split into sample fabrication and sample characterisation methods. Sample fabrication involves the growth and patterning techniques used to create magnetic micro-particle chips and suspensions, and magnetometry techniques are used to verify/evaluate their magnetic properties.

3.1.1. Sample fabrication

3.1.1.1 DC magnetron sputter deposition

Magnetron sputtering is a form of Physical Vapour Deposition (PVD). The most basic form of PVD sputtering is diode sputtering and can be seen schematically in Fig 3.1. In this setup, the material to be sputtered is used as the cathode and is generally referred to as the target. The substrate is naturally an anode as it is at a higher potential. This potential difference between the anode and the cathode creates an electric field that accelerates charged particles within it. Sputtering is the removal of atoms from the target surface by impacting charged ions. As a physical deposition process, sputtering uses chemically inert but chargeable particles to interact with the target (in our system, argon is used as a process gas). The electric field between target and substrate creates an Ar ion plasma as electrons are stripped from Ar atoms. These electrons ionise neighbouring argon atoms by knocking out electrons in an avalanche collision process leading to a plasma of positively charged ions. These ions are accelerated by the electric field into the target (cathode). If the ion transfers sufficient energy to overcome the binding energy of an atom to the target, the target ejects the atom. This is the process of sputtering. The sputtered atom then travels across the chamber and will condense on the substrate wafer. This will be either in line of sight, with the same

momentum as in ejection, or at a random angle with smaller momentum dependent on the mean free path of the particle in the chamber. This basic sputtering process is limited by low plasma density, leading to a low sputtering rate.
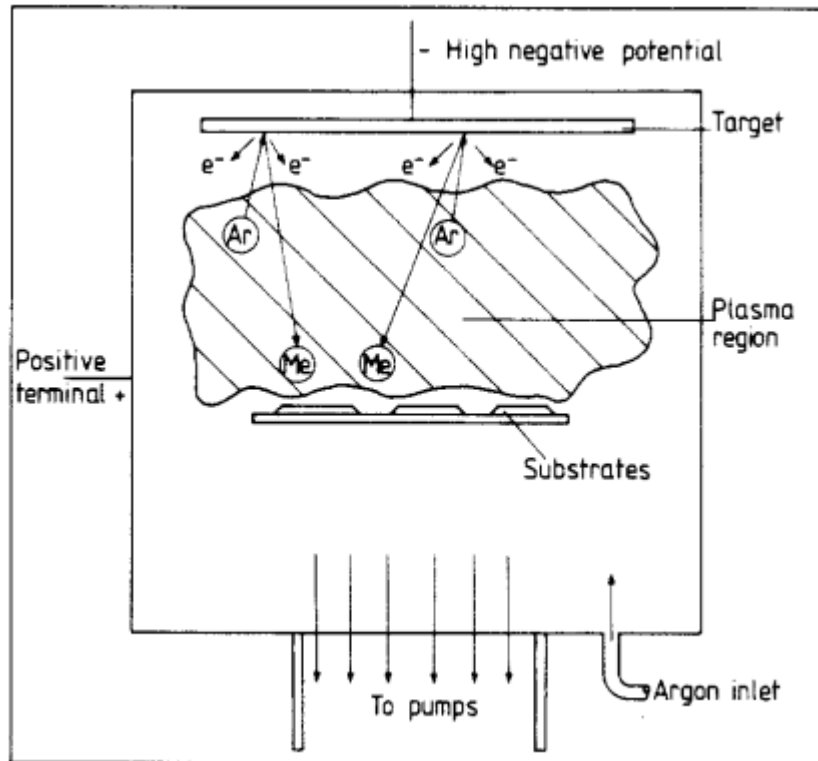
Fig 3.1 A schematic showing a basic diode sputtering set-up. From [1]. *Here Me depicts ejected material.*

Magnetron sputtering improves this process. Using a magnetic field with the geometry shown in Fig 3.2, the emitted secondary electrons are captured and become confined. Consider a force on a moving charged particle in an electric field $\vec{E}$, $\vec{F} = q(\vec{E})$. This produces linear motion. The force on a moving charged particle in a magnetic field $\vec{B}$, $\vec{F} = q(\vec{v} \times \vec{B})$, produces circular motion. Combining the two yields $\vec{F} = q(\vec{v} \times \vec{B} + \vec{E})$ and produces helical motion. This decreases the mean free path for these electrons, increasing the likelihood of interaction with an Ar atom which in turn increases the ionizing density [2]. This increase in the plasma density near the target increases the sputtering efficiency [3].
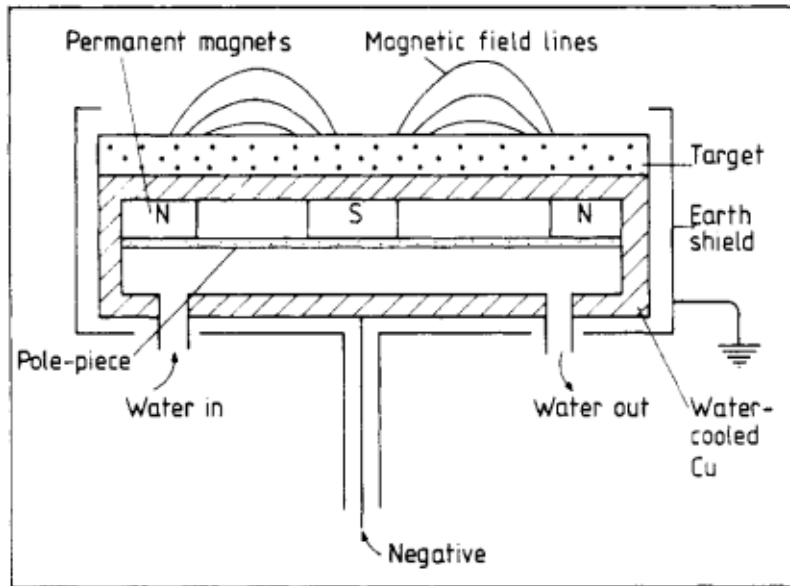
Films in this thesis are sputtered using DC magnetron sputtering in a 6-target vacuum chamber (Ru, CoFeB, Pt, Au, Ta and Al) with a load-lock to input samples. We achieve base pressures of the order 10^{-8} mBar, with growth pressures of 7-8x10^{-3} mBar. Growth is completed whilst rotating the sample stage to improve homogeneity. No substrate heating is used, but the magnetron is cooled using water cooling. Growth rates are calibrated when new targets are introduced into the system. This is completed by drawing lines on a Si substrate with a permanent marker followed by sputtering of the material to calibrate, which is then lifted-off of the substrate (in the marked areas only) using acetone. The step height is then measured using atomic force microscopy (AFM). This is completed across a minimum of 5 locations within the sample and averaged to provide one datum. By growing multiple samples with different growth times, a deposition rate can be obtained. This is completed for each sputter power (the power used to create a potential difference between the anode and cathode), which is used to adjust the growth rate: the higher the power the higher the growth rate. A typical growth rate is of the order of $0.04 - 1\ nm \cdot s^{-1}$ depending on material and sputter power. The largest error in this scenario is the shutter time, which has a minimum discretisation of 1 s.

3.1.1.2 Optical lithography

The brief for this project was to create discreet encoded magnetic markers that can be transferred through a solution. This is completed using particles manufactured from continuous thin films using optical lithography techniques atop a release layer. The process uses UV light to either degrade or crosslink a photo-sensitive material. In the case of positive photoresist (PR), light degrades the PR

causing it to be soluble in a developer solution. On the other hand, light interaction with negative PR causes crosslinking or polymerisation of the PR making it insoluble in the developer.

A Durham Magneto-Optics micro-writer MLIII is used for the lithography process. The system uses a 385 nm light source to direct-write a software developed pattern. Resist sensitivity and global focus correction are calibrated for every PR via a dose and focus test. A real-time focus lock correction is also used within the MLIII software using real-time interferometry.

When particle shapes are designed, the optical proximity effect has to be considered [4]. In a direct-write process, each pixel is written individually. For an optical technique delivered by a laser, the profile of the beam power is Gaussian. For adjacent pixels, the Gaussian distributions partially overlap. At vertices, this can lead to detrimental rounding. For external vertices (external angle >π), where fewer adjoining Gaussians are present, a serif should be applied [5]. The opposite applies for vertices of external angle <π, where an interstice reduces the number of combining Gaussians. This idea is shown in Fig 3.3, with an example of one of our designs in Fig 3.4- a cross-shaped particle.

After testing various processes (courtesy of Lucy Cunningham), we found that the optimum lift-off procedure used a Si substrate with a Ge release layer. The germanium is grown by evaporation and allows for lift-off using hydrogen peroxide. To allow for lithographic patterning, Micro-resist ma-N 1410 negative resist is spun on top of the Ge using an HDMS primer to increase surface adhesion. These are developed in MA D 533S, with the process fully explained in section 4.3.2.
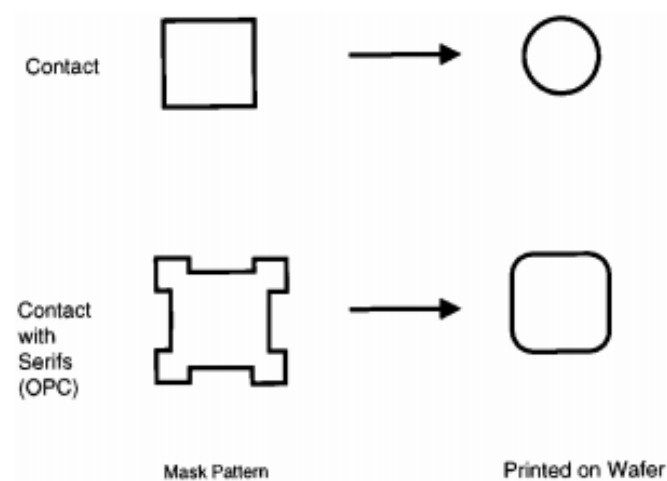
Fig 3.3 An example of the use of serifs to reduce the loss of shape due to the optical proximity effect. From [4]
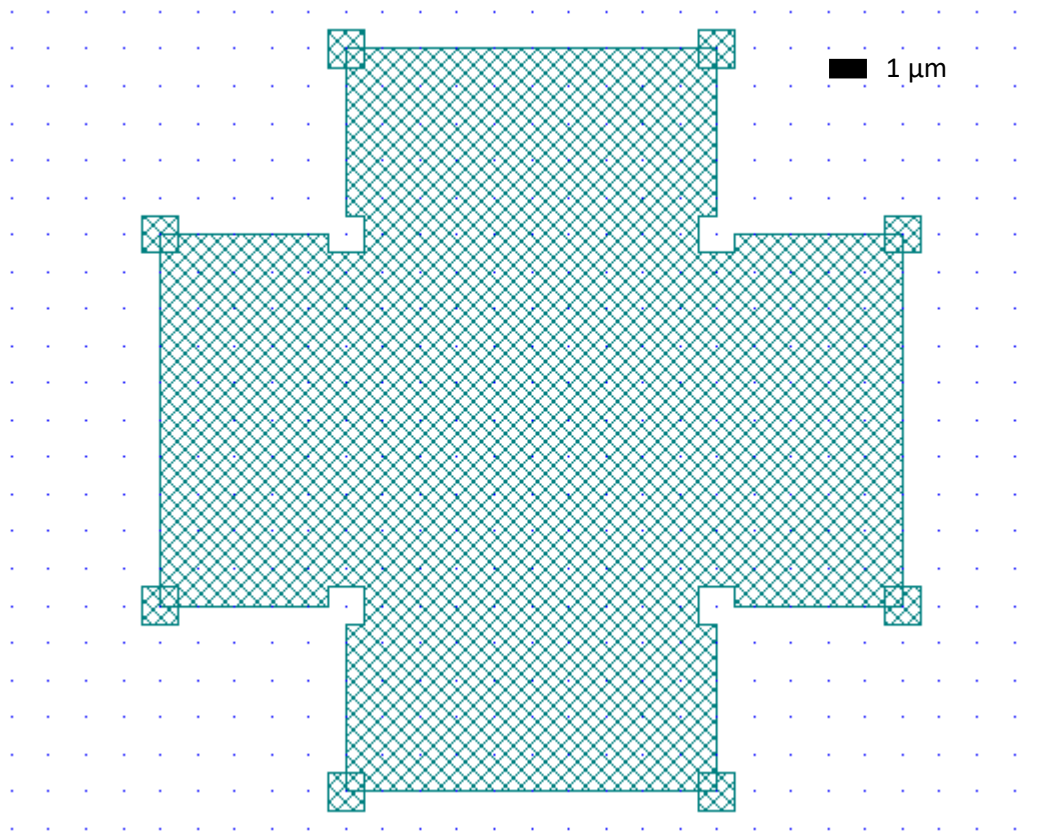
Fig 3.4 A schematic of a cross-shaped particle, designed using the Clewin software. This shows the optical proximity corrections used.

3.1.2. Sample Characterisation

We utilise two techniques for the characterisation of our samples. Focused Magneto-optical Kerr effect (MOKE) magnetometry allows us to characterise our samples with fast, local surface measurements of the magnetisation. MOKE also allows the measurement of the switching of individual particles. We couple this with Vibrating Sample Magnetometry (VSM) which is a bulk inductive measurement. This allows us to investigate switching distribution qualities of particles and eliminates any optical phenomena (such as dependence with stack depth) that are seen in MOKE. VSM is also a moment measurement, which allows us to quantitatively evaluate our films' saturation magnetisation M_S.

3.1.2.1 Vibrating Sample Magnetometry (VSM)

The concept of VSM was created by Foner in 1956 [6]. Although there have been improvements to the hardware, the concept has stayed largely the same since. An oscillatory driver vibrates a rigid sample holder to which a magnetic sample is attached. The driver oscillates at a single frequency, with the sample oscillating with a median position aligned with the centre of a gradiometer coil set. An applied field is applied transverse to the oscillation axis, and the stray field produced by the

magnetic moment of the sample induces an electromotive force (EMF, ε) in the coil set due to its motion along the z-axis in line with Faraday's law of induction.

$$\varepsilon = \oint \vec{E} \cdot d\vec{S} = -\frac{\delta\Phi}{\delta t} = -\frac{\delta\Phi}{\delta z}\frac{\delta z}{\delta t} \, , \qquad (3.1)$$

where $\vec{E}$ is the electric field, Φ the magnetic flux and the negative polarity as a result of Lenz's law. Measurements are taken at discrete values of field, but with DC field at each instance. As the field is unchanging through the measurement, it provides no EMF, which requires time variance. By optimising the design of the gradiometer coil set, the VSM can be made highly resilient to fluctuations in the applied field as well as to variations in the geomagnetic field strength [7][8][9]. This is further improved by utilising lock-in amplifiers, which filter and amplify the signal only for a frequency corresponding to a reference (provided by the oscillatory driver). In doing so, local variations in EMF and other spurious signals can be eliminated from the analysis.

If we consider the motion to be a normal cosine, we can describe the oscillatory motion along the z-axis as $z = A cos(\omega t)$. Using the Biot-Savart law to equate the magnetic field from a magnetic moment $\vec{m}$ into an equivalent field that would be produced by a conductive loop carrying a current I it can be shown that the induced voltage V is equal to:

$$V = \nabla\left(\frac{\vec{B}(\vec{r})}{I} \cdot \vec{m}\right) \omega A cos(\omega t) = mG(\vec{r})\omega A cos(\omega t), \qquad (3.2)$$

with $G(\vec{r})$ the spatial distribution of the sensitivity in the coil. Much work has been done in the optimisation of $G(\vec{r})$ with details found in [7], [8].

Measurements in this thesis were taken using a Microsense EZ7 VSM oscillating at 75 Hz. It has both a scalar and vector coil set, allowing for moment measurements both parallel to and perpendicular to the applied field simultaneously. The noise floor is $\sim 1 \, \mu emu$, and the maximum applied field is limited to 1.75 T. To obtain the results of our sample exclusively, all measurements are repeated for the quartz sample holder (8 mm – to measure magnetisation out of the film plane (OOP)) plus adhesive using the same field steps. This allows for the subtraction of their linear diamagnetic qualities from our measurements.

The VSM is calibrated regularly with a Ni reference sample to ensure that the absolute values of the moment are correct and that the sample position is centred with respect to the gradiometer coils.

3.1.2.2 Magneto-Optical Kerr Effect (MOKE)

The foundations for VSM are built on classical physics – extensions of the first findings of electromagnetism by Faraday. On the contrary, magneto-optical techniques were not explained until the emergence of quantum mechanics, even though their empirical findings were found by Faraday over a century earlier. Faraday noted the change in the polarisation of light transmitted through a semi-transparent medium. The magneto-optical Kerr effect (MOKE) was discovered by Reverend John Kerr $\sim$30 years after and describes the changes in polarisation state when light is reflected from a magnetic sample. Due to this being an optical phenomenon, MOKE is primarily a surface technique providing a contrast to the bulk measurement that we described in VSM.

Microscopically both the Faraday and the Kerr effect emerge from the spin-orbit interaction. Full derivations have been completed yielding an analytical model using perturbation theory, in which the relationship between spin-orbit interaction and the $\vec{E}$ field resulting from the incident light is considered. A full description of this work is outside the scope of this thesis but is found in the literature [10], [11]. It is sufficient to note that the spin-orbit interaction has a direct effect on orbital electron motion – the foundation for dielectric properties. Differences in dielectric properties constitute the macroscopic origins of the Kerr and Faraday effects. In MOKE, we illuminate the sample with a linearly polarised light source. This is a special case of elliptical polarisation where the superposing left circularly polarised (LCP) and right circularly polarised (RCP) elements have the same amplitude and phase. This is shown in Fig 3.5(a) in terms of linear s polarised (perpendicular to the plane of incidence) and p polarised (parallel to the plane of incidence) light, with the off-axis components cancelling to leave a linear $\vec{E}$ vector.

Experimental MOKE measures the change in the polarisation angle of the incident to reflected light as well as any induced ellipticity. These can be understood through the difference in dielectric properties of left and right circularly polarised light. The off-diagonal components of the dielectric tensor lead to an anisotropic interaction with linearly polarised light, causing dichroism in the reflected beam, i.e. right and left circularly polarised light are absorbed in different quantities. This leads to an ellipticity induced in the reflected light, which we denote by ε_K. Due to anisotropy in the refractive index, birefringence is seen. This creates a phase difference between left and right circularly polarised light, rotating the major axis of the electric field from the initial polarisation angle. We refer to this change in polarisation angle as the Kerr angle, θ_R. Both θ_R and ε_K are seen schematically in Fig 3.5b.
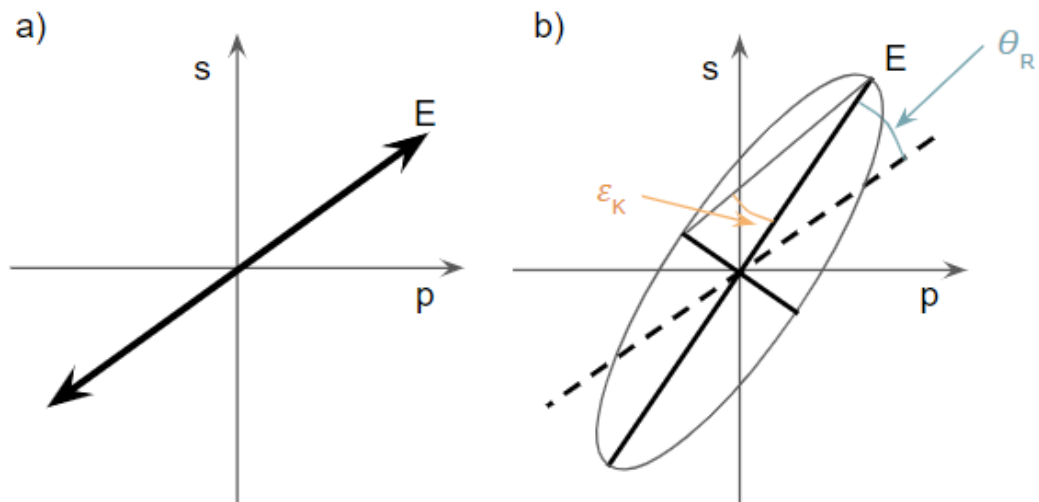
Fig 3.5 A schematic showing the initial (a) and reflected (b) polarisations in MOKE systems. $\vec{E}$ defines the electric field vector and is rotated at an angle θ_R in the reflected beam. Ellipticity results from the anti-symmetric dielectric tensor elements and is defined by the ratio of the long and short axes of the ellipse.

There are three MOKE orientations for films: longitudinal MOKE, where the direction of magnetisation lies parallel to the incidence plane and the sample plane - transverse MOKE, where the direction of magnetisation is perpendicular to the incidence plane but parallel to the sample plane - and finally polar MOKE, with magnetisation perpendicular to the sample plane but parallel to the incidence plane. These three scenarios are outlined in Fig 3.6. In each of these situations, considerations must be made as to whether p or s polarised light is changed by the Kerr effect and by what mechanism (rotation or amplitude).
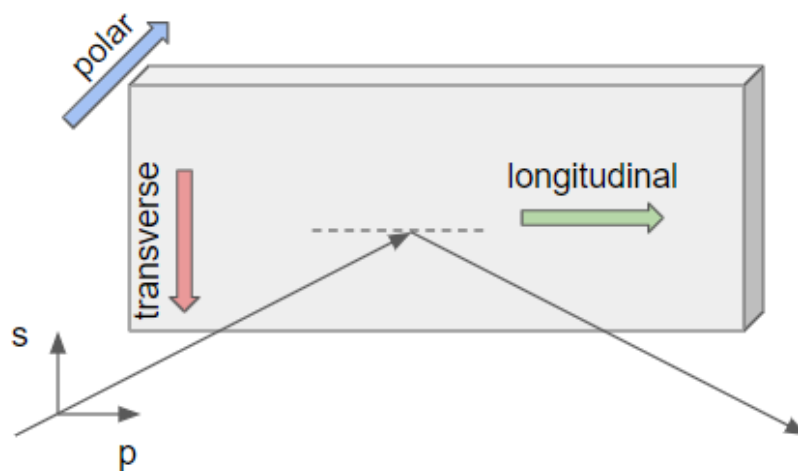
Fig 3.6 A schematic to show the three MOKE orientations for a film-shaped sample. The two components of light are defined as parallel to the plane of incidence (p) and perpendicular to the plane of incidence (s).

In this thesis, we utilise polar MOKE. In this regime, there is no difference between s polarised and p polarised light – both having phase changes with respect to magnetisation. The Kerr rotation (θ_R) and ellipticity (ε_K) in polar MOKE can be defined as

$$\theta_R(\omega) = -\frac{1}{2}[\phi_+(\omega) - \phi_-(\omega)], \tag{3.3}$$

$$tan\,(\varepsilon_K(\omega)) = \frac{r_+(\omega) - r_-(\omega)}{r_-(\omega) + r_+(\omega)}, \tag{3.4}$$

where ω and ϕ denote the frequency and phase of the light, and

$$\tilde{r}_\pm(\omega) = r_\pm(\omega)e^{i\phi(\omega)}, \tag{3.5}$$

defines the reflection coefficients for left ($-$), and right ($+$) circularly polarised light, respectively. These values can be extracted experimentally, with a comprehensive description given in [16]. Further descriptions of the polar Kerr effect can be found in [17].

Kerr rotation has a direct relation to the applied field in a manner proportional to the magnetisation of the sample and as such a plot of θ_R vs H yields the same profile as an MH (hysteresis) loop. We cannot obtain any quantitative values of moment, only a change in relative magnetisation. MOKE is a fast measurement that can be completed with a dynamic field, with sweep rates generally limited by eddy current generation in electromagnet yoke material and the accuracy of the power supply. Measurement errors can be reduced by averaging several field cycles.

Measurements were completed using a Durham Magneto-Optics NanoMoke III in polar configuration [18]. The focussed laser spot size is of the order of 3 [μm] but can be defocussed to allow for the measurement of larger areas. The system has a maximum field of around 0.65 [T] (with the frequency adjusted to maintain a viable sweep rate). In this thesis, a field sweep rate of 0.1 Ts^{-1} is maintained, giving a frequency range between 0.076-1 Hz.

3.2. Numerical methods

This thesis utilises the computational modelling of our proposed detector to analyse its viability and efficacy. This section will outline the methods that we have used to extract important parameters, mainly the calculation of magnetic fields as well as the concept of fuzzy logic which we implement for more accurate modelling of ferromagnetic material. Though many of these methods utilise iterative solvers, the details of how these operate are outside the scope of this thesis.

3.2.1. Field generation

The most useful parameter that we can extract from our modelling is the magnetic field. From this, we can understand the requirements of our sample's reaction to an applied field, as well as what constraints we have for applied field generation. The field can be found through various analytical models, each with its own assumptions and limitations. This section hopes to outline the processes that were utilised within this thesis and the areas where caution should be exercised. Many methods were tested though only the methods utilised within the final versions of our coding are presented.

3.2.1.1 Calculations for magnetic field

Before looking into the specific calculations used within this thesis, we should first understand the foundations of analytical magnetic field calculations. There are several ways to calculate the magnetic field produced by a magnetic object. The analytical tools generally utilise a constant magnetisation or adjacent volumes each of which possess constant magnetisation that changes very gradually. The only sources of a magnetic field are magnetised material and current-carrying conductors. Thus, in magnetostatics, all methods utilise one of these two assumptions. In the following constructions, we will maintain the nomenclature used by Coey [19]. The field can be considered as the summation of fields from a distribution of individual magnetic moments or current loops, generally referred to as the dipole approximation. In this method, the individual magnetisation elements are described by $\vec{M}d^3r$, with the field:

$$\vec{B}(\vec{r}) = \frac{\mu_0}{4\pi}\left[\int\left\{\frac{3\vec{M}(\vec{r}')\cdot(\vec{r}-\vec{r}')}{|\vec{r}-\vec{r}'|^5}(\vec{r}-\vec{r}') - \frac{\vec{M}(\vec{r}')}{|\vec{r}-\vec{r}'|^3} + \frac{2}{3}\mu_0\vec{M}(\vec{r}')\delta(\vec{r}-r')\right\}d^3r'\right]. \qquad (3.6)$$

Here, the final term is used to account for the divergence of the dipole field at the origin. In the Ampèrian approach, all magnetisation is replaced by an equivalent amount of moving charge. In this formalism, the field can be defined using a Biot-Savart law, with the bulk current distribution $\vec{J}_{Bulk} = \nabla\times\vec{M}$ and surface current distribution $\vec{J}_{surf} = \vec{M}\times\widehat{e_N}$ we find:

$$\vec{B}(\vec{r}) = \frac{\mu_0}{4\pi}\left\{\int\frac{(\nabla'\times\vec{M})\times(\vec{r}-\vec{r}')}{|\vec{r}-\vec{r}'|^3}d^3r' + \int\frac{(\vec{M}\times\widehat{e_N})\times(\vec{r}-\vec{r}')}{|\vec{r}-\vec{r}'|^3}d^2r'\right\}, \qquad (3.7)$$

where $\widehat{e_N}$ is the normal vector to the surface of the material and ∇' refers to differentiation with respect to r'. In the case of uniform magnetisation, even if the system is discretised the current loop manifests around the surface due to cancellations at contiguous boundaries. This cancellation, as well as the resulting surface current, is seen schematically in Fig 3.7 for a cylindrical object. This is understood mathematically as $\nabla \times \vec{M} = 0 = \vec{J}_{Bulk}$.
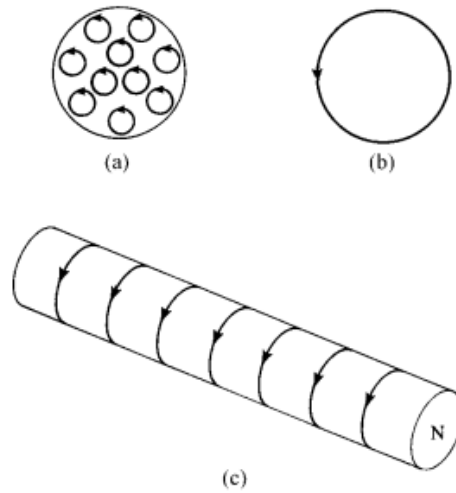
Fig 3.7 Schematic showing the manifestation of surface currents in an Ampèrian approximation. As the diameter of the loops are reduced and their number increased to represent single dipoles (a), the contiguous perimeters cancel leaving only the surface component (b). This is shown for a 3D cylinder in (c). From [20]

An alternative approach is the Coulombian method which involves considering an equivalent magnetic charge defined in the bulk by $\rho_m = -\nabla \cdot \vec{M}$ and at the surface by $\sigma_m = \vec{M} \cdot \widehat{e_N}$, yielding

$$\vec{H}(\vec{r}) = \frac{1}{4\pi} \left\{ -\int_V \frac{(\nabla' \cdot \vec{M}) \times (\vec{r} - \vec{r}')}{|\vec{r} - \vec{r}'|^3} d^3 r' + \int_S \frac{(\vec{M} \cdot \widehat{e_N}) \times (\vec{r} - \vec{r}')}{|\vec{r} - \vec{r}'|^3} d^2 r' \right\}. \qquad (3.8)$$

Note that in this method, the conservative field $\vec{H}$ is calculated as opposed to the solenoidal field $\vec{B}$. In free space, the conversion between both fields is purely a scalar factor μ_0. The Coulombian method is generally the easiest to compute, especially if the source of the magnetic field is purely from magnetic material. In such an instance, the field can be derived from a scalar potential:

$$\vec{H} = -\nabla \phi_m, \qquad (3.9)$$

where ϕ_m is the magnetic scalar potential. This results from the conservative nature of the field when the charge from conduction currents $\vec{J_c} = 0$, meaning Ampère's law becomes $\nabla \times \vec{H} = 0$ and Poisson's equation is satisfied by the scalar potential, $\nabla^2 \phi_m = -\rho_m = -\nabla \cdot \vec{M}$. The resulting calculation for the scalar potential yields:

$$\phi_m(\vec{r}) = \frac{1}{4\pi} \left\{ -\int_V \frac{\rho_m}{|\vec{r}-\vec{r}'|^3} d^3r' + \int_S \frac{\sigma_m}{|\vec{r}-\vec{r}'|^3} d^2r' \right\}.$$ (3.10)

Like previously, if the magnetisation is uniform the first integral equals zero and the calculation reduces to a surface charge model.

These models are the foundation for any magnetic field computation, with the methods described later in 3.2.1.3 and 3.2.1.4 building from the Coulombian approach.

3.2.1.2 Linearised unit vector combination (superposition principle)

In calculations of magnetic fields, the field from multiple macrospins can be extracted and superposed to find the field at any point. Maxwell's equations for a magnetic field are linear PDE's and as such can be constructed as the superposition of multiple sources. This is particularly useful for the calculation of magnetic fields resulting from bodies magnetised at an arbitrary angle, which can be considered as the superposition of the three pure cartesian axes. These axes benefit from symmetries and as such are the easiest to calculate. Again, due to the linearity of the equations, the magnitude can also be produced from scalar factors of a unit magnetisation. This means that if three cartesian unit vectors are calculated for a unit magnetisation within a system the field from any macrospin can be deduced. With this foundation, we will now investigate the methods employed in this thesis in more detail.

3.2.1.3 Analytical model for magnetised parallelepipeds (Akoun/Janssen model)

One of the first 3D analytical models for interactions between two magnetised bodies was proposed by Akoun and Yonnet who described the interaction energy between two parallelepiped objects [21]. In the same paper, the expression for the magnetic field of a 2D plane was given in the appendix. This was expanded into three dimensions by Janssen [22].

The geometry of this problem is seen in Fig 3.8. The magnetisation is uniformly distributed across the plane spanning $\pm a, \pm b$ in the x and y directions, respectively. This considers planes of magnetic charges in a Coulombian approach. In these models, the magnetisation is directly along the z-axis leading to charge accumulation on the top and bottom surfaces separated by a distance of $2c$.

Given the form for a magnetic field emanating from an array of uniform magnetic charge density and evaluating the integrals, the following form is found for the magnetic field at a point $\vec{r}$ from a magnetic body centred at (0,0,0):

$$\vec{B}(\vec{r}) = \frac{\mu_0 M_s}{4\pi} \sum_{i=0}^{1} \sum_{j=0}^{1} \sum_{k=0}^{1} (-1)^{i+j+k} \begin{pmatrix} \log(R - T) \\ \log(R - S) \\ \tan^{-1}\left(\frac{ST}{RU}\right) \end{pmatrix},$$ (3.11)

with $\vec{r} = r(x, y, z)$ and:

$$S = x - (-1)^i a, \qquad T = y - (-1)^j b,$$ (3.12)

$$U = z - (-1)^k c, \qquad R = \sqrt{S^2 + T^2 + U^2}.$$ (3.13)

It should be reminded that this derivation is for a sample with a uniform pure z magnetisation. Magnetisations about the x or y-axis can be completed through a permutation of axes, and through such a scheme we may superpose the values in a manner described in section 3.2.1.2 to obtain fields from parallelepipeds of arbitrary magnetisation.

The Akoun/Janssen method is limited by the shape of the sample. Superposition of parallelepipeds can produce fields from more complex shapes, but this increases computation time by a factor n, where n is the number of parallelepipeds required to create the shape. This is troublesome for curved surfaces which can only be approximated by parallelepipeds.
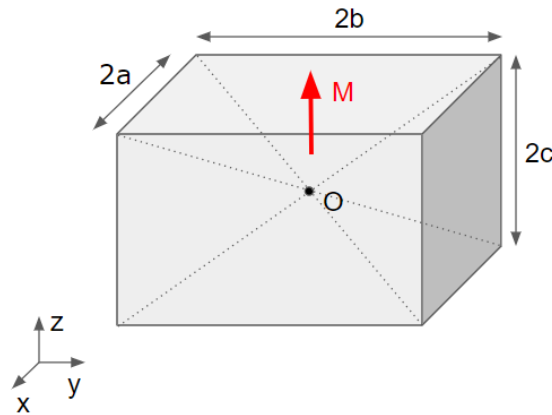
Fig 3.8 A schematic depicting the geometry used in the analytical field calculation presented by Janssen. The centre of the cuboid is depicted by the symbol O [22]

3.2.1.4 Analytical cylindrical model (Caciagli model)

The issue of curved surfaces in parallelepipedal models can be overcome by using an analytical model in a cylindrical reference frame. The instance of longitudinal magnetisation was found by Derby and Olbert in integral form [23], but this was extended to closed form for both transverse and longitudinal magnetisations by Caciagli et al [24]. Through the permutation of axes, any angle of magnetisation can be obtained. This is one of the few cases where 3D analytical solutions are available. The geometry for this formulation is seen in Fig 3.9.
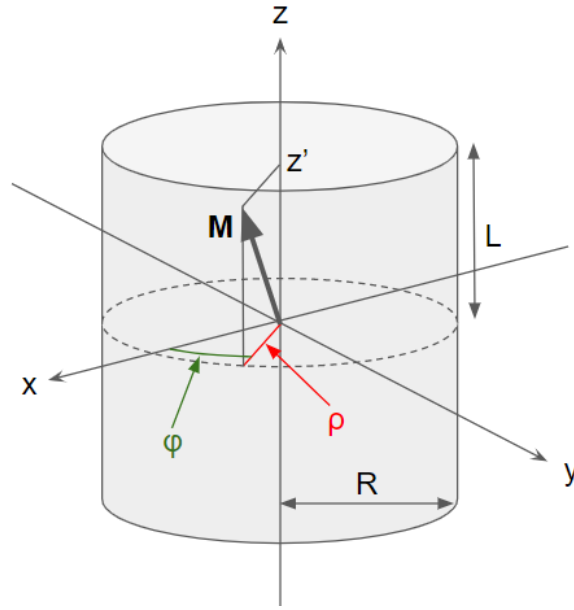
Fig 3.9 A schematic showing the geometry of the problem solved using the Caciagli method.

The model considers the scalar potential for a uniform magnetisation composed of a pure transverse or a pure longitudinal component, calculating the scalar potential ϕ_m in cylindrical coordinates. The integral form of the scalar potential for the transverse magnetisation is evaluated in terms of elliptical integrals, leading to a lengthy derivation that is presented within the appendix. Ultimately this leads to:

$$\phi_m = \frac{MRcos(\varphi)}{\pi}[\beta_+ P_4(k_+) - \beta_- P_4(k_-)]. \tag{3.14}$$

Using the relationship $H = -\nabla\phi_m$, the field components for pure transverse magnetisation are found to be:

$$H_\rho = \frac{\partial\phi_m}{\partial\rho} = \frac{MRcos(\varphi)}{2\pi\rho}[\beta_+ P_4(k_+) - \beta_- P_4(k_-)], \tag{3.15}$$

$$H_\varphi = -\frac{1}{\rho}\frac{\partial\phi_m}{\partial\varphi} = \frac{MRsin(\varphi)}{\pi\rho}[\beta_+ P_3(k_+) - \beta_- P_3(k_-)], \tag{3.16}$$

$$H_z = -\frac{\partial\phi_m}{\partial z} = \frac{MRcos(\varphi)}{\pi}[\alpha_+ P_1(k_+) - \alpha_- P_1(k_-)], \tag{3.17}$$

where M and R denote magnetisation and magnet radius respectively and (φ, ρ, z) are vector components in the cylindrical reference frame. So as to not to exhaust the reader, $\beta_\pm$, P_{1-4}, $k_\pm$ and $\alpha_\pm$ are broken down within the appendix, where an interdependence of 15 functions including the 3

complete elliptical integrals (first, second and third kind) is described. With the knowledge of the field for magnetisation in the circular cross section of the cylinder (from [23]):

$$B_\rho = \frac{\mu_0 M R}{\pi} [\alpha_+ P_1(k_+) - \alpha_- P_1(k_-)], \tag{3.18}$$

$$B_z = \frac{\mu_0 M R}{\pi(\rho + R)} [\beta_+ P_2(k_+) - \beta_- P_2(k_-)], \tag{3.19}$$

and using a similar process to that described in section 3.2.1.2, we can obtain the field at any point for any value of magnetisation in the circular cross section of the cylinder ($0 \geq \varphi \geq 360°$).

Cartesian reference frames are utilised in this thesis, so rotational matrices are employed to convert input points and fields into the correct frame for the application. The appropriate rotation matrices are presented in the appendix for completion.

3.2.1.5 Micromagnetic simulations

Micromagnetic solvers such as OOMMF [25] and Mumax [26] solve for the $\vec{M}$ state with minimum energy for a system with a given set of parameters. The solvers work by assuming that the system obeys the continuum approximation, i.e. the length scales are small enough to observe the formation of domain regions within the material but large enough to ignore atomic structure, replacing atomic spins with a continuous magnetisation, defined as a function of position and time. In a static system, this can be completed through a minimisation of the consolidated energy terms:

$$E = E_{exchange} + E_{anisotropy} + E_{Zeeman} + E_{demag}. \tag{3.20}$$

Brown's micromagnetic equation is used to minimize Equation 3.20, considering the total energy is a function of $\vec{m}(x)$ with $|\vec{m}(x)| = 1$ and the boundary conditions:

$$\nabla m_x \cdot \vec{n} = 0, \qquad \nabla m_y \cdot \vec{n} = 0, \qquad \nabla m_z \cdot \vec{n} = 0. \tag{3.21}$$

This is generally minimized using the Euler method in a finite difference approach, where the computation time can be reduced using Fast Fourier Transforms (FFTs).

Hysteresis and domain formation through this process can be analysed in dynamic processes through solving the Landau-Lifshitz-Gilbert (LLG) equation for an effective field:

$$\frac{\partial \vec{m}}{\partial t} = -\frac{|\gamma|\mu_0}{1 + \alpha_G^2} \vec{m} \times \vec{H}_{eff} - \frac{|\gamma|\mu_0 \alpha_G}{1 + \alpha_G^2} \vec{m} \times (\vec{m} \times \vec{H}_{eff}). \tag{3.22}$$

This partial differential equation considers the Larmor precession of the magnetisation around the effective field $\vec{H}_{eff}$ – the local field felt by the individual magnetisation point $\vec{m}$ on the mesh. Here γ is the gyromagnetic ratio and α is the Gilbert damping constant. Through this, the time evolution of the magnetisation is obtained, and hysteresis loops can be extracted.

$\vec{H}_{eff}$ is extracted in these solvers in conventional numerical techniques: OOMMF does this through evaluation of the demagnetisation kernel using the method described by Newell et al. [27] and Aharoni [28]. The field is then constructed using the equality $\vec{B}_{demag,i} = \hat{K}_{i,j} * \vec{M}_J$ where $\hat{K}_{i,j}$ and $\vec{M}_j$ the magnetisation vector at the position j. is the demagnetisation kernel. Mumax on the other hand constructs the demagnetisation kernel using the work of McMichael et al [29] but both programmes follow a similar pattern. Both Mumax and OOMMF utilise Fast Fourier Transforms (FFTs) in finite-difference arrays to increase the speed of the convolution. It should be noted that for a single macrospin approach or methods using a single cell of uniform magnetisation, the demagnetisation kernel is a single value and provides no insight into the sample shape.

3.2.1.6 Integrating non-idealised particles through membership functions

Within this thesis, we characterise individual transitions within a hysteresis loop, so that their qualities can be compared. We characterise our transitions as a logical function so that their response can be used as an input to a simulation.

Fuzzy logic allows us to define a value set between zero and unity for an input array, allowing for intermediate terms (named partial truths) rather than classical true/false values. The logic is defined by a membership function that attributes the level of truth to the input. This mathematical vagueness operates on inputs in a manner that mimics Boolean logic and can handle complicated functions. The basis of the logic does not lie within the scope of this work, but the foundations can be found in Zadeh's seminal paper [30]. Within this thesis, we create membership functions that follow a Boltzmann distribution. This is a symmetric sigmoidal function with equivalent sloping to each end of the sigmoid. This function can be designed with controllable centre value (midpoint between the maximum and minimum values) c and time constant a. The membership function is then defined by:

$$\chi(x; a, c) = \frac{A_1 - A_2}{1 + e^{-\frac{x-c}{a}}} + A_2,$$
(3.23)

where the final and initial values are defined by A_2 and A_1 respectively. Within the range zero to unity, this simplifies to logistical sigmoid function:

$$\chi(x; a, c) = \frac{1}{1 + e^{-\frac{x-c}{a}}}.$$
(3.24)

A comparison of standard binary logic and fuzzy logic through the above equation can be seen in Fig 3.10. Here, binary logic is a limit of the logistic sigmoid function, with $a \rightarrow 0$;

(a)   (b)
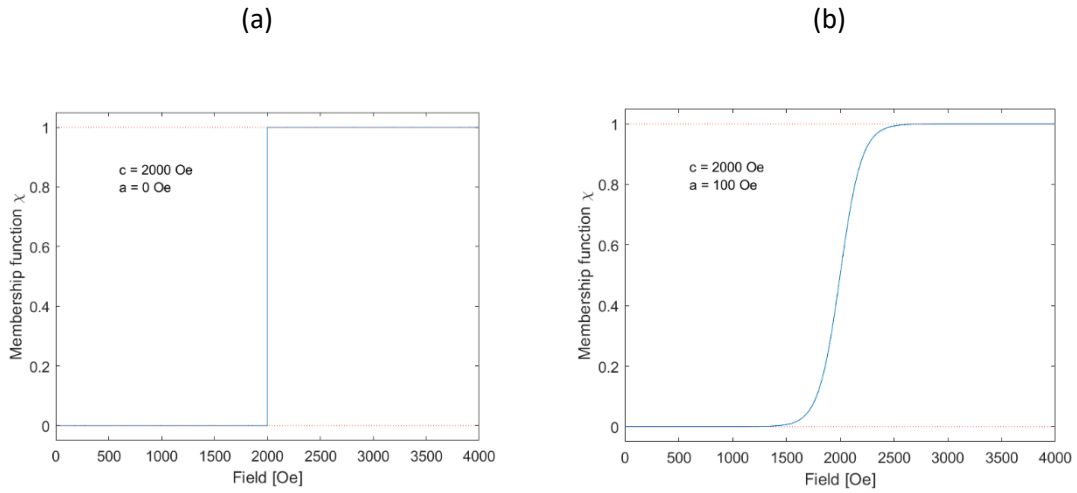
Fig 3.10. A schematic showing the differences between binary (a) and fuzzy logic (b) for use in particle modelling.

With knowledge of the methods used and the theory behind this work, we will now investigate the fabrication and characterisation of the samples to be detected.

[1]   S. Swann, "Magnetron sputtering," *Phys. Technol.*, vol. 19, no. 2, pp. 67–75, Mar. 1988, doi: 10.1088/0305-4624/19/2/304.

[2]   L. Eckertova, *Physics of thin films*, Second Edi. New York: Plenum press, 1986.

[3]   S. A. Campbell, *Fabrication engineering at the micro- and nanoscale,* 4th edition, Oxford University Press, 2012.

[4]   L. R. Harriott, "Limits of lithography," *Proc. IEEE*, vol. 89, no. 3, pp. 366–374, 2001, doi: 10.1109/5.915379.

[5]   A. Poonawala and P. Milanfar, "Mask design for optical microlithography - An inverse imaging problem," *IEEE Trans. Image Process.*, vol. 16, no. 3, pp. 774–788, Mar. 2007, doi: 10.1109/TIP.2006.891332.

[6]   S. Foner, "Vibrating Sample Magnetometer," *Rev. Sci. Instrum.*, vol. 27, no. 7, pp. 548–548, Jul. 1956, doi: 10.1063/1.1715636.

[7]   A. Zieba and S. Foner, "Detection coil, sensitivity function, and sample geometry effects for vibrating sample magnetometers," *Rev. Sci. Instrum.*, vol. 53, p. 1344, 1982, doi: 10.1063/1.1137182.

[8]   S. Tumanski, "Induction coil sensors—a review," *Meas. Sci. Technol*, vol. 18, pp. 31–46, 2007, doi: 10.1088/0957-0233/18/3/R01.

[9]   P. C. Fannin, B. K. P. Scaife, and S. W. Charles, "The field dependence of the complex frequency-dependent susceptibility of magnetic fluids," *J. Phys. D Appl. Phys*, vol. 21, pp. 533–534, 1988, Accessed: Sep. 19, 2017. [Online]. Available: http://iopscience.iop.org/article/10.1088/0022-3727/21/3/025/pdf.

[10]   H. R. Hulme and R. H. Fowler, "The Faraday effect in ferromagnetics," *Proc. R. Soc. London. Ser. A, Contain. Pap. a Math. Phys. Character*, vol. 135, no. 826, pp. 237–257, Feb. 1932, doi: 10.1098/rspa.1932.0032.

[11]   P. N. Argyres, "Theory of the Faraday and Kerr effects in ferromagnetics," *Phys. Rev.*, vol. 97, no. 2, pp. 334–345, Jan. 1955, doi: 10.1103/PhysRev.97.334.

[12]   Z. Q. Qiu and S. D. Bader, "Surface magneto-optic Kerr effect (SMOKE)," *J. Magn. Magn. Mater.*, vol. 200, no. 1–3, pp. 664–678, Oct. 1999, doi: 10.1016/S0304-8853(99)00311-X.

[13]   C. Y. You and S. C. Shin, "Generalized analytic formulae for magneto-optical Kerr effects," *J. Appl. Phys.*, vol. 84, no. 1, pp. 541–546, Jul. 1998, doi: 10.1063/1.368058.

[14] R. P. Hunt, "Fundamental magneto-optics," *Rev. Sci. Instrum.*, vol. 38, no. 4, p. 541, 1967, doi: 10.1063/1.1709738.

[15] R. C. Jones, "A New Calculus for the Treatment of Optical SystemsI Description and Discussion of the Calculus," *J. Opt. Soc. Am.*, vol. 31, no. 7, p. 488, Jul. 1941, doi: 10.1364/josa.31.000488.

[16] D. A. Allwood, G. Xiong, M. D. Cooke, and R. P. Cowburn, "Magneto-optical Kerr effect analysis of magnetic nanostructures," *J. Phys. D. Appl. Phys.*, vol. 36, no. 18, pp. 2175–2182, Sep. 2003, doi: 10.1088/0022-3727/36/18/001.

[17] P. Kielar, "Magneto-optical polar Kerr effect and dispersion relations," *J. Opt. Soc. Am. B*, vol. 11, no. 5, p. 854, May 1994, doi: 10.1364/josab.11.000854.

[18] Durham Magneto Optics Ltd, "Durham Magneto Optics Ltd NanoMOKE3 ® Specifications," 2014.

[19] J. M. D. Coey, *Magnetism and Magnetic Materials*, Cambridge University Press, 2010.

[20] B. D. (Bernard D. Cullity and C. D. (Chad D. . Graham, *Introduction to magnetic materials*. IEEE/Wiley, 2009.

[21] G. Akoun and J.-P. Yonnet, "3D analytical calculation of the forces exerted between two cuboidal magnets," *IEEE Trans. Magn.*, vol. 20, no. 5, pp. 1962–1964, Sep. 1984, doi: 10.1109/TMAG.1984.1063554.

[22] J. L. G. Janssen, *Extended Analytical Charge Modeling for Permanent-Magnet Based Devices Practical Application to the Interactions in a Vibration Isolation System*, no. december. 2011.

[23] N. Derby and S. Olbert, "Cylindrical Magnets and Ideal Solenoids," *Am. J. Phys.*, vol. 78, no. 3, pp. 229–235, Sep. 2009, doi: 10.1119/1.3256157.

[24] A. Caciagli, R. J. Baars, A. P. Philipse, and B. W. M. Kuipers, "Exact expression for the magnetic field of a finite cylinder with arbitrary uniform magnetization," *J. Magn. Magn. Mater.*, vol. 456, pp. 423–432, Jun. 2018, doi: 10.1016/j.jmmm.2018.02.003.

[25] M. J. Donahue and D. G. Porter, OOMMF User's Guide, Version 1.0, Interagency Report NISTIR 6376, National Institute of Standards and Technology, Gaithersburg, MD, (Sept 1999).

[26] A. Vansteenkiste, J. Leliaert, M. Dvornik, M. Helsen, F. Garcia-Sanchez, and B. Van Waeyenberge, "The design and verification of MuMax3," *AIP Adv.*, vol. 4, no. 10, p. 107133, 2014, doi: 10.1063/1.4899186.

[27] A. J. Newell, W. Williams, and D. J. Dunlop, "A generalization of the demagnetizing tensor for nonuniform magnetization," *J. Geophys. Res.*, vol. 98, no. B6, pp. 9551–9555, 1993, doi: 10.1029/93JB00694.

[28] A. Aharoni, "Demagnetizing factors for rectangular ferromagnetic prisms," *J. Appl. Phys.*, vol. 83, no. 6, pp. 3432–3434, 1998, doi: 10.1063/1.367113.

[29] R. D. Mcmichael,) M J Donahue, D. G. Porter, and J. Eicke, "Comparison of magnetostatic field calculation methods on two-dimensional square grids as applied to a micromagnetic standard problem," 1999. Accessed: Sep. 09, 2020. [Online]. Available: www.ctcms.nist.gov/rdm/mumag.html.

[30] L. A. Zadeh, "Fuzzy sets," *Inf. Control*, vol. 8, no. 3, pp. 338–353, Jun. 1965, doi: 10.1016/S0019-9958(65)90241-X.

Chapter 4.

Particle Studies

In this chapter, we outline the properties of our magnetic particles, as well as how they are produced. The particles' properties are primarily governed by two phenomena– Perpendicular Magnetic Anisotropy (PMA) produced by thin magnetic layers contiguous to a non-magnetic layer, and Ruderman Kittel Kasuya Yoshida (RKKY) coupling facilitated by a ruthenium spacer. We aim to characterize particle properties individually, starting with PMA in section 4.2, followed by RKKY in section 4.3. The effects of PMA are characterised on Pt/CoFeB/Pt stacks, where the thickness of the CoFeB layer influences the strength of the perpendicular anisotropy. RKKY effects are shown for Pt/CoFeB/Pt/Ru/Pt/CoFeB/Pt stacks, with varying Pt spacer thicknesses. Through this Pt thickness variation, we can modulate the interlayer exchange coupling (IEC) strength and as such have tuneable magnetic switching. This allows for transitions at various field strengths. These particles are non-remanent and exhibit zero moment below the switching field, meaning that they do not agglomerate in solution due to their stray fields.

We present characteristics of our magnetic stacks for thin-film samples, patterned films and finally particles that can be lifted off the substrate into solution. These are analysed through switching properties such as transition field and width. A comparison of the coupling constant J vs Pt thickness t_{Pt} is completed at each of the three steps to ensure that coupling characteristics are maintained throughout the fabrication process. We test the insensitivity of our particles to in-plane field components by measuring switching astroids under rotating fields. Finally, we evaluate the collective switching distributions of particles. This is analysed through the study of many single-particle MOKE measurements as well as bulk VSM measurements of many single particles.

The results from this chapter characterise the key magnetic properties of our particles that define the input parameters and constraints for our computational modelling in subsequent chapters.

4.1. Chapter introduction

In this chapter, we aim to design and test an encodable magnetic information carrier for use with an inductive detection scheme. The project brief outlines that these particles should be difficult to corrupt and have a tunable magnetic property on which the encryption scheme can be based. As we wish to transfer these to a tag, we also must be able to release our particles from the substrate into a liquid suspension. We aim to fulfil these requirements using Synthetic Anti-Ferromagnetic (SAF) micro-particles and controlling their inter-layer coupling strength.

SAF structures sandwich a non-magnetic spacer layer between two ferromagnetic layers. The two layers are not in contact, but the non-magnetic layer enables an interaction between the magnetic moments of the ferromagnetic layers through indirect exchange, facilitated by conduction electrons. The polarity of this exchange interaction depends on the thickness of the spacer layer, alternating between ferromagnetic and anti-ferromagnetic coupling as thickness increases.

The anti-parallel configuration stemming from anti-ferromagnetic coupling has the advantage of cancelling moment contributions for equally thick magnetic layers, minimizing the demagnetisation energy of the system. This makes particles with zero net stray field and limits interaction between neighbouring particles. This is particularly interesting for particles in solution – particles with non-zero remanent states interact and agglomerate in solution. This interaction of non-zero remanent particles minimizes demagnetisation energy and is usually permanent, so it should be avoided to ensure the effective dispersion of magnetic material. This makes SAF particles strong candidates for biological applications [1]–[4] and have shown uses in cancer therapeutics [5]–[7], contrast agents [8] and magnetic filtering [9], to name a few.

Though we need to remain as optically undetectable as possible, reducing the lateral dimensions of a particle also reduces its moment and the resulting field which would be measured inductively. As a result, we need to capture as much of the field as possible. This is made possible by Perpendicular Magnetic Anisotropy (PMA), causing the magnetisation to point out of the film plane. Top-down lithography techniques often mean samples have much larger lateral dimensions compared to their thickness. Re-deposited particles are statistically much more likely to adhere with the large dimension to the substrate. This means that, though IP materials allow for larger thicknesses, their most dense field regions are less accessible (as a collective) for detection. PMA orients the field dense areas in a direction that is easiest to measure collective fields– out of the plane. It also

drastically reduces the dependence on shape as demagnetisation energy is overcome by the anisotropy. This means that particles can be optimised for their application.

A secondary benefit of PMA materials is that stray fields from PMA particles are all oriented in the same direction. If we consider a collection of IP rectangular particles magnetised about their long axis, the random angle of landing will mean that their easy axes vary within the plane causing their components to add less constructively. In OOP materials, the easy axis is constrained perpendicular to the plane and is parallel in all samples.

4.1.1. PMA technology in memory applications

Since the effect was observed in Co-Cr layers in 1974 [10], perpendicular magnetic anisotropy (PMA) has provided a crucial foundation in the development of magnetic memory technology and is still at the forefront of pioneering technologies in the field. Synthetic anti-ferromagnetic (SAF) bilayers have been employed extensively for magneto-resistive random-access memory (MRAM) technologies to pin the fixed (reference) layer, providing no stray fields that influence the free layer [11]–[13]. The giant magnetoresistive (GMR) or tunnelling magnetoresistive (TMR) effect is utilised to differentiate between a parallel (low resistance state) and perpendicular (high resistance state) magnetic orientation of two layers, giving a binary output used to read information [14].

Perpendicular materials provide many advancements to this field. Magnetic memory is primarily used for non-volatile memory systems and as such requires high stability to external interference and long lifetimes. The effective anisotropy K_{eff} provides a direct measure of the stability of a memory element, with the energy barrier $E = \frac{1}{2} H_K M_S V$ and H_K directly proportional to K_{eff}. In data storage, magnetic materials are usually extremely thin, with memory elements being reasonably approximated by flat planes. The high interfacial anisotropy of perpendicular materials overcomes the thin-film demagnetisation energy. This eliminates the sensitivity to shape and provides improved thermal stability enabling stable bit sizes smaller than 20 nm [15]–[19]. The developments in this area have allowed for an order of magnitude increase to $> 1 \, Tbits/in^2$ [19].

4.1.2. Work in this thesis

SAF particles with PMA have driven much research in memory applications and shown strong promise in fluid-based biotechnology applications [3]. The project brief requires a tuneable set of encoded particles which can be transferred through a liquid suspension. It is intended that these are small enough to be invisible to the naked eye, increasing the difficulty of mechanical destruction of the tag. Through the engineering of the coupling, we can control the switching properties of magnetic films, providing 'channels' that switch at differing applied fields, creating the foundation blocks of a magnetic tag. In this scheme, the switching field (and corresponding moment) provides

the binary "on" and "off" states that will be used to carry information. Below the switching field, there is no magnetic moment or corresponding stray field. Above the switching field, the full magnetic moment is out of the plane and can be measured through its stray field. The switch then provides a distinct change in signal, which can be detected. With sharp transitions, we should have distinguishable channels, with spacing between to avoid blurring. This ideal scenario is shown schematically in Fig 4.1.
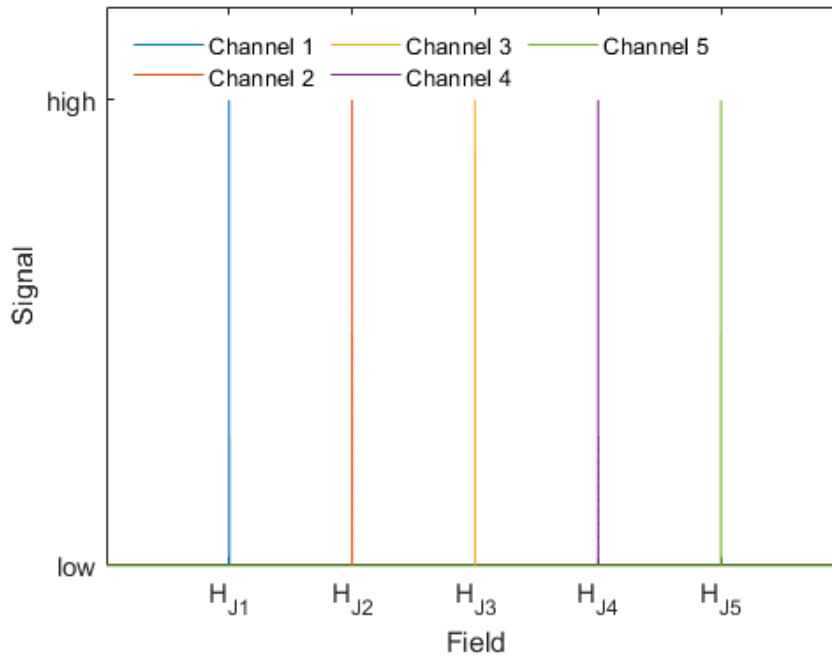
Fig 4.1 The differential of a switching curve from a set of ideal particles. Our ideal particles would have transitions that are as sharp as possible, for maximum resolution and spacing between neighbours. Here the field values are arbitrary, and signal represents the inductive voltage from the changes in field produced from our particle transitions, i.e. dB/dt.

One problem that is faced by many security tag technologies is removal. If the tag can be seen, it is easily removed or corrupted. Our data carriers can be made hard to intentionally mechanically corrupt by using top-down lithography techniques to pattern into micro-particles that are virtually invisible to the human eye. Throughout this, we must ensure that we do not compromise the magnetic properties of the structure. Lastly, with optimisation of the growth process and underlayers, these particles can be lifted from the substrate and transferred into a solution. If moment balance is maintained by growing SAF films with two nominally identical magnetic layers, the particles should possess zero moment at remanence and avoid agglomeration through mutual interaction. When in solution, particles with differing switching properties could be combined. We would then look to detect the presence or absence of a particular channel within the set. This will form the basis of the tag. As our particles have a high aspect ratio, they are likely to adhere with the easy axis of magnetisation perpendicular to the sample surface, ensuring that all particles are under the influence of the same applied field.

For this encoding scheme to be valid, all these features must be validated experimentally. This begins by growing magnetic films with strong interfacial PMA, using the $Co_{60}Fe_{20}B_{20}/Pt$ system. We aim to use a system with applied fields that are driven by permanent magnets. Therefore, we require our particles to be insensitive to fields perpendicular to the easy axis. To ensure that these particles are not affected by fields that do not lie along their easy axis, the angular magnetic properties should be tested. To do so, we measure a switching astroid for the continuous magnetic film. If the particles have high PMA, they will be mostly insensitive to IP fields and we have the possibility of using drive field systems with non-zero IP components, e.g., rotating systems.

We lastly should evaluate the collective properties of a channel. Individual particles may display sharp transitions, but if these vary between nominally identical particles it will affect the transition profile. The collective properties will be quantitatively examined, to provide realistic input parameters for computational modelling of the system later in this work.

Magnetic stacks in this thesis are written by growth order starting with the bottom-most layer (in contact with the substrate), using periodic table notation. The layers will be separated by a forward slash and the thickness of each in nanometres given in brackets. For example, $Ta(2)/Pt(2)/CoFeB(1)/Pt(2)$. If we are varying one of the thicknesses it will be in bold and written as $\boldsymbol{t}$, for example, $Ta(2)/Pt(2)/CoFeB(\boldsymbol{t_{CoFeB}})/Pt(2)$.

4.1.3. Previous work

The work in this chapter was built on the foundations established in our group. The tunable coupling of SAF particles was developed by Reinoud Lavrijsen et al in 2012 [20]. The patterning process was initiated by Lucy Cunningham in her thesis [21], which was extended to using a germanium release layer by Emma Welbourne [22] and Michael Stanton. The optimisation of underlayers uses work from Tarun Vemulkar [23]. All samples reported in this thesis were deposited, patterned and characterised by the author.

4.2. Single-layer CoFeB films

4.2.1. Perpendicular magnetic anisotropy in $CoFeB/Pt$ systems

In this work, we use extremely thin CoFeB/Pt layers, which exhibit PMA. This is a uniaxial, interfacial anisotropy that causes it to become energetically favourable for the magnetisation to align out of the plane of the sample when the magnetic layer is below a critical thickness. For the easy axis of a thin film to align out of the plane of the sample, the demagnetising field of the film must be overcome.

The physical description and phenomenology of PMA are described within section 2.1.2. In the CoFeB/Pt magnetic layers used in this thesis, the effective anisotropy can be described by $K_{eff} = K_V + 2K_S/t_{CoFeB}$. As such, if the $CoFeB$ layer is thin enough, the surface anisotropy dominates, and the system will have an easy axis out of the plane of the material.

We hope to achieve strong PMA and sharp transitions when the field is applied perpendicular to the plane of the film. We would also expect a coherent rotation of magnetisation when the applied field is parallel to the plane. This scenario is described within Fig 2.4. In these conditions, it is appropriate to describe the effective anisotropy K_{eff} as $K_{eff} = \frac{1}{2} M_S H_K$, where H_K is the hard axis saturation (measured experimentally) and M_S is the saturation magnetisation of $CoFeB$. Measurement of M_S has been completed using Vibrating Sample Magnetometry (VSM): taking an average of all the samples in a series of $CoFeB$ layers of different thicknesses, we obtain an estimation for $M_S = 1.05 \times 10^6 \ Am^{-1}$, which is in agreement with the literature [24]. H_K values were taken from the hard axis loops (applied field in the plane of the material) using VSM magnetometry. In this measurement, H_K is the point at which the sample saturates in the hard axis direction, in our case in the plane of the film. The data are shown in Fig 4.2, where the slope of the transition can be seen to change dramatically with $CoFeB$ layer thickness. From these values, it is easy to obtain K_{eff} for each sample (using $K_{eff} = \frac{1}{2} M_S H_K$).

As seen from the equation $K_{eff} = K_V + \frac{2K_S}{t_{CoFeB}}$ (Equation 2.16), if we consider a plot of $K_{eff} t_{CoFeB}$ vs t_{CoFeB} we should expect a straight line with a gradient K_V and y-intercept $2K_S$. This is shown in Fig 4.3 for continuous $Pt(2)/CoFeB(\boldsymbol{t_{CoFeB}})/Pt(2)$ films grown by magnetron sputter deposition onto Si substrates. From this, we estimate $K_V \approx -220 \ kJ/m^3$ and $K_S \approx 0.21 \ mJ/m^2$. The surface anisotropy must be extrapolated, as there is a lower limit for which we can grow a continuous layer of $CoFeB$.

It is also noted that there is a point where K_{eff} becomes negative, indicating that the hard anisotropy plane of the film has become an easy anisotropy plane. This occurs when the volume term has become the dominant component. This is referred to as the Spin-Reorientation Transition (SRT) and is estimated to be $t_{SRT} \approx 1.8 \ nm$ in our Pt(2)/CoFeB/Pt(2) samples. When the field is applied in the film plane, a loop for a sample above this thickness would show hysteresis and sharp transitions, characteristic of an in-plane easy axis. This was not tested experimentally.
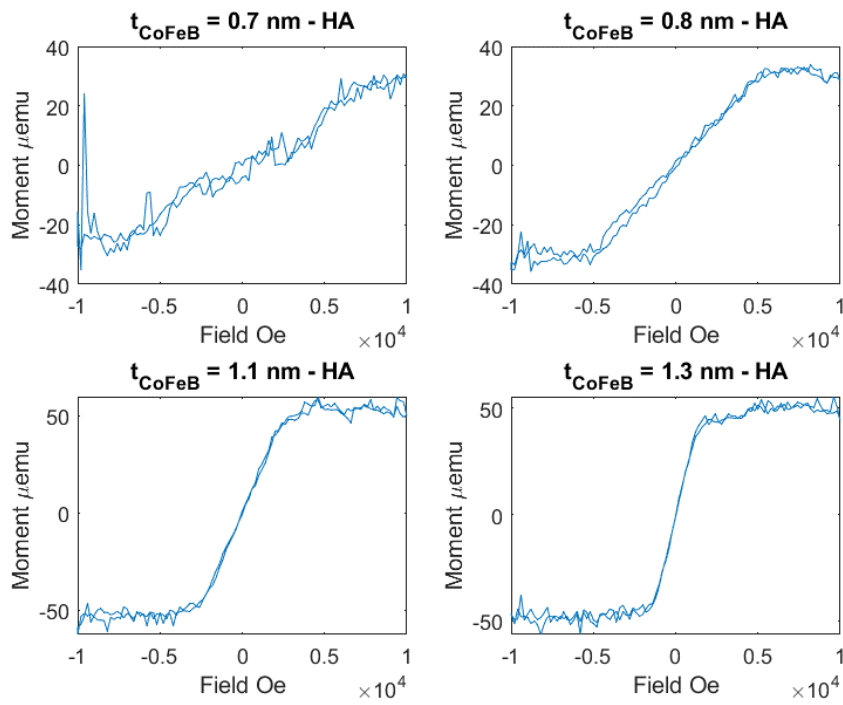
Fig 4.2 Hard axis VSM measurements for a series of $Pt(2)/CoFeB(t_{CoFeB})/Pt(2)$ layers grown on a Si substrate. This data is used to estimate the hard axis saturation field, used in Fig 4.3.
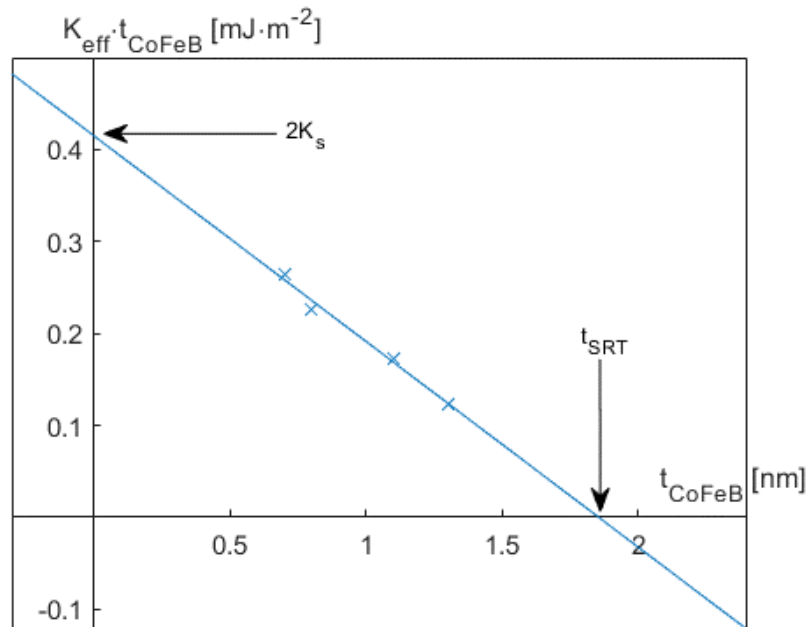
Fig 4.3 A plot of saturation field vs CoFeB thickness for a series of films. The linear fit allows us to ascertain estimates of both the surface and volume anisotropy terms, as well as the Spin-Reorientation Transition (SRT).

We can also analyse the coercivity as a function of CoFeB thickness. For this, easy axis (field out of the material plane) hysteresis loops can be taken using polar MOKE magnetometry. The variation of coercivity (H_C) with CoFeB thickness can be seen in Fig 4.4, with the individual loops in Fig 4.5. The coercivity is defined as the average of where both rising and falling sides of the hysteresis loop pass through the midpoint value. These are taken as the average of 10 measurements taken at 10 different locations on the film, each being the result of the average of <20 loops. The error bars show the standard deviation of the H_c values from the ten measurements at differing locations.

When we analyse the data in Fig 4.4, we observe a slight decrease in coercivity with increasing CoFeB thickness. We expect the coercivity to be roughly constant for OOP layers (between the limit of a continuous film and the SRT, $0.2 - 1.8\ nm$) due to their reversal properties. Transitions occur due to either the fast propagation of initial domain/domains sweeping through the layer or the accumulation of many different nucleation sites with slower propagation. Our data, as seen in Fig 4.5, shows extremely sharp switching characteristics typical of transitions occurring from rapid domain wall expansion of few nucleation sites [25]. Within our thickness parameter space, it has been shown that the nucleation field of perpendicularly magnetised CoFeB is only weakly affected by the film thickness [26]. As such, we should see a roughly constant value of coercivity.

An increase in coercivity indicates an increase in pinning sites – which limit the propagation of the domain. These are affected by growth conditions and local topological variations.
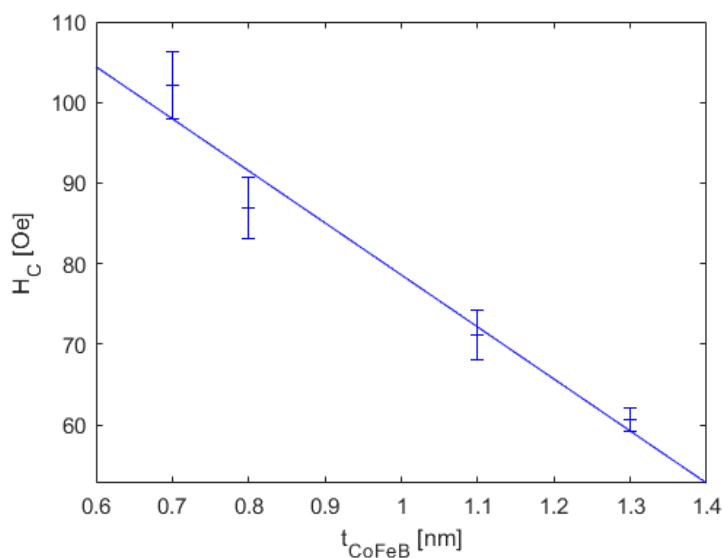
Fig 4.4 A comparison of the coercivity of $CoFeB$ layers probed using OOP polar MOKE magnetometry. A roughly linear decrease is seen, though the values do not differ considerably. Here, the error bars represent the last and first points of the saturation value – i.e. the full width of the transition.
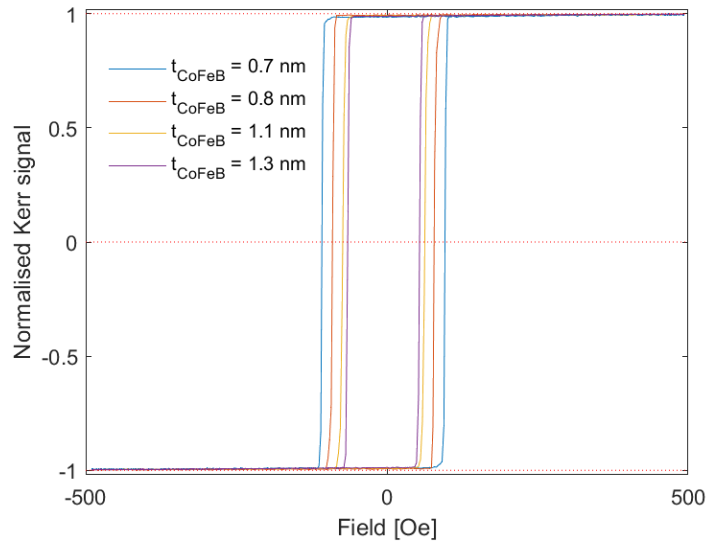
Fig 4.5 Easy axis measurements of a series of $CoFeB$ layers grown on Si. All transitions are sharp, and we see a slight decrease in coercivity for increasing $CoFeB$ thickness.

4.2.2. Rotational switching astroid

In our evaluation of current technologies in section 2.4, it was decided that drive fields from permanent magnets would be more advantageous for our proposed detector due to their compact nature and reduced inductive losses. AC field would be produced using a rotating cylindrical permanent magnet, providing a sinusoidal Z component of the field. Cylindrical permanent magnets also produce non-zero in-plane field components, which need to be considered. For this detector setup to be effective, we need our particles to be insensitive to these in-plane components. A method to check this is by measuring a switching astroid (section 2.1.1) using rotating fields. The difference between a linear and rotational switching astroid is outlined in Fig 4.6(a,b). To measure a conventional linear astroid for systems with uniaxial anisotropy, hysteresis loops are taken at varying field angles and the switch location for each angle is analysed. An example of this is shown in Fig 4.6c. The transition is seen as a discontinuity in a linear background, which arises due to diamagnetism in the sample holder and adhesive. In these measurements, the background was taken as a separate measurement and subtracted. The location of the transition is defined as the halfway point of the discontinuity, with the start and end of the transition defining the error bar.

In a rotating field switching astroid, the sample is saturated along the easy axis, but this time the field is reduced to the measurement field B_{set} in the same easy axis direction. The sample is then rotated in a constant field B_{set} and the magnetic moment is measured as a function of sample angle θ. An example is seen in Fig 4.6d. Again, the transition is seen as a discontinuity in sinusoidal $m_\perp$ that results from rotation of a highly anisotropic material. Here, the diamagnetic background from the

sample holder remains constant, as the field is unchanging. The location and errors of the transition are defined as in the linear transition but are with respect to field angle θ.
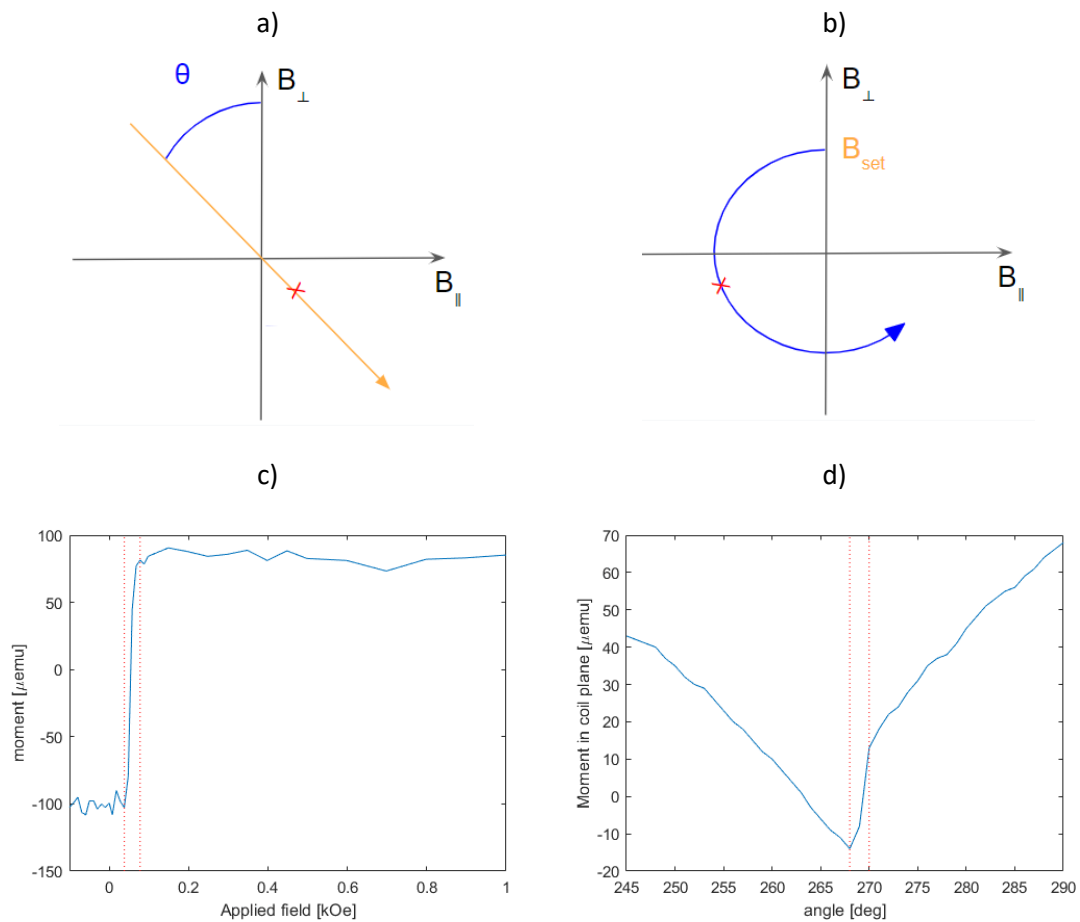
Fig 4.6 a) a linear switching astroid measurement. A sample is saturated along the EA, then a start angle θ is set, and a half loop is taken. b) a rotation switching astroid measurement. The sample is saturated along the EA, then the field is reduced to B_{set}. The sample is then rotated for $\theta = 0 - 180°$ at constant B_{set}. Here, arbitrary transition locations are shown with a red x but must occur after the sample has passed through the line $B_\perp = 0$. c) a normal half loop from a linear measurement. d) a normal rotating measurement.

Using our rotating field method, we can determine the angle of the transition for varying field strengths, B_{set}. These can be plotted, constructing the rotating field astroid. If our samples are insensitive to IP field components, we should observe an astroid with boundaries that are close to parallel to the $B_\parallel$ axis, i.e. the switch should occur at roughly the same value of $B_\perp$. This is because $H_K \gg H_c$ in our samples, elongating the astroid along the $B_\parallel$ axis, as is shown schematically in Fig 4.7. In our CoFeB layers, the ratio $\frac{H_K}{H_c} > 25$, as shown in section 4.2. For example, our 1 nm CoFeB sample has $H_C = 49\ Oe$ and $H_K \approx 4000\ Oe$.
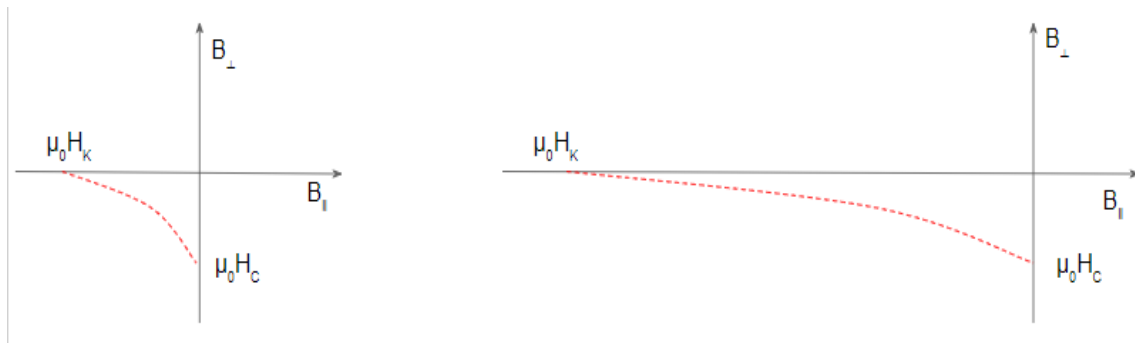
Fig 4.7 An example of a switching astroid for quadrant 2, the P-AP transition H_2, becoming increasingly flat for higher ratios of H_K/H_c. This demonstrates the idea and is not real data.

We obtain our astroid by taking measurements of the moment in a VSM using a vector coil arrangement. The sample is rotated in a constant field, B_{set}, with the moment parallel and perpendicular to the plane of the film deduced using simple rotation matrices. This is completed at multiple field strengths, saturating the sample along the easy axis at the beginning of each run. We then assess the moment perpendicular to the sample plane, where discontinuities indicate at which applied field angle the sample magnetisation switches at for a given field magnitude. The process can be broken down as follows:

- Saturate the sample at 1.5 T, with a direct OOP field.
- Set the field strength to B_{set}
- Rotate the sample in the field from $0 \rightarrow 180°$
- Repeat for a different field strength value, B_{set}.

Though we can also measure transitions in the second and fourth quadrant of the astroid, we will only consider the first transition as the second lacks consistent initial saturation. Due to the two-fold symmetry of the system, the complete astroid can be measured in a single $0 \rightarrow 180°$ rotation. We assess both directions ($0 \rightarrow 180° 360 \rightarrow 180°$) to correct for sample misalignment.

The resulting rotational switching astroid for a Pt(2)/CoFeB(1)/Pt(2) sample is seen in Fig 4.8. We observe near straight lines parallel to the $B_{\parallel}$ axis, consistent with a sample with $\frac{H_K}{H_c} > 25$. We present the easy axis VSM loop for this sample in Fig 4.9, with $H_c = 49\ Oe$. Note, this is does not agree with the fit in Fig 4.4, which was taken with MOKE at a higher frequency. We confirm that the switching at 180° is indeed consistent with this value. This shows switching at consistent $B_{\perp}$ values. From this, we can deduce that the sample is mostly unaffected by in-plane components of the field. This means that we can use drive fields that have non-zero IP components, confirming that our PMA films are compatible with a rotating permanent magnet drive field source.
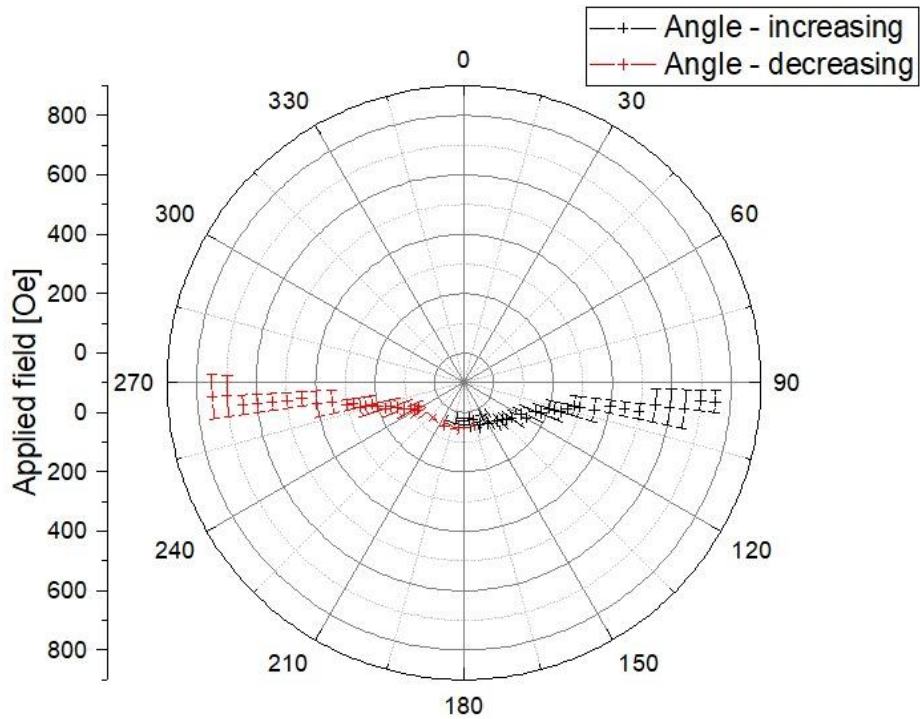
Fig 4.8 Rotational switching astroid for a CoFeB thin film of 1 nm thickness.
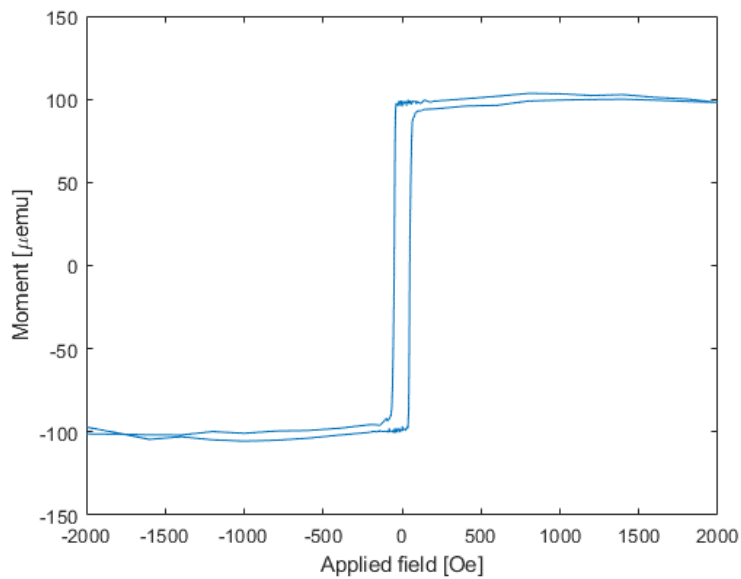
Fig 4.9 Easy axis VSM loop for a CoFeB thin film of 1 nm thickness.

4.3. Antiferromagnetically coupled bilayers

Now that we have confirmed the presence of PMA we can evaluate the effects of IEC on two coupled layers. IEC is an effect that originates in the SOI, with the spin polarisation of one magnetic layer interacting with the conduction electrons within a non-magnetic spacer. This polarisation propagates through the spacer layer and interacts with the spin of electrons in a second magnetic layer which the first magnetic layer is not contiguous to, again via the SOI. In such a situation, one

magnetic layer influences a second's magnetic state whilst maintaining no contact and is hence an indirect exchange effect. The phenomenology and microscopic origin are described in more detail in section 2.1.3.

In this section, we present evidence of the growth of controllable PMA SAF structures, starting with films grown straight on Si substrates in section 4.3.1. Following this in section 4.3.2, we pattern these films into particles using photolithography techniques, again straight onto a Si substrate. Finally, in section 4.3.3, we grow films with the potential of being lifted off as particles by using a Ge release layer.

The CoFeB used in all stacks has a nominal thickness of 1 nm, with Ru thickness nominally 0.8 nm – corresponding to the first AF peak. The functional layers in the PMA SAF stack are $CoFeB(1)/Pt(t_{Pt})/Ru(0.8)/Pt(t_{Pt})/CoFeB(1)$. t_{Pt} is the same on both sides of the Ru, maintaining the symmetry. We stabilise the PMA further by growing another Pt PMA layer on either side of this functional group. We provide a Ta underlayer between this group and the substrate as a smoothing buffer and cap the uppermost layers with a 6x $Pt(2)/Ta(2)$ buffer. This provides structural rigidity and ensures that our particles do not curl upon lift-off due to internal stresses, as well as providing a barrier to oxidation. This is important as oxidation of the CoFeB layers would alter the magnetic properties of the material. The curling is a result of the extremely high aspect ratio of the particles, which are microns wide and nanometres thick. Ta also grows as an amorphous layer when below 4 nm in thickness [23], allowing for the growth of strongly textured (1 1 1) Pt. PMA is highly dependent on the quality of the interfaces, so this Ta layer allows us to further increase our anisotropy [23]. A schematic of the complete structure, grown on a Si substrate, is given in Fig 4.10.

In this scheme, samples can be differentiated by their interlayer coupling strength, enabling a tag-based system that is distinguished with the presence or absence of a switch at a particular field value, corresponding to a sample of known Pt spacer layer thickness. To design a detection scheme, we first need to know how these switches occur – the width of each transition and the relative spacing between nominal channels. This can be evaluated through analysing hysteresis loops, which have been measured using MOKE magnetometry. The benefit of this method is that it is fast, but it is highly localised and therefore does not give any information about the distributions of switching parameters for different nominally identical particles/areas within the same sample.
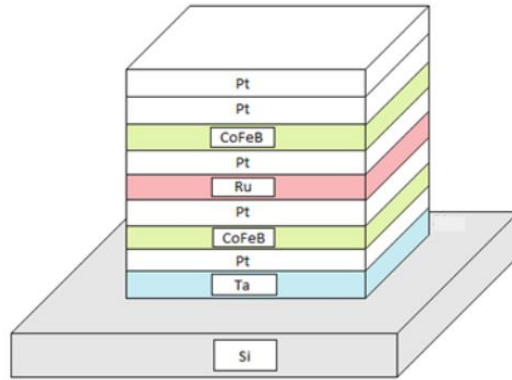
Fig 4.10 Schematic showing the SAF multilayer architecture for a continuous film on a silicon substrate.

4.3.1. Films

The simplest system to start with is a continuous thin film. Commercially available Si wafers are chosen as substrates due to them being close to atomically smooth, providing a foundation that offers little roughness to propagate through the stack. This is particularly important to ensure good interfaces which are critical to PMA and to minimise inhomogeneity in coupling across the film due to effects such as orange-peel coupling [27]. Substrates are cleaved from wafers before growth to roughly $1 \ cm^2$ squares and cleaned using acetone followed by isopropyl alcohol (IPA). The stack is grown with the configuration shown in Fig 4.10.

We probe these stacks using MOKE magnetometry, which confirms PMA SAF properties. An example MOKE loop obtained on one such film with Pt thickness of 0.58 [nm] is shown in Fig 4.11. In this measurement, the apparent non-zero remanent state is an optical artefact resulting from the skin depth of the laser, with layers closer to the surface of the stack causing a greater change in MOKE signal. For identical magnetic layers (confirmed for our samples using VSM), this allows us to differentiate between the signal coming from the top and bottom magnetic layers.
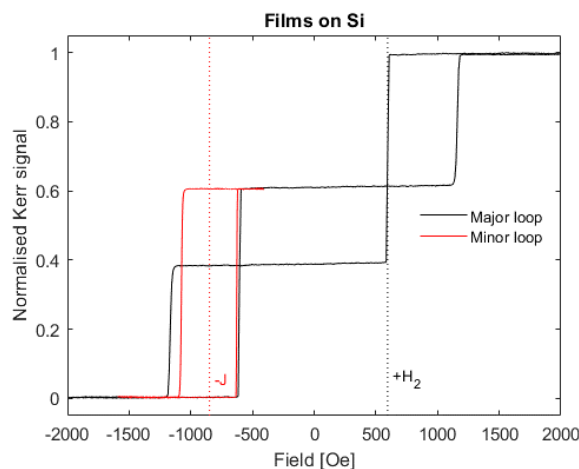
Fig 4.11 MOKE loop of a PMA SAF with a nominal Pt thickness of 0.58 nm. Here, the major and minor loops are shown in black and red respectively.
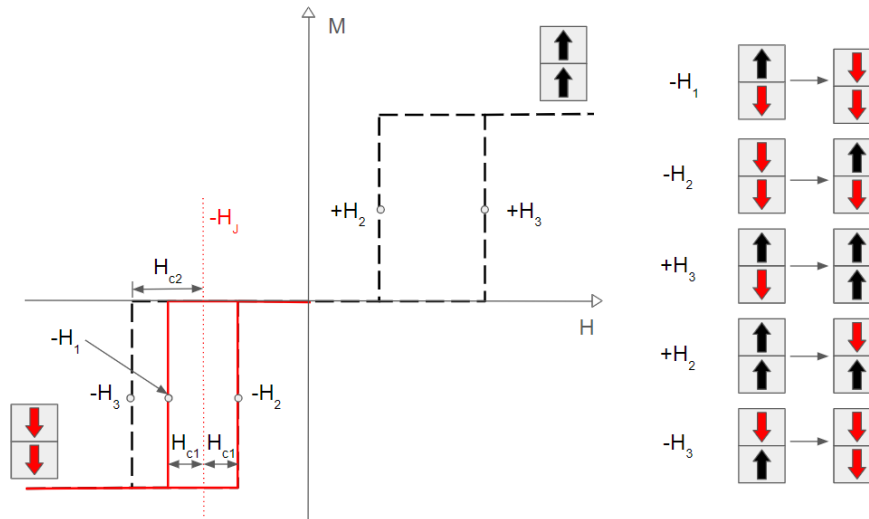
Fig 4.12 A schematic outlining the switches within a hysteresis loop. In this schematic, we also show the changes in the orientation of each layer for all of the transitions.

The loop starts at a negative saturation field, with both layers in a 'down' state. When the field is increased (towards zero), the magnetically easiest CoFeB layer switches. In the particular loop of Fig 4.10, we observe this to be the top layer, evidenced by a larger change in signal for nominally equal CoFeB layers, as previously described. The magnetic layers are now anti-parallel with the top layer in the 'up' state. The location of the transition is defined at the point where the change in the moment is equal to the midpoint between initial and final states which in this instance is labelled $-H_2$ in Fig 4.12, which shows a schematic of an ideal SAF hysteresis loop. This is generally the point of the highest gradient. Though the CoFeB layers are nominally the same, differences in anisotropy and other magnetic properties emerge between the two due to uncontrolled variations in growth conditions, such as propagation of roughness up the stack. This leads to one magnetic layer being less coercive and switching first. If both magnetic layers had the same magnetic properties, both AP states (top layer opposed to field direction, or bottom layer opposed to field direction) would be equally possible.

As the field is increased from zero to positive saturation, the harder of the two layers switches at a field value defined here as $+H_3$. As the field returns to negative saturation, the transitions follow the same order as before, with the easier layer switching first at H_2 and the harder layer at $-H_3$. The width of the major loop gives insight as to the total coercivity of both layers, $H_{C1} + H_{C2}$, but gives no insight into their individual values and only provides a range for the coupling field H_J. The coercivity of each layer is shown schematically in Fig 4.12.

Minor loops can be taken by cycling the field between (negative in Fig 4.11 and Fig 4.12) saturation and a value just after the P-AP transition $(-H_2)$. This alternates the state of the least coercive layer between parallel and antiparallel to the most coercive layer, whilst the latter remains unchanged in

the direction of saturation. $-H_2$ is the same as in the major loop – the least coercive layer switches, causing the system to go from a P to AP state. $-H_1$ is the transition where the least coercive layer goes back to the P state. The centre of the two transitions $(H_1 + H_2)/2$ defines the coupling field H_J, with the width of the minor loop $(H_2 - H_1)$ being two times the coercivity of the least coercive layer $- H_{C1}$. There is no way to isolate the switching of the most coercive layer on its own, but its coercivity, H_{C2}, can be deduced from $|H_3 - H_2| - H_{C1}$. The locations of the transitions, as well as the definitions of coercivity, are shown in Fig 4.12. The coupling field H_J is dependent on the thickness of the magnetic layers and related to the interlayer coupling energy density per unit area J, by $J = M_S H_J t_{CoFeB}$ $[Jm^{-2}]$.

To analyse how Pt spacer layers affect the coupling strength of our magnetic films, a series of samples were grown with functional magnetic layers $CoFeB(1)/Pt(t_{Pt})/Ru(0.8)/Pt(t_{Pt})/CoFeB(1)$ and Pt thicknesses in the range 0.22-0.72 nm. The positive P-AP transition (H_2) for all films in this series is seen in Fig 4.13a. It should be noted that switching parameters are frequency-dependent [28], so a field sweep rate of 1kOe/s was maintained for all measurements. In all films except the thinnest (0.22 nm Pt layer thickness), sharp, spin-flip switching is observed. For the thinnest Pt layer at 0.22 nm, it is likely that a continuous film has not been deposited, instead producing islands of patchy Pt coverage. This leads to more pinning defects and expansion via many small domains as opposed to a single domain that rapidly sweeps through the film, producing a sloping sigmoidal transition. This could be tested using domain wall imaging but is outside the scope of this thesis.
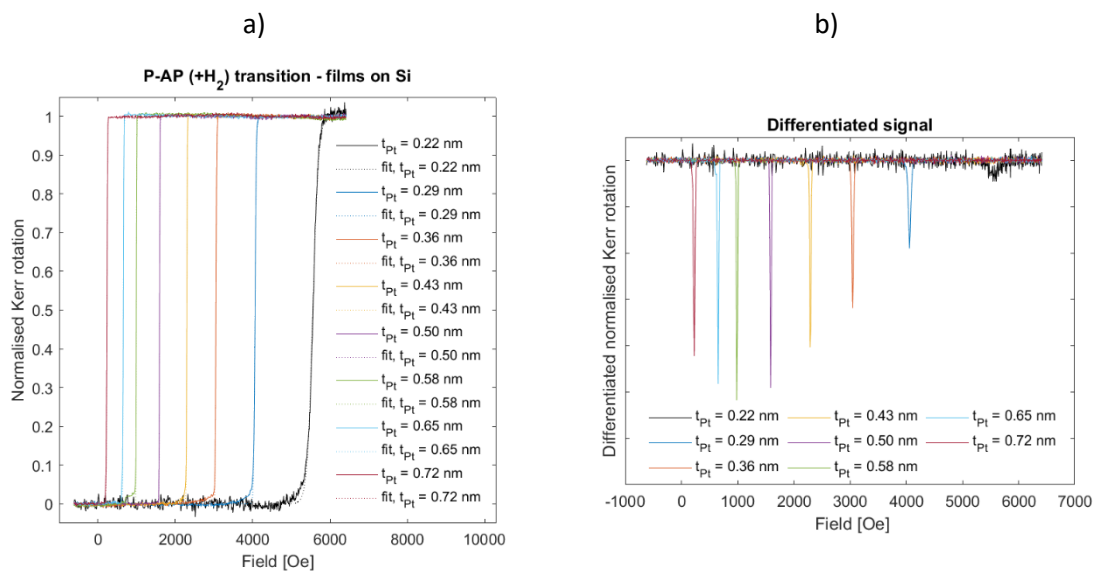
Fig 4.13 MOKE measurements of the H_2 transition for films in a $CoFeB(1)/Pt(t_{Pt})/Ru(0.8)/Pt(t_{Pt})/CoFeB(1)$ series, with t_{Pt} in the range 0.216-0.72 nm. $+H_2$ was taken from major loops using polar MOKE magnetometry. b) Differentiated signal. Here it is clear that there is no overlap between neighbouring channels.

The transitions have been modelled as a logistic sigmoidal function to provide qualitative information as to transition positions and widths. This derives from the Boltzmann function, normalised between 0 and 1. A logistic sigmoid is a symmetric function defined by,

$$y(x) = \frac{1}{1 + e^{-(x-c)/a}},$$ (4.1)

where c is the centre of the transition and a characterises the width of the transition. In this notation, a smaller a value defines a sharper transition. An example of a logistic sigmoid is shown in Fig 4.14. In this plot, we also display the transition width $W_{0.3-0.7}$, defined as the width between the 30 and 70% points of a transition. $2a$ corresponds to the width between the points defined by $c + a$ and $c - a$, which, using Equation 4.1, are equal to 0.73 and 0.27. The two values can be compared in Fig 4.14.
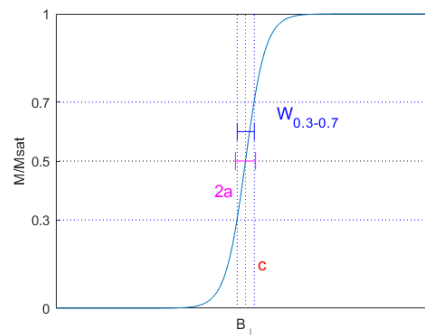
Fig 4.14 An example of a logistic sigmoid, with transition centre c and width parameter a. The 30-70% width is also shown.

One crucial feature of the results presented in Fig 4.13a is that the transitions seem to be reasonably sharp and well-separated, which gives us confidence that this can be used as an identifiable encoded property for a tuneable tag. This is seen more clearly when the differentiated signal is analysed, as is shown in Fig 4.13b. In this plot, the difference between sharp, spin-flip transitions seen for $t_{Pt} > 0.22\ nm$ and the rounded transition seen for the thinnest Pt layer is clear.

We also characterise the decay of the indirect exchange coupling strength with increasing Pt spacer thickness, which we expect to be exponential [26]. This is seen in Fig 4.15, where the coupling field H_J is plotted as a function of t_{Pt}. We also show the corresponding values of $J = H_J M_s t_{Pt}$. The data were fitted to an exponential with amplitude A and decay constant t_d:

$$y(x) = Ae^{-\frac{x}{t_d}},$$ (4.2)

 yielding an amplitude at zero $A = 1.24\ T$ and decay constant $t_d = 0.24\ nm$. This is consistent with literature values for a CoFeB/Pt/Ru system [29], [30]. The A parameter is larger than those found previously within the group [20], but this is attributed to better fabrication processes and a difference in Ru thickness.

Finally, we characterise each of the $+H_2$ (P-AP) transitions in the series of varying Pt spacer thickness by fitting them using Equation 4.1. Equation 4.1 is dependent on two parameters: the centre of the transition (c) and the transition width (a). From this set of data, we characterise their dependency on t_{Pt} and evaluate any trends that can be used in modelling. These relationships can be seen for films on Si in Fig 4.15(b,c), showing a and c as a function of t_{Pt}.

Apart from the value at $t_{Pt} = 0.22\ nm$, the transition width, characterised by a, shows little variation between samples. a is always above $5\ Oe$, with an average (excluding the point at $t_{Pt} = 0.22\ nm$) of $\bar{a} = 8.5\ Oe$ and standard deviation $\sigma_a = 4.0\ Oe$. The average transition width $\bar{a}$ for a series can also be considered as a figure of merit. a is dependent on the interfacial properties of the stack, therefore these values can be used to establish whether any interfacial properties are lost in the patterning process. It can also be used as quantitative evidence of the benefit of one fabrication process over another. We also analyse the series by evaluating the width of the $+H_2$ transition, which is denoted by $W_{0.3-0.7}$. We find an average value $\overline{W_{0.3-0.7}} = 15.4 \pm 3.7\ Oe$. Critically, we require high values of the ratio of channel separation to $W_{0.3-0.7}$, which we call the key ratio value (KRV). We can use the KRV as a figure of merit for comparing different series. For this series of films on Si, we calculate an average KRV of $\overline{KRV} = 40.0 \pm 14$, showing a large separation compared to the transition width. KRV will be an important quantity in further chapters when we wish to optimise particle series through simulations.
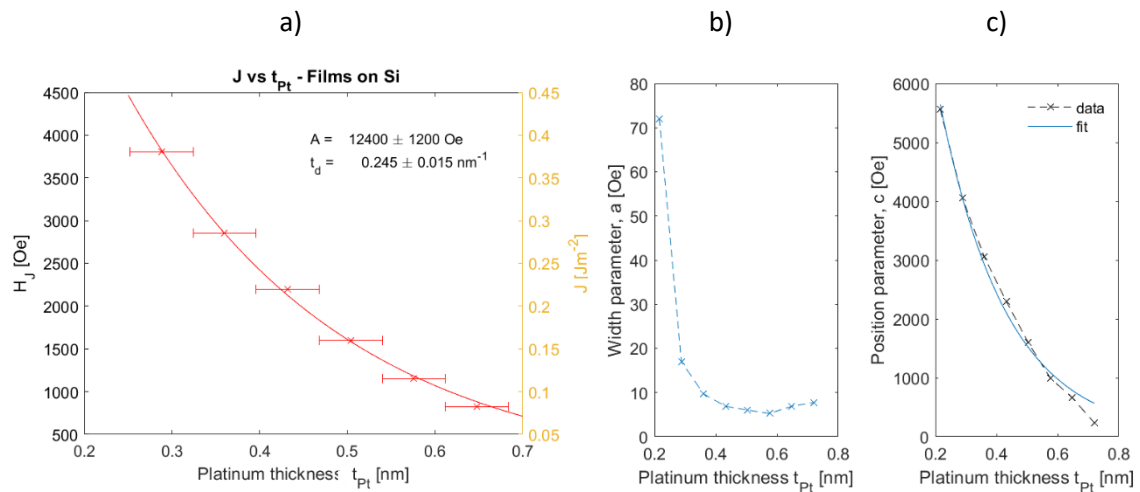
Fig 4.15 a) Plot displaying the decay characteristic of the interlayer exchange coupling field H_J with respect to Pt spacer layer thickness for the $CoFeB(1)/Pt(t_{Pt})/Ru(0.8)/Pt(t_{Pt})/CoFeB(1)$ series, with t_{Pt} in the range 0.216-0.72 [nm]. The red line is the result of the exponential fit (Equation 4.2), with the parameters shown in the inset. b) A comparison of the width parameter, a, for $+H_2$ transitions for the film series, taken from major loop MOKE data. c) A comparison of the position parameter, c, for $+H_2$ transitions for the film series, taken from major loop MOKE data. The line in (c) is an exponential fit according to Equation 4.2.

The fit in Fig 4.15c is a standard exponential decay, as in Equation 4.2. Note that this is the exponential fit of $+H_2$. This should show a similar characteristic to the coupling (H_J) shown in Fig 4.15a if the coercivity of different layers is constant. This has not been checked in this section.

4.3.2. Particles on Si

We showed in section 4.3.1 that we can produce the desired magnetic properties for continuous thin films on Si substrates. These magnetic properties need to be maintained when reducing the lateral dimensions. Patterning of our samples is completed in the following way: we clean the circa 1 cm^2 substrate using first acetone, then IPA, and dry our samples with clean dry nitrogen to ensure the sample is free of contaminants and water. We then grow our magnetic stack via magnetron sputtering. Once we have our functional magnetic stack, samples undergo a second cleaning cycle and are spin-coated using first an HDMS primer and finally ma-N 1410 negative photoresist. A post bake follows at $100°C$ for one minute. Patterning of the photoresist layer is then completed using a direct laser writing system with a 405 nm wavelength laser of nominal spot size 0.6 μm. Once patterned, the sample is developed in ma-D 533/S. This leaves a photoresist layer of the intended particle shape on the surface of the magnetic stack. The sample is then ion-milled using the same process as sputtering, with a reverse potential difference. The photoresist areas shield the magnetic stack, and the patterned particles remain. The patterning process is shown diagrammatically in Fig 4.16.
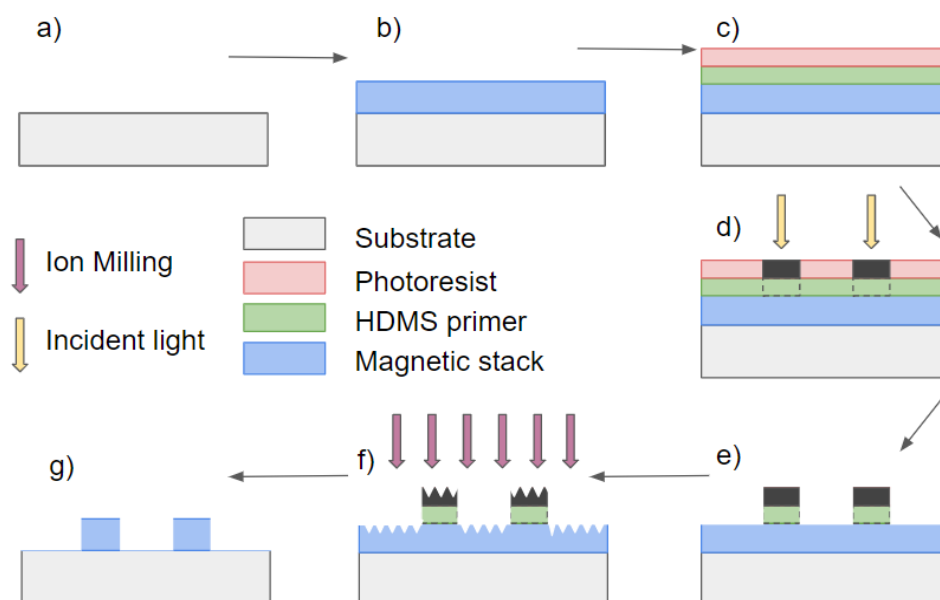
Fig 4.16 Schematic showing the patterning process, showing a) bare Si substrate, b) the magnetic stack is grown, c) photoresist is spun on top of the magnetic layer using HDMS as a primer to increase adhesion, d) the photoresist is patterned using direct-write lithography, exposing the desired pattern and cross polymerisation occurs, e) the photoresist is developed, leaving behind photoresist in the desired pattern, f) the stack is ion milled, creating particles of the desired shape (g).

To visually differentiate the particles in this series (particles on Si with varying t_{Pt}), we patterned each of our magnetic stacks into a different shape of size $\sim 20\ \mu m$. These are described in Table 4.1 below. Optical images of the particles attached to the substrate can be seen in Fig 4.17. A full schematic showing sizes and separation can be found within the appendix.

Pt thickness [nm]	Particle shape
0.22	Circles
0.29	Squares
0.36	Triangles
0.43	Pentagons
0.50	Rectangles
0.58	Ovals
0.65	Crosses
0.72	Stars

Table 4.1 A summary of the Pt thicknesses and particle shapes grown in the series deposited directly on a Si substrate.
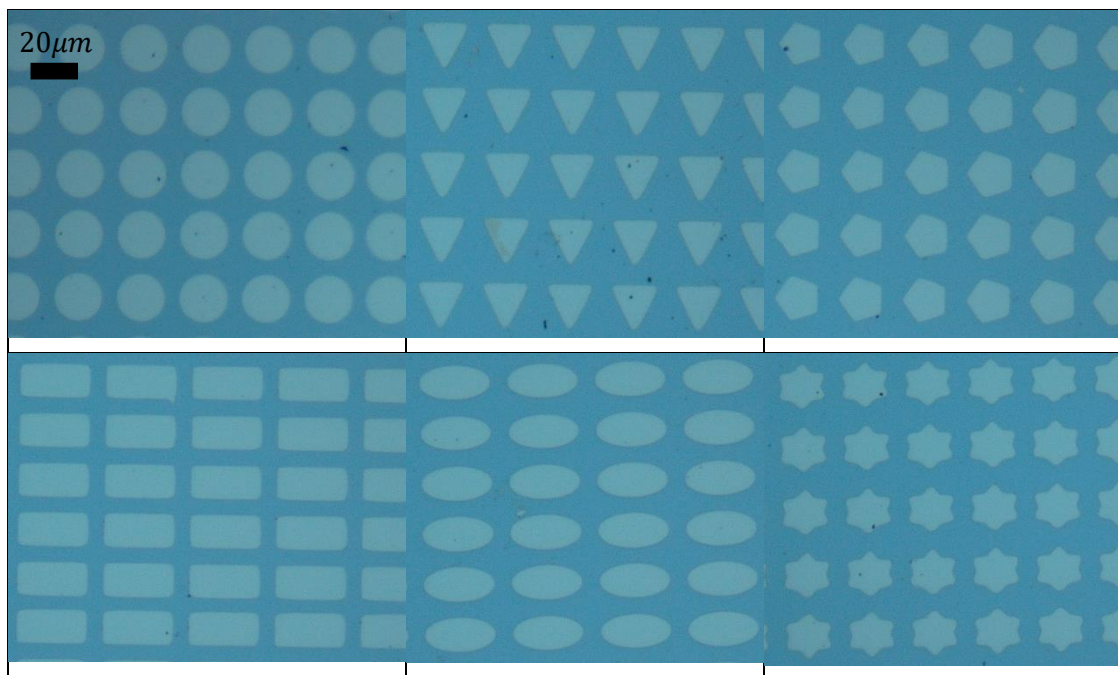
Fig 4.17 Examples of magnetic films patterned into shapes as described in Table 4.1, on a Si substrate. The scale is the same on all images.

We must ensure the magnetic properties are not compromised during the patterning process. Both major and minor hysteresis loops are taken using MOKE for a single particle of each Pt thickness, to compare with results found for the corresponding continuous film, which was deposited in the same

sputtering run. An example of this is shown for one of the oval-shaped particles of $t_{Pt} = 0.58\ nm$ in Fig 4.18. Once again, we observe sharp switching from both layers in the stack, though we observe a multistage AP-P transition for this particular sample. It is expected that this is a result of the sampling of adjacent particles, with different switching properties (though this was not confirmed). We verify that there is no overlap between channels by examining the $+H_2$ transition (positive P-AP), taken from major loop data for the whole series. This is seen in Fig 4.19a. We confirm that there is no overlap between channels using differential data, as shown in Fig 4.19b. The $+H_2$ transition width is evaluated, with an average value of $\overline{W_{0.3-0.7}} = 82 \pm 62\ Oe$. The KRV, defined as the ratio of near-neighbour separation to transition width ($W_{0.3-0.7}$), was found to be $\overline{KRV} = 9.6 \pm 10.7$ on average. This quantitatively shows that the patterning process has impacted the transition width, increasing its average by around 400%.

Fig 4.20a characterises the exponential decay of the coupling (H_J) with respect to t_{Pt} and shows an amplitude at zero of 1.46 T and decay constant of $0.21\ nm$. This is consistent with the continuous films, within one standard deviation of the fit. There is a slight shift in the coupling strength to a lower value at a given Pt spacer thickness. This is expected as the coupling strength is highly dependent on interfacial properties. As ion milling is an energetic process and heat dissipative, the interfaces are probably affected at the edges, and interfacial diffusion at the coupling spacer likely occurs, causing a reduction in coupling strength.
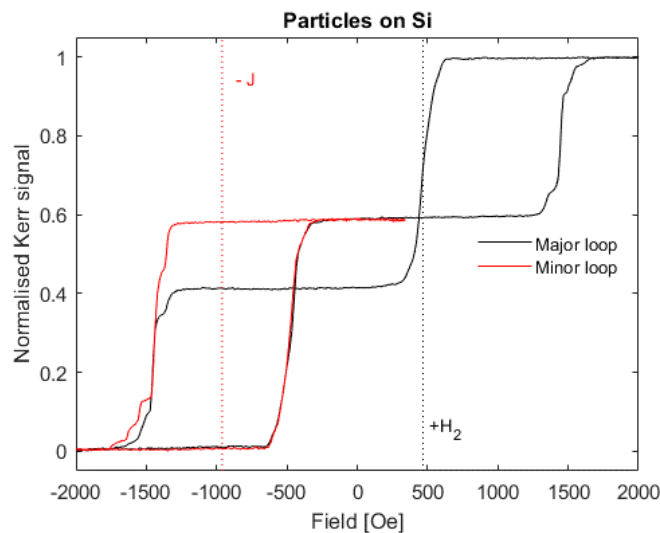
Fig 4.18 Major (black) and minor (red) loop M-H data for oval-shaped particles of 0.58 nm Pt spacer layer thickness, taken using MOKE magnetometry at a constant field sweep rate of 1 kOe/s.

Fig 4.20(b,c) shows the fit parameters (a, c) for $+H_2$ transitions across the series. Here, we observe $\bar{a} = 40\ Oe$ and a standard deviation $\sigma_a = 19\ Oe$. This confirms that the transition has become systematically less sharp by a factor of $\sim$400%, which can be attributed to the patterning process.
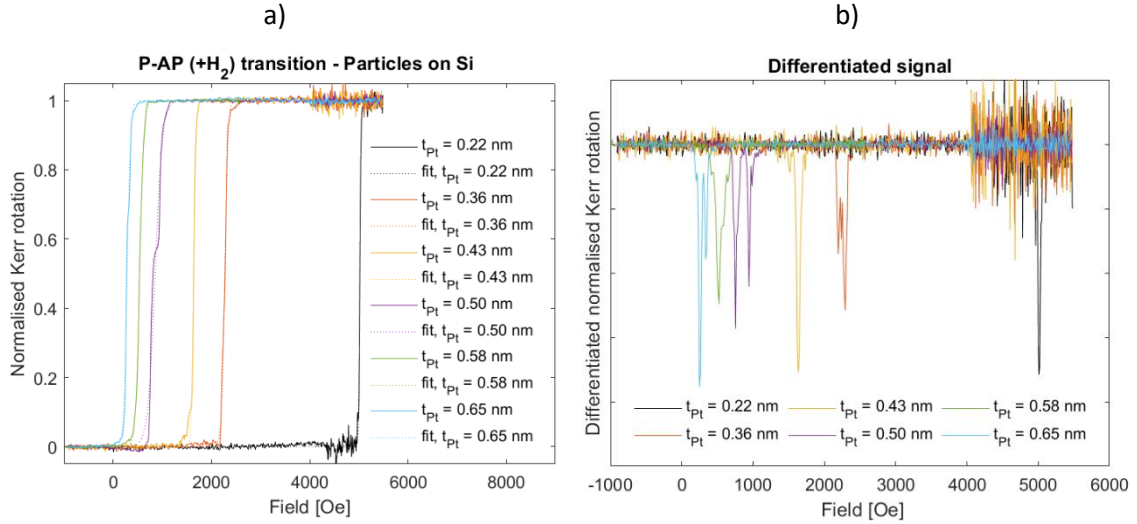
Fig 4.19 a) Experimental measurements of the $+H_2$ transition for patterned particles in a $CoFeB(1)/Pt(t_{Pt})/Ru(0.8)/Pt(t_{Pt})/CoFeB(1)$ series. Only one particle was measured for each Pt thickness. $+H_2$ was taken from major loops obtained using polar MOKE magnetometry. b) Differentiated signal for the H_2 transition.
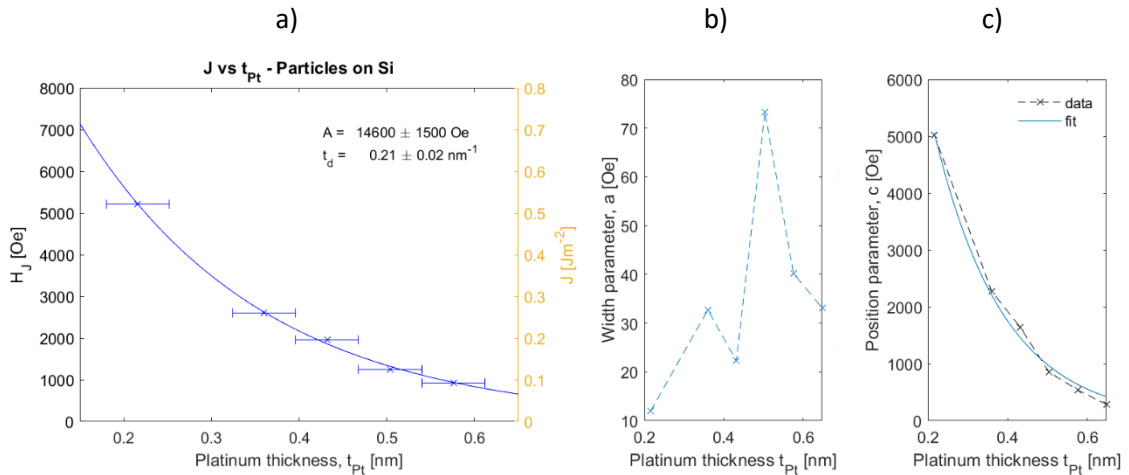
Fig 4.20 a) Experimental data and modelled exponential decay of coupling strength of single particles in a $CoFeB(1)/Pt(t_{Pt})/Ru(0.8)/Pt(t_{Pt})/CoFeB(1)$ series. b,c) A comparison of fit values for $+H_2$ transitions for the Si particle series, taken from major loop MOKE data.

4.3.3. Particles on Ge

As it has been shown that we can obtain patterned, tuneable magnetic particles, we now move to the next step towards lifting them off from the substrate. We perform this by using a release layer between the silicon substrate and the magnetic stack. We use a release layer that dissolves in a solution that does not affect the magnetic properties. After some iterations, germanium was chosen due to its ability to dissolve in hydrogen peroxide and to the way it was shown to retain the magnetic properties of the film [22]. Germanium is evaporated onto a silicon wafer (after a cleaning

cycle), after which the same process as for patterned films can be followed. To ensure that we do not significantly affect the magnetic properties, we again grow our magnetic stack series to compare their magnetic properties with those from the particles studied in the previous section. The data presented from this series were obtained for particles grown in the same sputter run as both the film and patterned particles on Si shown in 4.3.1 and 4.3.2.

A MOKE loop measured on one particle of the same sample (oval-shaped particles of 0.58 nm Pt spacer thickness deposited on Ge), is shown in Fig 4.21, before lifting off. We again see reasonably sharp transitions though there is rounding at both ends of the P-AP transition. The $+H_2$ transition for one particle from each group in this Ge series is shown in Fig 4.22a which again show sharp, well-separated transitions. This is confirmed again in the differential data, shown in Fig 4.22b. The $+H_2$ data yields $\overline{W_{0.3-0.7}} = 29 \pm 20\ Oe$ and $\overline{KRV} = 24 \pm 17$, evidence that the magnetic properties of the particles on Ge are better than those of the particles on Si. These values show a slight reduction in $\overline{KRV}$ and increase in $\overline{W_{0.3-0.7}}$ when compared to films on Si, but this is expected as an effect of the patterning process.

The exponential decay of coupling strength with Pt thickness yields an amplitude at zero Pt thickness of $1.36\ T$ and decay constant of $0.22\ nm$. Fig 4.24b compares the fits for the coupling strength for continuous films on Si, patterned particles on Si and patterned particles on Ge (before particle release). For each thickness of the Pt spacer layer, all three types of samples were grown in the same sputter run. This means that systematic magnetic changes between series are a result of the difference in substrate nature and processing. We note a reduction in coupling strength for both patterned series, which we expect is due to the strong interface dependence of the inter-layer coupling. This manifests as a lower value for coupling at zero Pt thickness, as well as a longer decay length. It should be noted that all three values are consistent with the errors of the fit which is confirmed in Fig 4.24(a,b), showing fit parameters, with errors, for all series.

We observe in Fig 4.24c that the transition width a for all $+H_2$ transitions are again roughly constant in the Ge particle series, with $\bar{a} = 16\ Oe$ and $\sigma_a = 10\ Oe$. This shows an increase in $\bar{a}$ from the films on Si by around 100% but is twice as small as those of particles on Si. The reduction from the film measurements is attributed to the slight loss of interface quality from the patterning process, but it does not significantly affect the potential for measurement as channels are significantly separated. The measurement is compromised if channels bleach into one another. In this series, each channel can be resolved individually. This confirms that we can effectively pattern our samples on top of a release layer without dramatically impacting their magnetic properties.
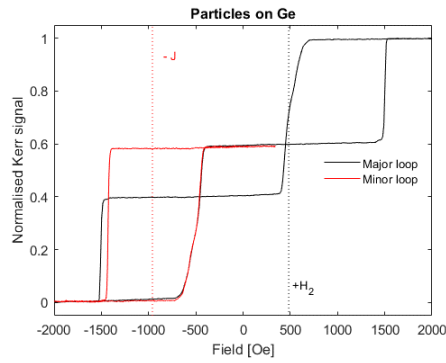
Fig 4.21 Major (black) and minor (red) loop M-H data for patterned oval-shaped particles of 0.58 nm Pt spacer layer thickness on Ge, taken using MOKE magnetometry at a constant field sweep rate of 1 kOe/s.

a)   b)
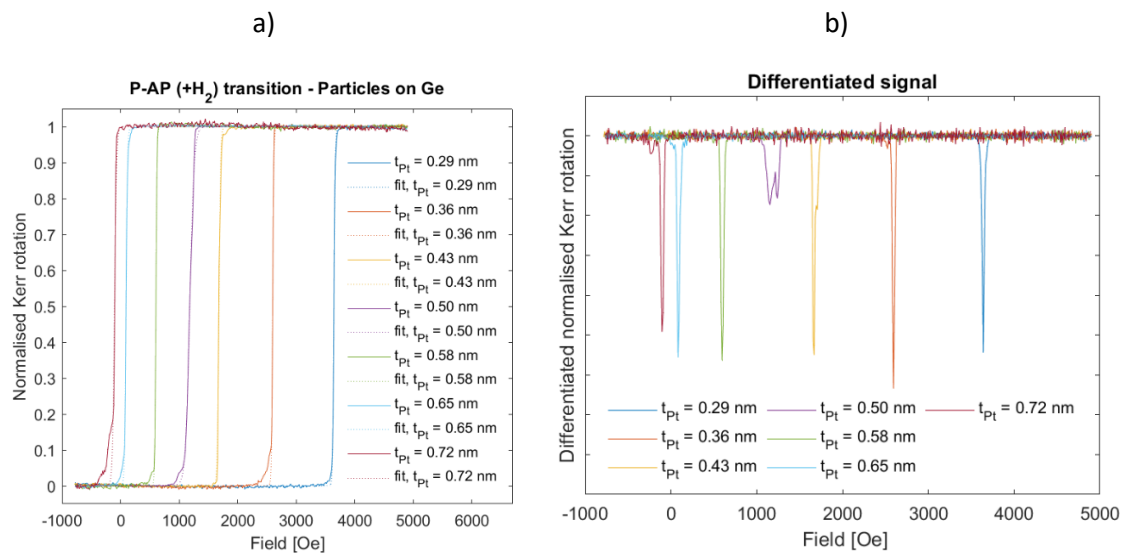
Fig 4.22 a) Experimental measurements of the $+H_2$ transition for patterned particles in a $CoFeB(1)/Pt(t_{Pt})/Ru(0.8)/Pt(t_{Pt})/CoFeB(1)$ series on a Ge release layer. $+H_2$ was taken from major loops on single particles using polar MOKE magnetometry. b) Differentiated signal for the $+H_2$ transition for single particles.
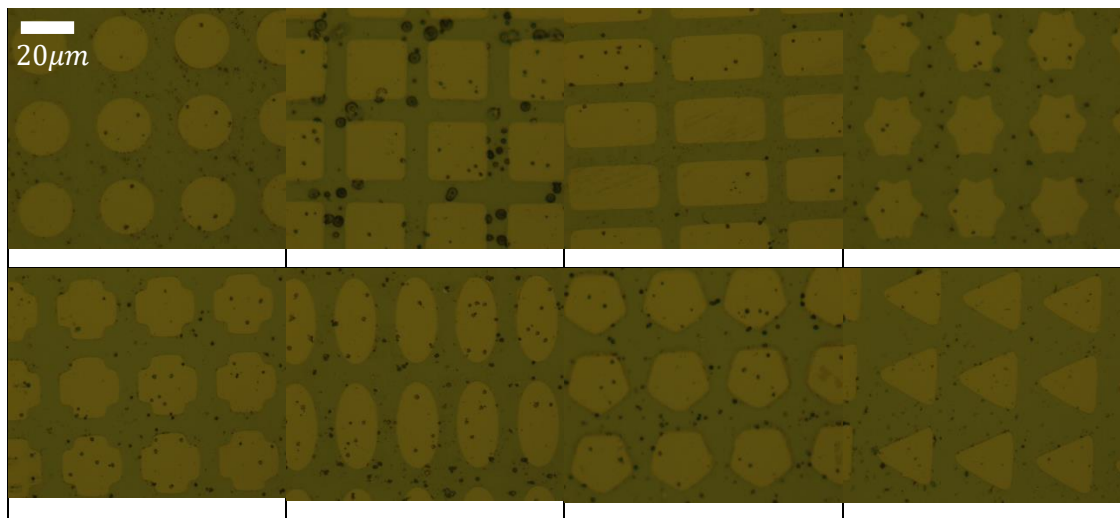
Fig 4.23 Patterned particles on a Ge substrate, before release. Here, remnants of resist can be seen in the form of black particles on top of the patterns.
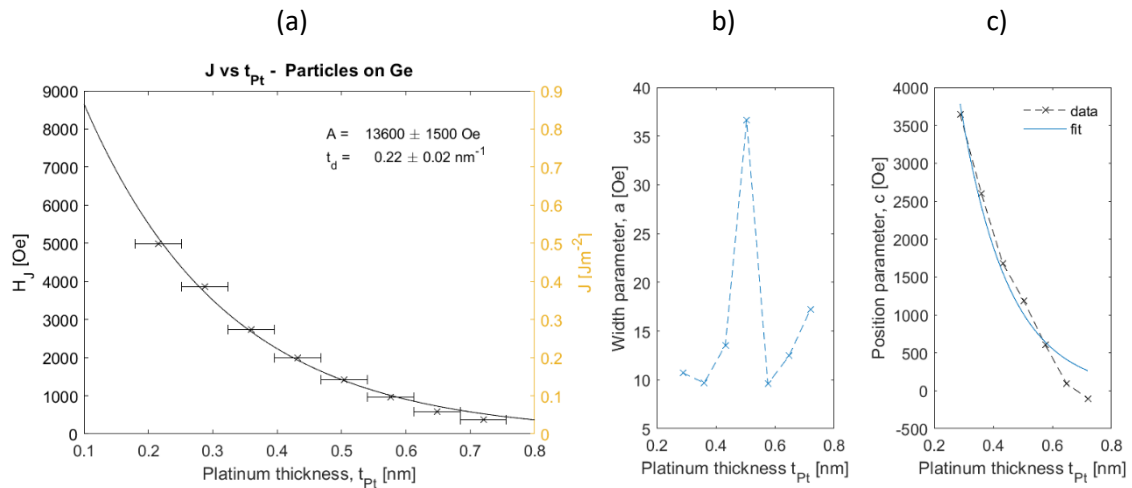
Fig 4.24 a) Experimental data and exponential decay fit of coupling strength of single particles in a $CoFeB(1nm)/Pt(t_{Pt})/Ru(0.8nm)/Pt(t_{Pt})/CoFeB(1nm)$ series on Ge. b,c) A comparison of fit values for $+H_2$ transitions for the Si particle series, taken from major loop MOKE data.
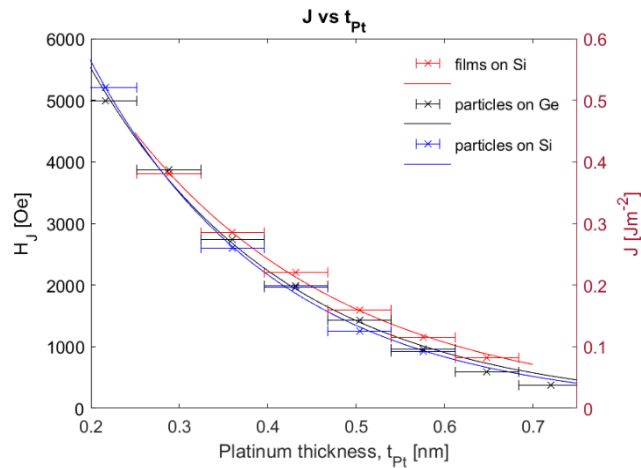
Fig 4.25) Comparison of the decay of coupling field (H_J) with increasing Pt spacer thickness (t_{Pt}) for continuous films on Si (red), patterned films on Si (blue) and patterned films on a Ge release layer (black). All are consistent within error.
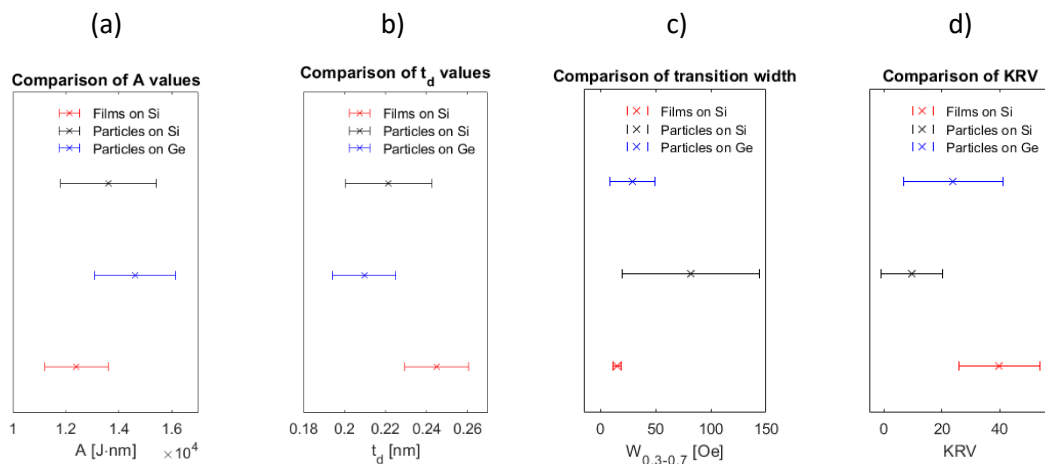
Fig 4.26 A comparison of fit parameters, with errors. a) amplitude at $t_{Pt} = 0$ b) decay constant of the exponential decay of coupling with increasing Pt spacer thickness. c) transition width $W_{0.3-0.7}$, d) KRV. The error bars in a,b) indicate the 95% confidence interval for the fit. Error bars in c,d) indicate the standard deviation within the set.

To show the effects on channel $W_{0.3-0.7}$ and separation more clearly, we plot these parameters for all three series in Fig 4.27. Here, we can see that the Si film series has consistently lowest transition widths ($\overline{W_{0.3-0.7}} = 15.4 \pm 3.7\ Oe$), leading to larger values of KRV ($\overline{KRV} = 40 \pm 14$). The Si particle series has consistently highest transition width and lowest KRV, with $\overline{W_{0.3-0.7}} = 82 \pm 62\ Oe$ and $\overline{KRV} = 9.6 \pm 10.7$. Our patterned particles that can be lifted off of the substrate and into a solution for re-deposition show properties that are much more favourable than those of particles on Si, though have similar transition width on average and slightly lower KRV than that of the films on Si ($\overline{W_{0.3-0.7}} = 29 \pm 20\ Oe$ and $\overline{KRV} = 24 \pm 17$) due to the impact the patterning process has on the interface quality.

For a given KRV requirement, the series can be evaluated to understand whether there is room between the current channels for an additional channel. For example, if the KRV requirement is 10, and two channels in the current series have a KRV > 20, there is the potential for another channel of an equivalent transition width. This is important as we wish to have as many channels as possible, to increase the number of possible identifiers that our encryption scheme can recognise. Note that whether or not the current Pt growth resolution allows an additional channel is not assessed here.
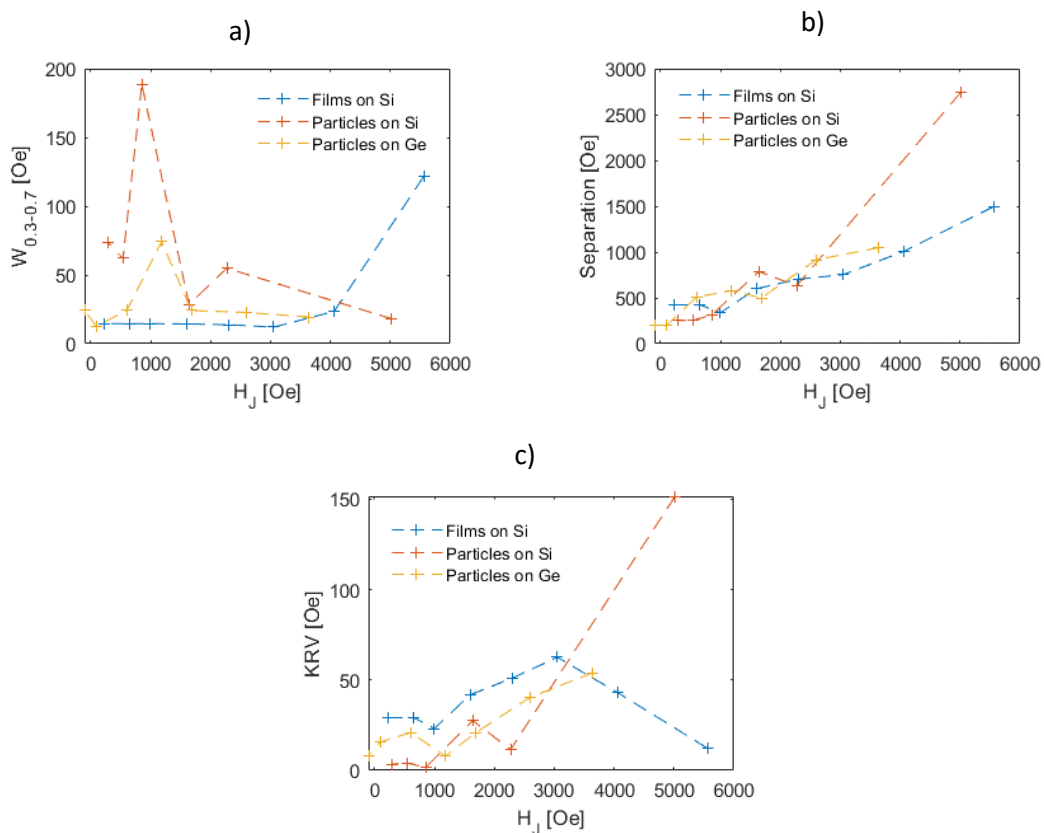
Fig 4.27 a) Transition width values for all channels in all series. b) separation of all channels in all series. c) ratio of separation to transition width, otherwise termed the Key Ratio Value (KRV).

4.3.4. Particle interactions

Due to the SAF nature of the particles, they tend not to agglomerate in solution. We expect that this is due to having coupling fields larger than the stray field from a single particle at a distance of twice the capping layer thickness. To confirm this, field calculations have been completed using Akoun's analytical method for the calculation of field from a parallelepipedal particle. The average field and the maximum field in a square XY plane of $20 \ \mu m$ length from a single square particle of side length $20 \ \mu m$ and thickness $2 \ nm$ are shown in Fig 4.28. This shows a maximum field of $\sim 85 \ Oe$, which is smaller than the activation field of any channel we can currently produce. This means that in principle, any interaction between particles will be overcome by the AF coupling field once the external field is removed.
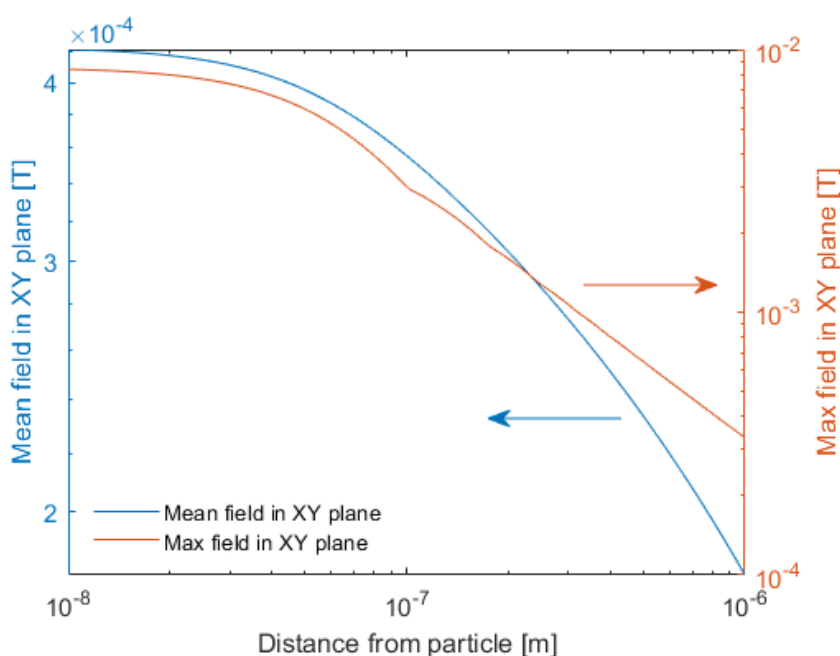
Fig 4.28 The maximum field, and the mean-field from a square particle of $20 \ \mu m$ length and 2 nm thickness in a square XY plane of $20 \ \mu m$ length. These results were produced using Akoun's analytical calculation of field within a parallelepiped.

4.3.5. Summary

It has been shown that we can produce particles with tuneable magnetic properties that can be subsequently lifted off into a solution for a dispersible magnetic tag. The channels are distinguishable, with distances between the start and end of adjacent channels that are far larger than the transition width, shown by the differential and KRV data. This minimises blurring between channels and allows us to still consider a presence/absence detection scheme. The data shown within this section were taken using single-particle MOKE magnetometry at a constant field sweep rate. The benefit of this method is that it is fast, but it is highly localised and therefore does not give any information about the distributions of switching parameters for different nominally identical

particles within the same batch. These measurements were also conducted under linear applied fields. In the next section, we investigate the effects of switching under rotating drive fields.

4.4. A comparison of SAF transitions using linear and rotating drive fields

In section 4.3, we evaluated our functional magnetic layers with respect to a linear field. As we are planning to use a rotating field source to generate our applied field, we need to check whether or not the parameters determined in section 4.3 are consistent with those for rotating fields. If we observe that magnetic transitions occur over a similar range of field values for both rotating and linear drive fields, we can continue with linear measurements knowing that their results will apply to our device. The transition contains all the relevant data, so we measure high-resolution transitions in both linear and rotating fields for comparison.

VSM provides a measurement platform where both linear and rotating fields are possible. This means that the measurement conditions are identical aside from the drive field configuration. It also maintains the same measurement errors such as misalignment of the sample and any calibration error. We begin with SAF films, then evaluate the changes that arise from patterning. In both sections, we use nominally identical SAFs grown in the same sputtering run, with $t_{Pt} = 0.50\ nm$.

4.4.1. SAF films

The transitions for SAF films in both linear and rotating fields can be seen in Fig 4.29 and Fig 4.30, and the parameters describing the transitions are summarised in Table 4.2. In this table, the transition widths are presented by $\pm$ values. As only the transition has been measured, there is a limited amount of data to calculate and subtract the background accurately. For this reason, we choose to define the start and end of the transition at the points where the fit of the straight line before/after the transition intersects a straight line fit of the transition. An example of these fits is shown in black (dots) in Fig 4.29.

The linear and rotating data are converted into equivalent values using

$$B_{eq} = B_{set} \cos(\theta), \tag{4.3}$$

where θ is the field angle, B_{set} is the rotating field amplitude (3 kOe) and B_{eq} is the perpendicular component of the field when the transition occurs. We compare B_{eq} directly with the transition field from linear field measurements. Taking the P-AP transition from rotating fields in Fig 4.30 as an example, $B_{eq} = 3\ kOe \cdot cos(73.2°) = 867\ Oe$. This is very similar to the linear field measurement (957 Oe), which is evidence of the equivalence of transition parameters between linear and rotating

fields. Rotating measurements show larger transition widths by around 50% on average, but again show smaller widths in P-AP as compared to AP-P transitions. These findings give us confidence that the results seen in earlier sections are valid, as linear and rotating fields show similar results.
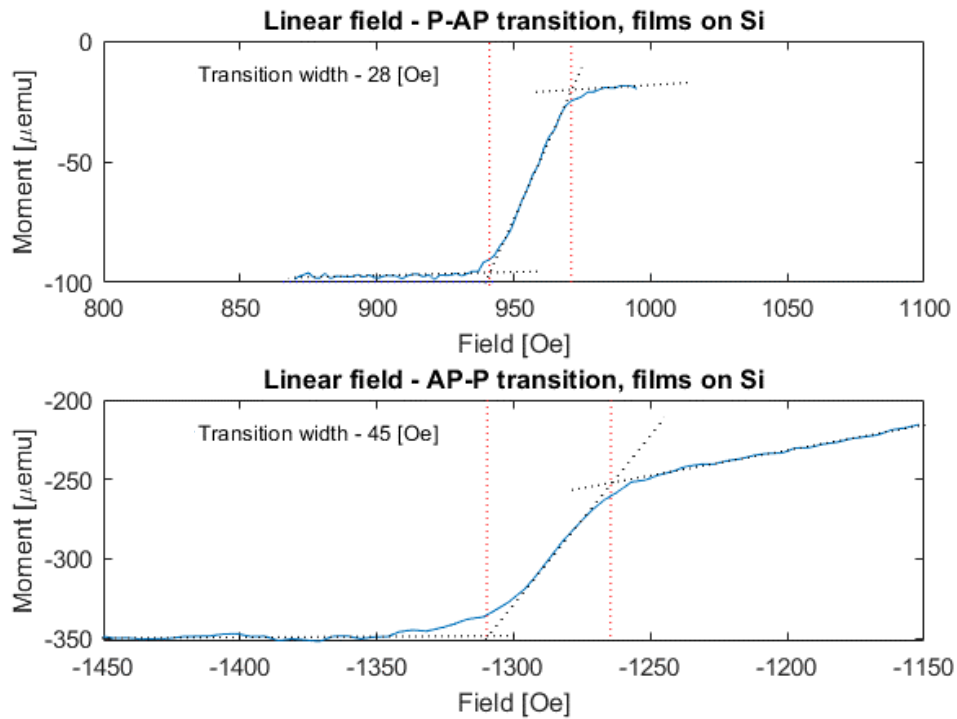
Fig 4.29 High-resolution transitions for films on Si in a linear field. The red dotted lines indicate the start and end of the transition, which we use to define its range.
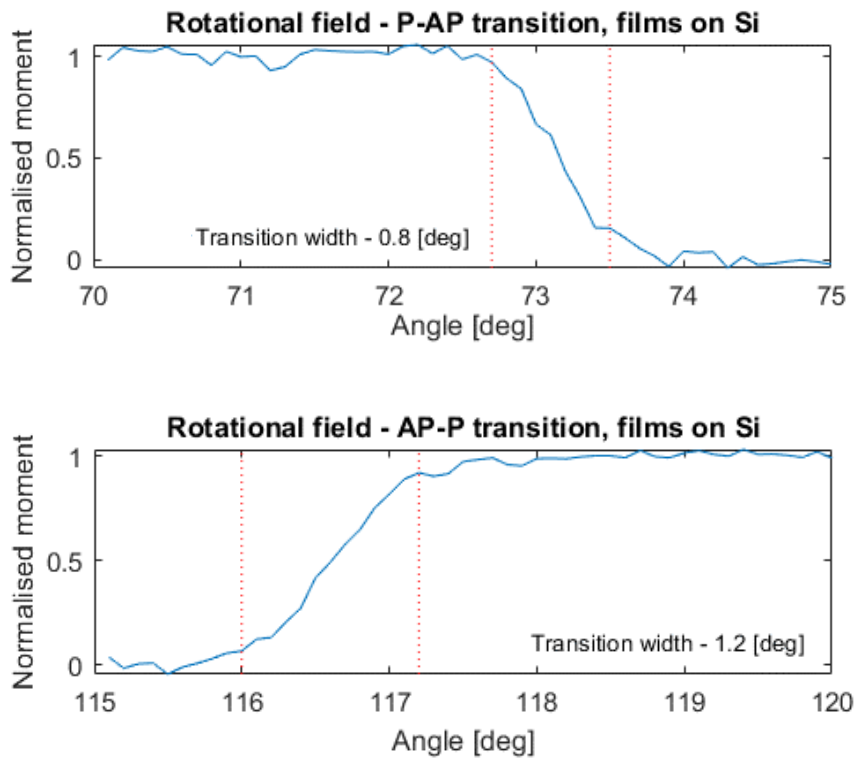
Fig 4.30 High-resolution transitions for films on Si in a rotating field. The red dotted lines indicate the start and end of the transition, which we use to define its range.

We observe that the full transition occurs over 28 Oe and 45 Oe in a linear field for P-AP and AP-P respectively, which is consistent with rotational fields (40 and 56 Oe). This shows a preference for P-AP transitions, though the ratio of transition range (ΔB) to transition location is similar.

	B_{set} [Oe]	θ [°] (measured)	B_{eq} [Oe]	B_{lin} [Oe] (measured)
P-AP	3000	73.2 ± 0.4	867 ± 20	960 ± 14
AP-P	3000	116.5 ± 0.6	-1339 ± 28	-1290 ± 23

Table 4.2 A comparison of transition parameters for linear and rotating fields in a SAF film of $t_{Pt} = 0.50\ nm$

4.4.2. SAF particles

When particles are patterned, each particle will be affected differently. This will lead to a range of changes to transition parameters and a wider transition when measured across all particles. This widening must be considered in our device. In the following, VSM loops are also measured. These include the contribution of many particles (typically >40000 on a 1 cm^2 chip).

The transitions for SAF particles on Si in both linear and rotating fields can be seen in Fig 4.31 and Fig 4.32, and the parameters describing them are summarised in Table 4.3. All transitions widths, which are presented as the $\pm$ values in Table 4.2 and Table 4.3, are increased as expected. In contrast to the SAF film measurements, the AP-P transitions are seen to be sharper than the P-AP. In a linear field, the P-AP transition width is over 4x as wide as the AP-P, with ΔB = 630 and 130 Oe respectively. In a rotating field, the difference is smaller at a ~10% increase but is still significant (2.5 and 2.7° respectively). This suggests that the properties that govern the P-AP transition are affected more severely than those that define the AP-P transition in this sample. This is explored further in Section 4.5.

To ensure that we have correctly subtracted the linear background, we compare the results with a full EA loop, as shown in Fig 4.33a. We can confirm that the AP-P transition is much sharper than the P-AP transition. To confirm that this is not an artefact present in this particular sample only, we confirmed this with another sample of different Pt spacer layer thickness, shown in Fig 4.33b. These transitions have been quantified in Table 4.4.

These findings must be considered for the design of our device. It is clear from VSM measurements that there is a benefit to using the AP-P transition as opposed to the P-AP. VSM provides bulk information, showing the superposition of the signal from all particles on the sample. The broader P-AP transition as measured by VSM could be due to broader individual P-AP transitions, or to sharp P-AP transitions with more variability in their location when many particles are measured at once. This can only be tested by probing the response of individual particles.
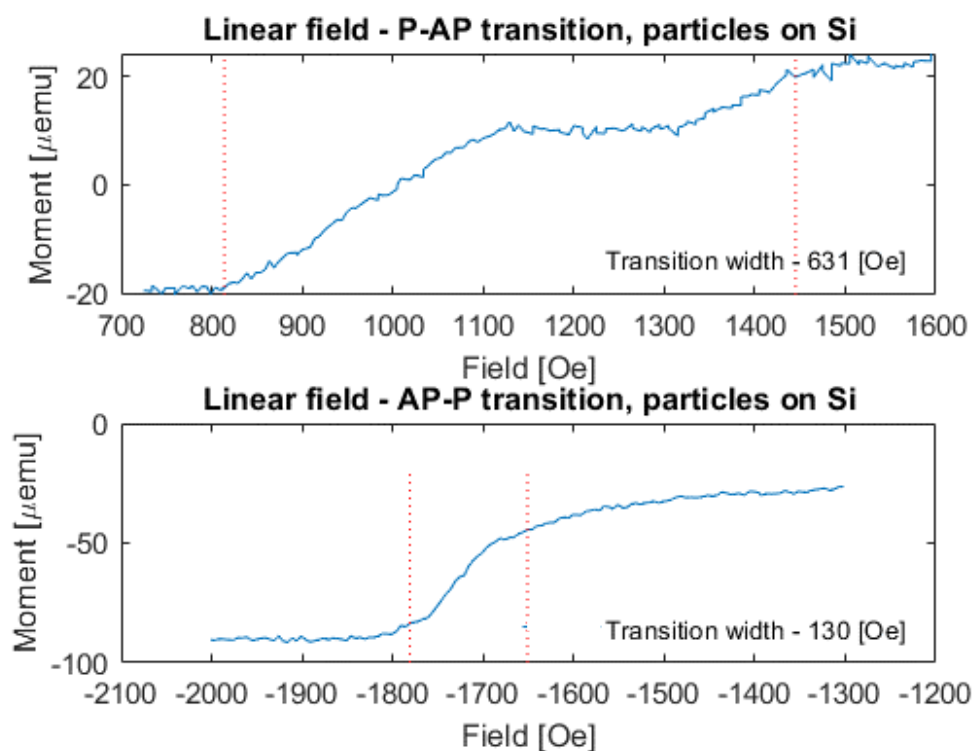
Fig 4.31 High-resolution transitions for particles on Si in a linear field. The red dotted lines indicate the start and end of the transition, which we use to define its range.
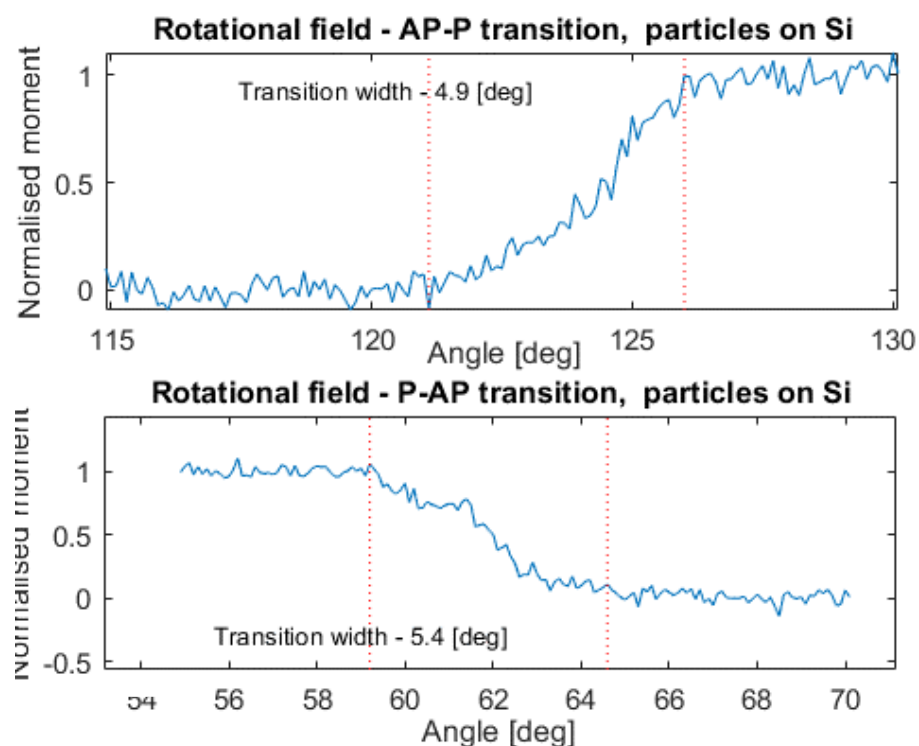
Fig 4.32 High-resolution transitions for particles on Si in a rotating field. The red dotted lines indicate the start and end of the transition, which we use to define its range.

	B_{set} [Oe]	θ [°] (measured)	B_{eq} [Oe]	B_{lin} [Oe] (measured)
P-AP	3000	62 ± 2.7	1408 ± 125	1130 ± 315
AP-P	3000	124 ± 2.5	-1678 ± 108	-1710 ± 65

Table 4.3 A comparison of transition parameters for linear and rotating fields in SAF particles of $t_{Pt} = 0.50\ nm$ on Si.
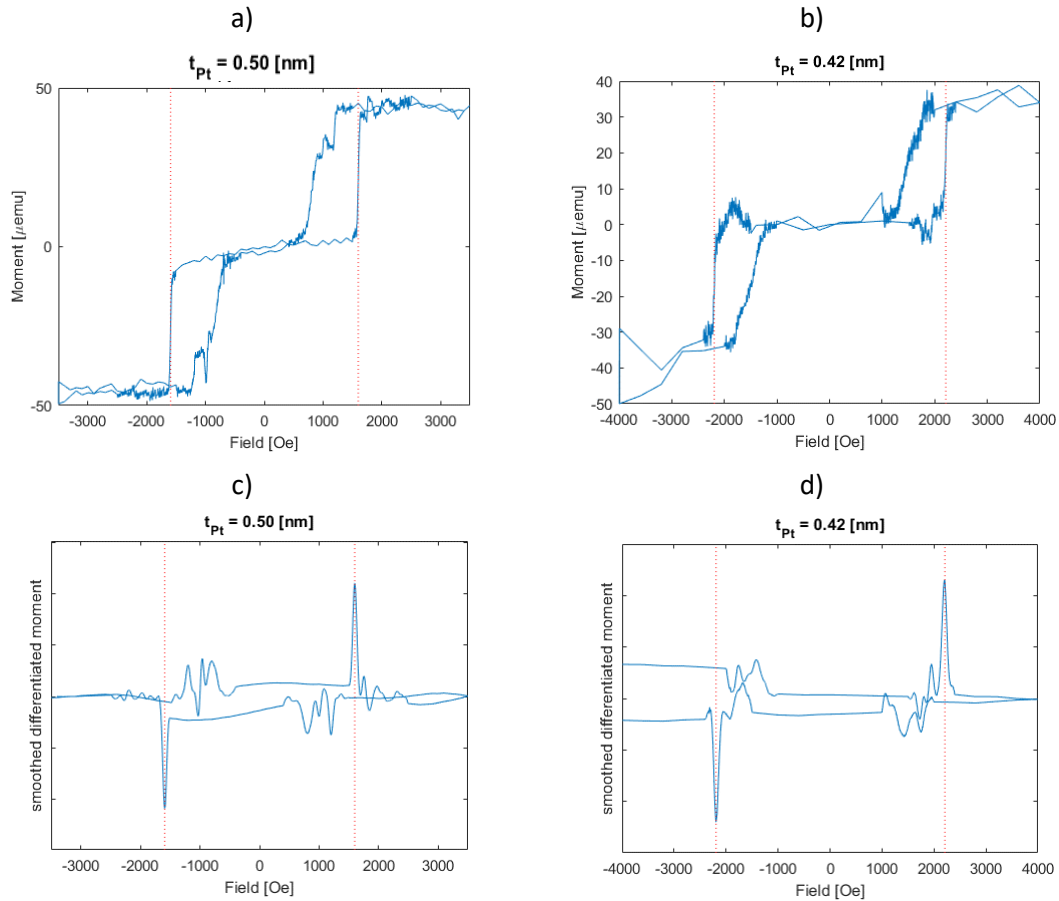
Fig 4.33 VSM loops showing moment vs applied field for a) a $CoFeB(1)/Pt(0.50)/Ru(0.8)/Pt(0.50)/CoFeB(1)$ film patterned as ovals; b) a $CoFeB(1)/Pt(0.42)/Ru(0.8)/Pt(0.42)/CoFeB(1)$ film patterned as rectangles; c,d) Smoothed, differentiated data for the two samples. Here, the difference in the P-AP and the AP-P transition profiles is easy to see.

		$t_{Pt} = 0.42\ nm$		$t_{Pt} = 0.50\ nm$	
Transition		*Transition centre* [Oe]	*Width* [Oe]	*Transition centre* [Oe]	*Width* [Oe]
$-H_2$	P-AP		689		644
H_3	AP-P	2209	284	1599	196
H_2	P-AP		689		635
$-H_3$	AP-P	-2193	255	-1593	201

Table 4.4 A summary of the fit parameters of all transitions in two particles on Si sets with differing Pt spacer layer thickness.

4.4.3. Rotational astroids

Lastly, we assess how the coupling of two layers affects the rotational switching astroid of a bilayer. The SAFs produced in this thesis have the same nominally identical CoFeB thicknesses to the sample used in section 4.2.2 - $t_{CoFeB} = 1\ nm$. For uncoupled CoFeB layers, we observed the transitions to be insensitive to IP drive field components, with switching astroid boundaries that, within the range of field amplitudes studied, are almost parallel to the $B_\parallel$ axis (Fig 4.8).

The coupling of two layers complicates the switching astroid. If we consider a SAF as pictured in Figure 4.11, and assume it is only sensitive to OOP field components, three situations may arise as a field of amplitude B_{set} is rotated by 180° around an axis parallel to the film after saturation in the EA direction:

$$High\ field\ \implies 2\ transitions\ (P - AP, AP - P) \qquad (4.4)$$
$$Intermediate\ field\ \implies 1\ transition\ (P - AP) \qquad (4.5)$$
$$Low\ field\ \implies no\ transition \qquad (4.6)$$

This shows that up to two transitions can occur in one $0 - 180°$ rotation, yielding up to two points on the astroid. In the low field scenario, it should be noted that the P-AP transition does occur, but this is prior to the measurement and as such is not observed – the sample is only measured in the AP state. The transition locations in a rotating field from the previous sections (Table 4.3) have been converted from an angle into field values and are summarised in Table 4.5.

	Films on Si	Particles on Si
P-AP (H_2)	$870 \pm 20\ Oe$	$1406 \pm 139\ Oe$
AP-P (H_3)	$-1339 \pm 29\ Oe$	$-1675 \pm 108\ Oe$

Table 4.5 A summary of the switch locations derived using rotating fields in the previous section.

If the samples are insensitive to IP field components, we should see switching events occurring at values of the perpendicular field equal to the transitions above. These should follow the system outlined in Equation 4.4 - Equation 4.6, i.e. merely the sinusoidal background at low fields, a single discontinuity in the sinusoidal background before 90° in intermediate fields, and two transitions in the sinusoidal background – one between $0 - 90°$ and a one between 90-180 [deg] for high fields. Example data for each of these situations are given for films on Si with $t_{Pt} = 0.50\ nm$ in Fig 4.34.

The resulting switching astroids are seen in Fig 4.35 for films on Si. In all astroids displayed in this section, the error bars define the transition width. In this astroid, the sample is always saturated at 0 [deg] to the sample normal (out of the sample plane). The red and black quadrants are taken using rotation in the positive direction (clockwise on the astroid), with the green and black quadrants

taken using rotation in the negative direction (anti-clockwise on the astroid). We observe the expected switching mechanism, following Equation 4.4 - Equation 4.6, and lines of transitions that lie largely parallel to the $B_\parallel$ axis. Three points are taken with the opposing rotation direction $(-\theta)$ to measure the angular misalignment between the EA of the film and the zero angle of the VSM, which was found to be negligible.
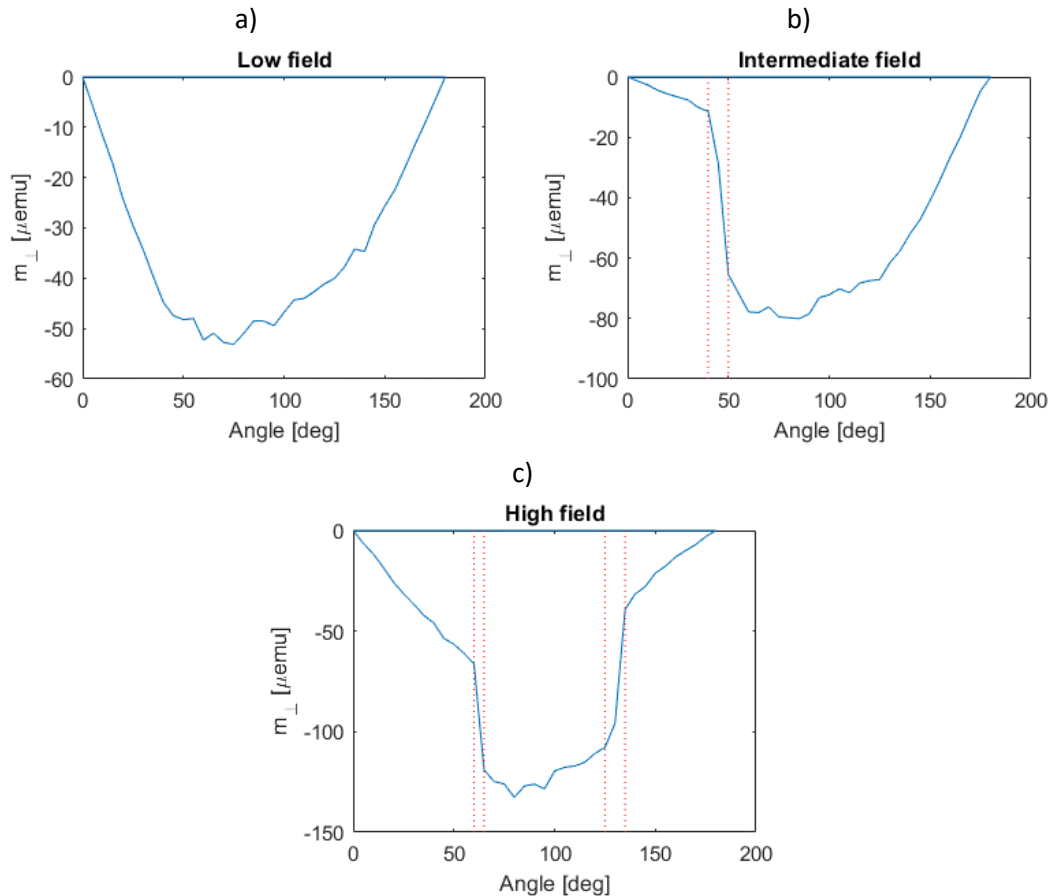
Fig 4.34 Example data for a) low fields (900 Oe), b) intermediate fields (1300 Oe), c) high fields (2000 Oe).

These astroids provide direct insight into the potential feasibility of using rotating fields from permanent magnets for our detector. Our detector looks to differentiate between different channels in a series by measuring the presence or absence of a transition. If the maximum field at a given magnet to sample distance p is higher than a channel field value, we will see the transition during the rotation of the magnet. By measuring and analysing the transition locations of many films in the series, we can directly evaluate the efficacy of our proposed detection method. Fig 4.36 shows the results for films on Si with four different Pt spacer layer thicknesses. To investigate the efficacy of our detector, the astroids should be interpreted as follows:

- Choose a set field B_{set}.This is equivalent to selecting a magnet to sample distance p corresponding to a maximum field B_{set}.
- Find the point $(B_{set}, 0)$ on the polar plot.

- Rotate about the astroid, along the perimeter (B_{set}, θ). θ is the drive magnet angle.
- If an astroid boundary is crossed at any point along this boundary, a transition occurs from that channel.
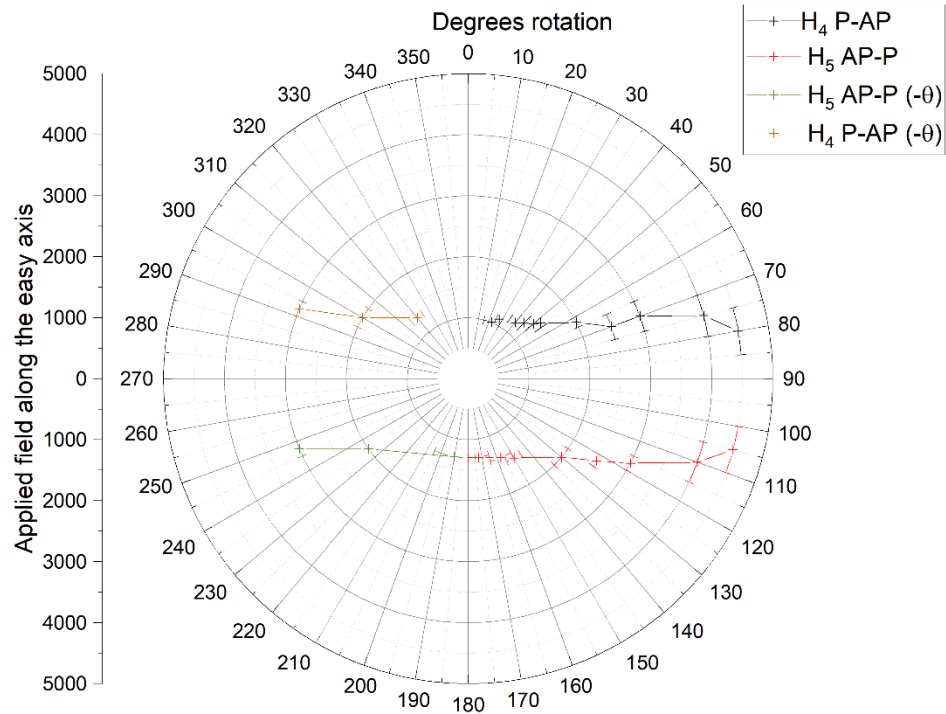
Fig 4.35 Rotational switching astroid for a SAF film of $t_{Pt} = 0.50$ nm grown on Si.
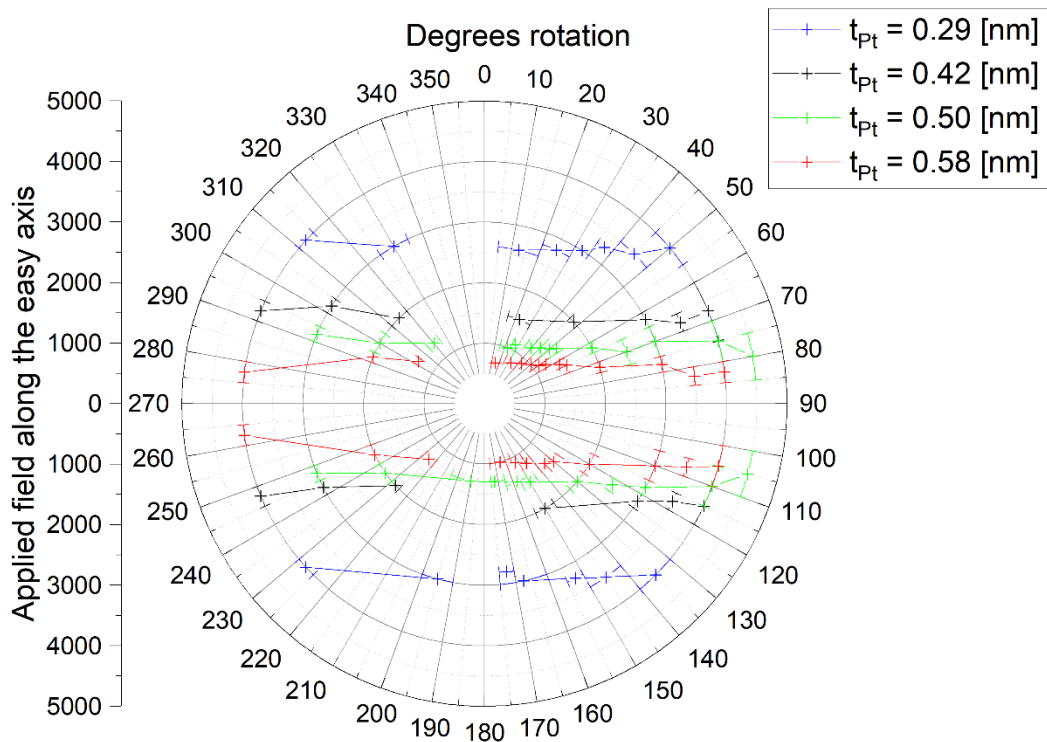
Fig 4.36 Rotational switching astroids for thin-film SAF samples on Si, with varying interlayer Pt thicknesses.

- By continued rotation, we can establish if and where all transitions occur in terms of the magnet angle θ for a given set of channels and start field values. From this, we can determine how well-separated channels are and whether a particular method of detection is better than another – e.g. measuring all channels in one theta rotation, or changing the start field value for each channel.

Fig 4.36 shows the rotational switching astroids for 4 different particles types, with transitions occurring at expected locations, following Equation 4.4-Equation 4.6. These switching astroids have near straight lines that are perpendicular to the HA, evidence that these films can be considered as insensitive to IP field components.

The previous results have been shown for thin film samples on Si. In earlier measurements, we observed changes in transition parameters (centres and widths) as a result of the patterning process. This means that we may expect a change in the astroid location for patterned films, with increased widths shown by the error bars. Note, as these are rotational transitions, the widths for particles should be larger than for films, but sharper than for those measured using linear field, as observed in section 4.4.2. We compare a rotational switching astroid for particles and films of nominally identical composition in Fig 4.37. Here, we again observe transitions following Equation 4.4 - Equation 4.6 and Table 4.5, with transition locations at increased field values. We also note that transitions at the same B_{set} are wider for the particles than for the film, as expected.

Though outside the scope of this thesis, future work in this area should include a rotational switching astroid for many different particle sets as opposed to films (such as in Fig 4.36). Additional data on particles patterned on Ge would provide results that are more representative of our proposed device as we require particles that can be lifted off into solution and transferred to a new surface. In previous results (section 4.3.3), we have seen sharper transitions for the particles on Ge compared to the equivalent particles on Si.

High-resolution transitions (both linear and rotating) indicated that properties defining the P-AP transition are more severely affected than the AP-P by the patterning process, leading to larger transition widths, seen more distinctly in linear applied fields. This widening of the distribution of transition properties was visible in this measurement due to VSM being a bulk measurement – it will measure all of the particles in one event and is unable to distinguish between individual particles. As this method samples many particles at once, we cannot establish whether this is caused by an increase in the average transition width, or a distribution in transition locations, or a combination of both.

We have established that there are differences between AP-P and P-AP transitions that manifest from the patterning process. Additionally, these differences are amplified (as shown in section 4.4.2.) in the case of rotational switching. In the following section, we look to assess the switching properties for many individual particles, to establish why the AP-P transition is sharper when measured as a collective transition of many particles.
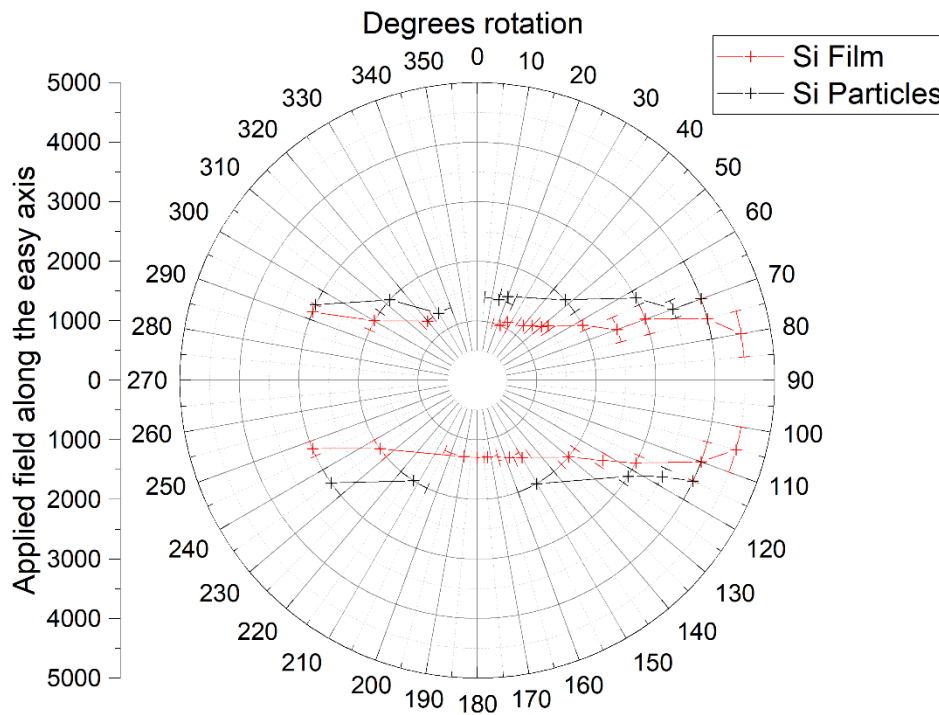
Fig 4.37 Rotational switching astroid for a SAF film ($t_{pt} = 0.50\ nm$) and SAF particles ($t_{pt} = 0.50\ nm$) grown on Si. Here, we can see the effect of patterning on the transition locations.

4.5. Statistical analysis of the switching characteristics of many particles

4.5.1. MOKE particle studies

MOKE magnetometry data in section 4.3 gives us confidence that our scheme is viable, but in section 4.4 we have seen that the width of the transition increases for patterned particles. This is especially significant in the P-AP transition compared to the AP-P. We confirm these findings by assessing the differences in switching characteristics between nominally identical particles. MOKE is a localised method. Given that our particle dimensions and spacing are 20 μm, the signal obtained using focused MOKE (laser width $\sim 3\mu m$) is mainly from a single particle, with a smaller contribution from the surrounding 1-2 rows of particles. By assessing the distribution of the switching characteristics of many individual particles, we can work out whether the wider transition found in an ensemble of particles with VSM measurements is due to sharp transitions for individual particles with a wide

range of individual switching fields, or to individual particles with similar switching fields and larger transition widths, or to wider transitions for individual particles coupled with a wider switching field distribution. A normalised summation of a high enough number of individual MOKE loops should yield the same loop as a normalised VSM loop.

The sample used has functional magnetic layers $(CoFeB(1)/Pt(0.50)/Ru(0.8)/Pt(0.50)/CoFeB(1))$ patterned into 40x20 µm rectangular particles grown on Ge. The particles are still attached to the Ge layer and are in a regular 2D array with 80x40 µm centre to centre distance between particles. 45 particles were probed in different regions of the 1 cm^2 chip, and we measured the major and minor loops. The transitions are modelled using a logistic sigmoid, described using

$$y(x) = \frac{1}{1 + e^{-\left(\frac{x-c}{a}\right)}}$$

(4.7)

as previously, with c defining the centre of the transition and a its width. The results can be seen in Fig 4.38, for all loops plotted at once. This clearly shows that there is a wider distribution of transition locations c within the P-AP transtitions compared to the AP-P. The field offset necessary for the transitions on the negative to positive branch to match the corresponding transitions on the positive to negative branch of each individual loop has been calculated to ensure no artificial widening of the field distribution due to an applied field offset. This offset has been found to be ~ 1.3 $[Oe]$ on average and, as the field resolution has a step size of ~ 12 Oe, is considered negligible, allowing us to merge both sets of data from either side of the major loop.

Each individual transition was then fitted using Equation 4.7 to extract the values of c and a. Our 45 major loops on 45 different particles gave us 90 different values for a and c corresponding to H_2 and 90 different values for a and c corresponding to H_3. 45 minor loops on 45 different particles gave us another 45 values of a and c corresponding to H_2 and 45 values of a and c corresponding to H_1. The amalgamated results from both major and minor loops that are shown in Fig 4.38 are summarised in Table 4.6 and Table 4.7.

We observe in Table 4.6 that, on average, AP-P transitions have an a parameter that is less than half as large as in the P-AP transition. This shows that particles have P-AP transitions with systematically larger widths than those of AP-P transition. The extended transition width of the P-AP transition compared to the AP-P seen in the loops for a whole collection of particles is at least partially due to a decrease in the transition width.

When considering the transition location (c), we find much higher standard deviations for P-AP transitions than for AP-P, with an average ratio of the standard deviation to average transition

location of 1.54% in AP-P, and 12.0% in P-AP – a 7.5x increase. This is evidence that not only is the average transition width (a) larger in P-AP transitions, but also the transition location (c) shows a much larger distribution between particles. Both these factors lead to an increased transition width for the P-AP transition.
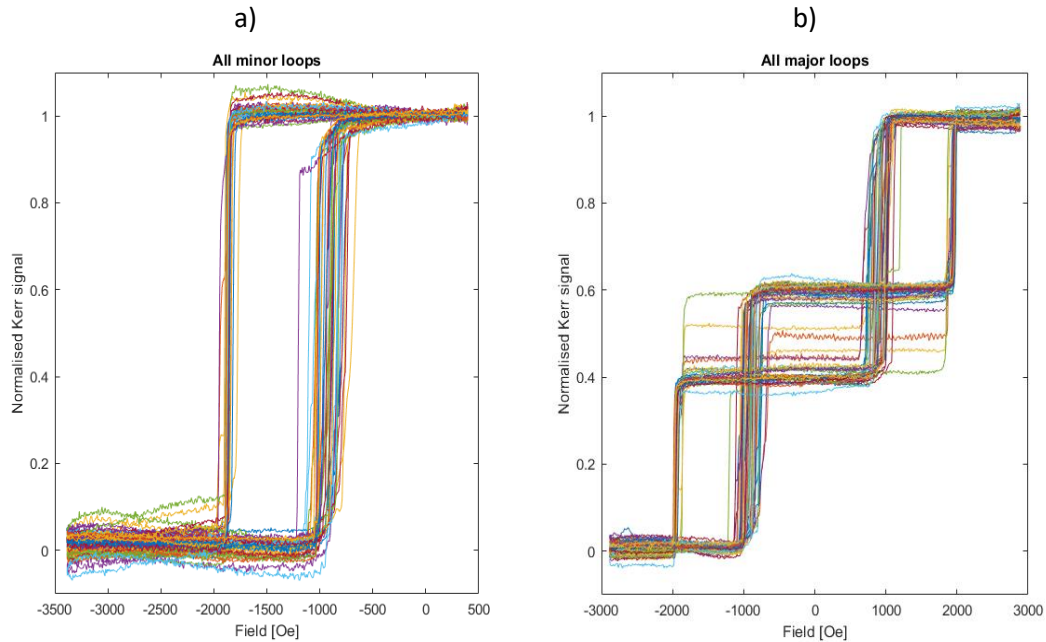
Fig 4.38 MOKE magnetometry loops for individual SAF particles grown on a Ge layer. Here a) shows all minor loops and b) all major loops. This shows the distribution in transition parameters, with an increased distribution in P-AP as opposed to AP-P.

Transition	$\bar{a}\ [Oe]$	$\sigma_a [Oe]$	$\frac{\sigma_a}{\bar{a}}\ [\%]$
H_1 (AP-P)	7	6	86
H_2 (P-AP)	21	11	52
H_3 (AP-P)	9	8	89

Table 4.6 A summary of the width parameter a from the analysis of individual MOKE transitions of many individual SAF particles grown on a Ge layer. Note, a smaller a parameter means a sharper transition.

Transition	$\bar{c}\ [Oe]$	$\sigma_c\ [Oe]$	$\sigma_c/\bar{c}\ [\%]$
H_1 (AP-P)	-1865	27	1.45
H_2 (P-AP)	920	110	12.0
H_3 (AP-P)	1950	30	1.54

Table 4.7 A summary of the field centre parameter c from the analysis of individual MOKE transitions of many individual SAF particles grown on a Ge layer.

The normalised sum of all loops should show the same distribution in switching field values. As such, if we plot a normalised sum of loops for the 45 particles we have measured, we should see an

extended transition width in the P-AP transition as compared to the AP-P. This is seen in Fig 4.39a and b.

The normalised summation of all minor loops indeed shows a much higher degree of sloping in the P-AP (H_2) transition than the AP-P (H_1), with a fitted a parameter that is 3x larger in P-AP transitions compared to AP-P (21 Oe and 7 Oe respectively). This again is confirmed in the major loop data, where the P-AP transitions ($\pm H_2$) have a width that is ~3.5x smaller than those of the AP-P transitions ($\pm H_3$). In these major loops, the AP-P transitions occur in the bottom magnetic layer (closest to the substrate), whereas the P-AP occur in the top magnetic layer. The minor loop only switches the uppermost layer but still has a larger degree of sloping in P-AP transitions as opposed to AP-P, proving that this is not specific to the location of the layer in the stack but rather to the type of transition which occurs (AP-P or P-AP).

We note that the increased transition width for the P-AP transition is mostly due to a larger distribution in the transition centre location (c). There is a decrease in the average transition width (a) by a factor of roughly 2.5 but this is dwarfed by an increase in the percentage variation in transition location. The percentage of the standard deviation to the average value, $[(\sigma/\bar{x}) \times 100]$ is around 1.5% in AP-P transitions, but around 12% in P-AP. Variation in this value is due to differences in defect distributions within particles, which are altered during the patterning process.

Our device requires channels to be distinct from one another. This means that we require a sharp transition for our particles as well as a tight distribution of transition parameters for nominally identical particles. It is clear from our data that we should use the AP-P transitions rather than the P-AP. This would mean performing our detection measurement when the absolute field value increases from remanence after saturation in the opposite direction.
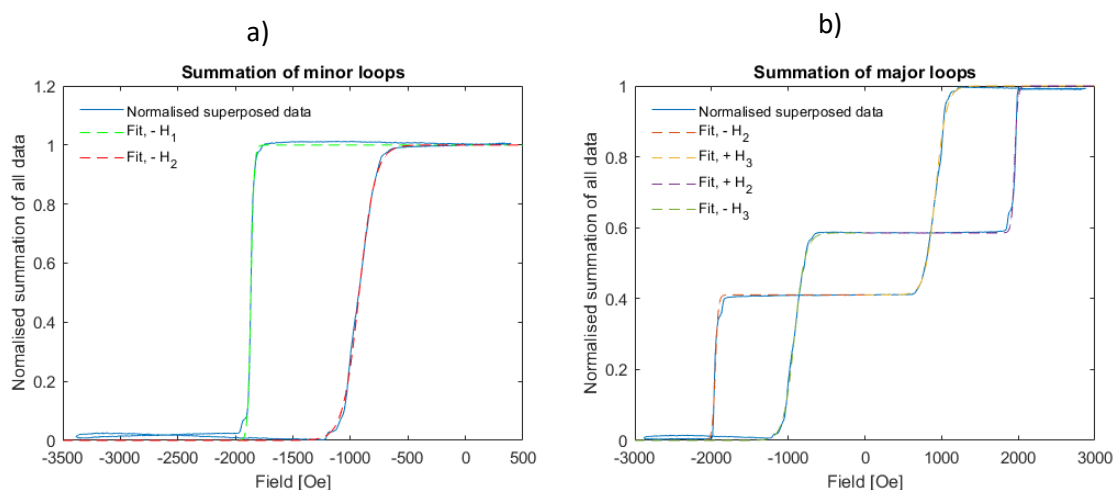
Fig 4.39 Normalised sum of minor loops (a) and major loops (b) of many individual particles with $t_{pt} = 0.50\ nm$, grown on Ge. The AP-P (green) and P-AP (red) transition have been fitted.

4.6. Chapter summary

This work aimed to design a viable magnetic system with suitable properties for a covert, encodable tag. The project requires that these be invisible to the naked eye (to avoid mechanical tampering), be able to be suspended in solution and be distinguishable with modulation of a magnetic property. We investigated the use of PMA based SAF technology due to their stability (energy barrier to change the magnetic state), the possibility to modulate the coupling strength and their ability to be patterned through top-down lithography techniques.

We first confirmed the presence of PMA within our CoFeB/Pt layers and demonstrated their insensitivity to in-plane field components through the measurement of rotational switching astroids. This demonstrates not only the high energy barrier required to switch the magnetic layers, which is proportional to the anisotropy field H_K, but also the viability of using drive fields with non-zero in-plane components. We intend to produce a drive field using a rotating permanent magnet, which we confirmed to be possible.

We then analysed the ability to control coupling strength through modulation of the Pt spacer layer thickness in a $\mathrm{CoFeB}(1)/\mathrm{Pt}(\mathbf{t_{Pt}})/\mathrm{Ru}(0.8)/\mathrm{Pt}(\mathbf{t_{Pt}})/\mathrm{CoFeB}(1)$ magnetic stack with a Ta seed layer and Ta/Pt capping layers for structural rigidity. We observed sharp switching, at clearly defined field values dependent on the spacer layer thickness, with decreasing coupling for increasing t_{Pt}. The films showed zero susceptibility at fields below the coupling field, allowing for an 'off' or 0 state below this and an 'on' or 1 state above this, with a sharp transition between both states. These films were patterned into micron-size particles using top-down lithography techniques. A small systematic reduction was seen in interlayer coupling energy density J and transition sharpness $(1/a)$, though differential information clearly shows no bleaching of channels at the current channel density. This patterning allows the information to be invisible to the naked eye, increasing the difficulty of physical tampering. Due to the balanced nature of the SAF, the particles have zero-moment at remanence and we calculated that they will not interact with near neighbours once the applied field is removed. This ensures non-agglomeration in solution which is key to re-deposition of our information carriers. The particles can be lifted off the substrate using a Ge layer deposited on the substrate which can be dissolved in hydrogen peroxide to release the particle from the substrate into solution. We confirmed that the patterning process, when performed on a Ge release layer, again does not compromise the detection scheme, with better transition sharpness than when the particles are patterned directly on Si and comparable to non-patterned SAF films. The magnetic state of the particles is non-volatile and cannot be corrupted through magnetic fields or electrical tampering, offering a robust, covert information system.

We next confirmed that the properties seen for linear fields are comparable to those seen in rotating drive fields by comparing high-resolution transitions using VSM. In these measurements, we observed that the effects of patterning disproportionately affect properties that influence P-AP transitions, as opposed to AP-P. This was evident in the transition widths, which show an increase in P-AP compared to AP-P transitions. This effect was amplified in linear fields, showing a difference in P-AP transition width compared to AP-P of over 300% ($\sim 20\%$ in rotating fields). This shows that, though there is a difference between linear and rotating fields, the amplification of the difference between AP-P and P-AP transitions may aid the characterisation of the underlying causes. This was confirmed using VSM measurements to obtain a collective measurement of all particles, which showed transition widths that are 3x larger for P-AP as compared to AP-P. We, therefore, concluded that there is a clear benefit to the detection of the AP-P transition rather than the P-AP, which must be considered in our design.

Rotational switching astroids were measured for SAF films and particles. These followed the expected order of transitions, evidence that our SAF films and particles are also insensitive to IP field components and compatible with rotating field sources. From these, we can confirm that rotating fields provide a viable method to distinguish different channels, with transitions being separated by more than their transition widths for many films in a series with differing Pt thicknesses.

Lastly, to try to understand why the P-AP transition is disproportionately affected by patterning, we obtained information about the inter-particle variation through analysis of distributions of many individual MOKE measurements. This difference was found to be less affected by variation in transition width for single particles (a) but by the location of the transition (c), which had a much larger variance in the P-AP transition than in the AP to P. The variation was stark and showed a minimum of 250% increase in variation between the AP-P and P-AP average transition widths.

It should be noted that though we have obtained 8 functional channels here, this is by no means the physical limit. This could be improved with a finer Pt growth resolution, so long as the interfacial properties are maintained. With knowledge of the transition width for a collective distribution, we can model the theoretical maximum channel number for our growth system, which we will evaluate in the following chapters. Before this, we must set up the idealised problem computationally, which we do in chapter 5.

[1]   B. Mora, A. Perez-Valle, C. Redondo, M. D. Boyano, and R. Morales, "Cost-Effective Design of High-Magnetic Moment Nanostructures for Biotechnological Applications," *ACS Appl. Mater. Interfaces*, vol. 10, no. 9, pp. 8165–8172, Mar. 2018, doi: 10.1021/acsami.7b16779.

[2]   L. Peixoto *et al.*, "Magnetic nanostructures for emerging biomedical applications," *Applied Physics Reviews*, vol. 7, no. 1. American Institute of Physics Inc., p. 11310, Mar. 01, 2020, doi: 10.1063/1.5121702.

[3]   T. Vemulkar, R. Mansell, D. C. M. C. Petit, R. P. Cowburn, and M. S. Lesniak, "Highly tunable perpendicularly magnetized synthetic antiferromagnets for biotechnology applications," *Appl. Phys. Lett.*, vol. 107, no. 1, p. 012403, Jul. 2015, doi: 10.1063/1.4926336.

[4]   S. Leulmi *et al.*, "Comparison of dispersion and actuation properties of vortex and synthetic antiferromagnetic particles for biotechnological applications," *Appl. Phys. Lett.*, vol. 103, no. 13, p. 132412, Sep. 2013, doi: 10.1063/1.4821854.

[5]   S. Leulmi Pichot, S. Bentouati, S. S. Ahmad, M. Sotiropoulos, R. Jena, and R. Cowburn, "Versatile magnetic microdiscs for the radio enhancement and mechanical disruption of glioblastoma cancer cells," *RSC Adv.*, vol. 10, no. 14, pp. 8161–8171, Feb. 2020, doi: 10.1039/d0ra00164c.

[6]   M. Goiriena-Goikoetxea *et al.*, "Disk-shaped magnetic particles for cancer therapy," *Applied Physics Reviews*, vol. 7, no. 1. American Institute of Physics Inc., p. 011306, Mar. 01, 2020, doi: 10.1063/1.5123716.

[7]   R. Mansell *et al.*, "Magnetic particles with perpendicular anisotropy for mechanical cancer cell destruction," *Sci. Rep.*, vol. 7, no. 1, p. 4257, 2017, doi: 10.1038/s41598-017-04154-1.

[8]   R. Van Roosbroeck *et al.*, "Synthetic antiferromagnetic nanoparticles as potential contrast agents in MRI," *ACS Nano*, vol. 8, no. 3, pp. 2269–2278, Mar. 2014, doi: 10.1021/nn406158h.

[9]   W. Hu, R. J. Wilson, C. M. Earhart, A. L. Koh, R. Sinclair, and S. X. Wang, "Synthetic antiferromagnetic nanoparticles with tunable susceptibilities," *J. Appl. Phys.*, vol. 105, no. 7, p. 07B508, Apr. 2009, doi: 10.1063/1.3072028.

[10]   C. W. Chen, "Fabrication and characterization of thin films with perpendicular magnetic anisotropy for high-density magnetic recording - Part II a review," *Journal of Materials Science*, vol. 26, no. 12. Kluwer Academic Publishers, pp. 3125–3153, Jun. 28, 1991, doi: 10.1007/BF01124655.

[11]   S. Bhatti, R. Sbiaa, A. Hirohata, H. Ohno, S. Fukami, and S. N. Piramanayagam, "Spintronics

based random access memory: a review," *Materials Today*, vol. 20, no. 9. Elsevier B.V., pp. 530–548, Nov. 01, 2017, doi: 10.1016/j.mattod.2017.07.007.

[12]   R. A. Duine, K.-J. Lee, S. S. P. Parkin, and M. D. Stiles, "Synthetic antiferromagnetic spintronics," *Nat. Phys.*, vol. 14, no. 3, pp. 217–219, 2018, doi: 10.1038/s41567-018-0050-y.

[13]   S. Ikegawa, F. B. Mancoff, J. Janesky, and S. Aggarwal, "Magnetoresistive Random Access Memory: Present and Future," *IEEE Trans. Electron Devices*, vol. 67, no. 4, pp. 1407–1419, Apr. 2020, doi: 10.1109/TED.2020.2965403.

[14]   L. B. Chandrasekar, K. Gnanasekar, and M. Karunakaran, "Spintronics – A mini review," *Superlattices and Microstructures*, vol. 136. Academic Press, p. 106322, Dec. 01, 2019, doi: 10.1016/j.spmi.2019.106322.

[15]   E. Chen *et al.*, "Advances and future prospects of spin-transfer torque random access memory," in *IEEE Transactions on Magnetics*, Jun. 2010, vol. 46, no. 6, pp. 1873–1878, doi: 10.1109/TMAG.2010.2042041.

[16]   W. Kim *et al.*, "Extended scalability of perpendicular STT-MRAM towards sub-20nm MTJ node," 2011, doi: 10.1109/IEDM.2011.6131602.

[17]   A. Hirohata *et al.*, "Review on spintronics: Principles and device applications," *Journal of Magnetism and Magnetic Materials*, vol. 509. Elsevier B.V., p. 166711, Sep. 01, 2020, doi: 10.1016/j.jmmm.2020.166711.

[18]   F. Walz, "The Verwey transition - a topical review," *J. Phys. Condens. Matter*, vol. 14, no. 12, pp. R285–R340, Apr. 2002, doi: 10.1088/0953-8984/14/12/203.

[19]   B. Tudu and A. Tiwari, "Recent Developments in Perpendicular Magnetic Anisotropy Thin Films for Data Storage Applications," *Vacuum*, vol. 146, pp. 329–341, Dec. 2017, doi: 10.1016/j.vacuum.2017.01.031.

[20]   R. Lavrijsen, A. Feránndez-Pacheco, D. Petit, R. Mansell, J. H. Lee, and R. P. Cowburn, "Tuning the interlayer exchange coupling between single perpendicularly magnetized CoFeB layers," *Appl. Phys. Lett.*, vol. 100, no. 5, p. 052411, Jan. 2012, doi: 10.1063/1.3682103.

[21]   L. K. Cunningham, "Multi-channel tag based on fluid-suspended magnetic microparticles," PhD thesis, University of Cambridge, 2019.

[22]   E. N. Welbourne, "Antiferromagnetic nanodiscs with perpendicular magnetic anisotropy for biological applications," PhD thesis, University of Cambridge,December, 2020.

[23] T. Vemulkar, R. Mansell, D. C. M. C. Petit, R. P. Cowburn, and M. S. Lesniak, "The effect of underlayers on the reversal of perpendicularly magnetized multilayer thin films for magnetic micro-and nanoparticles," *J. Appl. Phys*, vol. 121, p. 43908, 2017, doi: 10.1063/1.4974300.

[24] K. Wang, Y. Huang, R. Chen, and Z. Xu, "Investigation of magnetic properties in thick CoFeB alloy films for controllable anisotropy," *Appl. Phys. A Mater. Sci. Process.*, vol. 122, no. 2, pp. 1–5, Feb. 2016, doi: 10.1007/s00339-016-9633-6.

[25] J. H. Lee, D. Petit, R. Lavrijsen, A. Fernández-Pacheco, R. Mansell, and R. P. Cowburn, "Soliton propagation in micron-sized magnetic ratchet elements," *Appl. Phys. Lett.*, vol. 104, no. 23, p. 232404, Jun. 2014, doi: 10.1063/1.4882640.

[26] R. Lavrijsen, A. Feránndez-Pacheco, D. Petit, R. Mansell, J. H. Lee, and R. P. Cowburn, "Tuning the interlayer exchange coupling between single perpendicularly magnetized CoFeB layers," *Appl. Phys. Lett.*, vol. 100, no. 5, p. 052411, Jan. 2012, doi: 10.1063/1.3682103.

[27] J. Moritz, F. Garcia, J. C. Toussaint, B. Dieny, and J. P. Nozières, "Orange peel coupling in multilayers with perpendicular magnetic anisotropy: Application to (Co/Pt)-based exchange-biased spin-valves," *Europhys. Lett.*, vol. 65, no. 1, pp. 123–129, Jan. 2004, doi: 10.1209/epl/i2003-10063-9.

[28] A. Fernández-Pacheco *et al.*, "Dynamic selective switching in antiferromagnetically-coupled bilayers close to the spin reorientation transition," *Appl. Phys. Lett.*, vol. 105, no. 9, p. 092408, Sep. 2014, doi: 10.1063/1.4895032.

[29] S. Karayev, P. D. Murray, D. Khadka, T. R. Thapaliya, K. Liu, and S. X. Huang, "Interlayer exchange coupling in Pt/Co/Ru and Pt/Co/Ir superlattices," 2019, doi: 10.1103/PhysRevMaterials.3.041401.

[30] M. Belmeguenai *et al.*, "Interface Dzyaloshinskii-Moriya interaction in the interlayer antiferromagnetic-exchange coupled Pt/CoFeB/Ru/CoFeB systems," *Phys. Rev. B*, vol. 96, p. 144402, 2017, doi: 10.1103/PhysRevB.96.144402.

Chapter 5.

An idealised model of a detector

In this chapter, we use the particles described in the previous chapter and investigate the efficacy of an inductive detector with properties outlined in chapter 2. This will be tested using computational methods, modelling the switching of an assembly of nominally identical particles under a rotating field. The results from this section will be used in the following chapter to obtain a figure for the induced EMF in a pick-up coil.

We first model the 'ideal' detector and sample system. This corresponds to particles with infinitely sharp switching and perfect coil and sample positions. We evaluate the time-varying magnetic field from a rotating permanent magnet, its effect on the magnetic state of the particles and the speed at which transitions occur as a result.

The use of computational modelling is becoming more common, as it benefits from low financial and time costs and high iteration speed. Computational simulation allows us to optimise multiple parameter spaces and to understand the physical restraints of our system. We can define figures of merit – how effective the device is – and explore how this is affected by changes to inputs, ultimately understanding the device more fully.

5.1. Chapter introduction

5.1.1. A reminder of pre-requisites

Before describing the outline of the simulations, it is useful to review the particle's characteristics and detector requirements described previously. Our particles consist of synthetic antiferromagnetic (SAF) microparticles with perpendicular magnetic anisotropy (PMA). These have zero net moment at zero field, transitioning to saturation magnetisation at a characteristic switching field. Ideally, these transitions are infinitely sharp, and this will be our hypothesis for the initial calculations presented in this chapter.

The particles are highly anisotropic, with an easy axis perpendicular to the film plane. In section 4.4.3, the switching of our particles was found to be largely insensitive to the in-plane components of the applied field, allowing us to use a rotating permanent magnet to produce a sinusoidal drive field perpendicular to the sample plane with little concern about the additional transverse field components this method produces. A diametrically magnetised cylindrical permanent magnet is used, with equidistant pick-up coils to nullify the effects of the drive field. The sample is dispensed onto a substrate from a solution and placed in direct contact with one set of coils – minimising the distance to the sample to increase the induced voltage due to its switching. A simplified schematic of this geometry can be seen in Fig 5.1.
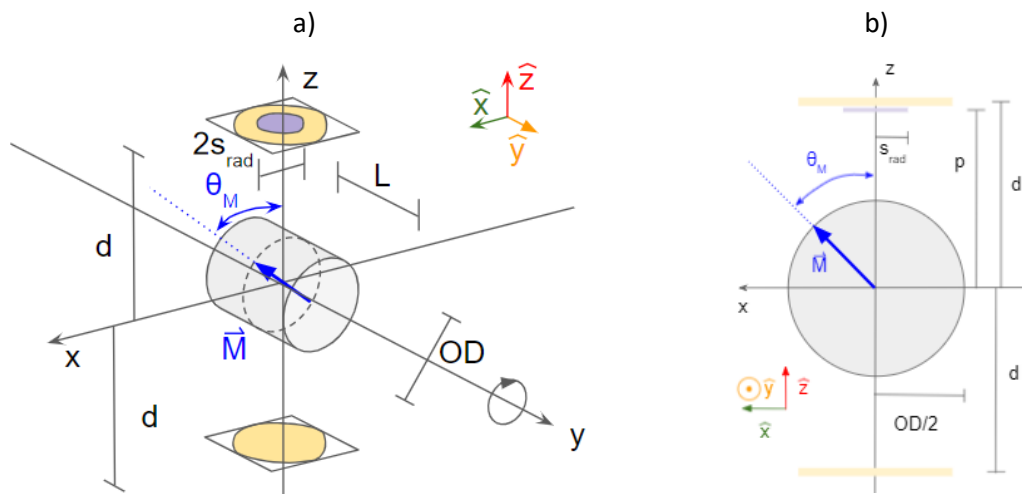
Fig 5.1 A simplified schematic of our setup. The yellow areas define the detection coils, with the sample dispersed within the purple area. The drive field is produced by the cylindrical permanent magnet (grey) with transverse magnetisation, shown in blue. The magnet rotates about the y axis, producing a sinusoidal B_z field at the sample position. b) cross sectional view.

The device will be used to detect the presence or absence of a transition at a particular field strength, so it must be able to accurately distinguish between two neighbouring channels with no bleaching, which we define as the overlap between adjacent transitions. To detect the switching of an assembly of particles with different switching fields, we are considering two potential methods of measurement:

- Method 1. A field higher than the highest switching field is applied by bringing the magnet with its magnetisation pointing up towards +z ($\theta_M = 0$) as close to the sample as necessary in order to saturate all the SAF particles. All channels are then measured during the same rotation of the magnet as the z-component of the field decreases (within one 90-degree rotation). A particular channel at a switching field B_n is then associated with the angle θ_n for which half of the particles within the sample area for a single channel has gone below B_n. The particles are assumed to be uniformly distributed, so θ_n occurs when half of the sample area $<B_n$.

- Method 2. The maximum starting field at $\theta_M = 0$ is varied, with new channels turning off (corresponding particles going from P to AP) by rotating the magnet at different magnet to sample distances. A particular channel is then related to both a magnet-sample distance and an angle.

More details on both methods will be given in section 5.4. We test the efficacy of both methods in 5.4 by assessing the maximum number of potential channels achieved using each method.

5.1.2. How we study the device

In this section, we identify the key characteristics of the device and explain the methods used to model them. Additionally, we define the metrics employed to evaluate the efficacy of the system as we optimise its design. Finally, as a large amount of data is produced, we look at the areas where we can introduce computational improvements.

5.1.2.1 Methods

Here we outline the structure of the simulations:

- For a given magnet geometry, defined by its diameter OD and length L, and for $\theta_M = 0$, the Z-component of the magnetic field $B_z(p)$ along the Z-axis is calculated as a function of the distance (p) from the magnet surface.

- The distance p_0 for which this $B_z(p_0)$ field is 5% above the switching field of the highest channel, B_0, is determined.

- The vector field is calculated into a disk of diameter $2s_{rad}$, hereafter called the probe area. The probe area is centred at $(0,0,p_0)$, with (dx, dy) the mesh resolution. The field is calculated for two magnetisations of length $|M|$, where $\vec{M}$ is the magnetisation of the magnet, that lie along $\hat{x}$ and along $\hat{z}$. The field components for any arbitrary magnetisation angle θ_M can be calculated using linear combinations of the fields created by both unit magnetisations.

- Whether each $ds = dx \cdot dy$ area of the probe area is above or below the first channel switching field, B_0, is determined. This allows an estimation of the total

area above the switching field, which is normalised to the full sample area ($\pi \cdot s_{rad}^2$) giving the Normalised Switched Area, or NSA. The dx and dy resolution in this work samples a minimum of 500 cells within the probe area, but usually ~2000. For a typical probe width $dx = dy = 40 \ \mu m$, a cell is still larger than a particle (typically 20 μm in diameter), although of the same order. We assume a uniform distribution of magnetic particles across the sample area.

- The NSA versus θ_M curve is obtained by varying θ_M and evaluating the field profile inside the probe area at each iteration. The field at the detection coil from the sample is proportional to the number of particles in the on or P state. This is shown by the NSA, which is a measure of the fraction of particles in the parallel state.

The magnetisation $\vec{M}$ from the cylindrical magnet at an angle θ_M from the Z-axis and in the XZ plane can be written as

$$\vec{M} = \begin{vmatrix} M_x \\ M_y \\ M_z \end{vmatrix} = \begin{vmatrix} |M|\sin(\theta_M) \\ 0 \\ |M|\cos(\theta_M) \end{vmatrix}. \qquad (5.1)$$

To be more precise, we decompose any magnetisation vector $\vec{M}$ upon $\vec{u}$ and $\vec{v}$, as seen in Fig 5.2. $\vec{u}$ and $\vec{v}$ are of length $|M|$, $\vec{u}$ is aligned along $\hat{x}$ and $\vec{v}$ is aligned along $\hat{z}$.
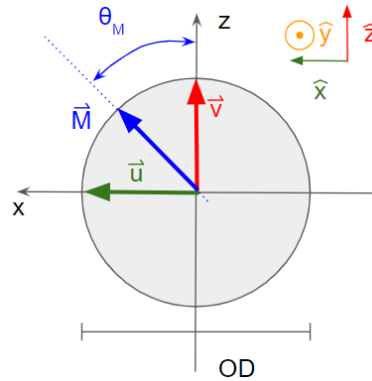
Fig 5.2 Schematic to show $\vec{u}$ and $\vec{v}$, the magnetisations vectors of length $|M|$ aligned along $\hat{x}$ and $\hat{z}$.

The base magnetisations $\vec{u} = (|M|, 0,0)$ and $\vec{v} = (0,0, |M|)$ produce fields $\vec{B}_u$ and $\vec{B}_v$ respectively, with components:

$$\vec{B}_u = \begin{vmatrix} B_{u,x} \\ B_{u,y} \\ B_{u,z} \end{vmatrix}, \qquad (5.2)$$

$$\vec{B}_v = \begin{vmatrix} B_{v,x} \\ B_{v,y} \\ B_{v,z} \end{vmatrix}. \tag{5.3}$$

From these, we can calculate the field from $\vec{M}$ at any angle θ_M by using a linear combination of $\vec{B}_u$ and $\vec{B}_v$:

$$\vec{B} = \vec{B}_u \sin(\theta_M) + \vec{B}_v \cos(\theta_M). \tag{5.4}$$

The switching of our particles is only dependent on the OOP component of the field B_z, as proven by the switching astroids in section 4.4.3. This is:

$$B_z = \vec{B}_{u,z} \sin(\theta_M) + \vec{B}_{v,z} \cos(\theta_M). \tag{5.5}$$

An example of the fields $\vec{B}_{u,z}$ and $\vec{B}_{v,z}$ for a magnet of $L = OD = 4\ cm$ at a height p_0 = 5.37 mm above the magnet surface are shown in Fig 5.3
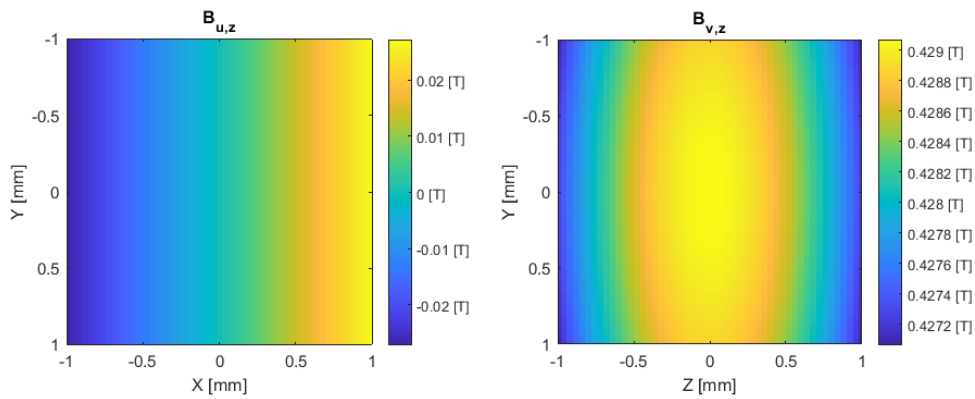
Fig 5.3 Fields $B_{u,z}(x, y, p_0)$ and $B_{v,z}(x, y, p_0)$ for permanent magnet OD = 4 cm and a 5% distance $p_0 = $ 5.37 mm .

These are combined using Equation 5.5 to obtain the z-field for any angle θ_M. For each value of θ_M and resulting $B_z(x, y, p_0)$ field map, the number of probe points above and below the switching field B_0 is evaluated using simple binary logic using Heaviside step functions:

$$f(x, y) = \begin{cases} 1, & B_z \geq B_0 \\ 0, & B_0 > B_z \end{cases} \tag{5.6}$$

defining areas above or below the switching field value. The number of probe points above B_0 is normalised by the total number of probe points defining the whole sample area, giving the NSA. As we will see in chapter 6, the time derivative of the NSA is directly proportional to the induced voltage due to Faraday's law.

$$\varepsilon = -\frac{\delta\Phi}{\delta t}, \qquad \Phi = \iint_S \vec{B}_{sample} \cdot d\vec{S}, \tag{5.7}$$

where $\vec{B}_{sample}$ is the field from the particles situated in the probe area and S is the surface of the detection coil – see Fig 5.1.

Though the principle of the calculation has been presented in Cartesian coordinates, the Caciagli method [1], which we use to analytically calculate the field from the cylindrical drive magnet, is implemented in cylindrical coordinates. This is described fully in section 3.2.1.4. A reminder of the Caciagli geometry is shown in Fig 5.4. In this geometry, the long axis of the cylinder runs along y. In Cartesian coordinates the coordinates of each point in the sample plane are transformed to cylindrical using the standard transformation:

$$\rho = \sqrt{x^2 + z^2}, \tag{5.8}$$

$$\phi = \tan^{-1}\left(\frac{x}{z}\right), \tag{5.9}$$

$$y = y, \tag{5.10}$$

with unit vector transformation:

$$\begin{bmatrix} \hat{\rho} \\ \hat{\phi} \\ \hat{y} \end{bmatrix} = \begin{bmatrix} sin(\phi) & 0 & cos(\phi) \\ cos(\phi) & 0 & -sin(\phi) \\ 0 & 1 & 0 \end{bmatrix} \begin{bmatrix} \hat{x} \\ \hat{y} \\ \hat{z} \end{bmatrix}. \tag{5.11}$$

The coordinates of the probe points (ϕ, ρ, y) are then fed into the Caciagli model for an analytical calculation of the magnetic field from a cylindrical permanent magnet. These vector fields are output in cylindrical coordinates and must be transformed back into Cartesian coordinates in order to analyse the OOP field component (B_z). The transformation from cylindrical vector field components back to cartesian field components [2] is:

$$\begin{bmatrix} B_x \\ B_y \\ B_z \end{bmatrix} = \begin{bmatrix} sin(\phi) & cos(\phi) & 0 \\ 0 & 0 & 1 \\ cos(\phi) & -sin(\phi) & 0 \end{bmatrix} \begin{bmatrix} B_\rho \\ B_\phi \\ B_y \end{bmatrix}. \tag{5.12}$$
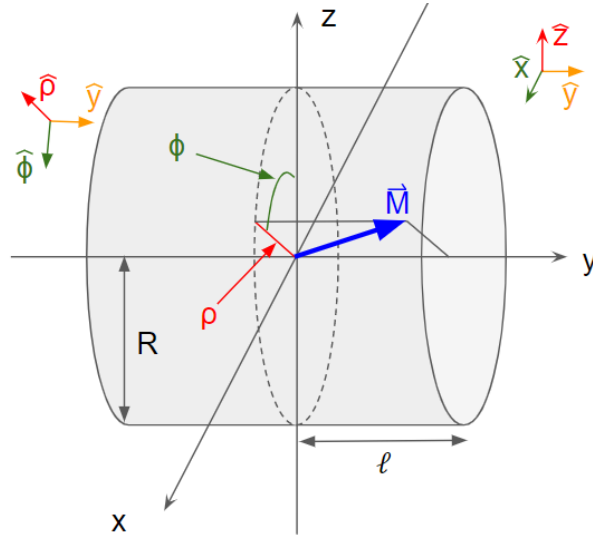
Fig 5.4 A schematic showing the geometry of the problem solved using the Caciagli method – the analytical solution for the magnetic field produced by a cylindrical object with a uniform magnetisation The Caciagli method can be used for any magnetisation by a superposition of longitudinal and transverse components. In this thesis, only transverse components are used and presented.

5.1.2.2 Quantities used to assess the device efficacy.

The methods described above allow us to understand how the simulations work, but importantly we need to define characteristics to assess the efficacy of the device and objectively decide whether a change in the design has improved its efficacy. An optimal device will allow for the accurate detection of the largest number of channels, η. These channels must be well separated, with no blurring between neighbours.

Even in an ideal system where the transition is perfectly sharp, the spatial inhomogeneity of the field over the sample area will lead to gradual switching events that will be captured in the variation of the NSA vs θ_M. The measure we have chosen to use to quantify the sharpness of the NSA vs θ_M transition is the angle between the 30% and 70% points, $W_{0.3-0.7}$. We can then define a criteria KRV (key ratio value) to describe the distance between two adjacent channels as a multiple of $W_{0.3-0.7}$, so that

$$KRV = \frac{nearest\ neighbour\ separation}{W_{0.3-0.7}}. \tag{5.13}$$

In this scheme, a higher KRV ensures less risk of mixing consecutive channels. For a given KRV, we can calculate the number of possible channels, giving a figure of merit (η) by which to assess the optimisation of the device geometry.

5.1.3. Optimisation parameters

Now that we have defined an objective way to estimate the performance of the device, its optimisation is undertaken. Among the parameters that can be optimised are those defining the

geometry of the permanent magnet: its length L and outer diameter OD. We can also assess the effect of changing the starting field, the sample area (defined by $\pi \cdot s_{rad}^2$) and KRV.

The figure of merit η can also be used to test the effect of the measurement method (whether all channels are detected at once using a large rotating field amplitude, or whether each new channel is detected individually by decreasing the rotating field amplitude).

5.1.4. Efficiency

The most computationally expensive element of our simulations is the calculation of the magnetic field. To increase efficiency, we minimise the number of probe points. By using an analytical function, however, we can limit the probe area to the sample area only. This is contrasting to finite-difference approaches, which, due to the scale differences between the micron-scale particles and centimetre scale measurement range, would require a vast number of cells. In addition, we only calculate the field for two magnetisations of length $|M|$ aligned along $\hat{x}$ ($\vec{u}$) and $\hat{z}$ ($\vec{v}$). The field from a magnetisation at an arbitrary angle in the XZ plane, $\vec{M}(\theta_M)$, can be computed as a linear combination of each component meaning that the computational time is much less dependent on the θ_M resolution.

The number of probe points is also decreased by exploiting the spatial symmetries of the system. In our case, one symmetry axis remains (about the $Y = 0$ plane, see Fig 5.1), allowing us to reduce the number of calculated points by half.

To limit the quantity of data stored, only the maximum field value for each magnet-sample distance (p) are saved. An example of this $B_{max}(p)$ relationship can be seen later in this chapter in Fig 5.17 and Fig 5.20b. The field in the rest of the plane can be calculated when needed. Intertwined functions are used to reduce stored data, and only the probed metrics are saved within each iteration. A separate version of the code is also available which saves full information about a single set of parameters (rather than just figures of merit for an extended parameter space). This gives access to additional information about a particular data point, or to validate that the code is running as expected.

5.2. Model validation

This section expands on section 5.1.2, providing graphical demonstrations of the methods to validate their correct implementation by comparing their results to those obtained using the well-established micromagnetic package Mumax [3].

5.2.1. Akoun/Janssen parallelepipedal field validation

The Akoun/Janssen method can be used to calculate the magnetic field from a parallelepipedal magnetic sample. In our simulations, it is used to calculate the stray field from our particles at the sense coil, situated microns away. The geometry of this system is shown schematically in Fig 5.5.
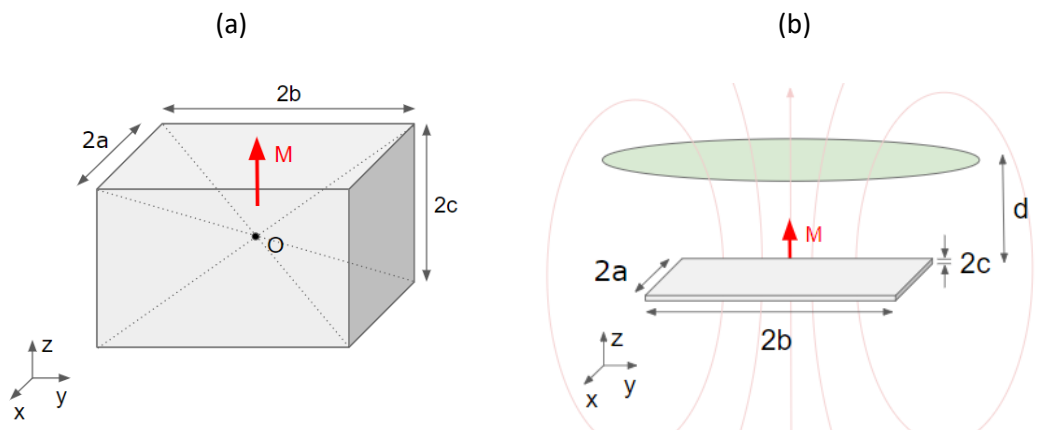
Fig 5.5 a) The Akoun/Janssen geometry and b) how we use it in our simulations. In b), the green area represents the detection coil, at a distance d from the sample. Light red lines represent field lines from the sample.

To ensure that our code yields accurate results, we use the same geometry in both Mumax and our code and perform a cell-for-cell comparison between the stray field obtained with both methods. We start with a cuboid of side lengths $2a = 2b = 2c = 20\ \mu m$ at the centre of a space consisting of (50x50x50) (1 mm x1 mm x 1 mm) cells. In Mumax, the magnetised body consists of 2 by 2 by 2 cells at the centre (cells 25 and 26, in all directions). It is uniformly magnetised in the Z direction, with a saturation magnetisation $M_S = 10^6\ Am^{-1}$, roughly equivalent to that of CoFeB [4]. We are not using Mumax to compute the micromagnetic state of the particle, only to calculate the demagnetising field [5].

Mumax employs Fourier transforms to compute the magnetic field [6], and as a finite difference method, it must have cells of equal volume and computes the field as an average in the volume of a cell. The Akoun/Janssen method, on the other hand, estimates the field at a finite point in space.

When the probe points are chosen as the centre of the equivalent Mumax cells, consistent results are obtained. A plot to show the relative difference in the magnitude of the field, defined by the quadrature addition of all three components, is shown in Fig 5.6a and b. We notice immediately that the main differences are located at the boundary of the sample. This is because of the different boundary conditions between methods, as well as this being the location of the highest field value. However, out of 125,000 probe points, only 22 (<0.02% of sampled points) were observed to deviate by 1% or more, but by less than 6%. The 3D index of their cell can be seen in Fig 5.6b, at and around the magnet (index 24 to 28 in all 3 dimensions). Note that the colour scale in Fig 5.6a is limited to aid the eye, with a true range of $-5.103 < x < 1.178$.

In this work, we are interested in the component of the field perpendicular to the plane of the sample, which will ultimately lead to an inductive voltage in the coil. In the geometry defined in Fig 5.5a, this is the Z component B_z. When the difference in B_z values are compared, see Fig 5.6a, we see a variation in values at the region where the B_z component changes from positive to negative, see Fig 5.7b. The colour scale in 5.6a has been limited in order to amplify the differences. These are expected, as the values become extremely small. These results show that the Akoun method has been integrated sufficiently well into the code to model the stray fields from the particles.
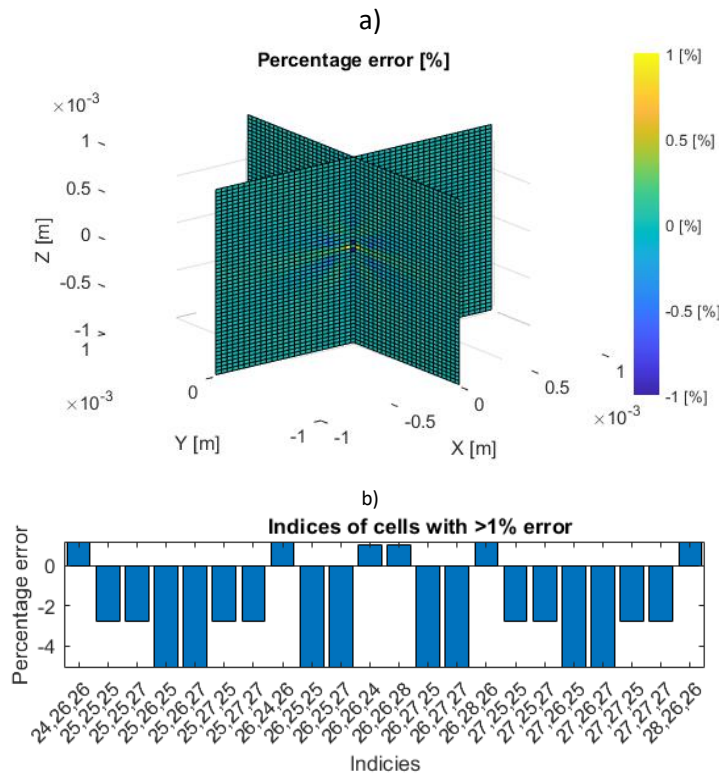
Fig 5.6 a) Percentage difference in magnitude between fields calculated from using our code (Akoun model) and MuMax. b) Index number of the 22 cells for which our simulation and Mumax differ by 1% or more. Note the colour scale in a) has been limited.
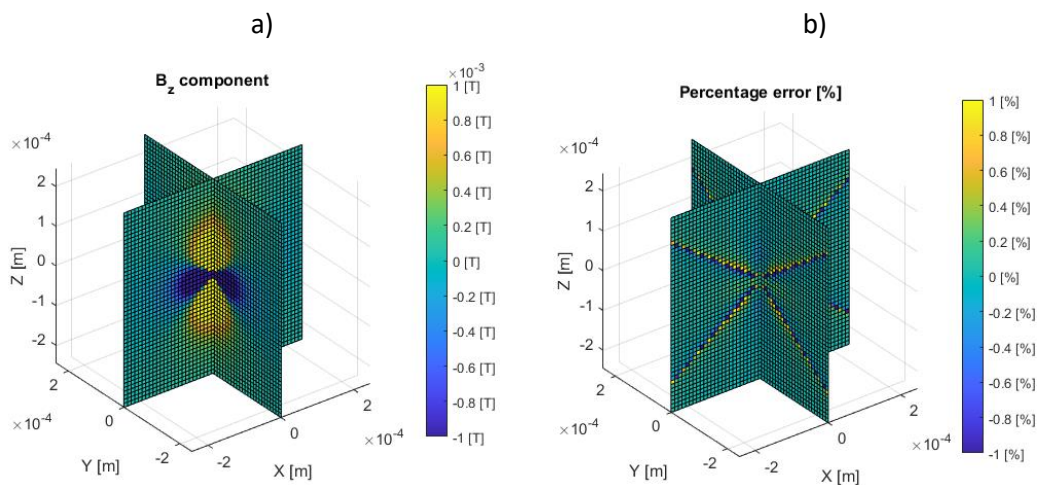
Fig 5.7 a) B_Z field profile $2\ mm^2$ centred at (0,0,0) calcuated using our simulations (Akoun method). Note the colour scales have been limited to aid the eye. b) Percentage difference in B_Z values between our simulations and Mumax

5.2.2. Caciagli cylindrical model validation

The drive magnet in our apparatus is cylindrical, as shown in Fig 5.1. A cylindrical analytical model is, therefore, more appropriate for accurate modelling of the drive field. In this section, we validate the accuracy of our implementation of Caciagli's model for the analytical calculation of the field from a cylindrical permanent magnet [1]. Again, we verify this using Mumax. For our Mumax model, we maintain the same reference frame as used in the simplified model of our proposed detector, with the cylinder's long axis along Y. This is shown in Fig 5.8.

To compare the models, a cylinder with radius and length $OD/2 = L = 1\ cm$ is created in both models, with a radial magnetisation of length $|M|$ along $\hat{z}$ ($\vec{v}$). We use $M_S = 1.27 \times 10^6\ Am^{-1}$ for NdFeB [7]. The Mumax model uses $(50x50x50)$ cells with a total world size of $(40x40x40)$mm. As in the case of the Akoun/Janssen model validation (section 5.2.1), the centre of the Mumax cells are used as probe points in the Caciagli model.
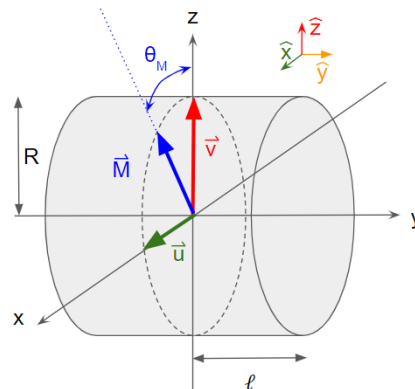
Fig 5.8 Geometry used in the Mumax and Caciagli models, for comparison of field values.

The field profile in an XY plane situated at a distance of 0.95 cm from the surface of a cylindrical permanent magnet is calculated using both models and for all 3 field components, see Fig 5.9. These show similar field magnitudes.
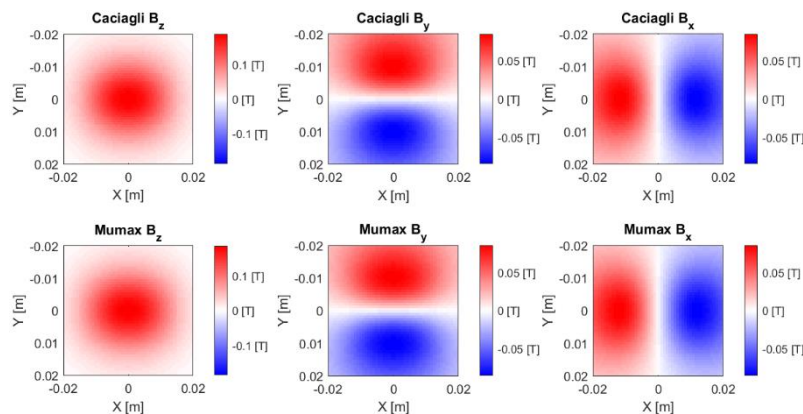
Fig 5.9 A comparison of the field profile in an XY plane situated at a distance of 0.95 cm from the surface of a cylindrical permanent magnet using both the Caciagli model and Mumax.

Fig 5.10 shows the Z component of the field in the $Y = 0$ plane calculated using both methods and using different cell sizes to cover the explored volume $(64\ cm^3)$, with $dx = dy = dz = 0.8, 0.4, 0.2\ mm$ respectively. We again observe slight variations at the surface of the magnet as well as at polarity changes, as described in the previous section where we looked at the Akoun model. The differences are more pronounced here because of the differences in shape construction. In Mumax, the cylinder edge is approximated by a staircase, whereas the Caciagli model uses the exact cylindrical shape. The apparent staggered edging in the Caciagli model is due to the plotting tool, rather than a true staggered edge. The Caciagli model defines the field at a point, whereas Mumax defines the average field over a volume. The plotting tool used here displays the field at a point, which, for the image, extends to halfway between adjacent points. This is like the Mumax method (which averages over the cell) and displays representative results for the Mumax fields. It is not a true description of the results for the Caciagli method but it allows us to compare these visually.
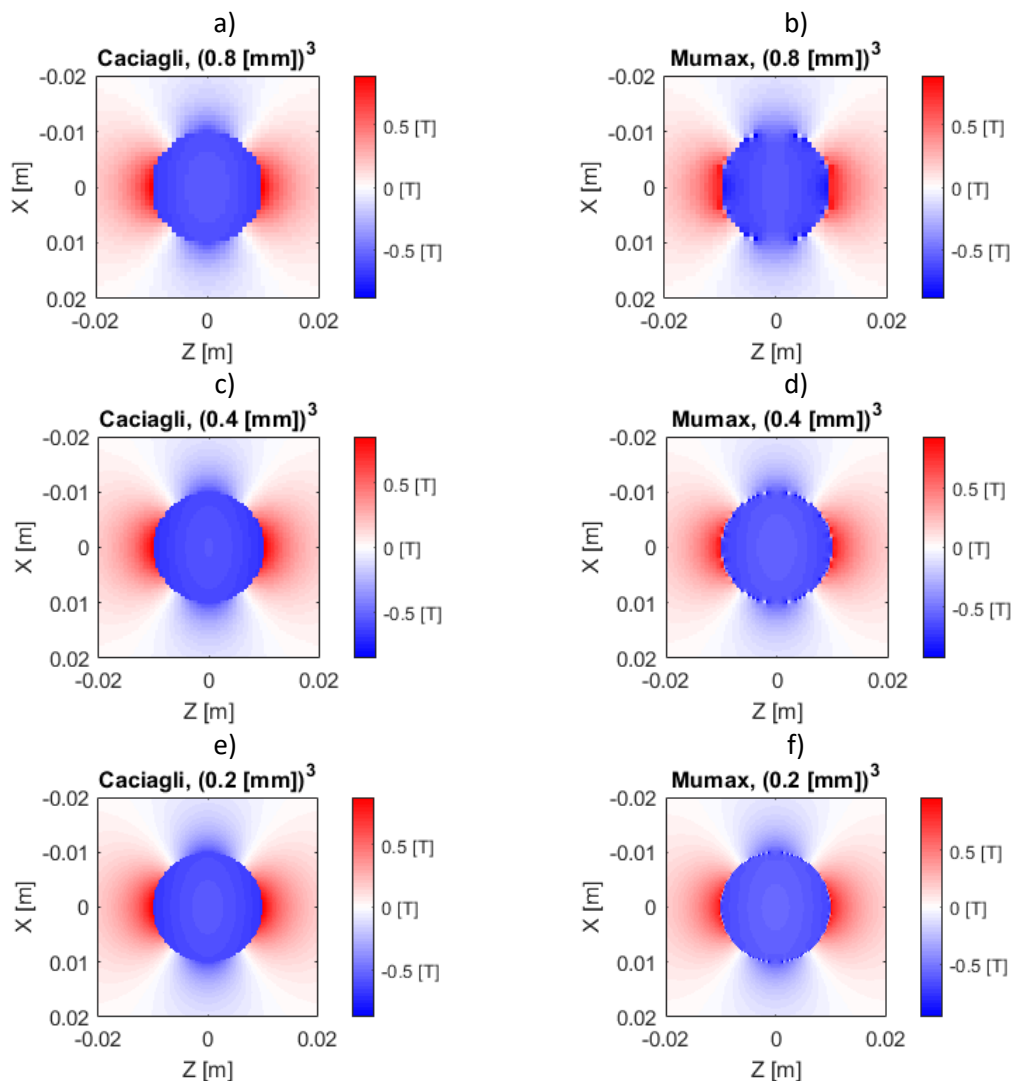
Fig 5.10 A close up of the B_z component of the field produced by a cylindrical permanent magnet of OD = L = 2 cm. at the magnet boundary. An XZ cross-section through Y = 0 is shown for cell sizes of a,b) 0.8 mm, c,d) 0.4 mm, e,f) 0.2 mm..

As the cell size becomes smaller, we should see a convergence of the two models. This was tested, with the results seen in Fig 5.11. Fig 5.11 a, c and e show line scans of the Z component of the field versus height p, $B_z(p)$; the planar (XY) averages of the z component of field versus height p, $\overline{B_z}(p)$, are shown in (b,d,f), in both cases for three cell sizes (0.8, 0.4 and 0.2 mm). We confirm the decrease in the difference between both models for decreasing cell size, giving strong evidence that the differences showed between the two models are due to Mumax pixelation at the magnet surface. This shows that Caciagli's method has been effectively implemented in our simulations.
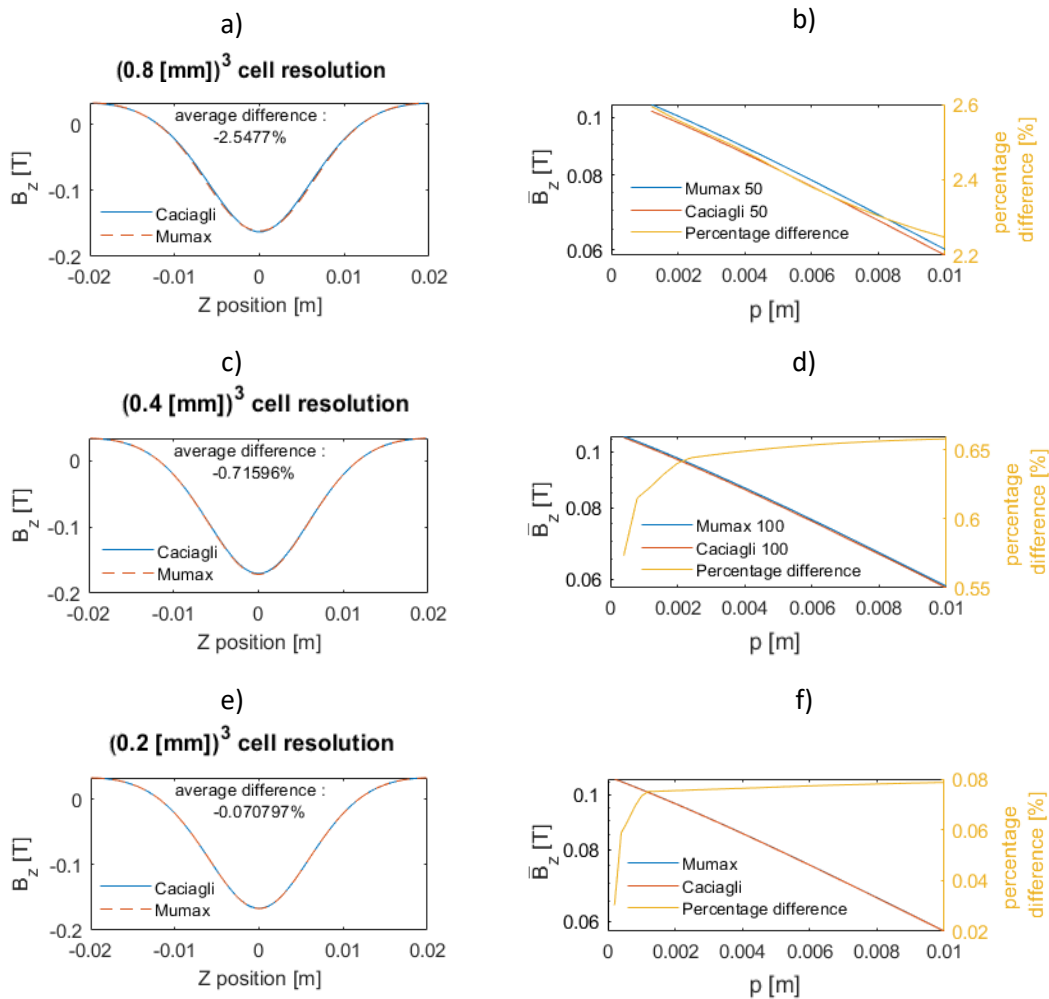
Fig 5.11 B_z linescan comparisons (a,c,e) and planar average field values $\overline{B_z}$ (b,d,f) for the field produced by a cylindrical permanent magnet where OD = L = 2 cm, calculated using both Mumax and the Caciagli model using different cell sizes. The linescan comparisons were taken at $x = 5.6\ mm$ and $y = 0.8\ mm$. The mean fields are taken as an average in the XY plane, for changing magnet to surface distance p.

5.2.2.1 Stray field from the rotating magnet

As previously mentioned, in order to reduce the number of field calculations required, we calculate the stray field from a cylindrical magnet oriented with a magnetisation of length $|M|$ along $\hat{x}$, $(\vec{u})$, and from a cylindrical magnet oriented with a magnetisation of length $|M|$ along $\hat{z}$, $(\vec{v})$, only. The stray field from any arbitrary magnetisation angle in the XZ plane (θ_M) is built by linear superposition of $\vec{u}$ and $\vec{v}$. More specifically, if $\vec{B}_u$ is the stray field created by the cylindrical magnet with a magnetisation oriented along $\hat{x}$ and $\vec{B}_v$ the stray field created by the cylindrical magnet with a magnetisation oriented along $\hat{z}$, then for any arbitrary magnetisation angle θ_M defined in the XZ plane with respect to the X-axis, so that $\vec{M} = (|M|\sin(\theta_M), 0, |M|\cos(\theta_M))$, the Z component of the stray field is $B_z = B_{u,z}\sin(\theta_M) + B_{v,z}\cos(\theta_M)$.

We compare our B_z results with Mumax for two angles that do not lie on any symmetry planes, at $23°$ and $67°$. The results for B_z in the $y = 0$ plane for a $23°$ rotation are seen in Fig 5.12, with a comparison of linescan values displayed in Fig 5.13. The calculations were performed again for 3 different cell sizes. We confirm that our model correctly implements the linear combination of magnetisation vectors. The line-scans were again taken at (X, Y) position $(5.6, 0.8) mm$.
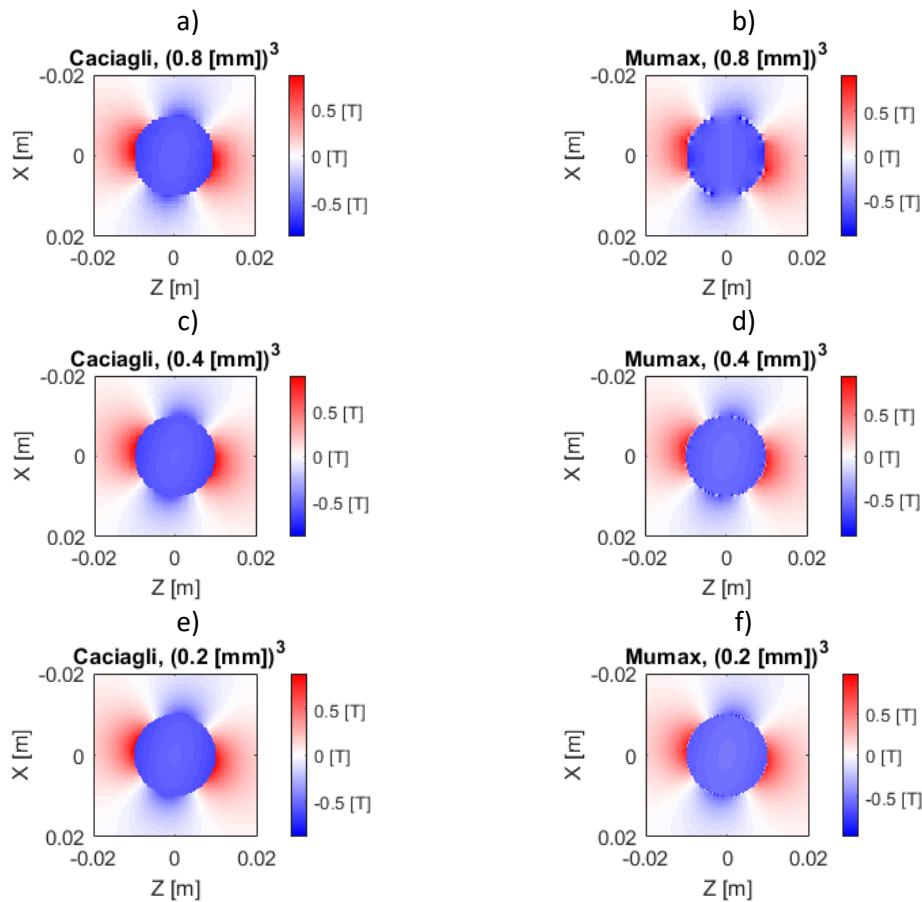
Fig 5.12. A close up of the B_z component of the field produced by a cylindrical permanent magnet where OD = L = 2 cm at a magnetisation 23° from the Z axis. An XZ cross-section at $Y = 0$ through the magnet is shown for cell sizes of a,b) 0.8 mm, c,d) 0.4 mm, e,f) 0.2 mm.
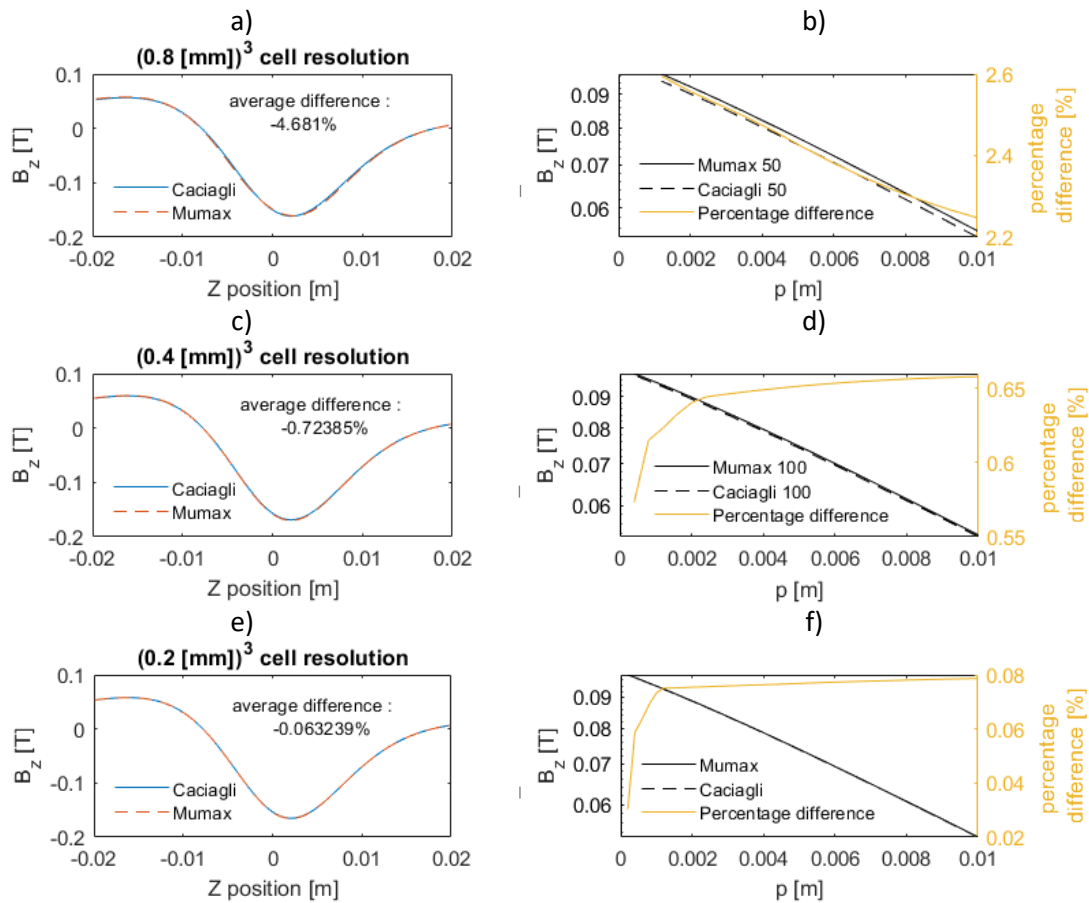
Fig 5.13 B_z linescans (a,c,e) and planar average field values $\overline{B_z}$ (b,d,f) for the field produced by a cylindrical permanent magnet where OD = L = 2 cm, calculated using both Mumax and the Caciagli model using diffent cell sizes and at magnetisation angle 23°. The line scans were taken at (x,y) position (5.6,0.8) mm above the magnet surface. The mean fields are taken as an average in the XY plane as a function of magnet to surface distance p.

5.2.2.2 Toroidal magnet

We are planning to use a rotating permanent magnet for the drive field, which was shown in Fig 5.1. We used a cylinder, due to its symmetry being highly beneficial to rotational fields, with a constant sample to surface distance and smooth field variation with respect to angle. A toroid also shares the same symmetry but allows us to mount the magnet onto an axle. This is shown schematically in Fig 5.14. However, this adds another parameter, the inner diameter (ID), which can be optimised.

Here, we use the superposition principle to calculate the field from a toroidal magnet, by subtracting the field from the inner core from the field of the whole cylinder. To ensure that this is implemented correctly, we compare our calculated fields with the same structure simulated using Mumax. This model uses the same cylinder as in section 5.2.2 but with a subtracted inner cylinder of diameter $ID = 6\ [mm]$. The results can be seen in Fig 5.15 and Fig 5.16. Again, we observe differences at the surfaces and polarity changes, but the overall accuracy of the model is sufficient for our use. These results are compared in the same fashion as in sections 5.2.2 and 5.2.2.1, with similar trends to those shown before. This shows that the superposition principle is implemented correctly within our code.
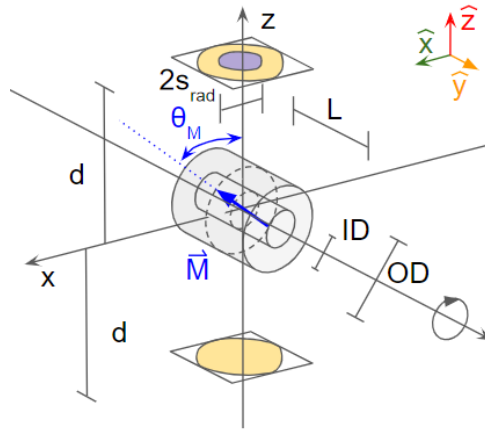
Fig 5.14 An updated simplified schematic for the detector, with the addition of an inner bore, creating a toroid.

We can combine all the methods in this section to create an efficient system to calculate magnetic fields from a toroidal structure at various angles, which we will utilise in the code.
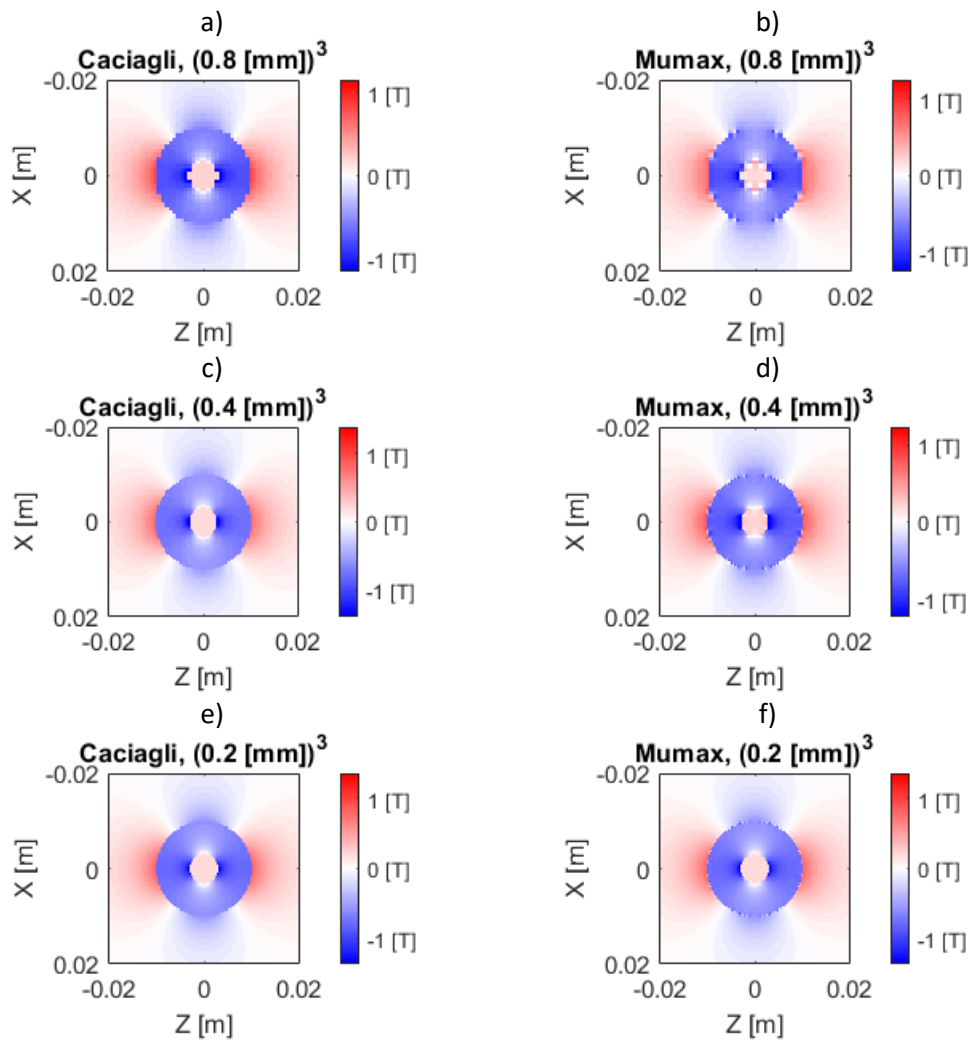
Fig 5.15 A close up of the B_z-component of the field produced by a toroidal permanent magnet of OD = L = 2 cm and ID = 6 mm at a magnetisation 23° from the Z axis. An XZ cross-section at $Y = 0$ is shown for cell sizes of a,b) 0.8 mm, c,d) 0.4 mm, e,f) 0.2 mm
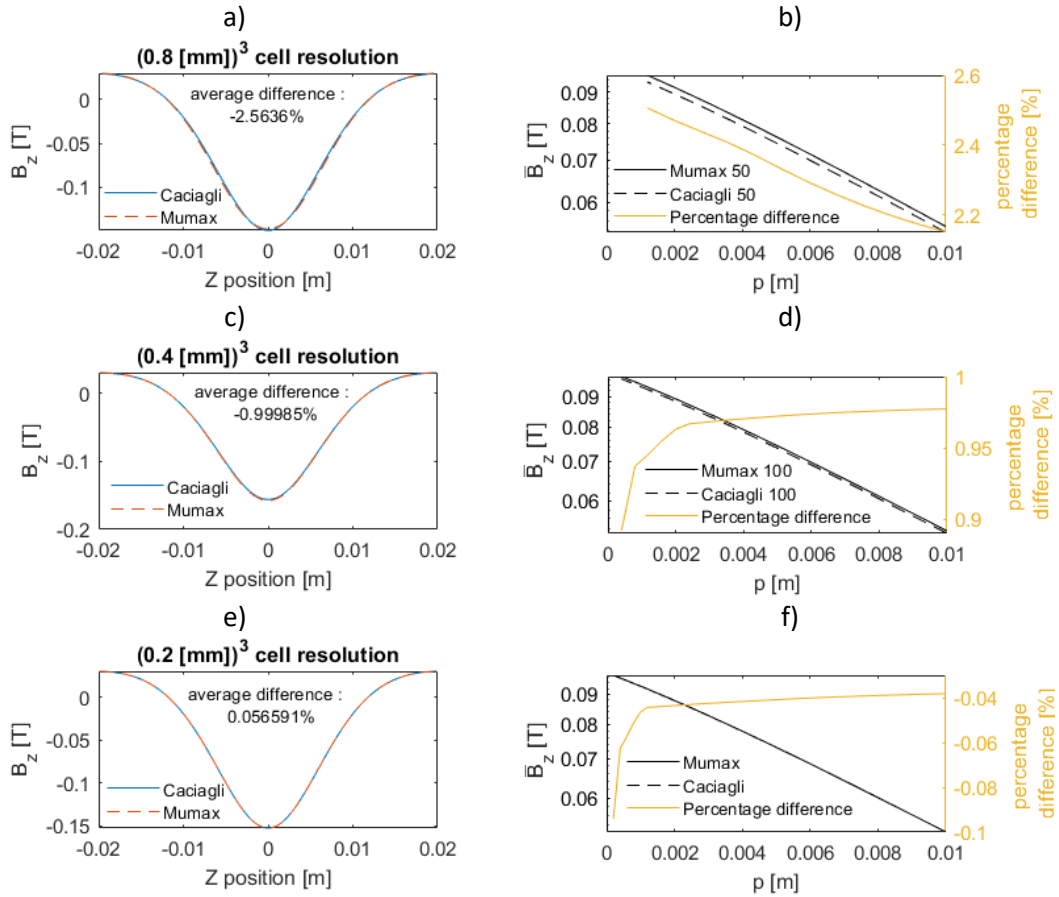
Fig 5.16 Linescan comparisons (a,c,e) and planar average field values $\overline{B_z}(x,y,p)$ (b,d,f) for the field produced by a toroidal permanent magnet of OD = L = 2 cm and ID = 6 mm, calculated using both Mumax and the Caciagli model using different cell sizes. The linescan comparisons were taken at a value (5.6,0.8) mm above the magnet surface in X and Y respectively. The mean fields are taken as an average in the XY plane, for changing magnet to surface distance in Z.

5.3. Code structure and device characterisation

This section outlines how our simulations are structured and show how we extract the parameters that allow us to compare the performance of our device under different conditions. We have outlined how the NSA, a measure of the proportion of the sample area above the switching field, is calculated, and how the KRV is used to determine the next possible channel in a series. The NSA has a direct correlation to the number of channels a detector will be able to resolve (η), which in turn is a direct and objective assessment of the performance of the device. Calculating it for different input parameters, such as the geometrical details, allows us to optimise the device.

Part of what is presented in this section has already been shown in section 5.1.2.1. The method is explained in more detail here. For a given set of inputs parameters (L, OD, ID), we first calculate $B_{z,max}(p)$, i.e., the Z component of the field on the Z axis obtained from the magnet pointing in the Z-direction ($\theta_M = 0$) as a function of distance p from the magnet surface. The $B_{z,max}(p)$ curves are shown in Fig 5.17 for several toroidal magnet lengths L and outer diameters OD, all with an inner bore diameter ID of 6 mm.
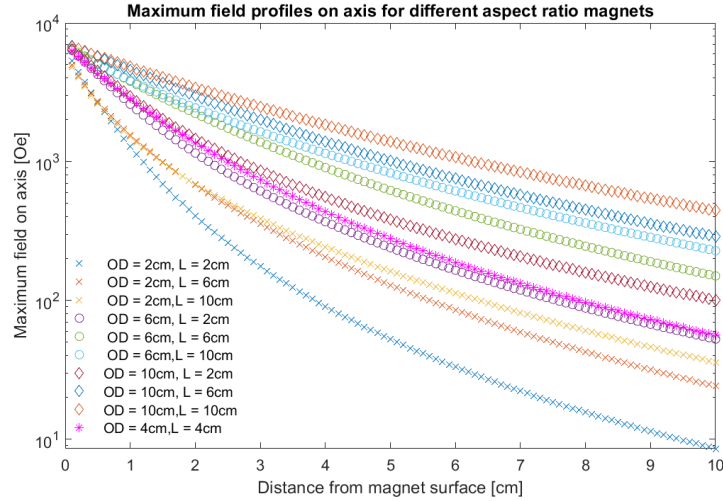
Fig 5.17 $B_{z,max}(p)$ for magnets of various geometries estimated using the Caciagli model.

In this section, we illustrate the process with a permanent magnet of outer diameter $OD = 4\ cm$ and length $L = 4\ cm$, shown by the pink asterisks in Fig 5.17. For a start channel B_0, we first extract the distance p_{start} that corresponds to a B_{start} value at 5% over B_0 from the $B_{z,max}$ vs p data. For $B_0 = 0.4\ T$ for instance, B_{start} is found at $p_0 = 5.37\ mm$. We then evaluate the two base field maps required for the rest of the calculation: the $B_{u,z}\ (x, y, p_0)$ map obtained when the permanent magnet points in the X-direction, and the $B_{v,z}\ (x, y, p_0)$ map obtained when the permanent magnet points in the Z-direction, see Fig 5.18(a-b). The base stray fields are evaluated within an XY square plane centred around $(0,0,p_0)$ and of length $2s_{rad} = 2$ mm. The fields are evaluated on a grid of $(50x25), 40\ \mu m^2$ cells, using the Y axis symmetry to reduce the number of cells in this direction by half (as described in section 5.1.4). The field at this plane, for $\theta_M = 0$ is equal to $B_{v,z}$ and is displayed in Fig 5.18c.

We propose to dispense the sample in solution, which will form as a droplet [8]. As such, the sample area is considered to be circular (Fig 5.18d) and we assume that the distribution of the particles is uniform within it, allowing us to equate the ratio between areas above and below the switching field with the ratio between the number of switched and unswitched particles.

The next step consists of identifying the probe points above and below the switching threshold B_0, using the Heaviside step functions described in Equation 5.6. The number of cells above the switching field is summed and normalised to the total number of cells in the mask, providing a value for the NSA at this angle. At $\theta_M = 0$, the whole of the sample area is above the switching field value, giving an NSA of 1. As θ_M increases, the field produced in the sample area is the sum of $B_{v,z}\cos(\theta_M)$ and $B_{u,z}\sin(\theta_M)$, as previously described, and areas of the sample will gradually fall under the switching field B_0. The resulting B_z for various θ_M is shown in Fig 5.19 a-j. We record the NSA at each θ_M increment, giving the profile of the transition – see Fig 5.20a.
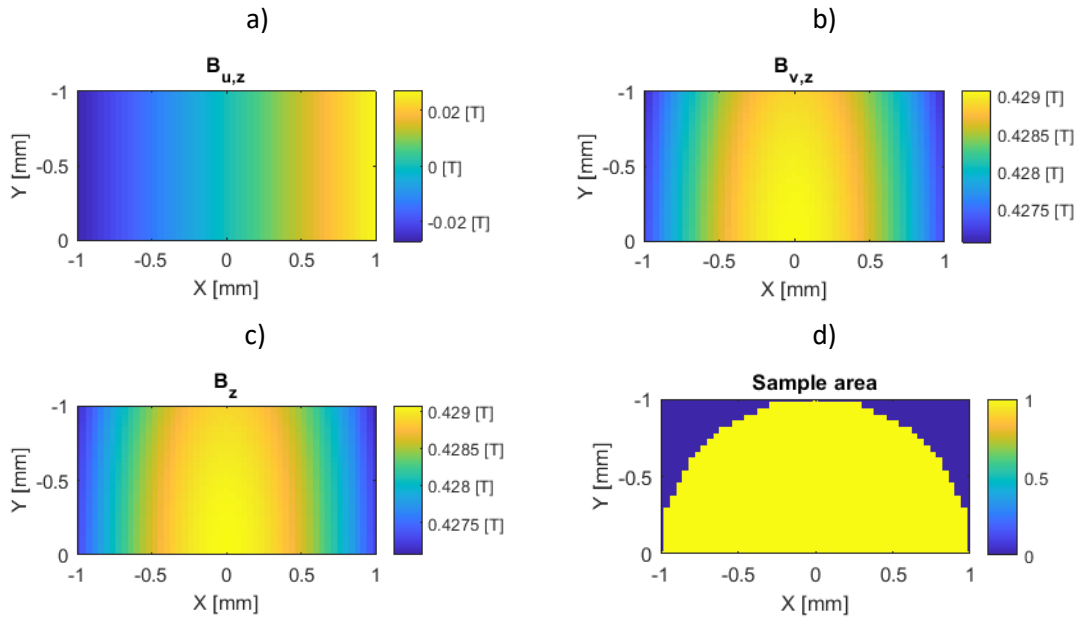
Fig 5.18 Field perpendicular to the sample (B_z) at the sample plane from a cylindrical permanent magnet of OD = L = 2 cm at a height $p_0 = 5.37\ mm$ using a) a magnetisation along X, b) a magnetisation along Z, c) linear combination with $\theta_M = 0$. d) The field mask for a sample radius $s_{rad} = 1\ mm$.
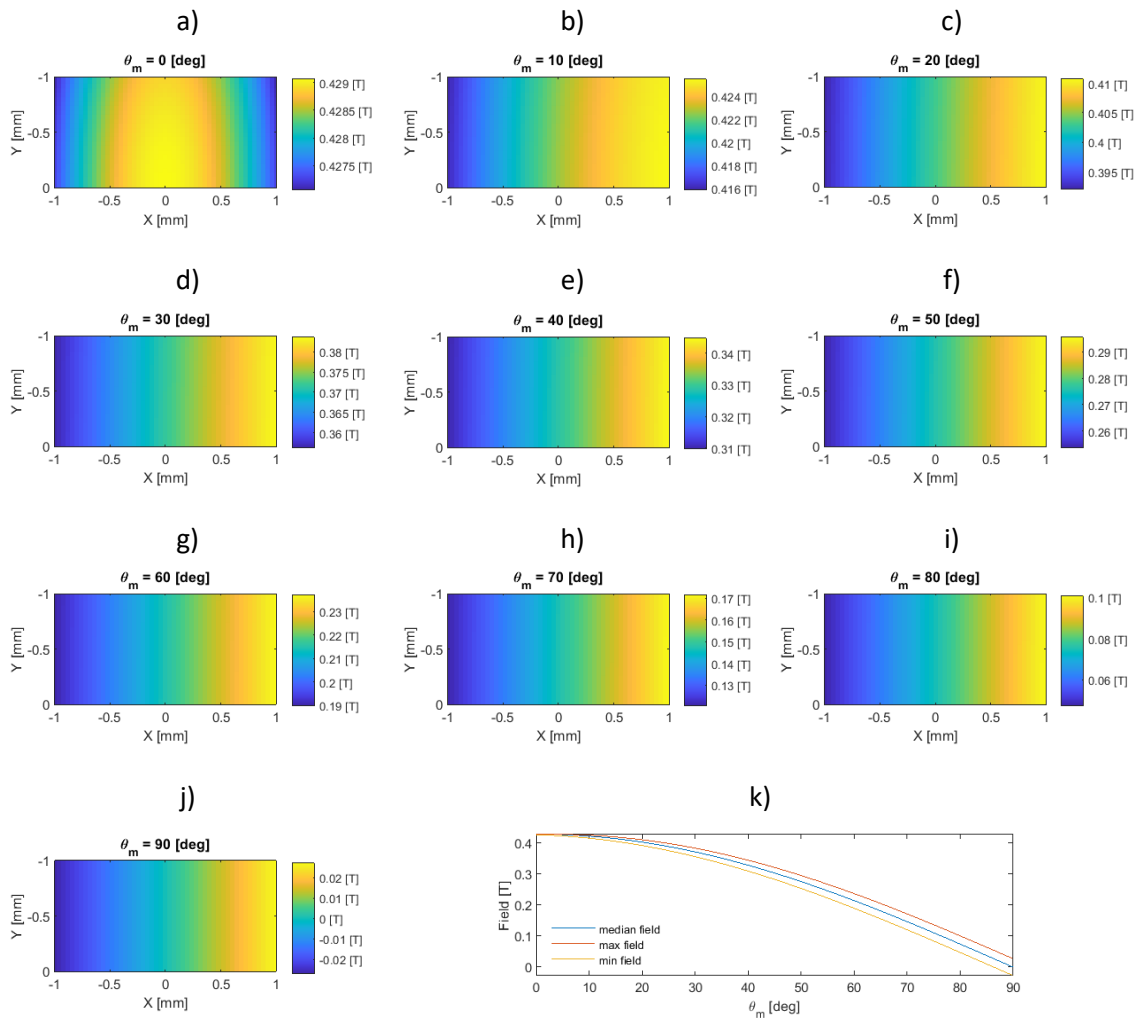
Fig 5.19 a-j) the Z component of the field from a cylindrical permanent magnet of OD = L = 2 cm at a height $p_0 = 5.37\ mm$ for varying magnetisation angles θ_M. k) maximum, minimum and median fields at each θ_M value.

The spatial inhomogeneity of the field leads to the transition profile described by the NSA. A rough measure of this inhomogeneity is provided by the range of field within the sample plane. This is displayed in Fig 5.19(k), with a range increasing as $\theta_M \Rightarrow 90°$. The median field $B_z^{0.5}$ is also displayed.

In the example considered here ($B_0 = 0.4\ T$), and as mentioned previously, B_{start} is found at $p_0 = 5.37\ mm$ (Fig 5.20b). To visualise how the NSA is calculated, Fig 5.20c shows the data for $\theta_M \approx 17.8\ °$, corresponding to an NSA of 0.5 (circled in the NSA profile in Fig 5.20a). Fig 5.20d shows the area of the sample below (blue) and above (yellow) the threshold field (B_0), showing a 50/50 ratio of switched to unswitched particles. The field that defines this point, where half of the sample is in the on state, is by definition the median field $B_z^{0.5}$.
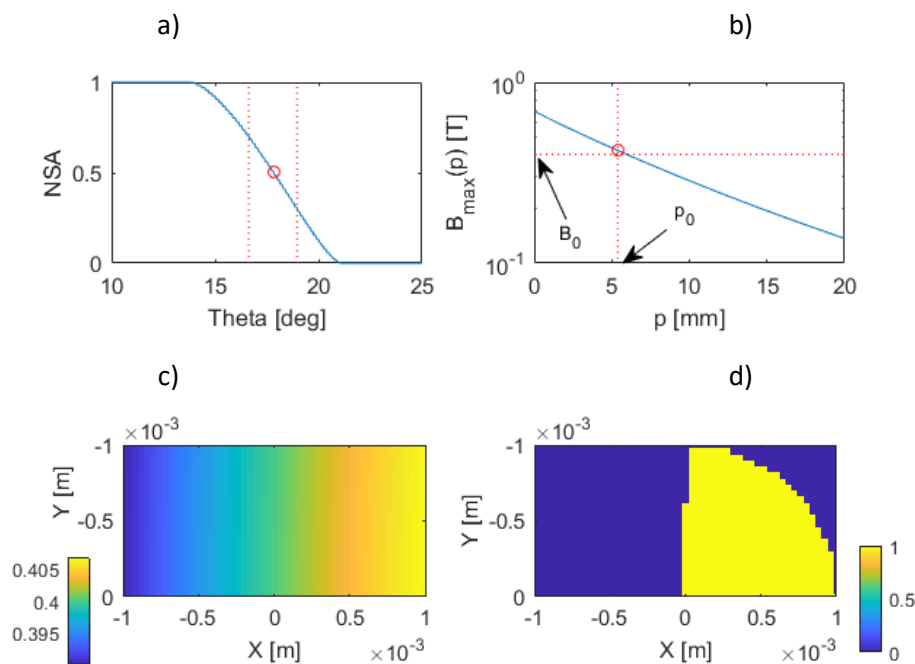
Fig 5.20 a) $NSA(\theta_M)$ for a 0.4 T channel using a $OD = L = 4\ cm$ magnet, showing the location of $NSA = 0.5$ (circled) and $W_{0.3-0.7}$ points (dotted lines) b) Maximum field decay profile for an increasing magnet to sample distance (p). The distance p_0 for which $B_{z,max}$ is 5% above the start channel B_0 is indicated, at $B_{0.42[T]} = 5.37$ mm. c) B_z profile at the sample plane (x,y,p_0) at NSA=0.5 (θ_M=17.83 °). d) sample area above (yellow) and below (blue) the switching field, at θ_M=17.83°.

Once the full NSA profile ($0 - 90°$) has been calculated, we can characterise the transition. In the case we illustrate here, the transition width, defined as the 30-70% width (shown in red in Fig 5.20a, and Fig 5.21a), is ≈ 2.33 [°]. We can then use the definition of KRV (Equation 5.13) to find the nearest possible channel, i.e.:

$$nearest\ neighbour\ separation\ [°] = KRV \cdot W_{0.3-0.7}\ [°] = \theta_F\ [°], \tag{5.14}$$

and the field of the next channel is found using

$$B_1 = B_{z,p_0}^{0.5}(\theta_0 + \theta_F). \tag{5.15}$$

Fig 5.21 describes this process schematically. $B_{z,p_0}^{0.5}$ is the median field at p_0, which defines the field which yields an NSA of 0.5 at an angle θ_0. In other words, θ_0 is the halfway angle of the transition. The switching field B_1 defining the next channel is determined as the field strength at the centre of the nearest channel which fulfils the KRV requirement: centre to centre separation of an angle θ_F.

One useful characteristic of the NSA is that it does not depend on which transition is considered within a single sample. In section 4.4.2, we demonstrated the preferential switching characteristics for our magnetic information carriers for the AP-P transitions compared to the P-AP transition. The gradual change in the NSA measures the spatial inhomogeneity of the field and the $W_{0.3-0.7}$ is independent of whether the field increases or decreases. Though the equations presented here model a P-AP transition, they are also applicable to AP-P transitions, which we will be using in the real device. Though the NSA curves will possess the same properties, a detector using the AP-P transition would instead start at zero field, increasing to $B_{start,0}$, though in this instance this would be the smallest channel value. In this method, the channels begin in the off state, transitioning to the on state. This means that the results would be extracted for magnet angles within the range $270 - 360\,°$, which would be a mirror image of those in Fig 5.21a.
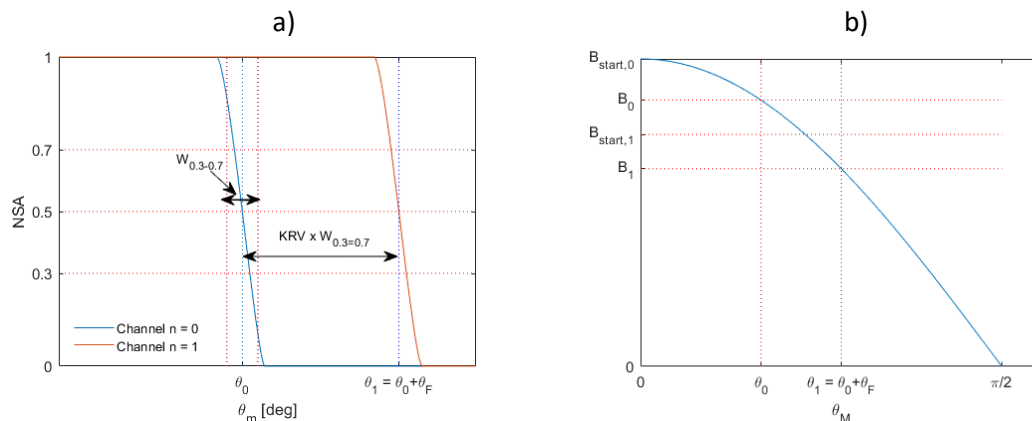
Fig 5.21 a) a close up of the NSA profile for a magnet of L = OD = 4 cm at $p_0 = 5.37\ mm$, showing the locations of the 30% and 70% points, and θ_0. The definition of $W_{0.3-0.7}$ is also given. b) an equivalent plot for B_z vs θ_M, showing the location of the initial channel (B_0 ,θ_0) and the nearest possible channel for a given KRV (B_1, $\theta_0 + \theta_F$). The start field for the following iteration $B_{start,1}$ is also shown, being the midpoint of the two channels. This is explained more in the next section.

5.4. Detection scheme

From the previous section, we understand how the switching profile of a given channel is constructed and characterised. This allows us to understand how sharp our transitions are and where their nearest neighbour would be, but we still require a global figure of merit for comparing the effects of changing the geometry of the device. We define this as the maximum number of possible channels for a given KRV, η, as mentioned in section 5.1.2.2. This means that we must explore the full field range, repeating the process outlined in section 5.3 for every subsequent channel B_{n+1}.

5.4.1. Simulation constraints

In any simulation, we must understand the constraints. Importantly, we must understand when (or not) the code is designed to stop iterating, as this will artificially affect the figure of merit. In our case, depending on the measurement method (see below), if left totally unconstrained, the simulations could keep iterating, with smaller and smaller channel fields and smaller and smaller separation between consecutive field values, leading to infinite and meaningless η values. When necessary, artificial constraints will be introduced and their effects will be discussed. The simplest constraint we introduce is to impose a minimum channel field value of 25 Oe, after which the iterative process is stopped. This constraint might still lead to experimentally unrealistic η values. However, it has the advantage of not interfering with the underlying physics at the root of parameter optimisation.

We also use two practical constraints, which lead to realistic η values. The first one is the imposition of a minimum separation between adjacent field channels. We have seen in the previous chapter that the individual channels have a finite width. To ensure that channels are distinguishable from one another, we impose a minimum separation $(B_{n+1} - B_n)$ of 50 Oe, as this is of the order of magnitude of the width of the AP-P transition from an experimental SAF thin film in a rotating magnetic field (as seen in chapter 4). The second practical constraint we impose is a maximum working range (magnet to sample distance) p_{max} of 10 cm. A working range limit works similarly to the minimum channel field, but in this instance the minimum channel field value is determined by the maximum possible applied field at p_{max}. The relationship between maximum field and p is shown for various magnet sizes in Fig 5.17.

In later sections, we will refer to a simulation that only employs a minimum channel field value as having simple constraints. A simulation that uses a working distance limit and a minimum separation between channels will be referred to as having practical constraints. We use simple constraints when trying to understand the effect of changes in η caused by changes in geometrical parameters.

5.4.2. Method 1

The simplest way to complete a measurement is in a single rotation. In this process, the magnet to sample distance p is kept constant at p_0 for all measurements. Once B_1 is estimated using the method outlined in section 5.3, the new NSA curve for B_1 is calculated, as well as the corresponding $W_{1,0.3-0.7}$. The same KRV criteria are used to calculate the next angle θ_2 as $\theta_1 + KRV \times W_{1,0.3-0.7}$, and the corresponding field B_2 is estimated as the median field of the map at θ_2. This process is then iterated as the magnet keeps rotating. The simulation is set up to stop once $\theta_2 \geq 90\,°$, as after this point a negative drive field is applied. This means that a minimum channel field is unnecessary, as the simulation cannot iterate indefinitely. A working range limit is also unnecessary, as a single p

value is used. Finally, for the case presented in this section, the 50 Oe minimum separation also never applies – see below.

In this method, all channels are detected in the same rotation, making this the fastest method. It is also less subject to error as there are fewer moving parts in the device, ensuring the gradiometer coils are precisely at equal distance from the magnet. An example of the results from such a measurement is shown in terms of field in Fig 5.22a and angle in Fig 5.22b. This model uses $KRV = 10$, $B_0 = 0.4\ T$, $OD = 6\ cm$, $L = 2\ cm$, $ID = 6\ mm$ and $s_{rad} = 1\ mm$. This shows a maximum number of channels $\eta = 5$, with an average $W_{0.3-0.7}$ of $1.48\ °$. The differentiated signal is seen in Fig 5.22c, which is more representative of the inductive EMF we would measure. As will be shown in chapter 6, since we intend to use our system with a constant angular momentum, our angular signal can convert to EMF by a scalar factor.

We note that in this case the simulation is halted because no other channel is found at an angle below 90 °and none of the practical or simple constraints are reached.
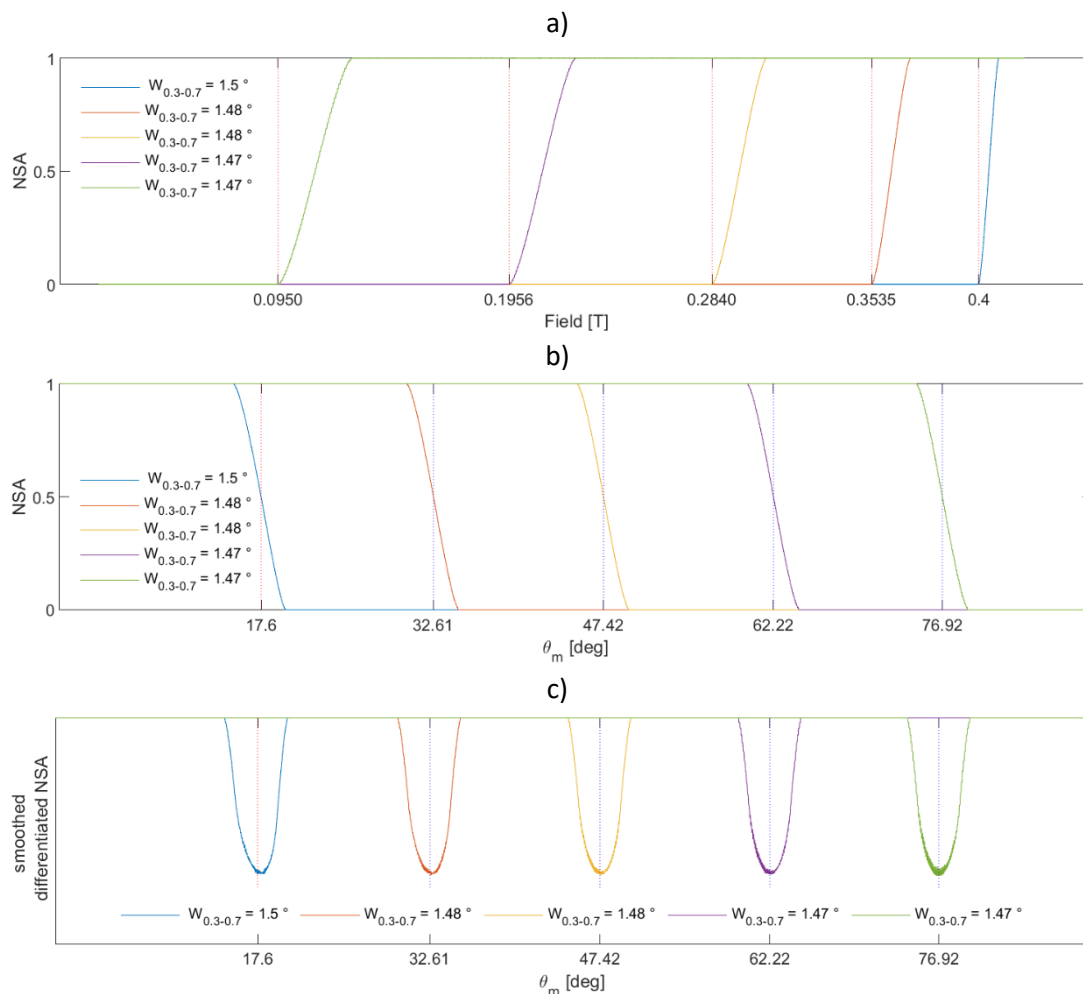
Fig 5.22 a) NSA of an ideal channel set for a measurement scheme using method 1, with $KRV = 10$, $B_{start} = 0.4\ T$, $OD = L = 4\ cm$, $ID = 6\ mm$ and $s_{rad} = 1\ mm$ as a function of field channel value, b) as a function of field channel angle value, and c) smoothed, differential signal of b), proportional to induced EMF.

5.4.3. Method 2

An alternative detection scheme involves adjusting p for each transition or channel within a single ideal set. In this case, after the initial steps described in section 5.3 (identifying the distance p_0 corresponding to $B_{start,0} = B_0 + 5\%$, measuring the NSA corresponding to B_0, extracting θ_0 and the corresponding $W_{0,0.3-0.7}$, then θ'_0 as $\theta_0 + KRV \times W_{0,0.3-0.7}$ and finally B_1 as the median z field at θ'_0), the distance is then increased to a p_1 value corresponding to a $B_{start,1}$ at $\theta = 0$ so that

$$B_{\text{start},1} = \frac{B_0 + B_1}{2},$$ (5.16)

and the magnet is rotated back to $\theta = 0$. $B_{\text{start},1}$ is the maximum field at p_1 for the detection of the second channel. The magnet then rotates again, decreasing the Z field in the sample area and the new NSA corresponding to B_1 is recorded. θ_1 is the angle for which the NSA corresponding to B_1 is 0.5 and $W_{1,30-70}$ is extracted, as well as $\theta'_1 = KRV \times W_{1,0.3-0.7}$. In this simulation, the practical constraints are used, i.e. the process is iterated until either consecutive channels become less than 50 Oe apart, in which case we impose a minimum separation of 50 Oe, or B_{n+1} is outside the working range of the magnet, i.e., $B_{n+1} < B_{max}(p = 100\ mm)$. The minimum separation of $50\ Oe$ is chosen as this is of the order of magnitude of the width of the AP-P transition from an experimental SAF thin film in a rotating magnetic field (as seen in chapter 4).

A crucial element to the nullification of the drive field is the equidistance of the two inductive coils on either side of the drive magnet. In this measurement scheme, the inductive coil distances have to be set with high precision on both sides of the magnet between each measurement, which will greatly increase measurement time. An example of the NSA curves calculated using method 2 and with the same parameters as for method 1 with $KRV = 10, B_0 = 0.4\ T, OD = 6\ cm, L = 2\ cm,$ $ID = 6\ mm$ and $s_{rad} = 1\ mm$ is seen in Fig 5.23a, with the differentiated signal in Fig 5.23b. With method 2, the available number of channels is $\eta = 32$, showing a 6.4 times increase compared to method 1. We also note that the transition width $W_{0.3-0.7}$ gradually reduces throughout the series leading to sharper transitions (as seen in the differential data). The minimum separation ($50\ Oe$) is reached for channels after $n = 18, (B_n \approx 793\ Oe)$, at which point the minimum separation is assumed. The code continues iterating until the last channel is reached before the working range limit ($59.3\ Oe$). – which in this instance is equal to a channel at $\approx 93\ Oe$.
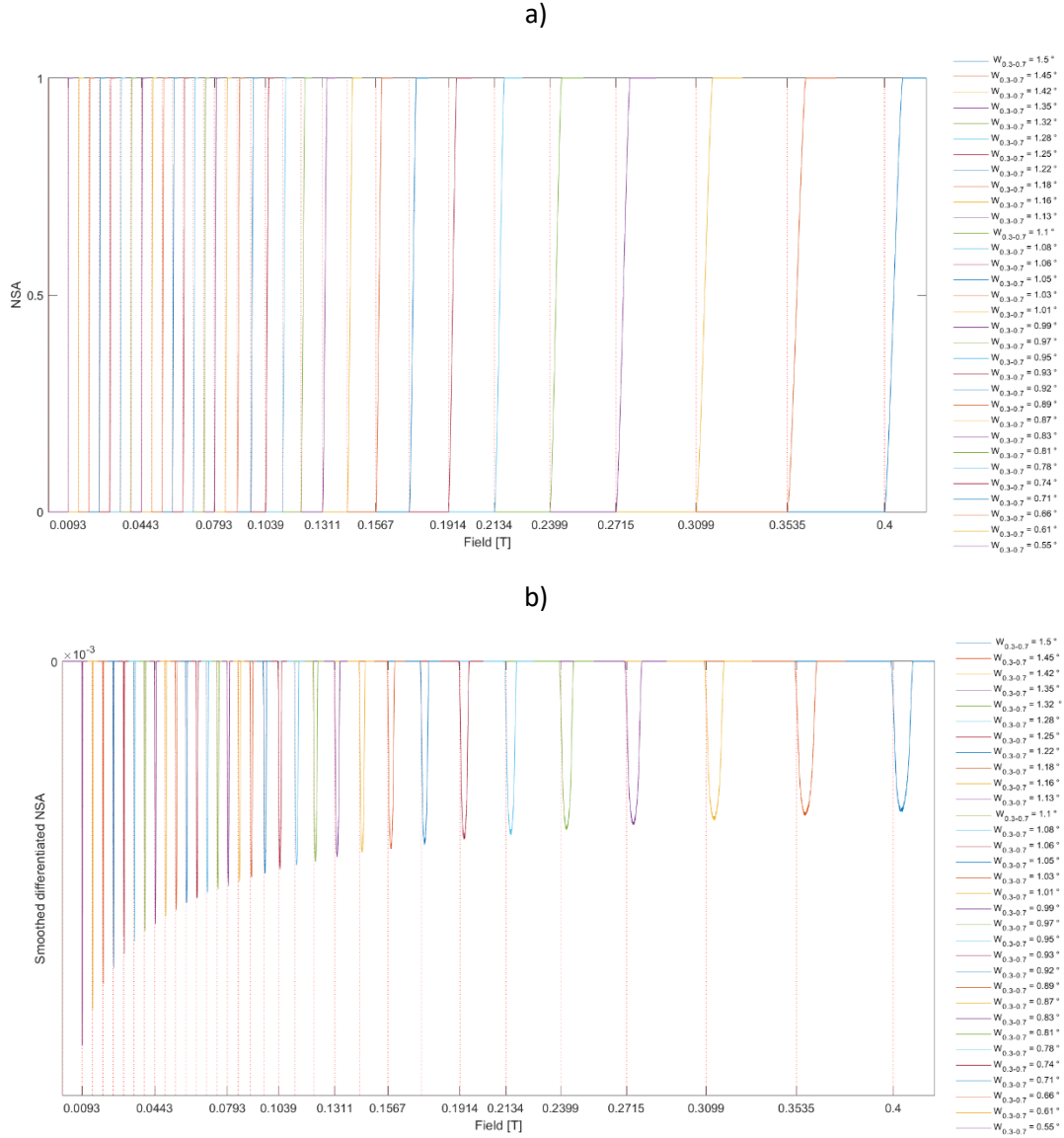
Fig 5.23 a) NSA of an ideal channel set for a measurement scheme using method 2 for the same parameters as in Fig 5.22 and b) differential signal. Method 2 assumes scheme involves adjusting the distance between the magnet surface and the sample plane (p) for each transition or channel within a single measurement set.

5.4.4. Channel progression

The increased number of channels η for method 2 is due to the progression of channel fields as the channel number n increases. If we consider all channels to have constant $W_{0.3-0.7}$ values, defining $\theta_F = W_{0.3-0.7} \cdot KRV$, we can approximate the position of the next channel as $B_n = B_{start,0} cos(\theta_0 + n \cdot KRV \cdot W_{0.3-0.7})$, where $B_{start,0} = 1.05 \times B_0$. This is shown in Fig 5.24, with an coefficient of determination, $r^2 = 1.0000$. This allows a comparison to the model's results. With $\theta_0 = 17.6\,°$, $W_{0.3-0.7} = 1.48\,°$ and a KRV of 10, these approximations yield the results seen in Fig 5.25a.

Method 2 cannot be approximated so easily, as the p value varies for each iteration, and a reducing $W_{0.3-0.7}$ is observed as n increases. Results for method 1 and method 2 can be seen in Fig 5.25a, showing that the B_n values for method 2 decrease more slowly with channel number n than the B_n

values for method 1. This is because method 2 makes use of an additional degree of freedom – the magnet to sample distance p – in order to prevent consecutive channels from bleaching.

The limited number of channels available using method 1, though using this method would be preferable in terms of ease of measurement and apparatus, has led us to pursue method 2 in the design of the detector.

In method 2, we use $B_{start,n+1} = \frac{B_n + B_{n+1}}{2}$ to calculate start field values for each new channel. It should be noted that this does not produce the largest possible η. We can improve η by using a start field that is as close as possible to the expected channel B_{n+1}. We observe that if the start field is higher, then θ_n is higher and $W_{0.3-0.7}$ is increased too, as is illustrated in Fig 5.25b for the initial channel at B_0. These data were taken for a magnet of $OD = 6\ cm$, $L = 2\ cm$, $s_{rad} = 1\ mm$ and $B_0 = 0.4\ T$, varying the start field, i.e., the value above B_0 that the simulation uses as a maximum field by adjusting p_0.
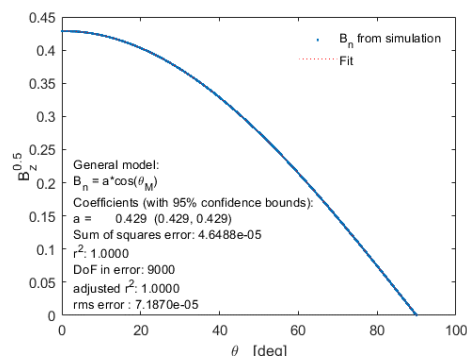
Fig 5.24 Simulation results and fit for the median field in the XY plane as θ_M increases. A pure cosine is observed.
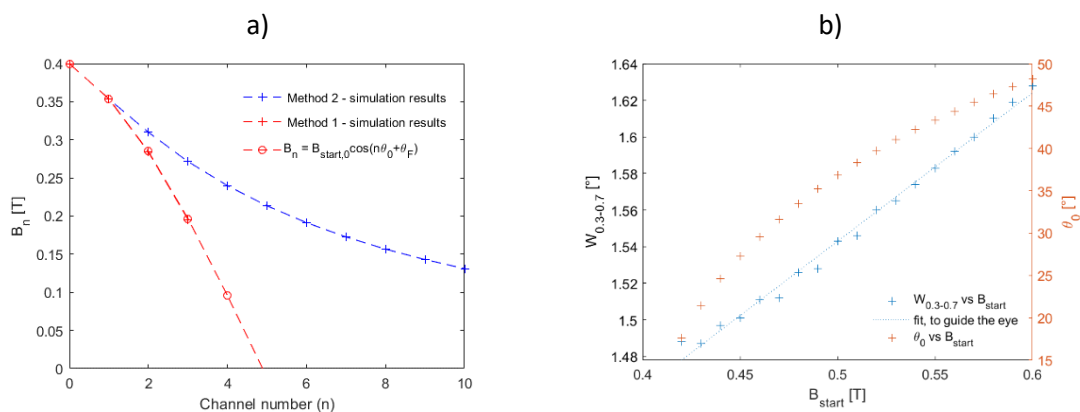
Fig 5.25) Field progression with channel number n for both measurement methods. For method 1, $\theta_0 = 17.6\ °$, $W_{0.3-0.7} = 1.48\ °$ and KRV = 10. b) $W_{0.3-0.7}$ and θ_0 for a $B_0 = 0.4\ T$ channel at various start fields. As the start field comes closer to the channel value ($B_0 = 0.4\ T$), a decrease in $W_{0.3-0.7}$ is also seen. For this reason, an increase in η can be achieved by using start values closer to the channel value.

5.5. Optimising detector specifications

Now that the structure of the code has been presented, we can optimise the geometry of the device. Our key metric to assess its performance is the number of available channels η, which is dependent on the $W_{0.3-0.7}$ deduced from the $NSA(\theta_M)$ profile. The NSA is a measure of how fast a line of equal field progresses across the sample area as θ_M varies. As such, any changes to a parameter that affects the NSA will change the efficacy of the device: if the NSA transition is sharper, $W_{0.3-0.7}$ is lower and more channels will be able to be defined and η will increase.

We begin by evaluating η with the simple constraints presented in section 5.4 (a minimum channel field value of 25 Oe only). This allows us to understand how changing magnet dimensions affects the total channel number, and why. We then reintroduce the practical constraints to provide more realistic η values.

5.5.1. Magnet length

In this study, we look at the effect of changing the length of the cylindrical drive magnet, L. All other simulation inputs remain constant and are chosen to be $OD = 4\ cm, B_0 = 0.4\ T, KRV = 5, ID = 6\ mm$ and $s_{rad} = 1$. We sample 81 values of L from $2\ cm$ to 10 at $1\ mm$ intervals and with $dx = dy = 40\ \mu m$. The results of this study are seen in Fig 5.26. We observe a monotonic increase of possible channel number η with increasing L.
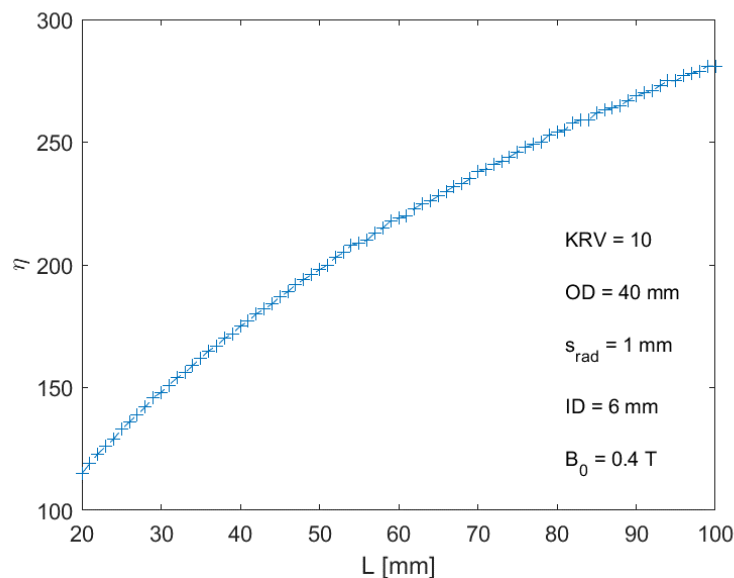
Fig 5.26 Results for a simulation evaluating the number of possible channels for a changing L.

Higher η is achieved if the transition width W_{30-70} is smaller; we suggest that the transition width is mainly affected by two factors:

- The homogeneity of the field B_z in the sample area: If the field is more homogenous across the sample area, it requires a smaller θ_M change for the entire area to drop below the switching field – decreasing the transition width.

- The angular variation of the field $\left(\dfrac{dB_z}{d\theta_M}\right)$ in the sample area: A higher angular variation will cause the entire sample to transition more quickly.

We investigate how the homogeneity of the field profile changes for different L. First, we must understand the origin of the additional channels. This is completed by an assessment of the channel distribution. For this, histograms showing the number of channels present in a given field interval (bin size) are calculated. We use $L = 2\ cm$ as a reference, as it has the lowest η. The histogram data for $L = 2\ cm$ with a bin size of 50, and 12.5 Oe is shown in Fig 5.27a and b, respectively. The latter is shown, as it illustrates how no channels are produced in the final two bins, evidencing the stop condition at the minimum channel field (25 Oe). The increase in the number of channels in each histogram bin is calculated with respect to $L = 2\ cm$ and is shown in Fig 5.28. Here, it is clear that the increase in η originates from a larger amount of channels at low channel field values, with the majority of the changes occurring at fields $< 500\ Oe$.
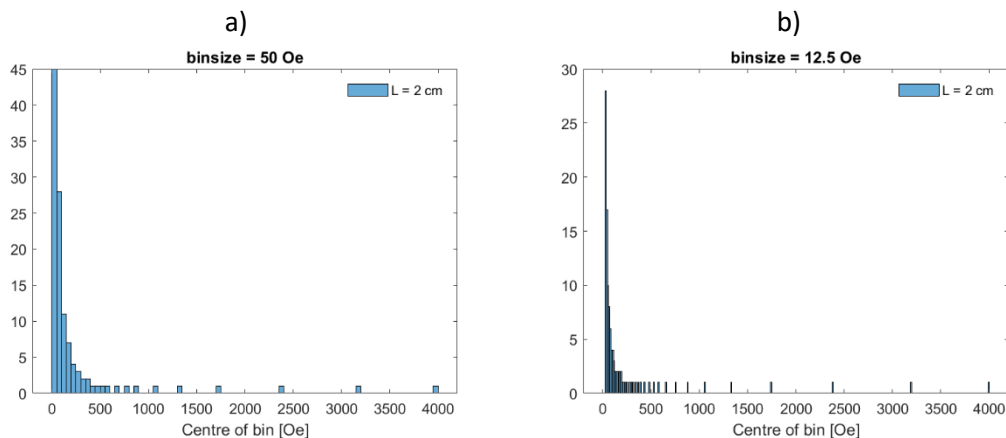
Fig 5.27 Histogram showing the distribution of channels for L = 2 cm with a binsize of a) 50 Oe, b) 12.5 Oe.
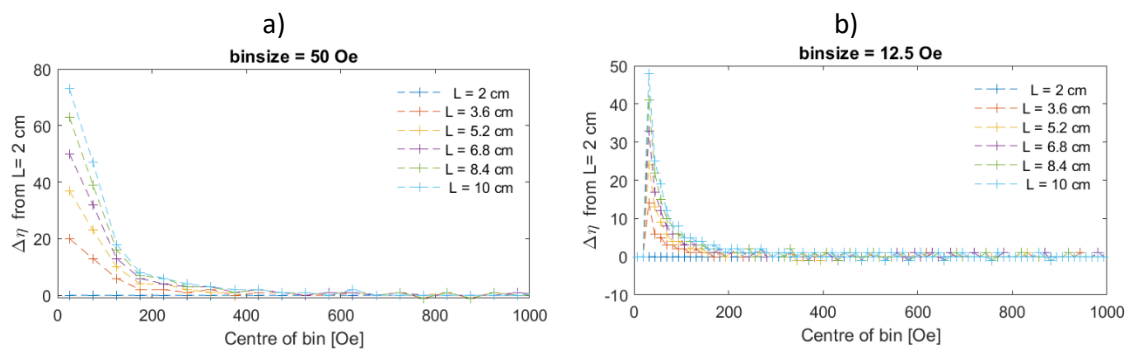
Fig 5.28 Changes in the number of channels in each bin for different L values, calculated with a bin size of 50 Oe (a) and 12.5 Oe (b). Here, we note that the greatest increase in channels is produced at low channel fields.

In order to understand the reason for the increase in η with L, we first assess the field homogeneity at $500\ Oe$, or smaller. We confirm the homogeneity improvement quantitatively by calculating the field maps for different L values at $NSA = 0.5$ and $B_0 = 500\ Oe$. These are shown in Fig 5.29 a) - c) for magnets of $L\ =\ 2, 6$ and $10\ cm$. Fig 5.29 d-f) show corresponding line scans across $X = 0$ and $Y = 0$. These confirm that the field maps are largely independent of Y. The range of B_z across $Y = 0$ is plotted as a function of L in Fig 5.30 a), showing a monotonous decrease with L and confirming the increased homogeneity as L increases. We can also calculate the angular variation $\frac{dB_z}{d\theta_M}$ of B_z at the transition, by taking the difference between the field map at the transition, and the field map one degree before the transition. The $\frac{dB_z}{d\theta_M}$ maps are shown in Fig 5.29 g-i) for $L =\ 2, 6$ and $10\ cm$. These are also largely independent of Y across our sample area. The mean value of $\frac{dB_z}{d\theta_M}$ across X for $Y\ =\ 0$ at the centre of the transition is plotted as a function of L in Fig 5.30c. This shows that the mean value of $\frac{dB_z}{d\theta_M}$ does not change significantly with L. The steady decrease of the B_z range and the relatively constant angular variation of B_z with increasing L confirm that the increase of η with L is indeed due to an increase in field homogeneity with L, across the X direction.
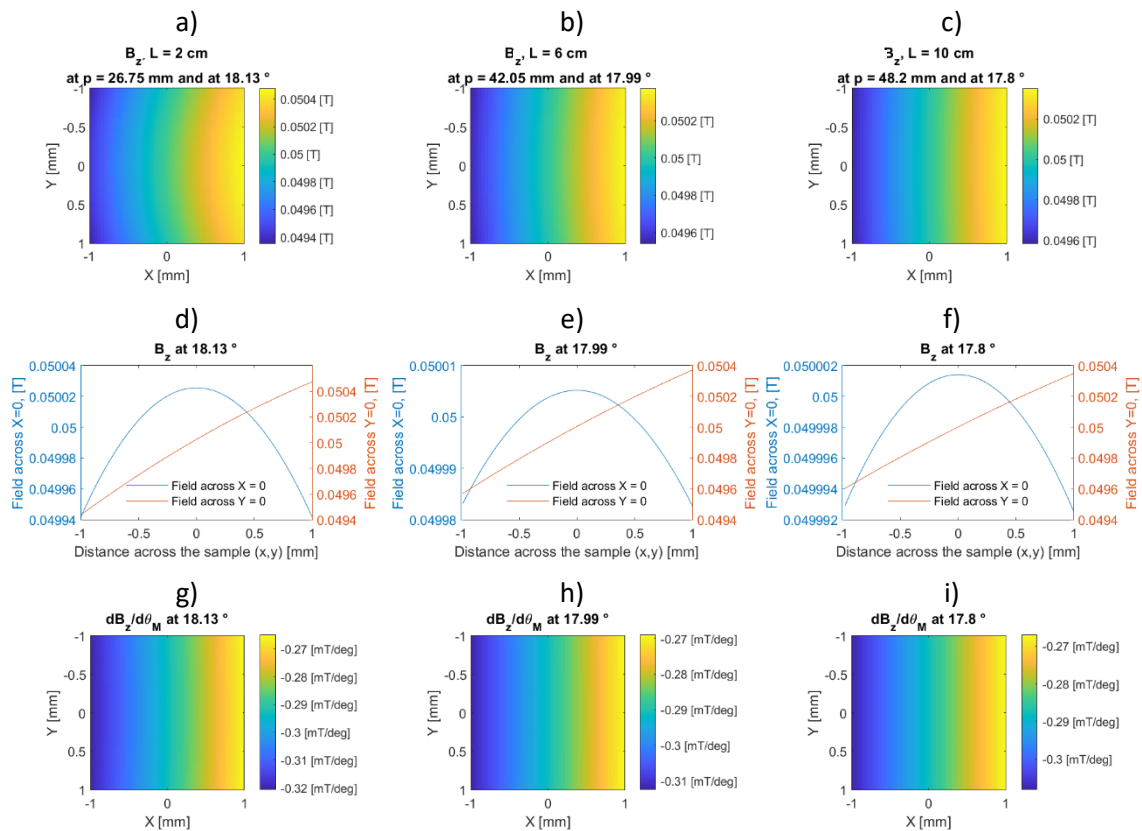
Fig 5.29 a,b,c) Field profiles from a toroidal magnet of OD = 4 cm, ID = 6mm and varying L at the transition where $B_0 = 500\ Oe$. d,e,f). B_z line profiles across Y = 0 and X = 0, showing the range g,h,i). angular variation across the transition at NSA = 0.5.
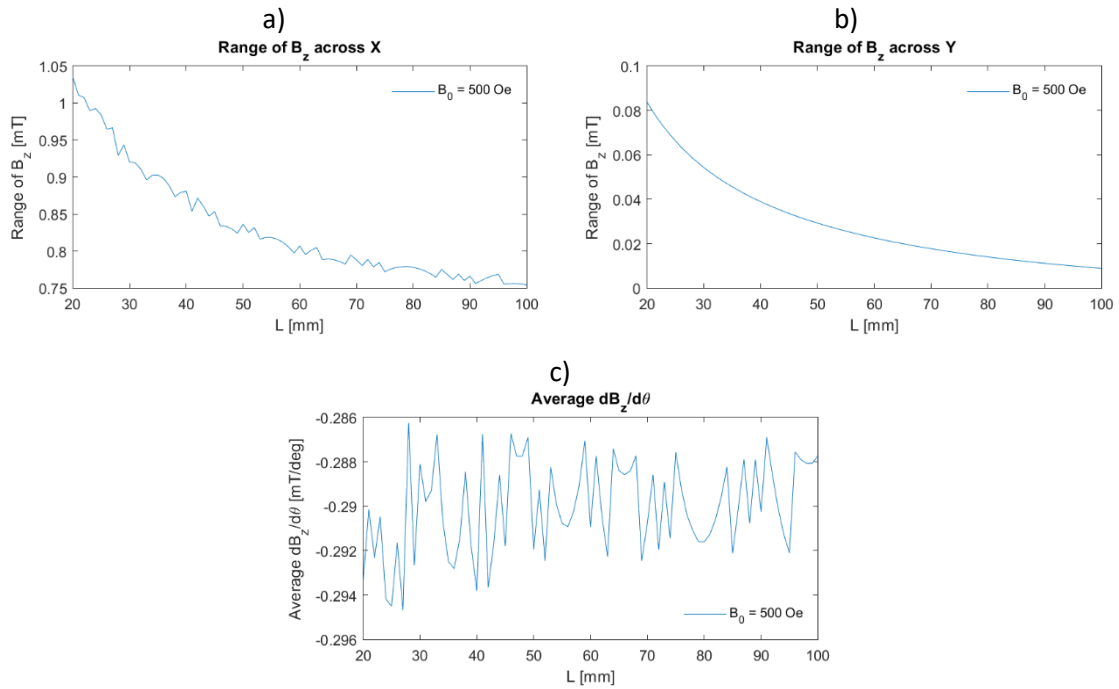
Fig 5.30 Range in the field B_z across a) X and b) Y respectively from a toroidal magnet of OD = 4 cm, ID = 6 mm and varying L, giving a quantitative evaluation of spatial homogeneity for a transition at 500 Oe. c) mean of the angular variation across the sample plane – taken as the difference between NSA = 0.5 and 1 [deg] before.
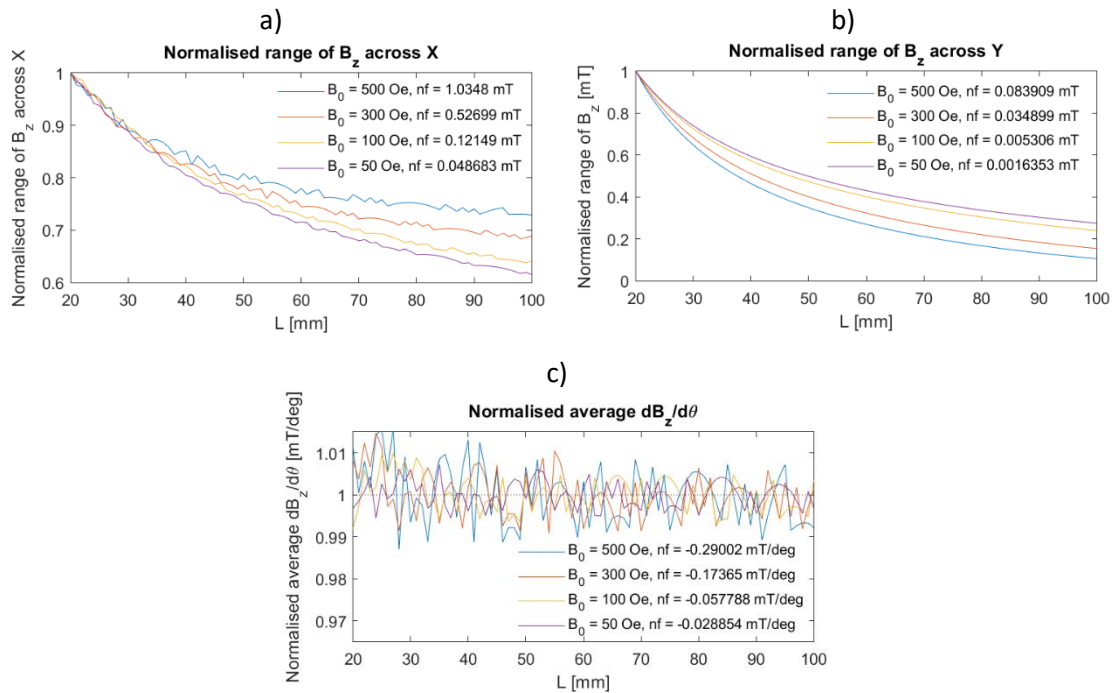
Fig 5.31 Normalised range of B_z along X (a), Y (b) and normalised average $dB_z/d\theta$ as a function of L and for various B_0 values. Here, the normalising factors (nf) are shown in the inset.

We confirm that these results are representative of all fields below 500 Oe. Fig 5.31 a and b show the ranges of B_z across X and Y as a function of L and for different values of B_0 below 500 Oe, normalised by the range value at $L = 2\ cm$ (the normalisation factor (nf) is indicated in the inset of the figure). These show that B_z is systematically more homogeneous as L increases, giving us

confidence that the results shown above are representative for channel fields less than $500\ Oe$, where most of the channels are present. We confirm that there is little change in $dB_z/d\theta$ in Fig 5.31c. Here, the results are normalised by the average value in the series. The results from this section show that we can achieve larger η by using a magnet of larger L.

5.5.2. Outer diameter

In this study, we look at the effect of changing the outer diameter OD of the cylindrical drive magnet on the number of available channels η. All other input parameters remain constant and are chosen to be $L = 4\ cm$, $B_0 = 0.4\ T$, $ID = 6\ mm$ and $KRV = 10$. We sample 81 values of OD from $2\ cm$ to $10\ cm$ at $1\ mm$ intervals. The sample area is made of a circular mask of radius $s_{rad} = 1\ mm$ and with resolution $dx = dy = 40\ \mu m$. The results of this study are seen in Fig 5.32
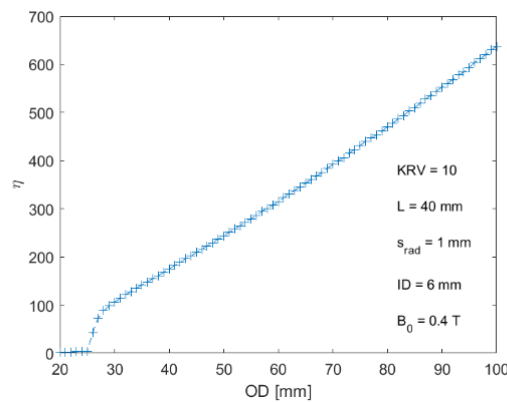
Fig 5.32 number of possible channels, η, as a function of magnet outer diameter OD. The other input parameters are shown in the inset.

We observe a monotonic increase of η with OD. As in the previous section, we first assess where the improvement in η arises. Fig 5.33 is a histogram showing the increase in channel number as a function of field and for various OD at two bin sizes: 50 Oe and 12.5 Oe. The results are presented with respect to the value at $OD = 2\ cm$. Note, as $OD = 2\ cm$ only has 2 channels, these plots roughly show the full bin populations. We again observe that the increase in η arises from channels at $< 500\ Oe$.
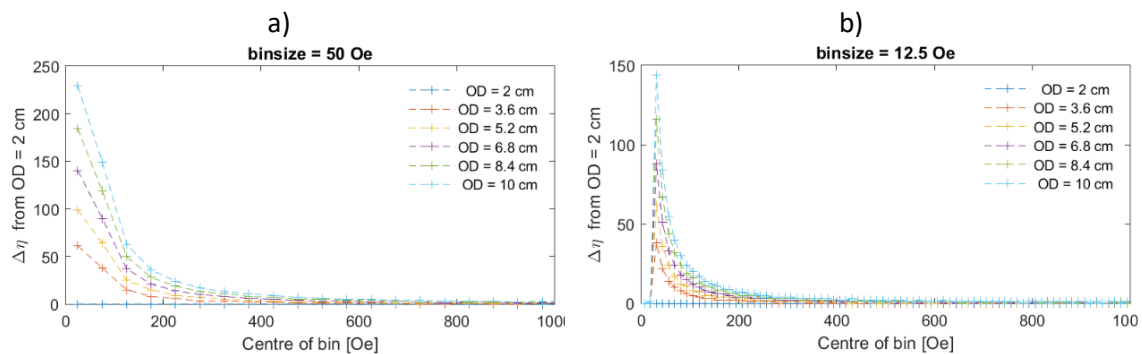
Fig 5.33 Changes in the number of channels in each bin, for differing OD. These have a bin size of a) 50 [Oe] and b) 12.5 [Oe], respectively.

The homogeneity is assessed from the field maps. The field profiles at the angle where $NSA = 0.5$ for a $B_0 = 500\ Oe$ are shown for different OD values in Fig 5.34 a-c) with the B_z field across $X = 0$ and $Y = 0$ in d-f) and the $dB_z/d\theta_M$ in g-i). The B_z range across X (where $Y = 0$) and across Y (where $X = 0$) is presented in Fig 5.35 a and b respectively for varying magnet OD. A reduction mean angular change is roughly constant, as seen in Fig 5.35c. From these results, we can again confirm that the spatial variation in the B_z field across X has the highest influence on the number of channels η.
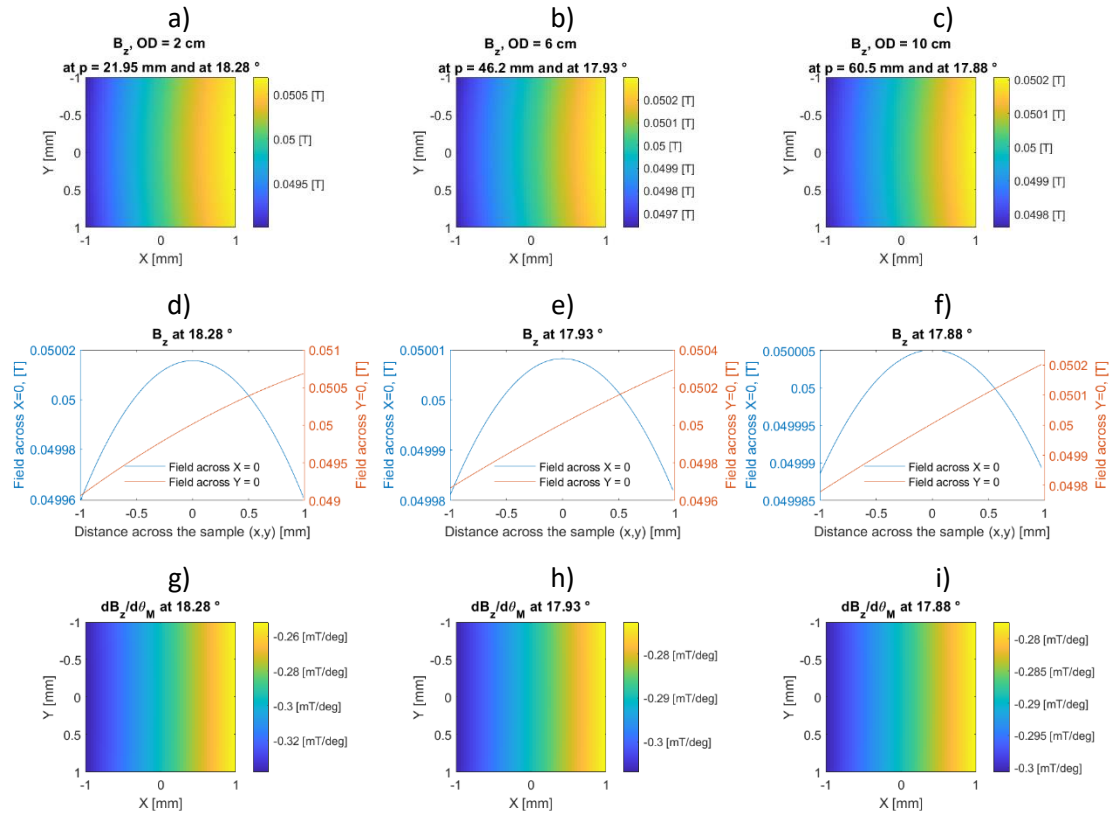
Fig 5.34 a,b,c) Field profiles from a toroidal magnet of L = 4 cm, ID = 6mm and varying OD at the transition transition where $B_0 = 500$ Oe. d,e,f). B_z line profiles across Y = 0 and X = 0, showing the range g,h,i). angular variation across the transition at NSA = 0.5.

To gain confidence that these results are representative of all fields less than 500 Oe, we again evaluate the homogeneity for different B_0. Fig 5.36 a and b show the ranges of B_z across X and Y as a function of OD and for different values of B_0 below 500 Oe, normalised by the range value at $OD = 2\ cm$. These show that B_z is systematically more homogeneous as OD increases, giving us confidence that the results shown above are representative for channel fields less than $500\ Oe$. We again confirm that there is little change in $dB_z/d\theta$ in Fig 5.36c.
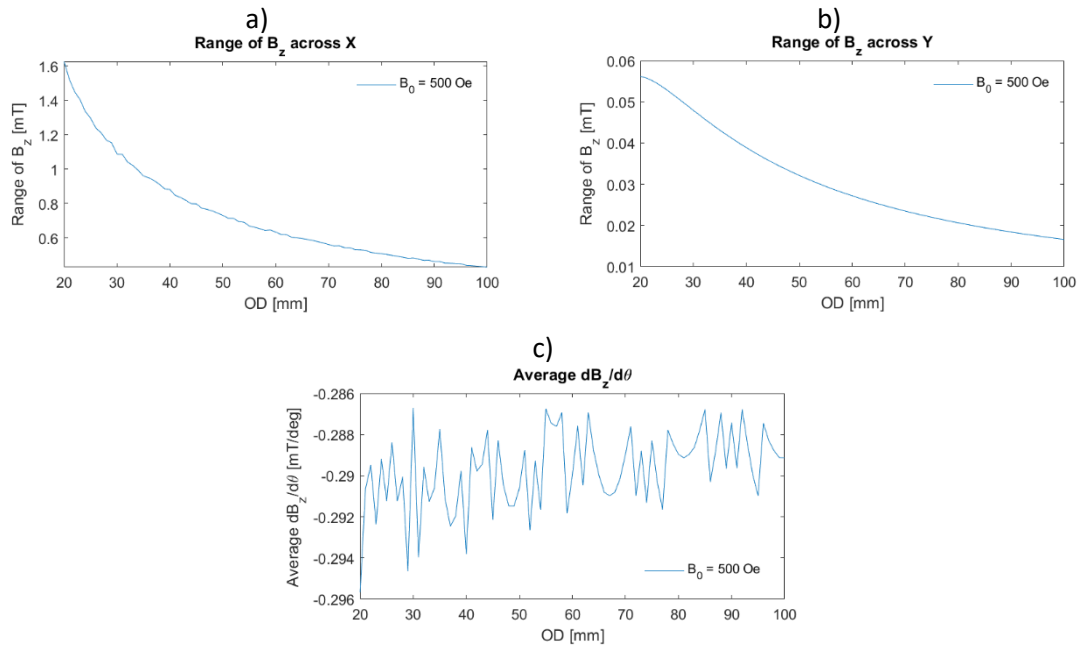
Fig 5.35 a,b) Range in B_z across a) X and b) Y respectively from a toroidal magnet of L = 4 cm, ID = 6 mm and varying OD, giving a quantitative evaluation of spatial homogeneity for a transition at 500 Oe. c) mean of the angular variation across the sample plane – taken as the difference between NSA = 0.5 and 1°before.
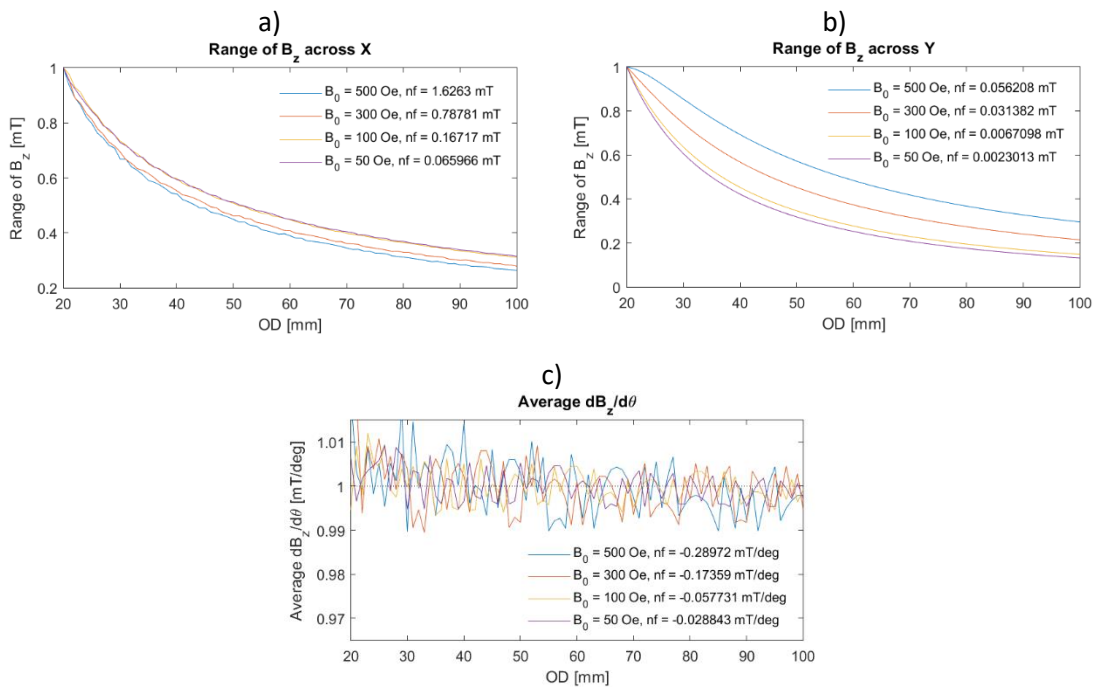
Fig 5.36 Normalised range of B_z along X (a), Y (b) and normalised average $dB_z/d\theta$ (c) as a function of OD and for various B_0 values. Here, the normalising factors (nf) are shown in the inset.

The scale invariance of magnetic fields can be used to understand the results of these OD studies. Scale invariance means that, if all parameters are scaled by a factor k, we should observe the same field profile within the scaled sample area. This idea is seen schematically in Fig 5.37.
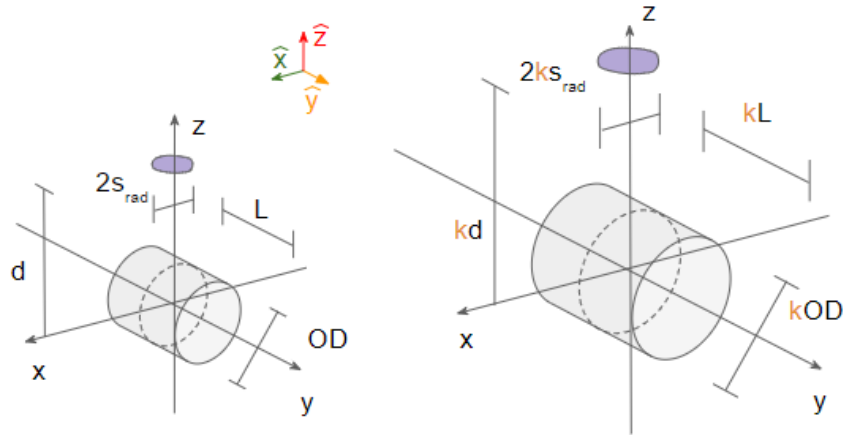
Fig 5.37 A schematic to describe the scale invariance of magnetic fields.

Though in our system we are not scaling all dimensions by the same factor, we can use the concept to understand how the field homogeneity may improve at higher OD. In a scale-invariant system, OD, L, p and s_{rad} ought to be scaled by the same factor k. In our case, the distance $\left(p(B_0)\right)$ at which a field of a particular value B_0 is found follows the curve presented in Fig 5.38: as the OD is multiplied by 5 to go from 20 mm to 100 mm, p is multiplied by 4.2 (from 2.5 mm to 10.5 mm). The two factors being different reflects the fact that the magnet length L is kept constant, and owe are not considering a proper scaling transformation. However, the two scale factors are very close, suggesting that L is not a crucial parameter here. If we did a proper scaling transformation, the field map for $k \cdot OD$, $k \cdot p$ away from the magnet surface and across a disk of radius $k \cdot s_{rad}$ would be the same as the field map for OD, p away and across a disk of radius s_{rad}. For the scaled-up system, a disk of radius s_{rad} only probes the central part of the scale-invariant field map, which is obviously the same or more homogeneous than the full field map, leading to a higher η value as OD increases. This model is not applicable to models of changing L, as near linearity is not observed as only one-dimension changes.
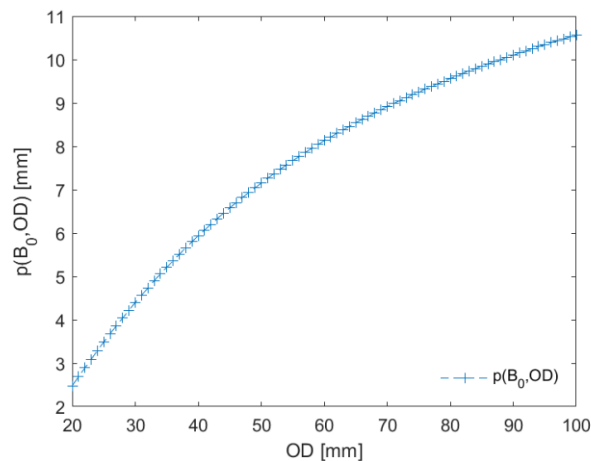
Fig 5.38 $p(B_0)$ relationship for changing OD. Though we keep L constant at $L = 4\ cm$, the near-linear relationship here validates our use of the scale invariance of magnetic fields to consider homogeneity.

The results from this section show that we should increase the OD as much as practicable for our detector, as the field profile over the sample area becomes more homogenous. Though we must also consider the practicality of rotating a larger magnet – both in terms of motor requirements and stray magnetic fields. A larger permanent magnet will have a slower decay of field strength (smaller $\frac{dB}{dZ}$), meaning that larger fields are applied to surrounding material for the same nominal separation.

5.5.3. Suppressing unrealistic outputs

We have seen that an increase in OD or L improves the average homogeneity of the field profile throughout a series of channels and improves the number of possible channels η. In the results shown previously, we observe extremely high η; up to 281 in L studies and up to 637 in OD studies. In these series, the first channel is always B_0, which in these simulations was equal to $0.4\ T$. It is obvious that if >600 channels are possible between $2.5 - 400\ mT$, the separation must be extremely small, with $\sim 0.6\ mT$ average separation. The channel switching field progressions and separations for the first 50 channels in series for changing OD and L are shown in Fig 5.39.
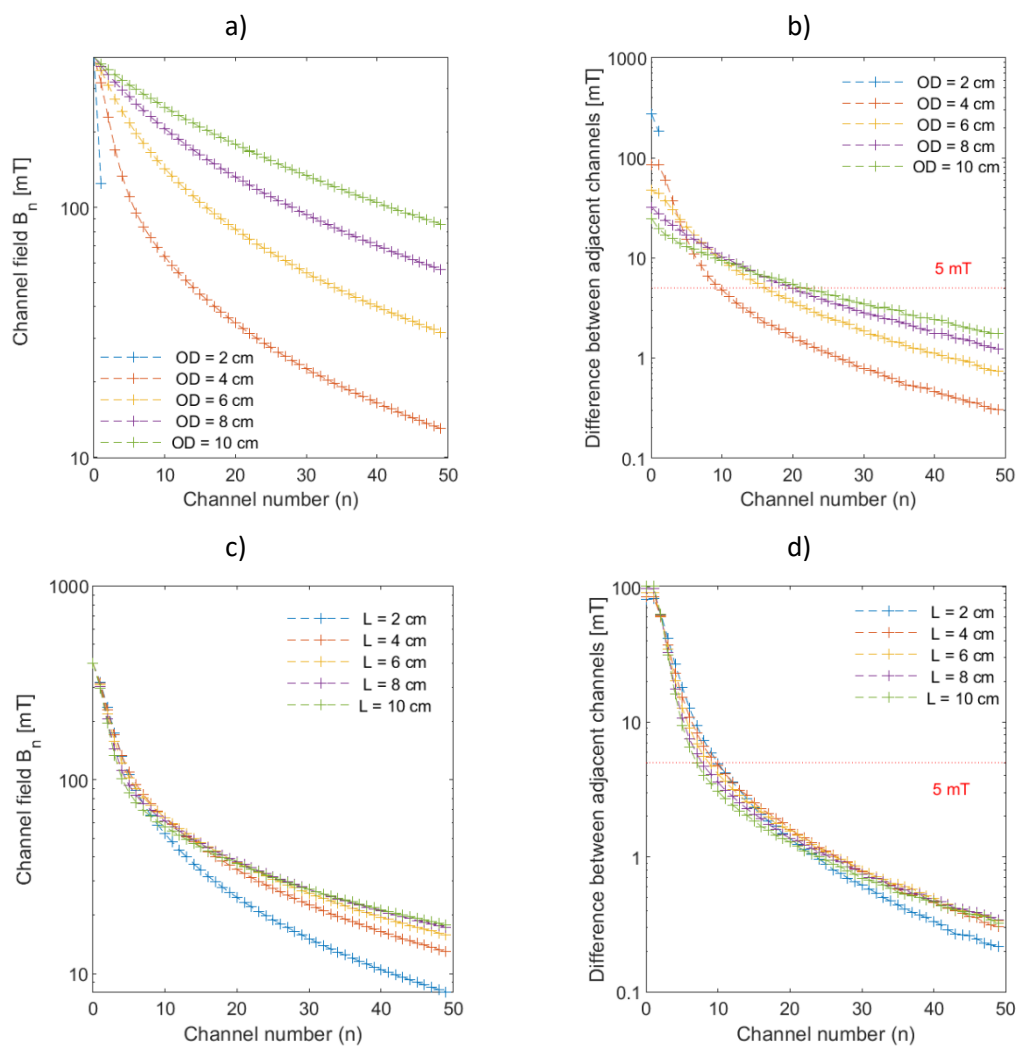
Fig 5.39 Channel switching fields and separations for the first 50 channels in a series for a,b) changing OD and c,d) changing L.

In section 5.4, we discussed sensible constraints to our series:

- We cannot reliably fabricate particles with switching field separations of less than $5\ mT$. For this reason, a minimum separation is imposed. If the next ideal channel falls within the minimum separation, the minimum separation is used instead.

- The device will have a finite working range – the distance the detection coils are able to move. We consider $p_{max} = 10\ cm$ to be appropriate. For this reason, a maximum distance between sample and magnet is imposed. The series ends when the maximum distance is reached.

By imposing these two practical constraints, we suppress some simulation outputs but provide more realistic values of η. Simulations identical to those in Fig 5.32 and Fig 5.26 were run using the practical constraints, with the results seen in Fig 5.40.
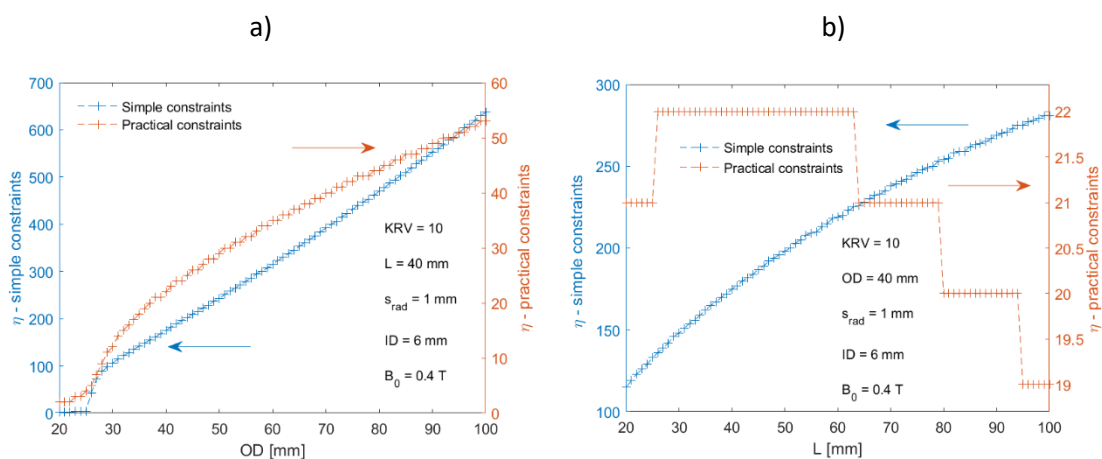
Fig 5.40 A comparison of the number of channels, η, for both the simulation using simple constraints (left scale) and the simulation using practical constraints (where $p < 10\ cm$ and $B_{n+1} - B_n > 5\ mT$) (right scale) with a) changing OD, b) changing L.

When changing OD, we observe a similar trend in both the simulation using simple constraints and the simulation using practical constraints – a monotonic increase in η for increasing OD. As expected, we see a large reduction in η when limiting p and ΔB – with a maximum of 53 channels for the largest OD.

Differing results are seen for simulations with changing L. When simple constraints are used, a monotonic increase in η for increasing L is observed. When p and ΔB are limited in a simulation with practical constraints, a monotonic increase is no longer seen. Instead, we observe an increase in η followed by a decrease as L increases beyond $L \approx 60\ mm$. Changes in η due to variation in L are

much less severe than in the case of changes in OD, with η changing by three across the full range of length (compared with ~ 50 for OD).

We compared the number of possible channels for a 2D matrix of OD and L values for a simulation using the practical constraints; the results are seen in Fig 5.41a. When L is increased, η first increases and then decreases. This leads to an optimum L for each OD. For example, with $OD = 10\ cm$, the η is highest when $L \approx 4.25\ cm$. The maximum η for any given OD, as well as the L to produce the maximum η is given in Fig 5.41b. In this plot, the error bars show the range where the maximum η is achieved. This confirms the initial increase, and then decrease in the optimal L, as OD increases. Fig 5.41 also shows that the magnet length is of much less importance than the magnet OD.
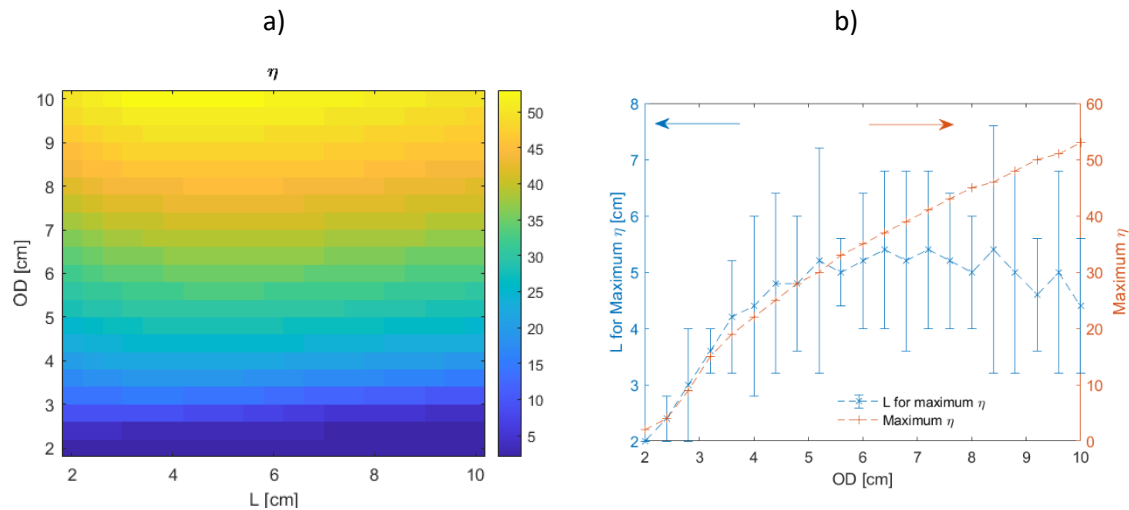
Fig 5.41 a) The number of available channels, η, for a 2D array of OD and L values. b) L for maximum η values, and maximum η for a given OD.

5.5.4. Sample area size

Now that the drive magnet has been optimised, it is important to examine the other elements of the detector, starting with the sample area. The sample area is a disk of radius s_{rad}. When s_{rad} is changing, the field profile at the sample plane remains unchanged since the magnet geometry and sample plane to magnet distance p remain the same. As s_{rad} decreases, however, a smaller, more central portion of the field profile is probed, leading to a more homogeneous field profile. In turn, this leads to sharper transitions and a higher number of channels η. We have verified this with simulations. All other inputs remain constant and are chosen to be $OD = L = 4\ cm$, $B_0 = 0.4\ T$, $ID = 6\ mm$ and $KRV = 10$. We sample 27 values of s_{rad} from $0.35\ mm$ to $1\ mm$ at $0.025\ mm$ intervals. We tested the results for two different resolutions (cell size $\Delta x = \Delta y = 40\ \mu m$ and $\Delta x = \Delta y = 20\ \mu m$) with identical results, showing that the cell size is small enough for accurate results at all s_{rad} values studied. The results of this study are seen in Fig 5.42 a), for both a simulation using

simple constraints and a simulation using practical constraints: the number of channels η indeed decreases as the sample area radius s_{rad} increases.

We show that increasing s_{rad} also has the expected effect on $W_{0.3-0.7}$. In Fig 5.42b, we show $W_{0.3-0.7}$ vs s_{rad} for a few channels in the series. $W_{0.3-0.7}$ indeed decreases as s_{rad} increases. These findings suggest that a sample area that is as small as possible should be used, though this must be weighed against a lower number of particles present in the sample area (and therefore a lower signal strength) when s_{rad} decreases.

a) b)
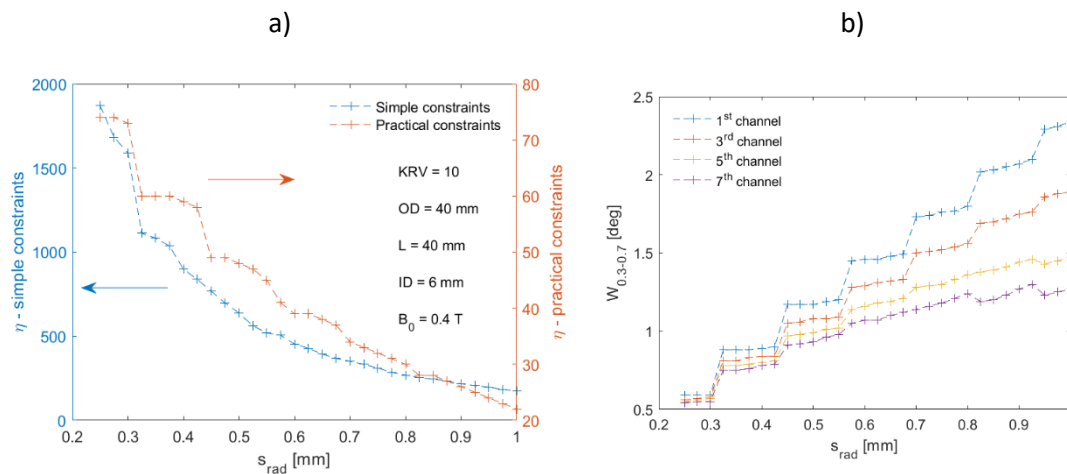
Fig 5.42 a) Results of the simulations evaluating the number of possible channels for a changing s_{rad}. b) $W_{0.3-0.7}$ versus s_{rad}. $W_{0.3-0.7}$ is plotted for the 1st, 3rd, 5th and 7th channels in the simulation using practical constraints.

5.5.5. Start field

We can also study the influence of the starting channel B_0, defined as the highest used channel magnetic field value. Again, all other simulation inputs remain constant and are chosen to be $OD = L = 4\ cm$, $s_{rad} = 1\ mm$, $ID = 6\ mm$ and $KRV = 10$. We sample 51 values of B_0 from $0.1\ T$ to $0.6\ T$ at $0.01\ T$ intervals. The results of this study are seen in Fig 5.43a for both a simulation using simple constraints and a simulation using practical constraints. We observe an increase in the number of possible channels up to $0.3\ T$, after which no benefit is seen, with a decrease in η at high values. As shown in Fig 5.43b, series with lower start fields have consistently lower $W_{0.3-0.7}$ values, but a more limited range of measurement. The number of channels that will ultimately fit in a given field range is a compromise between these two effects. At low start field/channel field, $W_{0.3-0.7}$ is small, so the channel density is high, but the range is limited. The average separation, which is the inverse of channel density, is plotted for each B_0 in Fig 5.44.
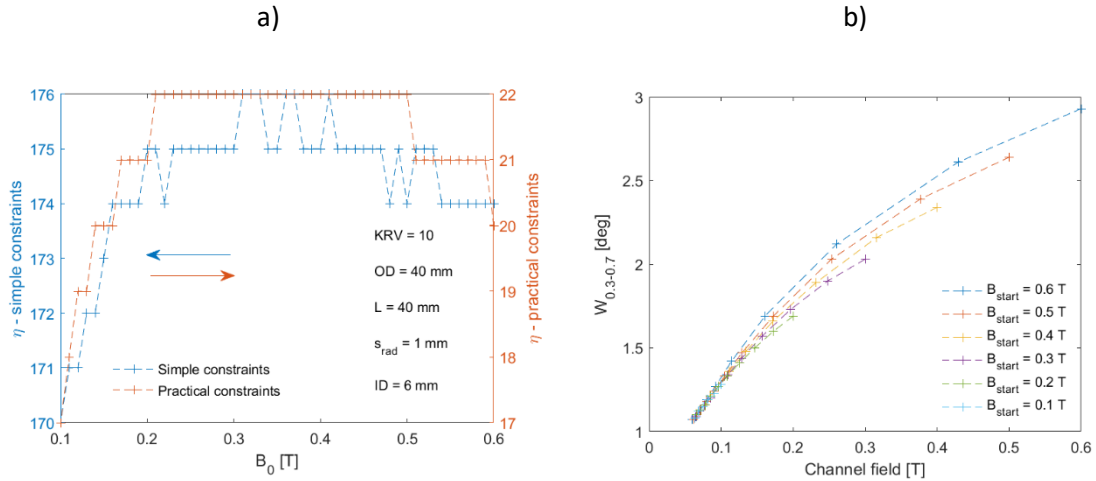
Fig 5.43 a) Results for a simulation evaluating the number of possible channels for a changing start channel B_0 b) $W_{0.3-0.7}$ versus channel field for a series with different start field values in the simulation using practical constraints.
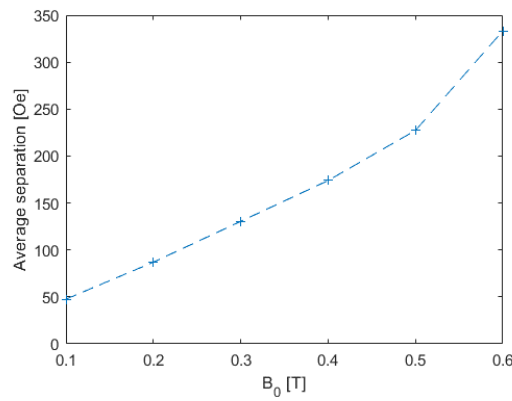
Fig 5.44 Average field separation of channels within a series for differing start field B_0 in the sinulation using practical constraints. This is the inverse of channel density and shows that smaller start fields have series with a much higher channel density.

This shows that for this magnet geometry, a start field above $0.3\ T$ is most beneficial. This was confirmed for a small range of additional OD and L values, consistently showing no benefit above $0.3\ T$. Though there is no increase in the number of possible channels above $B_0 = 0.3\ T$, we may choose to use higher values as they allow a larger particle fabrication range at no expense to the number of possible channels. An increase in B_0 between 0.3 and 0.5 T allows for the same number of channels but at a larger absolute separation, which, because of the finite Pt growth resolution, would mean that particles are easier to fabricate.

5.5.6. KRV

All of the results in this section have maintained the same degree of stringency in their KRV – keeping a value of 10. Increasing KRV will obviously decrease η, as it forces a larger and larger separation between consecutive channels. However, it is also beneficial to understand how many channels we could expect for different levels of stringency. As a reminder, the KRV defines the distance between adjacent channels in terms of multiples of $W_{0.3-0.7}$:

$$KRV = \frac{W_{0.3-0.7}[°]}{nearest\ neighbour\ separation\ [°]}. \qquad (5.17)$$

As previously, we calculate η for an evenly spaced array of KRV values, and all other simulation inputs remain constant. They are chosen to be $OD = 6\ cm, L = 4\ cm, s_{rad} = 1\ mm, ID = 6\ mm$ and $B_0 = 0.4\ T$. We sample 33 values of KRV from 3 to 35 at integer intervals, and practical constraints are used. The results of this study are seen in Fig 5.45. We observe a rapid decay as KRV is increased. For these particular parameters, the device cannot accommodate more than a single channel for any KRV higher than 30. This is understandable, as for values this large, the $W_{0.3-0.7}$ must be extremely small.
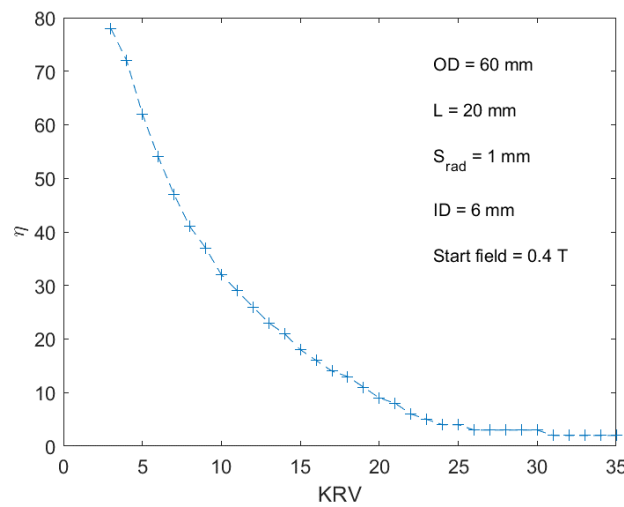
Fig 5.45 Results for a simulation evaluating the number of possible channels for a changing KRV.

5.5.7. Minimum field separation

We can similarly evaluate the effect of the minimum field separation between consecutive channels. When a realistic minimum separation was applied in this section we have used a value of $50\ [Oe]$. It is quite obvious that limiting the distance between consecutive channels to a smaller and smaller value will allow a larger and larger number of channels to exist. By quantitatively establishing the effect of the minimum separation, we can understand more precisely how improving particle fabrication will affect the efficacy of the device.

The results for a magnet of $OD = 60\ mm, L = 20\ mm$ and $ID = 6\ mm$, with $s_{rad} = 1\ mm$, a KRV of 10 and $B_0 = 0.4\ T$ can be seen in Fig 5.46 for a simulation using practical constraints. Rapid decay of η is indeed again observed as the minimum separation increases. This shows how good fabrication is crucial to the efficacy of our system.
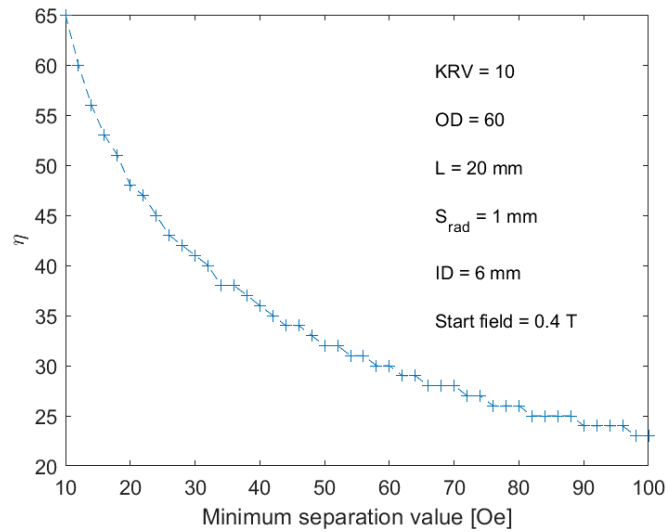
Fig 5.46 Results for a simulation evaluating the number of possible channels for a changing minimum separation.

5.6.   Chapter summary

This section outlines the design of a device able to detect the switching of SAF particles via an inductive detector and activated using a rotating permanent magnet producing a sinusoidal drive field component perpendicular to the sample plane. Numerical simulations were performed in order to assess the viability of such a device as well as optimise it. The cylindrical nature of the drive magnet allowed for the use of an exact analytical cylindrical field calculation [1]. The simulated magnetic fields of superposed cylinders with magnetisation at any angle in the XZ plane have been validated against Mumax to ensure their accuracy. Our calculated field results show convergence as cell size decreases, with Mumax approaching the analytical values.

These fields were used to simulate the switching of an assembly of SAF particles distributed over a sample area as a function of permanent magnet angle (θ_M). The Normalised Switched Area (NSA) was defined, which allowed the characterisation of the transition, and in particular its width ($W_{0.3-0.7}$). We then assessed the progression of switching fields for an ideal parameter set, given a separation relative to their $W_{0.3-0.7}$. The number of possible channels η provided a figure of merit that allowed us to assess the efficacy of our device for different input geometries and different detection methods.

Using our figure of merit η, we first tested whether it was more effective to measure all channels at one distance from the magnet surface (method 1) or to vary the magnet to sample distance p for each new channel (method 2). The results were strongly in favour of using method 2, with a 6.4 times increase in the number of possible channels for the given geometry.

Next, we assessed the figure of merit η for various changes to the input geometry. We suggested that any changes to the device that increased homogeneity, or the angular variation in the field

would lead to smaller transition widths ($W_{0.3-0.7}$) and higher η. This was first tested for a simulation using simple constraints, with a minimum channel field of 25 Oe but no working range limit or minimum separation. In these simulations using simple constraints, larger magnet diameters or magnet lengths produced larger η values, with improved average homogeneity throughout the series. These series led to an unachievably small separation between channels. For this reason, we repeated the simulations with the addition of practical constraints, consisting of a minimum separation between channels of $50\ Oe$, and a stop condition when a $p = 10\ cm$ working range for the detector was exceeded. In these simulations, increasing OD produced more homogenous fields, monotonically increasing η, whereas increasing L showed a parabolic relationship with η, first increasing the number of channels and then decreasing it. For this reason, we propose that a drive magnet with a large OD, and small L is used – e.g. $OD = 6\ cm$ and $L = 2\ cm$. This also increases the rotational stability of the drive magnet, as more mass is added away from the rotation axis.

We next observed an increasing channel number as the sample radius decreases. This is expected, as a smaller, more homogenous region of the field profile is sampled for smaller s_{rad}. This is confirmed by the analysis of transition widths for varying s_{rad} for different channel number n. We see that smaller s_{rad} have systematically smaller transition widths and secondly, that transition width decreases throughout a series (with increasing n).

For changing start field, we observed increasing η with increasing start channel value B_0 up to $B_0 = 0.3\ T$. This suggests that a starting channel $B_0 = 0.3\ T$ is sufficient, though there is no detrimental effect of higher values which allow for easier fabrication.

We lastly looked at the effect of different stringency levels by examining η for various KRV and minimum separation values. These plots can be used to show the highest separation for an ideal set of particles consisting of n different channels.

Though these results are indicative of the behaviour of our device, we must note that they use an idealised transition. Particles with instant switching events are impossible to fabricate, and the effects of imperfect fabrication must be considered to obtain more realistic values. In the following chapter, we assess the impact of these effects by considering particles with finite switching widths within the simulation.

[1]   A. Caciagli, R. J. Baars, A. P. Philipse, and B. W. M. Kuipers, "Exact expression for the magnetic field of a finite cylinder with arbitrary uniform magnetization," *J. Magn. Magn. Mater.*, vol. 456, pp. 423–432, Jun. 2018, doi: 10.1016/j.jmmm.2018.02.003.

[2]   D. Fleisch, *A Student's Guide to Maxwell's Equations*. Cambridge University Press, 2008.

[3]   A. Vansteenkiste, J. Leliaert, M. Dvornik, M. Helsen, F. Garcia-Sanchez, and B. Van Waeyenberge, "The design and verification of MuMax3," *AIP Adv.*, vol. 4, no. 10, p. 107133, 2014, doi: 10.1063/1.4899186.

[4]   K. Wang, Y. Huang, R. Chen, and Z. Xu, "Investigation of magnetic properties in thick CoFeB alloy films for controllable anisotropy," *Appl. Phys. A Mater. Sci. Process.*, vol. 122, no. 2, pp. 1–5, Feb. 2016, doi: 10.1007/s00339-016-9633-6.

[5]   M. Reis, *Fundamentals of magnetism*. Academic Press, 2013.

[6]   A. Vansteenkiste and B. Van De Wiele, "MUMAX: A new high-performance micromagnetic simulation tool," *J. Magn. Magn. Mater.*, vol. 323, no. 21, pp. 2585–2591, Nov. 2011, doi: 10.1016/j.jmmm.2011.05.037.

[7]   J. F. Liu *et al.*, "Microstructure and magnetic properties of sintered NdFeB magnets with improved impact toughness ARTICLES YOU MAY BE INTERESTED IN," *J. Appl. Phys*, vol. 97, pp. 10–101, 2005, doi: 10.1063/1.1847215.

[8]   K. F. Eid, M. Panth, and A. D. Sommers, "European Journal of Physics The physics of water droplets on surfaces: exploring the effects of roughness and surface chemistry The physics of water droplets on surfaces: exploring the effects of roughness and surface chemistry," 2018, doi: 10.1088/1361-6404/aa9cba.

Chapter 6.

Non-idealised modelling and virtual build of a detector

Simulations were completed using ideal particles with instant switching. These provided an insight into how the device efficacy is affected by changes to the device geometry but produce unrealistic values for the potential number of channels η.

In this chapter, we consider the non-zero transition width of our particles using sigmoidal membership functions. We then evaluate the field from a collection of particles and calculate the EMF in a detection coil that is produced by the change in the field captured by the coil when particles transition. The uncertainty due to detection coil misalignment is then calculated, allowing us to establish the electronic requirements and component constraints.

The outcomes of the parameter optimisation simulations are built into the design of the device. The detector is visualised virtually through computer-aided design, where we outline the materials and processing needed to generate such a device.

We finish this chapter by assessing the viability and expectations of such a detector.

6.1. Integration of switching distributions to the simulation

6.1.1. Fuzzy logic and membership functions

This section looks to outline how we integrate finite – and hence non-ideal - switching events into the simulations. The results from the previous chapter (section 5.5) were produced in a system with transitions of zero width or infinite sharpness. We know this is not observed experimentally in our particles, with the results of chapter 4 showing transitions occurring over a finite range of field.

In section 4.5, we analysed the statistical distribution of transition parameters from many individual particles. These and other measurements in chapter 4 were fitted as a logistical sigmoid to assess the transition locations c and widths a, with the transition equation:

$$y = \frac{1}{1 + e^{-\frac{x-c}{a}}} = \chi. \tag{6.1}$$

An example of a modelled sigmoid is given in Fig 6.1, with a transition location $c = 1950\ [Oe]$ and a transition width $a = 15\ [Oe]$. This is equivalent to the modelled H_3 transition in the multiparticle modelling of particles with a platinum spacer layer thickness $t_{Pt} = 0.50\ [nm]$ (section 4.5).
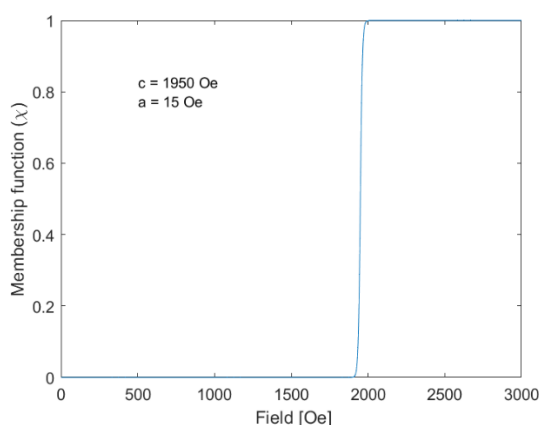
Fig 6.1 An example of a sigmoid generated from the Boltzmann model. This approximates an AP-P transition $(+H_3)$ from the normalised summation of many individual loops in section 4.5.

The logistical sigmoid is used as a membership function, which we term χ. Using the transfer function that was introduced in section 3.2.1.6, the field from the drive magnet can be correlated to the position of a particle to provide a non-binary value of magnetisation. This allows us to attribute realistic switching events to the particles.

If we consider a magnet of $OD = L = 4\ [cm]$, inner bore $ID = 6\ [mm]$, $B_0 = 0.4\ [T]$ and $s_{rad} = 1\ [mm]$, we achieve a field of $B_0 + 5\%$ at $p_0 = 5.37\ [mm]$, as seen in Fig 6.2a, and we calculate the NSA profile seen in Fig 6.2b. Fig 6.2c shows the field at the sample area at this distance p_0 for an angle of $17.84\ [deg]$, corresponding to θ_0, the angle of the B_0 transition. The Z component of the

field is correlated to the membership function, causing a smooth gradient at the border between on and off regions (Fig 6.2d). This smooth gradient is a result of the membership function χ, and demonstrates how the transition width will be widened as a result of non-ideal switching.
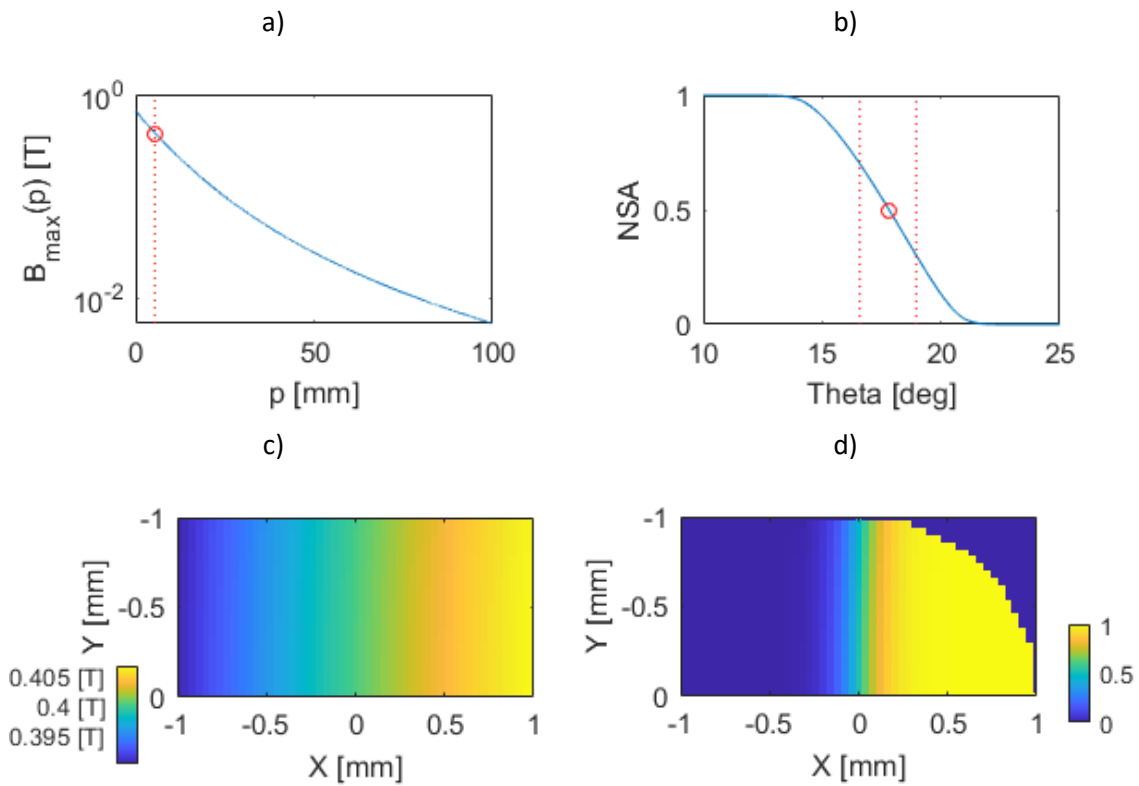
Fig 6.2 a) Z-component of the magnetic field along the Z axis, at $\theta_M = 0$ [deg], with the p value at which $B = B_0 + 5\%$ highlighted b) NSA profile for a sample with $OD = L = 4$ [cm], $IB = 6$ [mm], $B_0 = 0.4$ [T] and $s_{rad} = 1$ [mm].). c) B_z profile at p_0 and magnet angle 17.84 [deg]. d) The sample area, with the membership function applied. Here we see a smooth gradient between the on/off states.

Profiles like Fig 6.2d are calculated for drive magnet angles between $0 - 90$ [deg] in order to construct the NSA profiles. These are characterised by their location θ_n and width $W_{0.3-0.7}$, and the channel progression can be evaluated as previously explained in chapter 5. Note, only method II is used in this chapter.

In section 4.3, we observed that the transition sharpness was a roughly constant value throughout the series, independent of transition location c (see fig 4.15b, 4.20b and 4.26c). From the measurements in this section, as well as those in section 4.5, we observe an average a value of ~ 10 [Oe]. Throughout this section, we assume a constant value for a, at 10 [Oe]. An example of many transitions with constant a is shown in Fig 6.3. These transitions have c values that are multiples of 500 [Oe], to demonstrate how a series may look.

Channels centred around n*500 Oe
All with a = 10 Oe
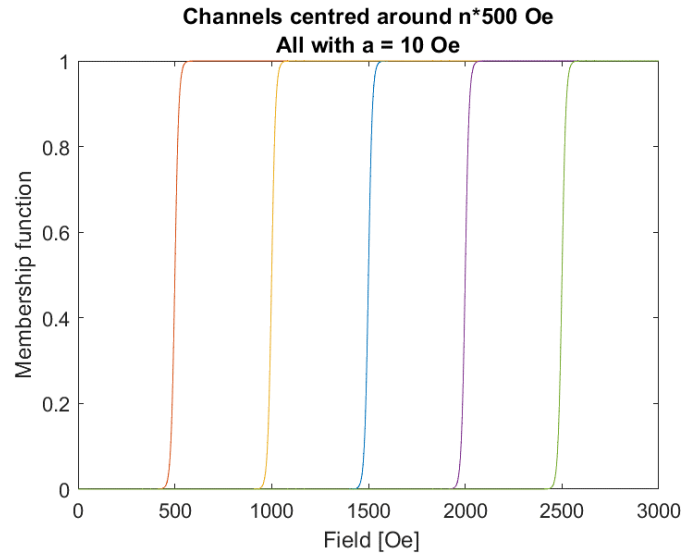
Fig 6.3 Many transitions with varying location (c) but constant sharpness (a).

6.1.2. Optimising detector specifications

Intuitively, we expect the wider particle transitions to lead to wider NSA transitions and therefore to smaller η. Here, we seek to understand how a finite transition width exactly affects the figure of merit η. In section 5.5 we investigated the effects on η due to changes in geometrical parameters, firstly using simulations with simple constraints (a minimum channel field of 25 [Oe] to stop infinite iterations). This demonstrated how the field homogeneity is affected by geometrical changes and its effect on the optimum channel number η. In this section, however, we do apply the practical constraints (a working range limit ($p \geq 10 \; [cm]$) and minimum separation ($B_n - B_{n+1} > 50 \; [Oe]$)) as these lead to more realistic η values. To understand the effect of considering finite-width transitions, we compare the results from this section with results from section 5.5, where the practical constraints were applied. Only simulations with these applied have been plotted.

6.1.2.1 Drive magnet outer diameter

In this study, we look at the effect of changing the outer diameter OD of the cylindrical drive magnet on the number of available channels η. All inputs parameters remain the same as in the ideal transition study (section 5.5.2), with $L = 4 \; [cm]$, start field $B_0 = 0.4 \; [T]$ and $KRV = 10$. We sample 81 values of OD from 2 $[cm]$ to 10 $[cm]$ at 1 $[mm]$ intervals. Again, the sample area is made of a circular mask of $s_{rad} = 1 \; [mm]$, with resolution $dx = dy = 40 \; [\mu m]$. The results of this study are compared with those in the ideal transition study in Fig 6.4a. The same trend is seen, with a monotonic increase in η with increasing OD. However, there is a large reduction in the number of available channels for a given OD, with around a 3.5x decrease from the ideal transition case. This is attributed to a larger transition width ($W_{0.3-0.7}$), which is expected. We see a maximum of 15 channels for the largest OD (10 $[cm]$), compared to 53 in the simulations with ideal transitions. We also note that the curve appears to begin to plateau at higher OD, unlike in the ideal transition case.

Fig 6.4b shows that the channel separation never goes below 50 $[Oe]$ for any OD value, with a minimum separation between two adjacent channels of around 200 $[Oe]$. This is due to the increased transition width as a result of the non-ideal transition.

6.1.2.2 Drive magnet length

Again, we quantify the change in η for changes to the magnet length L. The inputs remain the same as in the ideal model, with $OD = 4\ [cm]$, $B_0 = 0.4\ [T]$ and $KRV = 5$. We sample 81 values of L from 2 $[cm]$ to 10 $[cm]$ at 1 $[mm]$ intervals. The sample area is made of a circular mask of $s_{rad} = 1\ [mm]$, with resolution $dx = dy = 40\ [\mu m]$. The results of this study are compared with the results from the ideal simulation in Fig 6.4c.

We see very little variation in η, reducing from 9 to 8 channels at $L = 7\ [cm]$. As demonstrated in chapter 5, L should be optimised for a given OD. In this example of $OD = 4\ [cm]$, η is highest when $L < 8\ [cm]$. In this instance, it would be most beneficial to keep the magnet length small (to reduce the inertial load), so $L = 2\ [cm]$ would be chosen. We also note that the minimum channel field separation of 50 [Oe] is again never reached in any channel series, as is shown in Fig 6.4d, with the smallest separation between two channels at circa 170 [Oe].

6.1.2.3 Sample area

Now that the drive magnet has been optimised, it is important to examine the other elements of the detector, starting with the sample radius. All simulation inputs remain the same as in the ideal model, with $OD = L = 4\ [cm]$, $B_0 = 0.4\ [T]$ and $KRV = 10$. We sample 31 values of s_{rad} from 0.30 $[mm]$ to 1 $[mm]$. In this simulation, the cell size remains constant, though the number of cells comprised in the sample area changes. We tested the results for two different resolutions (cell size $\Delta x = \Delta y = 40\ [\mu m]$ and $\Delta x = \Delta y = 20\ [\mu m]$) with identical results, showing that the cell size is small enough for accurate results at all s_{rad} values. The results of this study are compared with the results from the ideal simulation in Fig 6.5a.

Similarly to the ideal transition case, a monotonic decrease of η with increasing sample radius is observed again, though η is a lot smaller in the non-ideal transition case. This decreases almost linearly, with a reduction of η by roughly one channel per 0.1 [mm] increase in s_{rad}. We confirm that there is a systematically increased transition width ($W_{0.3-0.7}$) for larger s_{rad} in Fig 6.5b. This is especially pronounced at high channel field. We observe that the channel density is much higher for smaller s_{rad}, which is the result of smaller $W_{0.3-0.7}$. A reduction in $W_{0.3-0.7}$ would inevitably lead to larger η. Though, as previously mentioned, the increase in η when reducing s_{rad} must be weighed against the decreasing sample moment, which reduces with s_{rad}^2 for the same particle density, ultimately reducing the strength of the signal.
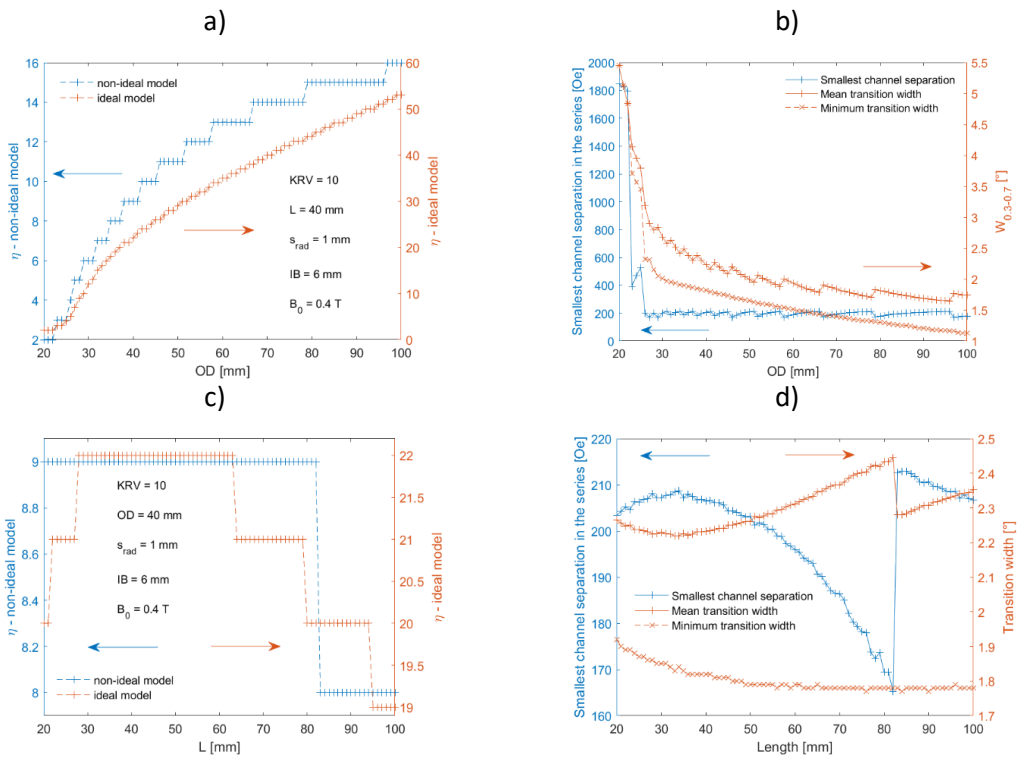
Fig 6.4 a) results for a simulation evaluating η for a changing OD in the case of non-ideal transitions, compared with the ideal transition case. b) Smallest channel separation, mean and minimum transition widths ($W_{0.3-0.7}$) within a series of magnets of changing OD. c) Results for a simulation evaluating η for a changing magnet length L in the case of non-ideal transitions compared with the ideal transition case. d) Smallest channel separation, mean and minimum transition widths within a series of magnets of changing L.
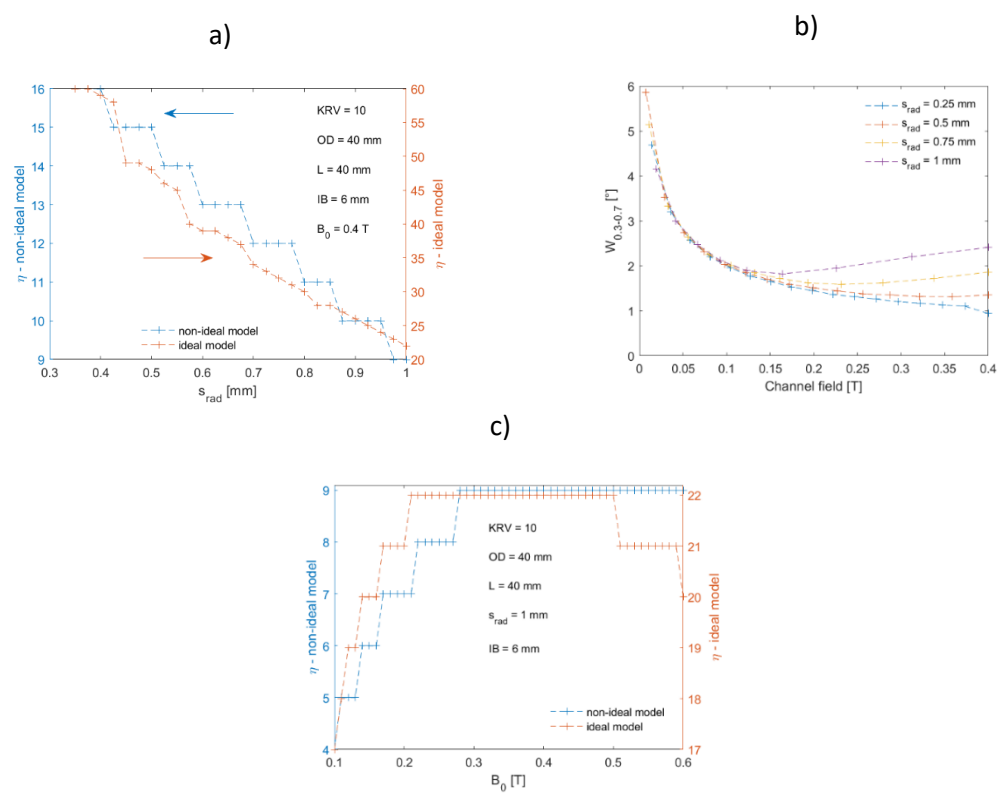
Fig 6.5 a) Results for a simulation evaluating η for a changing s_{rad} in the case of non-ideal transitions, compared with the ideal transitions case. b) A comparison of the progression of transition widths ($W_{0.3-0.7}$) through the series for different sample radius. A smaller transition width and hence higher η is observed for decreasing s_{rad}. c) Results for a simulation evaluating η for a changing start field B_0 in the case of non-ideal transitions, compared with the ideal transition case.

6.1.2.4 Start field

B_0 – defined as the highest used channel value (measured first) - is also tested. Again, all other simulation inputs remain the same as those used in the ideal model, with $OD = L = 4\ [cm]$, $s_{rad} = 1\ [mm]$, $ID = 6\ [mm]$ and $KRV = 10$. We sample 51 values of from $0.1\ [T]$ to $0.6\ [T]$ at $0.01\ [T]$ intervals. The results of this study are seen in Fig 6.5c. We observe an increase in the number of possible channels up to $0.3\ [T]$ where the maximum η seen for this magnet length and outer diameter is reaches. The ideal model reached its maximum $\approx 0.2\ [T]$. In the non-ideal case, we also note that there is no reduction in η at high values of B_0 within our parameter space, as was observed in the ideal case.

6.1.3. Testing the effects of changing particle properties

6.1.3.1 Transition sharpness (a)

We can also evaluate the effect of changing particle properties to determine how our patterning process may impact our device. We start with the transition sharpness a. All simulation inputs except a remain constant, with $OD = L = 4\ [cm]$, $s_{rad} = 1\ [mm]$, $ID = 6\ [mm]$, $B_0 = 0.4\ [T]$ and $KRV = 10$. In this simulation, KRV is now a minimum requirement, rather than a characteristic of the channel. We sample a spaced array of a values, characteristic of the sharpness of the sample, ranging from $0.01 - 100\ [Oe]$, with the results seen in Fig 6.6a.

In the ideal model, $a = 0$, and $\eta = 22$ for the given input parameters. This channel number, $\eta = 22$, is seen for all values below $a \approx 1.4\ [Oe]$, showing the expected convergence to the ideal case as a tends to zero. We also note that for a above $\approx 57\ [Oe]$ only two channels are available as transitions become too broad. Our previous simulations have used $a = 10\ [Oe]$, with $\eta = 9$ at this value.

The large increase in channel number η between $1.4[Oe] \le a \le 57\ [Oe]$, shows that a good patterning process is critical to the device efficacy.

6.1.3.2 KRV

Lastly, we study the effect of KRV on η. The simulations keep all other values constant, with $OD = 6\ [cm]$, $L = 2\ [cm]$, $s_{rad} = 1\ [mm]$, $ID = 6\ [mm]$, $a = 10\ [Oe]$ and $B_0 = 0.4\ [T]$. The results can be seen in Fig 6.6b and are compared with the ideal transition case. In the ideal transition case, we observed an exponential decay of x with y, with an r^2 of 0.9984 to an exponential fit. This is again seen for simulations with sigmoidal transitions, though with a smaller amplitude and decay length.
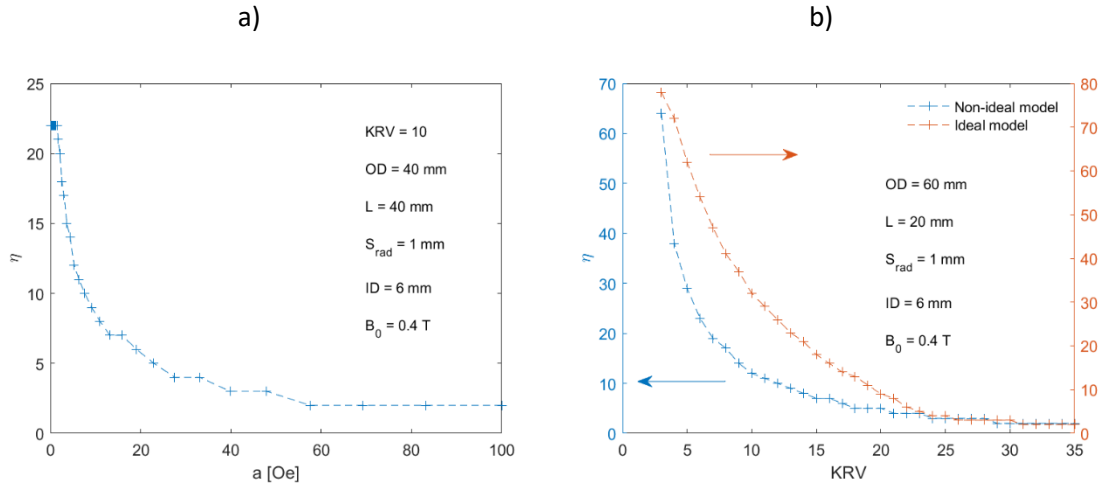
Fig 6.6 a) Results for a simulation evaluating η for a changing transition width a. b) Results for a simulation evaluating η for a changing KRV.

6.2. Estimated signal

In this section, we test two areas:

1. The average field and flux captured within a search coil for a droplet of ~ 1000 particles, and their dependence on the coil size and coil-sample separation

2. The induced EMF, with a comparison of results using the ideal particles of chapter 5, and the realistic particles of section 6.1

To understand the feasibility of our proposed detector, we must understand the signal strength. An inductive voltage is produced by the changes in the magnetic state of our particles, and can be described by Faraday's law of induction:

$$\varepsilon = -\frac{\partial \Phi}{\partial t}\,,$$
(6.2)

where ε, Φ and t are the induced voltage, magnetic flux captured by the coil and time. The magnetic flux can be calculated using Gauss' law:

$$\Phi = \oint_S \vec{B} \cdot d\vec{S},$$
(6.3)

with $\vec{B}$ the field created by the magnetic particles and S is the oriented surface defined by the pick-up coil. Numerically, this is evaluated by dividing the surface defined by the coil in square elements of size $8\,[\mu m]$ by $8\,[\mu m]$ and summing the discrete values of the component of B perpendicular to the surface defined by the coil, $B_\perp$, over the surface of the coil:

$$\Phi \approx \sum_S (B_\perp \, dS).$$
(6.4)

As dS is constant, we may rewrite Equation 6.4as:

$$\Phi = dS \sum_S B_\perp = \frac{\sum_S B_\perp}{N_{el}} \times N_{el}dS = \overline{B_\perp} \cdot A_S \,, \tag{6.5}$$

with $\overline{B_\perp}$ the mean-field across the surface S, N_{el} the number of elements within the summation and A_s the area of the surface S.

To effectively model this inductive voltage, we must first obtain the captured flux in the detection coil from our particles in the on, or P state. This can be evaluated through modelling.

6.2.1. Optimising the captured flux

In this simulation, we consider square particles to enable the use of Akoun's analytical expressions for the calculation of fields from parallelepipedal magnets [1], [2]. The particles have 20 $[\mu m]$ lateral dimensions and 2 $[nm]$ thickness, corresponding to the 2×1 $[nm]$ CoFeB layers in our coupled SAF particles. We assume that our dispersed particles are distributed homogenously across the full sample area, which is considered to be circular as the particles are dispensed in a liquid solution [3]. We maintain a constant centre-to-centre separation of 50 $[\mu m]$ in X and Y and create a circular arrangement of particles within a 1 $[mm]$ sample radius. This arrangement can be seen in Fig 6.7. For these geometrical parameters, 1184 particles are present in the sample area.
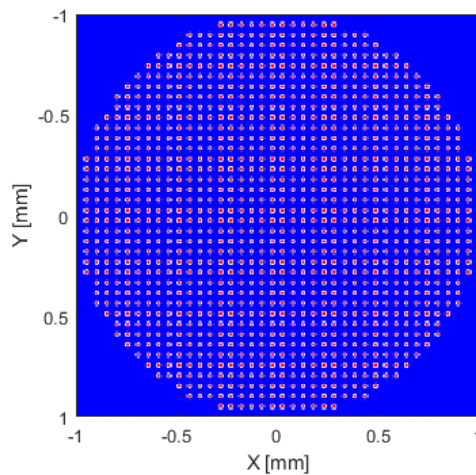
Fig 6.7 Circular arrangement of particles used in this simulation. Red indicates the location of a particle.

We begin with the case where all particles are in a saturated state, the parallel configuration of a SAF. To optimise the detection coil parameters, we assess the captured flux within a circular detection coil of varying radius and different sample plane – coil separations d_p. For this, the field from each particle in the detection coil is calculated individually, and the superposition of the field from each individual particle is calculated to produce the total field map. This is shown in Fig 6.8 for two particles. The flux is then evaluated using Equation 6.5.
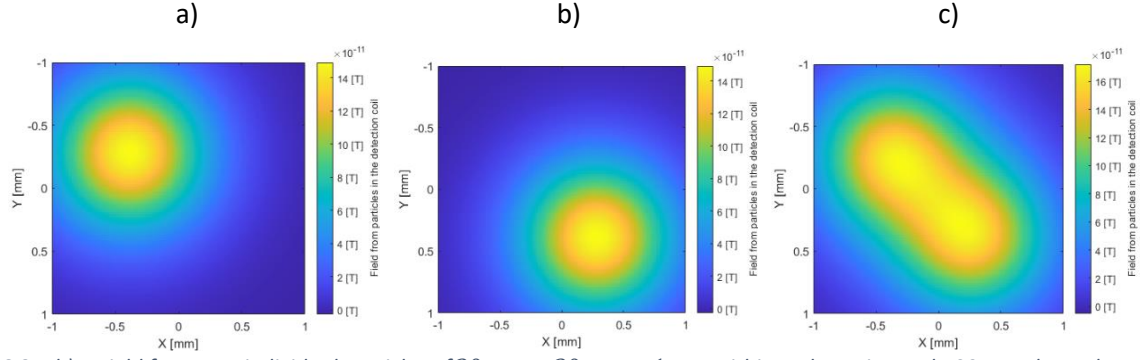
Fig 6.8 a,b) – Field from two individual particles of $20\ \mu m\ \times 20\ \mu m\ \times 1\ nm$ within a plane situated $100\ \mu m$ above the surface in Z and c) their superposition.

We evaluate the average perpendicular field and flux for 491 detection coil radii (R_{coil}) between $100\ [\mu m]$ and $5\ [mm]$ at $10\ [\mu m]$ intervals. The particle to coil separation (d_p) is varied using a logarithmically spaced array of 100 values between $100\ [\mu m]$ and $1\ [cm]$, and all coils are centred at $(0,0,d_p)$ from the particles. The average field $(\overline{B_\perp})$ and captured flux (Φ) for all values in these simulations are shown in Fig 6.9. The differing symmetry between the two plots is a result of the areal dependence of the captured flux, which of course is proportional to the square of s_{rad}.
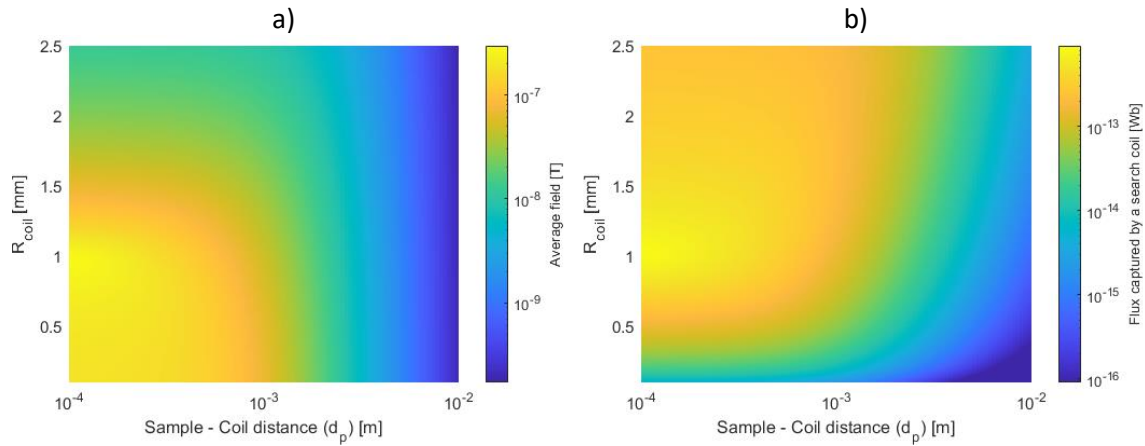
Fig 6.9 a) The average perpendicular field within a search coil of varying radius R_{coil} and at different sample to coil distances. b) Flux captured for the same simulation parameters.

We observe the largest captured flux when the coil radius is equal to the radius of the dispersed particles, s_{rad}. The captured flux decreases with larger sample-coil distances. This is shown clearly in Fig 6.10, which displays the average field and flux for varying sample-coil distances for $R_{coil} = 1\ [mm]$. We estimate that the minimum separation is of the order of $\sim100\ [\mu m]$, the approximate thickness of a protective capping layer. At this separation, we expect an average field of $\overline{B} = 2.84 \times 10^{-7}\ [T]$ and a flux of $\Phi = 9 \times 10^{-13}\ [Wb]$ within a coil of $R_{coil} = 1\ [mm]$.

As we have established the optimum coil size (R_{coil}) and the relationship with separation (d_p) for our circular array of ~1000 particles over a $1\ [mm]$ sample radius, we can now use these values to estimate the induced EMF from the particle transitions in a rotating field.
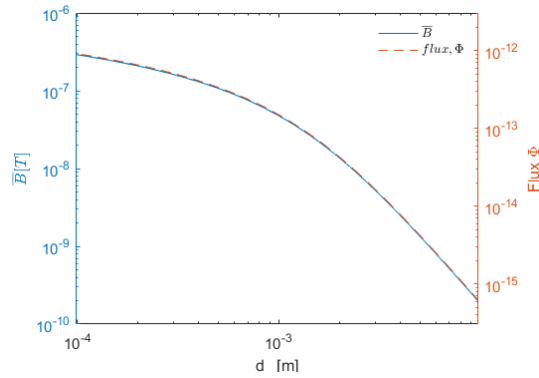
Fig 6.10 Average field and flux captured within a coil of $R_{coil} = 1\ [mm]$ at varying sample to coil height d_p

6.2.2. Evaluating the induced EMF

In chapter 5 we used Caciagli's analytical expression to model the field from a rotating cylindrical magnet that is diametrically magnetised. We evaluated the field profiles within the sample area for a changing drive magnet angle to obtain the normalised switched area, or NSA, which is also the normalised number of magnetic particles in the on, or parallel state. Our detector measures the inductive voltage from the change of flux produced as the particles transition between the P and AP states (or vice versa). Section 6.2.1 estimated the flux captured from a collection of particles dispersed over a circular area of radius s_{rad}. We can combine these two parts to estimate the flux captured by the detection coil for particles in a rotating field source. By calculating the captured flux with respect to the drive magnet angle θ_M, we can use Equation 6.2 to estimate the induced EMF in the detection coil. We summarise this process as follows, with the geometry shown in Fig 6.11.

- Calculate B_z within a sample region of radius s_{rad} for a drive magnet angle θ_M at a magnet surface to sample distance p_0, the distance at which the maximum field at $\theta_M = 0$ from a magnet of length L and diameter OD is equal to $1.05 \times B_0$.
- Correlate the field B_z with the locations of the circular array of particles using the logic functions for either ideal, or non-ideal particles.
- Calculate the Z component of the field from particles in the on state within a detection coil of radius R_{coil} at a particle to coil separation d_p.
- Evaluate the average field $\overline{B_\perp}$ and the captured flux Φ.
- Repeat for all values of drive magnet angle θ_M over the region defining the transition.
- Convert the $\Phi(\theta_M)$ data into induced voltage $\varepsilon(t)$ using Equation 6.2 and assuming that the magnet rotates at angular velocity ω_m.

6.2.2.1 Ideal model

The procedure is illustrated here in the case of ideal particles. In the ideal case, particles transition with zero width. This means that the state of each particle is binary – on or off. The point at which the particles transition is the switching field B_n, with the particle in the on state for $|B_z| \geq B_n$ and

off if $|B_z| < B_n$. We evaluate the average field $\overline{B_\perp}$ and flux Φ over a series of magnetisation angles in the region where the particles transition. In this section, $OD = 6\ [cm]$, $L = 2\ [cm]$ and $B_0 = 0.4\ [T]$. As in chapter 5, the start field is set to $1.05 \times B_0$, which is found at a magnet surface to particle distance of $p_0 = 5.12\ [mm]$. In this ideal case, we observed the transition to occur over the angles $15[deg] < \theta_M < 20\ [deg]$. We probe this region only, in $0.05\ [deg]$ increments. At each angle, the field in the sample area defined by $s_{rad} = 1\ [mm]$ at a separation of p_0 is calculated. The field is then correlated with the particle locations, with particles being on when the field is above B_0 and off when below. The stray field from particles at locations where $B_z \geq B_0$ is evaluated in the detection coil ($R_{coil} = 1\ [mm]$ at a Z-separation $d_p = 100\ [\mu m]$), allowing the evaluation of the captured flux with respect to the drive magnet angle.

At drive magnet angle $\theta_M = 17.5°$, the field within the sample area is shown in Fig 6.12a. The areas above and below B_0 can be seen in Fig 6.12b. This is correlated to the particle locations, allowing us to calculate which of the particles are in the on, or off state, see Fig 6.12c. The z-component of the magnetic field from the particles in the on state, within the detection coil, is shown in Fig 6.12d. This allows the evaluation of the average Z-field $\overline{B_\perp}$ and captured flux Φ within the detection coil, which we find to be $\sim 0.53\ [\mu T]$ and $\sim 1.7 \times 10^{-12}\ [Wb]$ respectively.

This is evaluated for all θ_M in the transition region. An example of the fields within a detection coil for various θ_M can be seen in Fig 6.13. The NSA over the transition is shown in Fig 6.14a, with the evaluated $\overline{B_\perp}(\theta_M)$ and $\Phi(\theta_M)$ presented in Fig 6.14b. Here, we see that there is not a direct relationship between $NSA(\theta_M)$ and $\Phi(\theta_M)$, but we observe the widths to be identical, as expected. Here, we define the width as the angle subtended between the start ($NSA \neq 1$) and end ($NSA = 0$) of the transition.
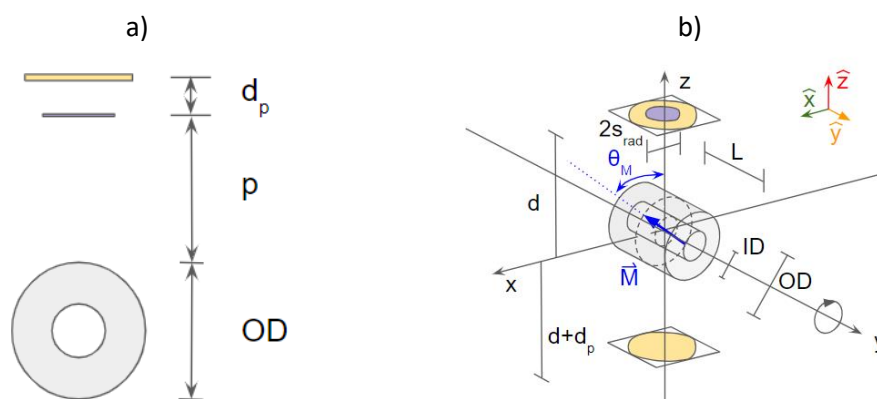
Fig 6.11 simple a) and extended b) geometry of the combined system used in this section (not to scale). The purple area defines the area which the particles are dispersed over, and the yellow areas define the detection coils. The field from the drive magnet is first calculated within the purple area, defining the regions above/below the switching field. This defines which particles are in the on state. The field from these particles is then calculated within the detection coil at a sample-coil separation d_p. This two stage process can be completed at all drive magnet angles θ_M to calculate $\Phi(\theta_M)$, which is converted into induced voltage $\varepsilon(t)$ using Equation 6.2.
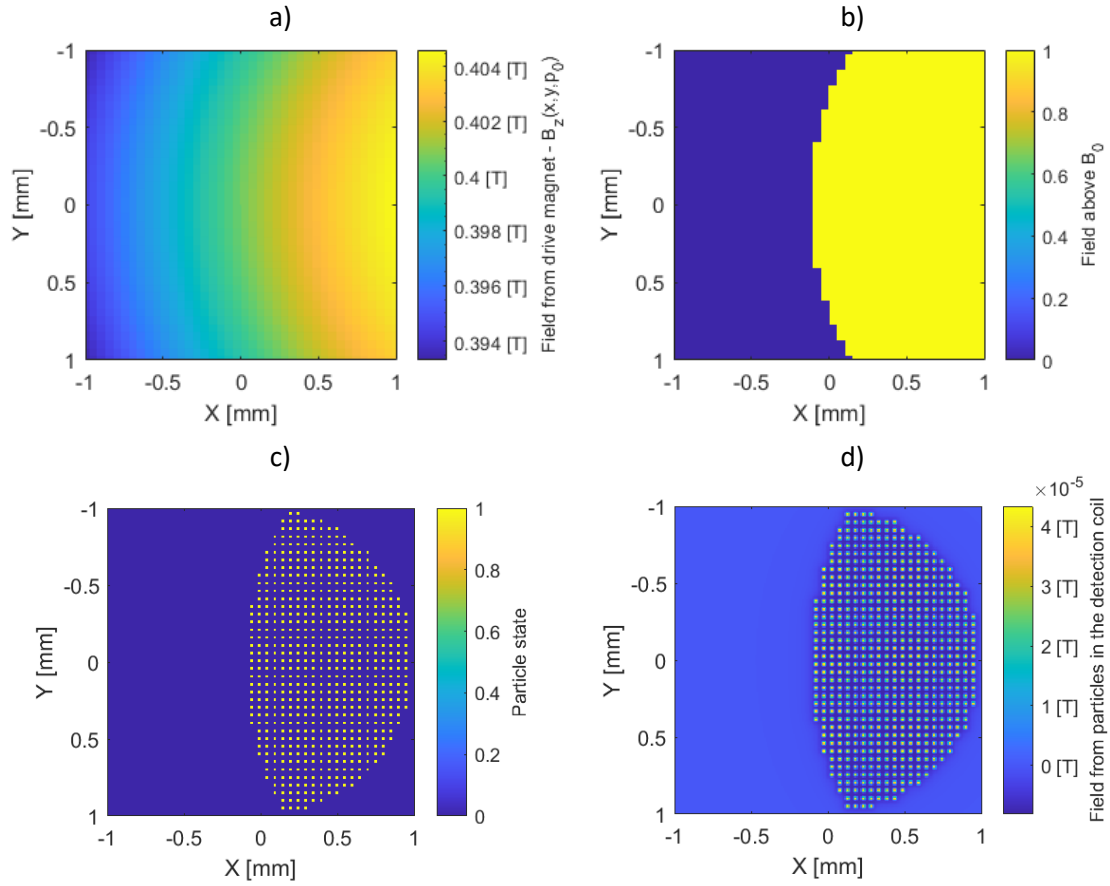
Fig 6.12 a) The field from a drive magnet of $L = 2\ [cm]$ and $OD = 6\ [cm]$ within a sample area of $s_{rad} = 1\ [mm]$ at a separation of $p_0 = 5.12\ [mm]$ and a drive magnet angle $\theta_M = 17.5\ [deg]$. b) The area of the sample region above and below the switching field B_0. c) particles in the circular arrangment shown in Fig 6.7 that are in the on state at $\theta_M = 17.5\ [deg]$. d) Fields from the particles in the on state in a detection coil of length R_{coil} at a separation $d_p = 100\ [\mu m]$.

The induced EMF ε can be obtained using Equation 6.2, with

$$t = \theta_M \cdot \omega_m^{-1} \tag{6.6}$$

where ω_m is the angular velocity of the drive magnet, given by $\omega_m = 2\pi f$ where f is the rotational frequency. The resulting $\Phi(t)$ and EMF ε given a rotational frequency $f = 20\ [Hz]$ are shown in Fig 6.15. We observe a roughly constant ε, as expected from a decreasing $\Phi(t)$ that is close to linear. Assuming that all our particles switch instantly at the same field (B_0) the average value of EMF over the transition is $\overline{\varepsilon} = 3.0\ [nV]$, which is smaller than the noise of a good op-amp ($\sim 5\ [nV/\sqrt{Hz}]$). This signal is detectable if the noise present in the system is low enough and the bandwidth of the amplifier is small ($\sim 0.01\ [Hz]$). We observed in section 4.5 that this is not the case, with nominally identical particles transitioning at different values. We now investigate the induced EMF in the case of non-ideal particle transitions.
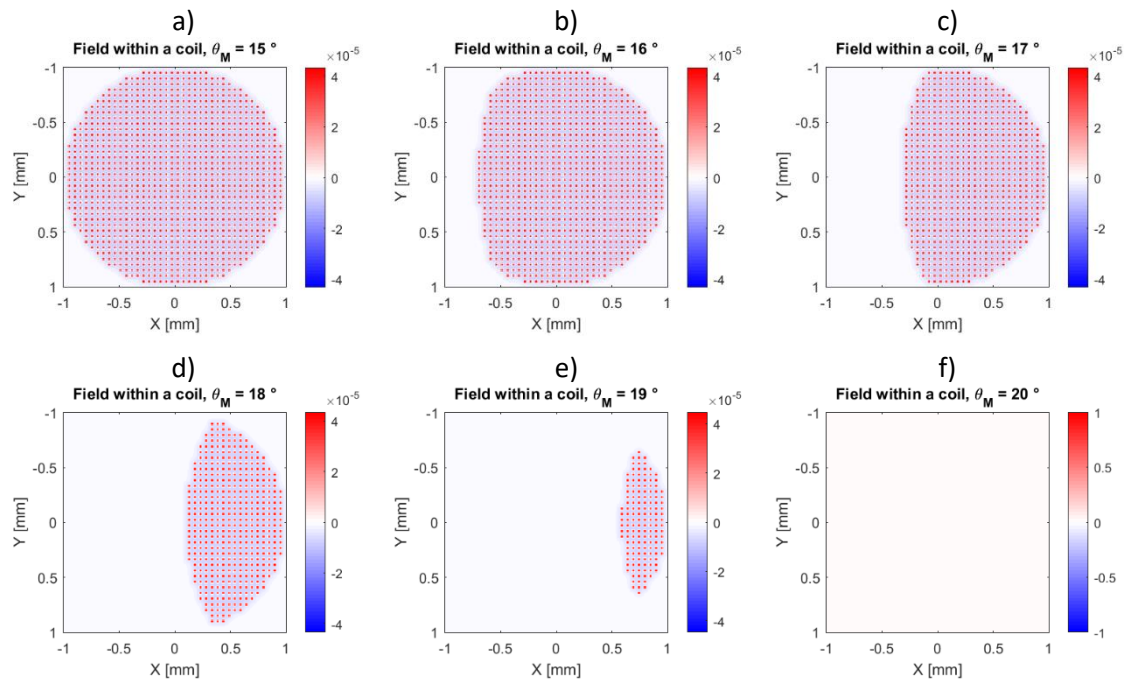
Fig 6.13 Fields from ideal particles at different angles across the transition at a sample to coil height $d_p = 100\ [\mu m]$.
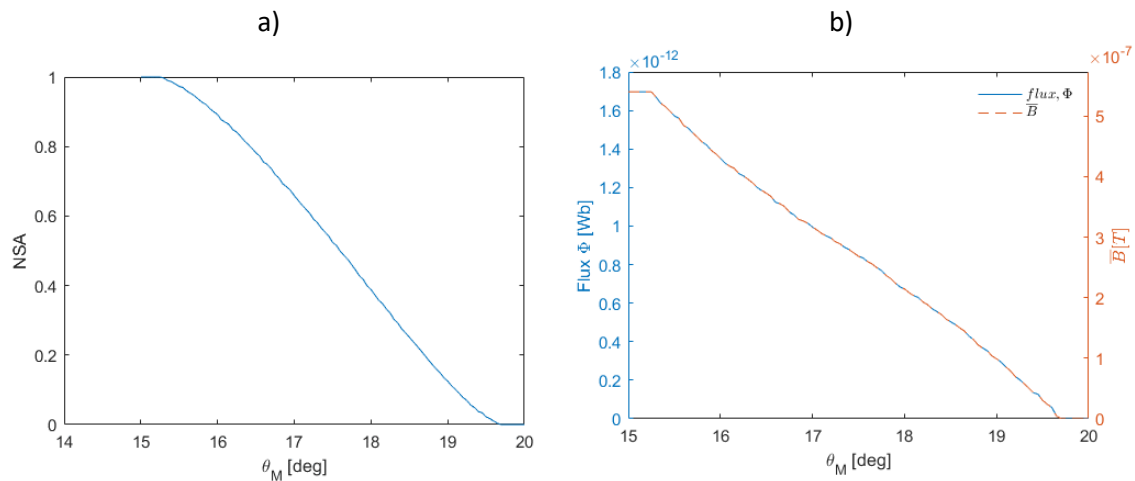
Fig 6.14 a) NSA profile with respect to the drive magnet angle (θ_M) for the circular arrangement of 1184 ideal particles. b) Captured flux and average field with respect to θ_M.
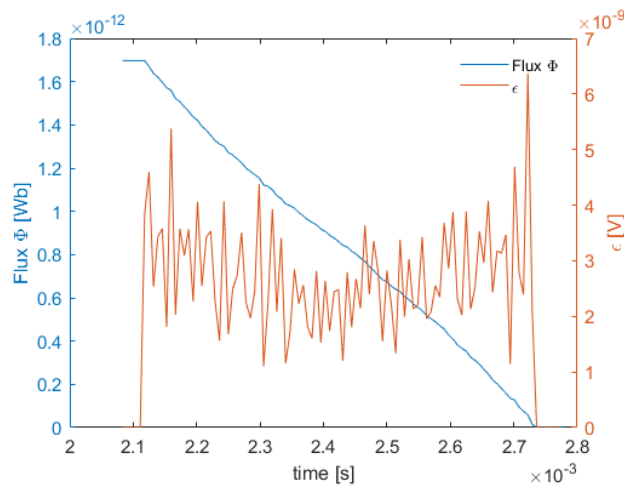
Fig 6.15 Flux captured, and EMF with respect to time, considering a rotational speed f of 20 [Hz] in the ideal transition case.

6.2.2.2 Non-idealised model

In a non-ideal model, we consider the distribution of switching fields of individual particles by modelling their collective transition as a logistical sigmoid, defined by Equation 6.1. This means that individual particles can have a normalised moment that is non-binary. In this simulation, we use the same particle array and drive magnet as in the ideal model, with $OD = 60\ [mm], L = 20\ [mm], p_0 = 5.12\ [mm]$ and $B_0 = 0.4\ [T]$. In the simulations in section 6.1.2, we observed the transition to occur over the drive magnet angles $12.5\ [deg] > \theta_M > 22.5\ [deg]$. We probe this region at $0.1\ [deg]$ resolution. A similar process to section 6.2.2.1 follows, though the particles are correlated to the drive magnet field using the Boltzmann sigmoid shown in Fig 6.16a, centred at $c = B_0 = 0.4\ [T]$ and with a transition width $a = 10\ [Oe]$. We again consider the field from each of the particles. In this instance, each particle has an effective M_{eff} equal to the value of the membership function calculated for a field value equal to the drive magnet field value at the particular particle position, i.e. $M_{eff} = M_s \cdot \chi$, where χ is the membership function.

The field profile from the drive magnet, $B_z(\theta_M)$ is the same as in the ideal case and is seen in Fig 6.16b for a drive magnet angle $\theta_M = 17.5\ [deg]$. When this field profile is correlated to the membership function, a smooth gradient is seen from 0 (particle is in the AP state) to 1 (particle is in the P state), as is seen in Fig 6.16c. We then superpose the fields from all particles. The effective magnetisation of all particles at $\theta_M = 17.5\ [deg]$ is seen in Fig 6.16d, with the superposed fields within a detection coil of $R_{coil} = 1\ [mm]$ and $d_p = 100\ [\mu m]$ seen in Fig 6.16e.

We display the field within the detection coil for varying drive magnet angle θ_M in Fig 6.17. Note, there is a large change of scale in Fig 6.17f, with a 100x reduction from Fig 6.17e, which again has a change in scale from Fig 6.17a-d. The corresponding $NSA(\theta_M)$ curve can be seen in Fig 6.18a, with $\overline{B}(\theta_M)$ and $\Phi(\theta_M)$ presented in Fig 6.18b.

We evaluate $\Phi(t)$ and EMF (ε) given a rotational frequency $f = 20\ [Hz]$ in Fig 6.19a. We again observe a roughly constant ε, as expected from a near linear $\Phi(t)$. The maximum value of the EMF over the transition is $\overline{\varepsilon} = 2.5\ [nV]$, which is slightly smaller than in the ideal case, as expected. This signal can be detected, if the bandwidth of an amplifier system is low enough, and the system noise within this bandwidth does not exceed the signal.

Finally, the NSA is compared with the normalised $\Phi(\theta_M)$ in Fig 6.19b, showing that the field at the detection coil is not directly proportional to the number of particles the field is produced by, but it does provide a reasonable approximation. This means that the speed of the simulation may be reduced by using:

$$\varepsilon = \frac{d\Phi}{dt} = \frac{d\Phi}{d(\text{NSA})} \frac{d(\text{NSA})}{dt} \approx \frac{d(\text{NSA})}{dt} \cdot \Phi(\theta_M = 0), \qquad (6.7)$$

where $\Phi(\theta_M = 0)$ is the proportionality factor between NSA and Φ. As NSA has a range between 1 and 0, this can be defined by the captured flux within the detection coil from the array of particles at a drive magnet angle of zero (highest B_z field).

Noise in the system will arise due to misalignment in the nominally equidistant coil sets. We investigate this further in section 6.3.
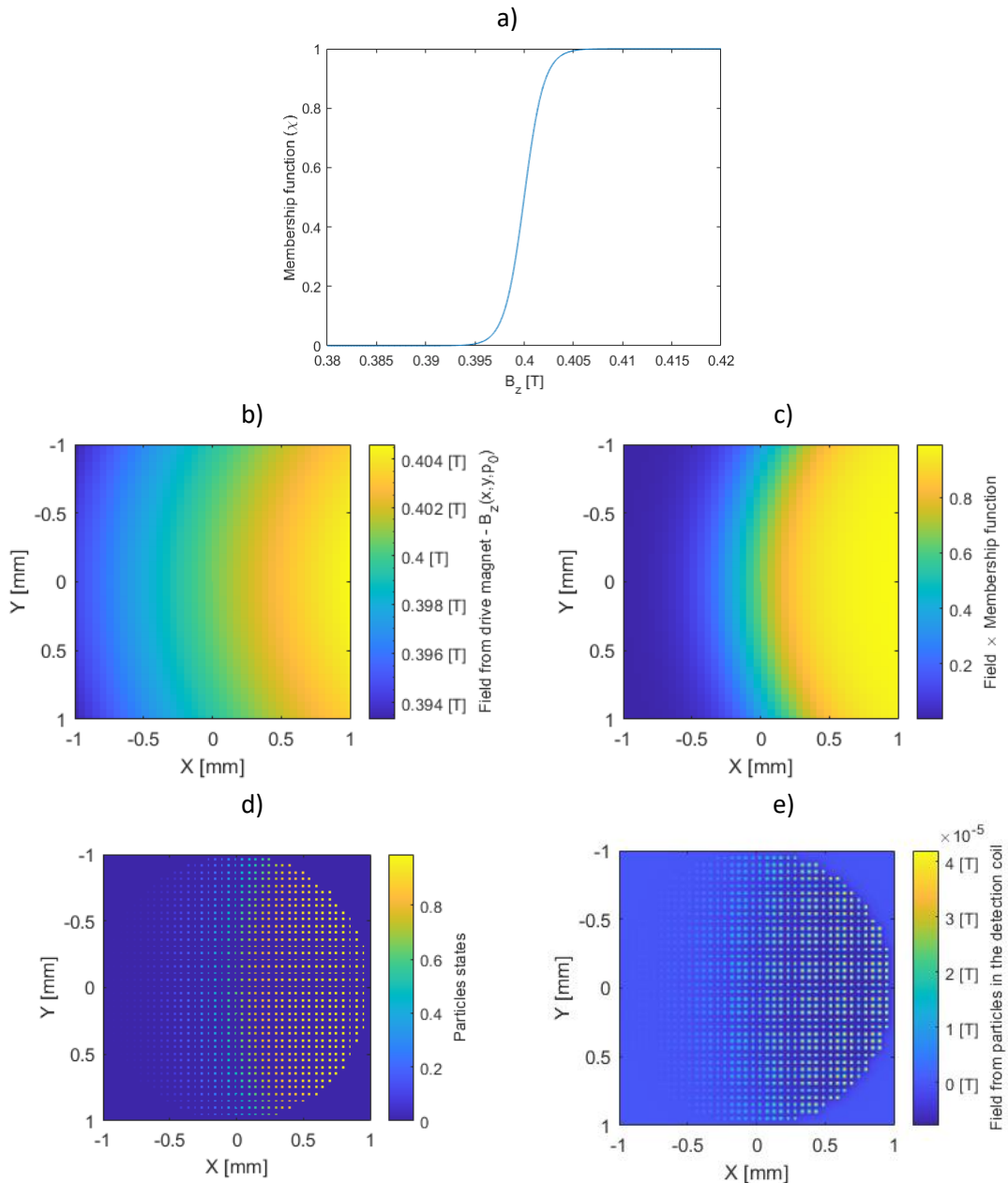
Fig 6.16 a) membership function profile for a particle series with transition centre $c = 0.4$ $[T]$ and transition sharpness $a = 10$ $[Oe]$. b) The field from a drive magnet of $L = 2$ $[cm]$ and $OD = 6$ $[cm]$ within a sample area of $s_{rad} = 1$ $[mm]$ at a separation of $p_0 = 5.12$ $[mm]$ and a drive magnet angle $\theta_M = 17.5$ $[deg]$. c) The profile from the membership function, showing the smooth transition over the switching field. d) Normalised moment of the particles at the locations given in Fig 6.7 at $\theta_M = 17.5$ $[deg]$. e) Fields from the particles in the non-zero state in a detection coil of length R_{coil} at a separation $d = 100$ $[\mu m]$.
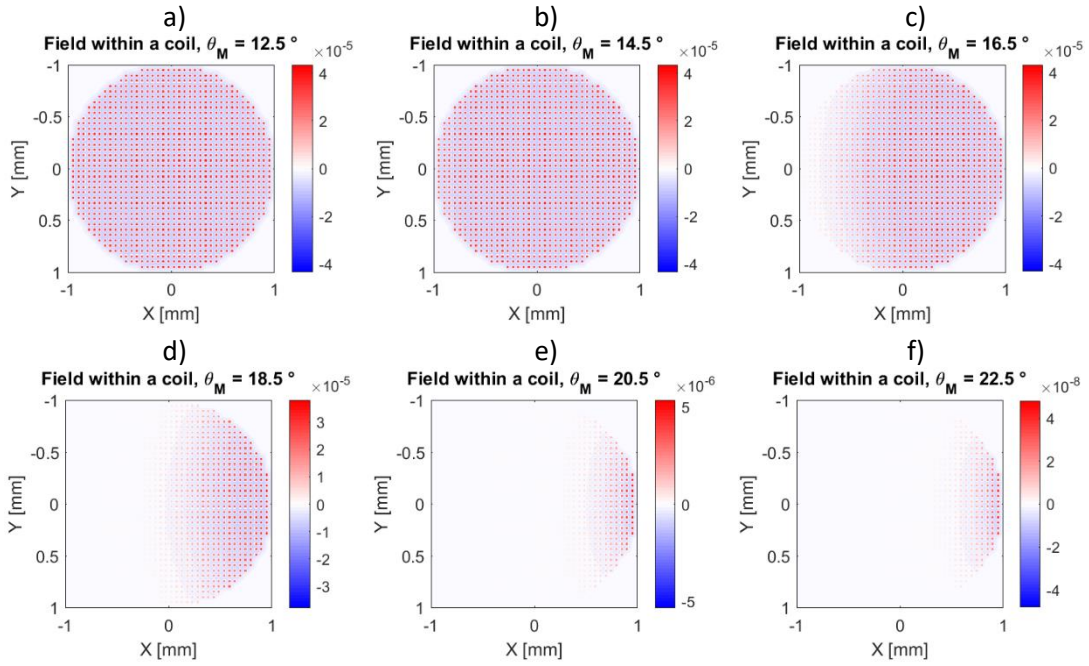
Fig 6.17 Field in the detection coil from non-ideal particles at different drive field magnetisation angles across the transition at a sample to coil height $d_p = 100 \ [\mu m]$.
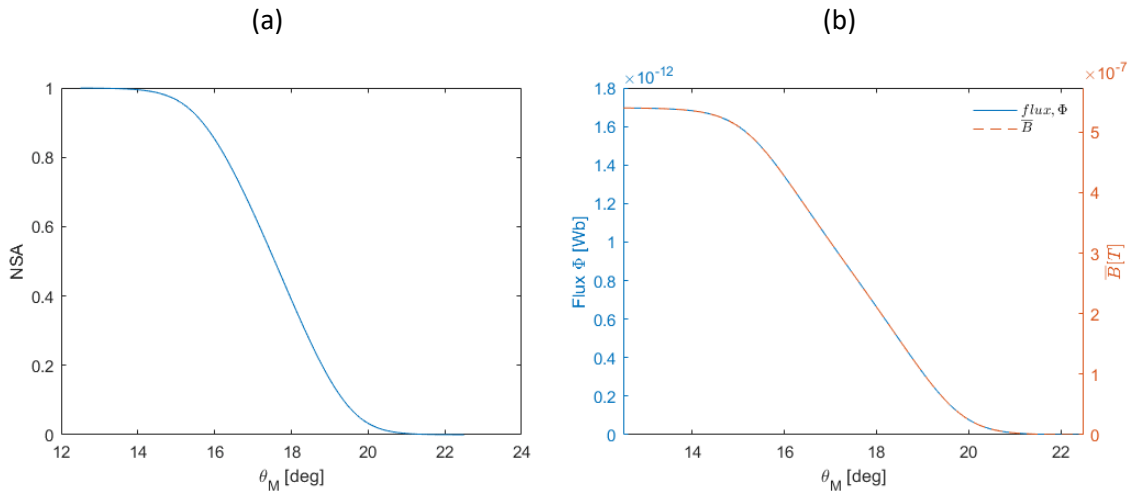
Fig 6.18 a) NSA profile with respect to the drive magnet angle (θ_M) for the circular arrangement of 1184 non-ideal particles. b) Captured flux and average field with respect to θ_M for the non-ideal particles.
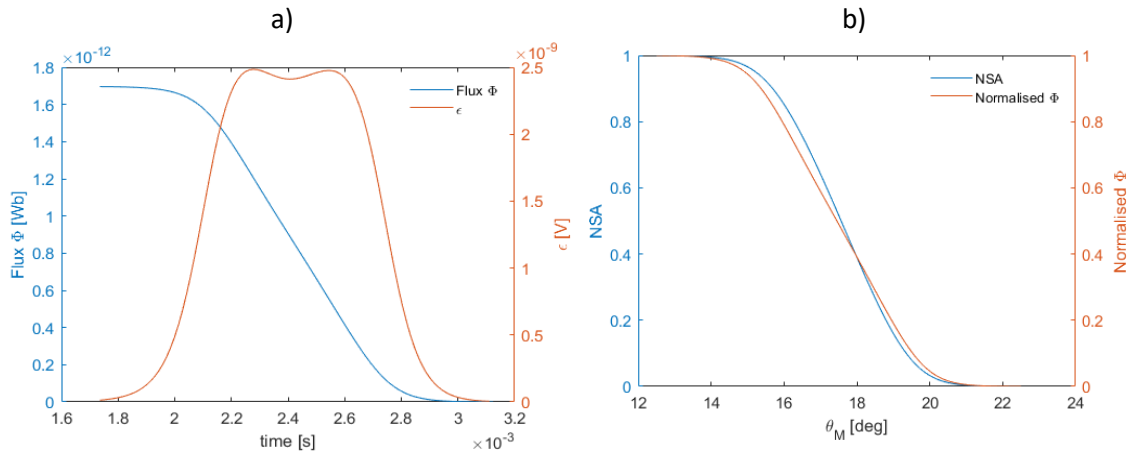
Fig 6.19 a) Flux captured, and EMF with respect to time, considering a rotational speed f of 20 [Hz] b) Comparison of NSA and normalised Φ, showing they are not equivalent but can be considered as a good approximation.

6.3. System constraints

Now that we have obtained an estimate of the signal for the proposed detector, we investigate potential sources of induced voltage ε that may arise which are not due to the transition of the particles. This will allow the assessment of the viability of such a device and any build constraints.

We propose to null the induced EMF from the drive magnet by using a pair of back-wired coils that are equidistant from the source. This idea is seen below in Fig 6.20, where coil 2 is placed at the same distance from the surface of the magnet as coil 1 and should therefore see a field exactly opposite to coil 1. The nullification of the drive field relies on the symmetry of the field profile from the source magnet, and the equidistance/symmetrical positioning of both coils in the set. We hypothesise that the main source of noise will arise from differences in the average field within each of the detection coils. We aim to test the magnitude of an EMF produced by a misalignment of one of the coils in the pair.
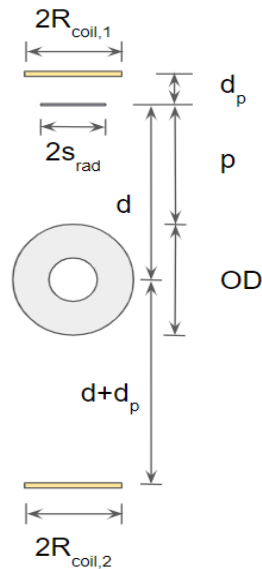
Fig 6.20 Schematic showing the two detection coils (yellow) and the relevant parameters.

The induced voltage within these coils has a magnitude that is defined by Faraday's law:

$$\varepsilon = -\frac{d\Phi}{dt} - \frac{d}{dt}\left(\oint_S \vec{B} \cdot d\vec{S}\right) = -\frac{d}{dt}\left(\sum_S (B\,dS)\right) = -\frac{d}{dt}(\overline{B} \cdot A). \qquad (6.8)$$

Noise arises through a difference in the average field between the two detection coils, such that:

$$\Delta\varepsilon = -\frac{d}{dt}(\Phi_{\text{coil 1}} - \Phi_{\text{coil 2}}) = -\frac{d}{dt}\left(\oint B_{z,1} \cdot dS_1 - \oint B_{z,2} \cdot dS_2\right) \qquad (6.9)$$

$$\Delta\varepsilon = -\frac{d}{dt}\left(\Delta\overline{B_z}(t)\right) \cdot A, \qquad (6.10)$$

where $\Delta\overline{B_z}$ is the difference between the two average fields perpendicular to the detection coils of area A. We first investigate how the average field changes with drive magnet angle θ_M. We consider a drive magnet with $OD = 6\ [cm]$ and $L = 2\ [cm]$, and calculate the Z component of the field during a $0 - 90\ [deg]$ rotation at $0.1\ [deg]$ intervals. The field is calculated using Caciagli's analytical equations, with the field at an angle calculated using the linear combination of magnetisation in X and Y as in section 5.2. The average field is calculated within a circular coil area of radius $R_{coil} = 1\ [mm]$ at a drive magnet surface to detection coil separation of $1\ [cm]$, with the results seen in Fig 6.21. We observe a cosine dependence with drive magnet angle, meaning that the average field at any magnet angle can be considered as:

$$\overline{B}(\theta_M) = \overline{B_{v,z}}(\theta_M = 0) \cdot \cos(\theta_M), \tag{6.11}$$

where $\overline{B_{u,z}}(\theta_M = 0)$ is the average z-field at $\theta_M = 0$. We show that this is the case in Fig 6.21, showing a difference between the two calculations that is roughly equal to the floating-point precision used in MATLAB (2.22×10^{-16}). This can be understood by evaluating the field at each point, which is calculated using $B_z(\theta_M) = B_v, z\cos(\theta_M) + B_u, z\ sin(\theta_M)$. In chapter 5, we observed that $B_{v,z}$ has a concentric profile, whereas $B_{u,z}$ is close to invariant in Y, and is antisymmetric in X. This shows that, on average across the plane that is centred at (0,0), the $B_{u,z}$ term cancels, leaving only the cosine $B_{v,z}$ term. By using $\theta_M = 2\pi ft$, Equation 6.11 simplifies to

$$\varepsilon = -\frac{d}{dt}\left(\overline{B_z}(t)\right) \cdot A = -\frac{d}{dt}\left(\overline{B_{v,z}}(t = 0) \cdot \cos(2\pi ft)\right) \cdot A \tag{6.12}$$

$$\varepsilon = 2\pi fA \cdot \overline{B_{v,z}}(t = 0) \cdot \sin(2\pi ft) \tag{6.13}$$

This is a sinusoid of amplitude $2\pi fA \cdot \overline{B_{v,z}}(t = \theta_M = 0)$ and frequency f.

Equation 6.13 shows that we can obtain the EMF due to misalignment of the detection coils by calculating the differences in the average field within the coil area. As it has a cosine dependence, it can be considered as a systematic background, which we term ε_{bg}. We can assess the magnitude of this background in three situations:

- Misalignment in the XY plane
- Misalignment in the Z distance
- Differing coil areas.

We can use these results to understand the build constraints and available tolerances of components.
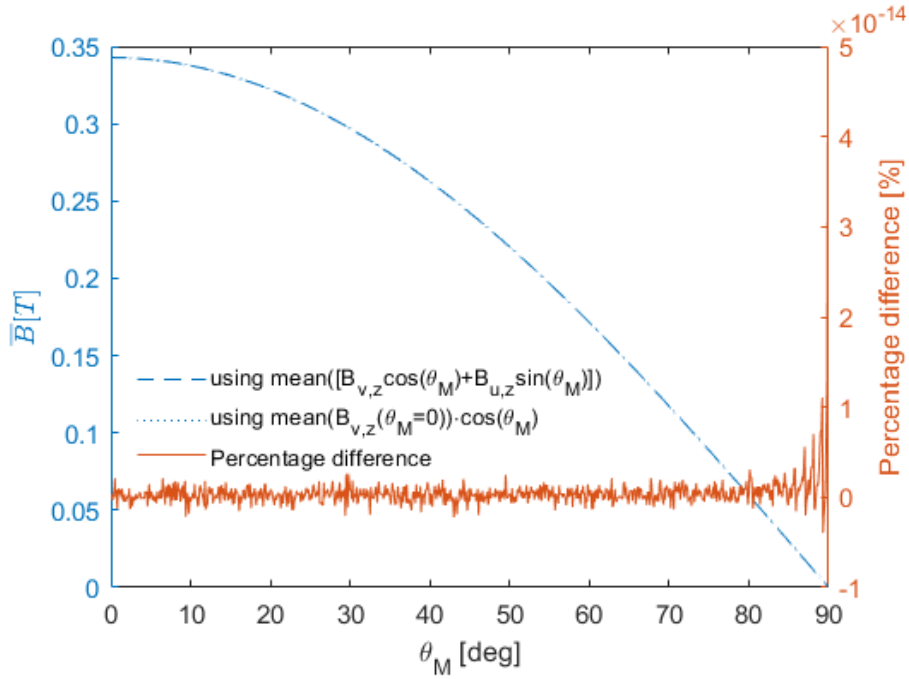
Fig 6.21 Calculations of the average field at differing drive magnet angles.

6.3.1. Coil misalignment in the XY plane

The effect of coil misalignment in the XY plane is assessed with a drive magnet of $OD = 6 \, [cm]$ and $L = 2 \, [cm]$. The first coil is centred at $(0,0)$ in the XY plane at a drive magnet surface to sample distance of $p = 1 \, [cm]$. The position of the second coil is varied in the X and Y direction from $\left(0,0,-\left(\frac{OD}{2}+p\right)\right)$. We calculated the ε_{bg} for 51 displacements between 0 [mm] and 1 [mm] at 0.02 [mm] intervals in both X and Y, respectively. We only calculate ε for positive values of X and Y due to the symmetry of the field about the X and Y axes. The ε_{bg} results for a frequency $f = 20 \, [Hz]$ can be seen in Fig 6.22.

We observe an increasing voltage with increasing displacement in both X and Y, as expected. We also note that this system has a larger ε_{bg} for changes in X than changes in Y. This is due to the field profile being more homogeneous in Y than X, as is seen throughout chapter 5. The ε_{bg} becomes larger than the signal at a displacement of $\sim230 \, [\mu m]$ in X and $\sim320 \, [\mu m]$ in Y, shown by the intersection with the line of $\varepsilon_{bg} = 3 \, [nV]$.

We finally look to obtain a 2D map of the ε_{bg} produced by a displacement in both X and Y, with the results seen in Fig 6.23. The line where $\varepsilon_{bg} = 3 \, [nV]$ is shown in red and follows an elliptical profile between the ΔX and ΔY points shown above.
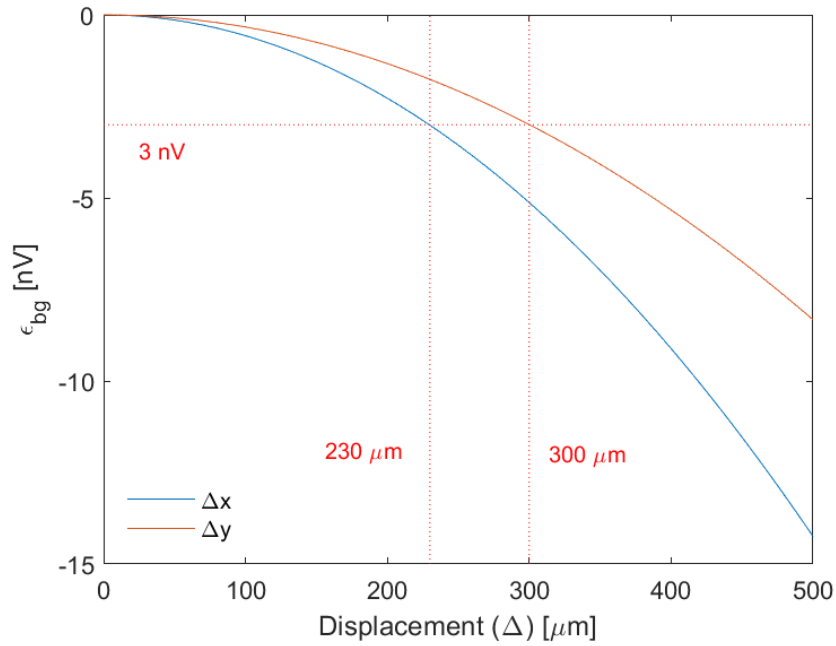
Fig 6.22 ε_{bg} for various displacements in X and Y. The value of 3 [nV] is shown in red.
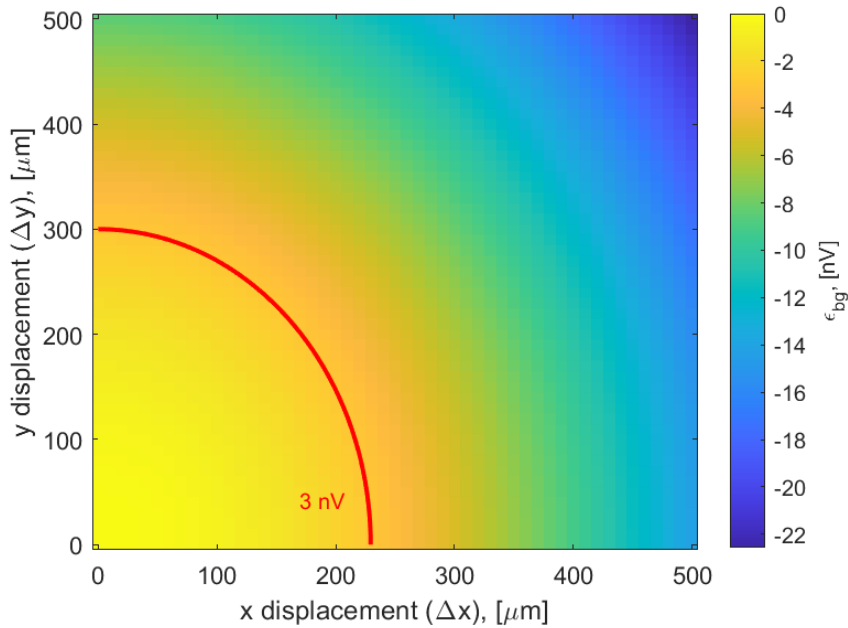
Fig 6.23 2D array of XY values, showing the ε_{bg} profile.

6.3.2. Coil misalignment in the Z distance

Misalignment in the XY plane is likely to arise from the initial setup. If method 2 from chapter 5 is used, the magnet surface to sample separation will be changing throughout the measurement. This could lead to errors in the equidistance of the back-wired coil set. The ε_{bg} for a misalignment in Z can be calculated with the same method as used in the misalignment in XY. We use the same magnet ($OD = 6 \, [cm], L = 2 \, [cm]$) and keep the magnet surface to coil distance of coil 1 at $p_1 =$

$1\ [cm]$. The second coil is placed at $(0,0,\frac{OD}{2} + p_1 + \Delta Z)$ where ΔZ is the Z displacement, varying from -0.5 to $0.5\ [mm]$ in $5\ [\mu m]$ increments. The results are seen in Fig 6.24.
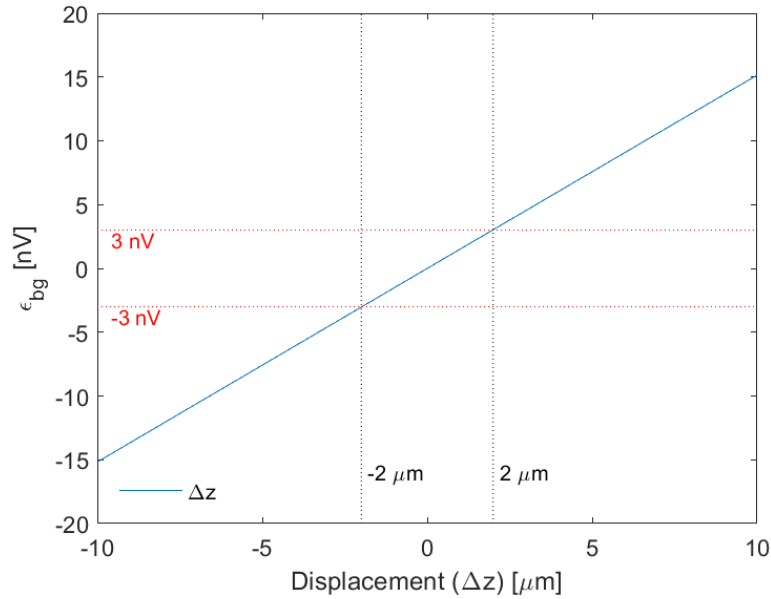
Fig 6.24 ε_{bg} for a misalignment in the z direction.

Here the calculated EMF is very slightly larger for a negative displacement than for an equivalent positive displacement as the field decay is non-linear, though it makes a negligible effect on these small length scales.

ε_{noise} is larger than $3\ [nV]$ at a z displacement $\Delta Z = \pm 2.0\ [\mu m]$. This provides a tolerance on the precision of the translation used to change coil distance in a detector using either method 1 or method 2. At this resolution, small effects such as the thermal expansion of the apparatus would need to be considered, meaning an optical measurement would be necessary. This would increase the complexity and cost of the instrument, which must be considered.

6.3.3. Differing coil areas

Lastly, we look to obtain a tolerance on the coil area. If the two detection coils have different area, an $\varepsilon_{bg,1}$ will be produced. This provides a tolerance for the fabrication of the coil sets. We consider both coils to be centred at the points $(0,0,\frac{OD}{2} \pm p)$, perfectly equidistant from the drive magnet surface. In this simulation, $p = 1\ [cm]$, with a drive magnet of $OD = 6\ [cm]$ and $L = 2\ [cm]$. We consider that coil 1 is defined by a circular area of radius $R_{coil,1} = 1\ [mm]$. The radius of coil 2 is varied from $0.95\ [mm] \leq R_{coil} \geq 1.05\ [mm]$ in $20\ [\mu m]$ increments. The resulting background voltage arising from a difference in coil areas are seen in Fig 6.25.
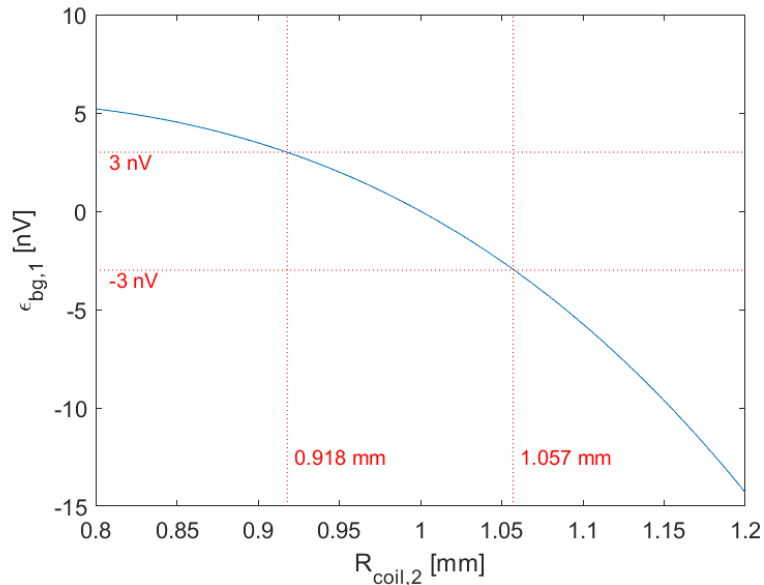
Fig 6.25 $\varepsilon_{bg,1}$ for coils that are perfectly aligned but possess different areas. The radius of coil 1 is fixed as $R_{coil,1} = 1 \, [mm]$.

Here we observe the noise due to differing coil areas to be smaller than the signal for $0.918 \, [mm] \geq R_{coil,2} \leq 1.057 [mm]$. This allows a large tolerance (8% smaller – 5% higher) due to the homogeneity of the drive field. This assumes a single circular coil – which could be produced using PCB processing techniques. To produce a coil set for this detector, any chosen fabrication process must be able to achieve a resolution less than $50 \, [\mu m]$.

6.3.4. Summary and build constraints

In this section, we have seen that the background due to misalignments in the system are sinusoidal and have an amplitude proportional to the difference in average fields within the two detection coils. We summarise the build tolerances in Table 6.1.

Misalignment	Δ to achieve $\varepsilon_{bg} = 3 \, [nV]$
ΔX	$\pm 230 \, [\mu m]$
ΔY	$\pm 300 \, [\mu m]$
ΔZ	$\pm 2 \, [\mu m]$
$\Delta R_{coil,2}$	$\pm 50 \, [\mu m]$

Table 6.1 Summary of build tolerances for parameters defining the detection coil location and size.

Here, we show that we are mostly dependent on the Z alignment – the drive magnet-detection coil separation. This requires extremely high tolerance, within $\Delta Z \leq \pm 2 \, [\mu m]$. An acetal piece part of $7.5 \, [mm]$ length would experience a $2 \, [\mu m]$ change in length for a $2.74 \, [K]$ temperature change (using a thermal expansion coefficient of $97.2 \, [\mu m/m/K]$ [4]). This demonstrates that the detector should be used in a stable thermal environment. If the detector were to employ method 2 – with changing detection coil distance, an advanced carriage assembly with optical alignment would be

required. This would be expensive and may present challenges when created from insulating materials.

It should be noted that there is a possibility that the signal may still be extracted digitally. Misalignment will produce ε_{bg} with a sinusoidal amplitude, at a frequency matching the drive field rotation. If the amplitude of ε_{bg} can be accurately obtained, it may be possible to digitally subtract the sinusoid background, leaving only the ε_{signal}. This could be achieved using phase-sensitive amplification, which would be able to distinguish between the background ε_{bg} and ε_{signal}, even though they share the same frequency. To demonstrate this idea, we present results for a non-ideal transition (as shown in Fig 6. 19b), with a $3\ [nV]$ background in Fig 6.26. In this, we consider that the AP-P is the same as the P-AP, i.e., there is no hysteresis.
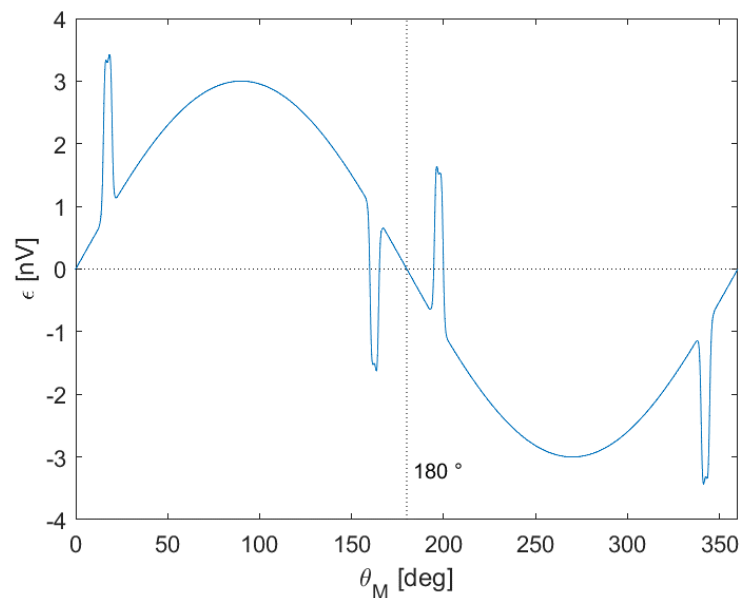
Fig 6.26 Combined signal and noise with $\varepsilon_{bg} = 3\ [nV]$. This assumes AP-P = P-AP, i.e. zero hysteresis.

We must also consider other noise sources that cannot be ignored. These include Johnson noise, shot noise and 1/f noise. These will be incoherent but must be considered in the total noise base for the system.

6.4. Virtual build process

6.4.1. Visualising our detector

In this section, we present a CAD model of a potential detector. This could be used as a foundation, should the project be taken forward. We propose that a system should move the equidistant coil sets in the same plane as the breadboard. This means that the effects of gravity on translation components are similar in both carriages and can be ignored.

The model is seen in Fig 6.27 and Fig 6.28. Drawings for each component are found in the appendix and should be used to identify each item.

6.4.2. Materials and processing

When constructing a device with a changing drive field, the eddy current generation in surrounding materials must be considered. Eddy currents arise in conducting materials that experience a changing magnetic field [5]. As we are looking to use a detection scheme with a rotating permanent magnet as a detection source, any conducting object surrounding the drive magnet could be a source of noise. For this reason, the device should be made of insulating material where possible. Insulating plastics such as Acetal provide a cheap, easily machinable solution. We suggest that the carriage assembly, bearing holder, motor holder and breadboard be made from insulating materials.
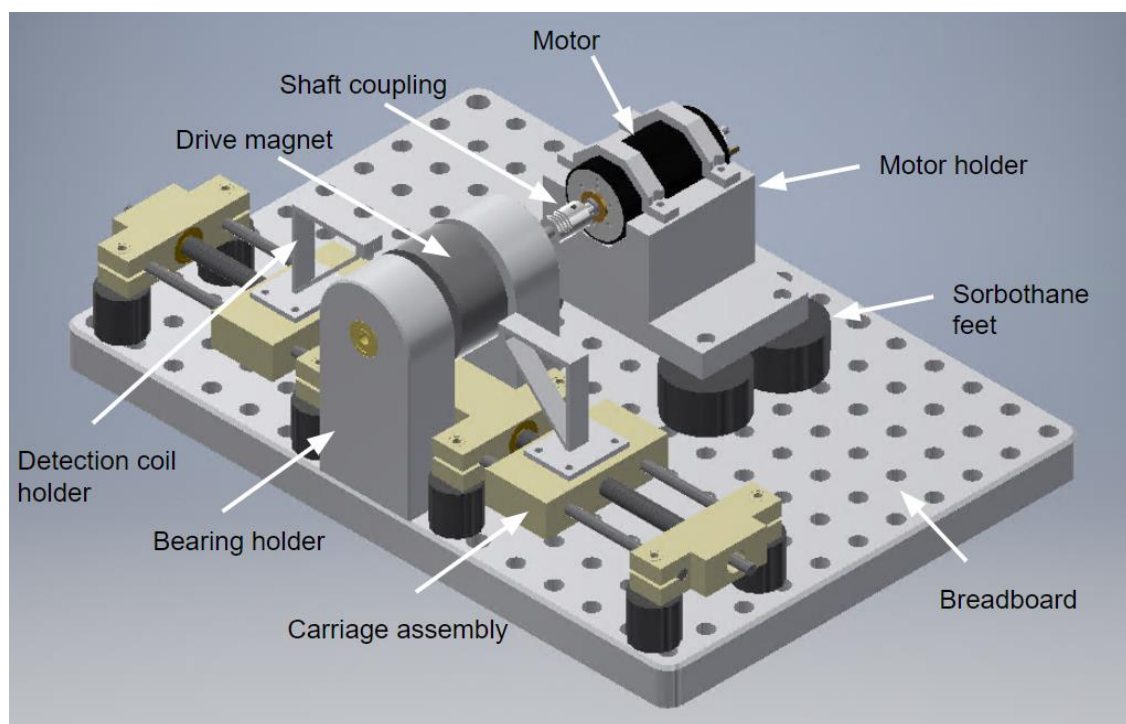
Fig 6.27 CAD model of a detector.
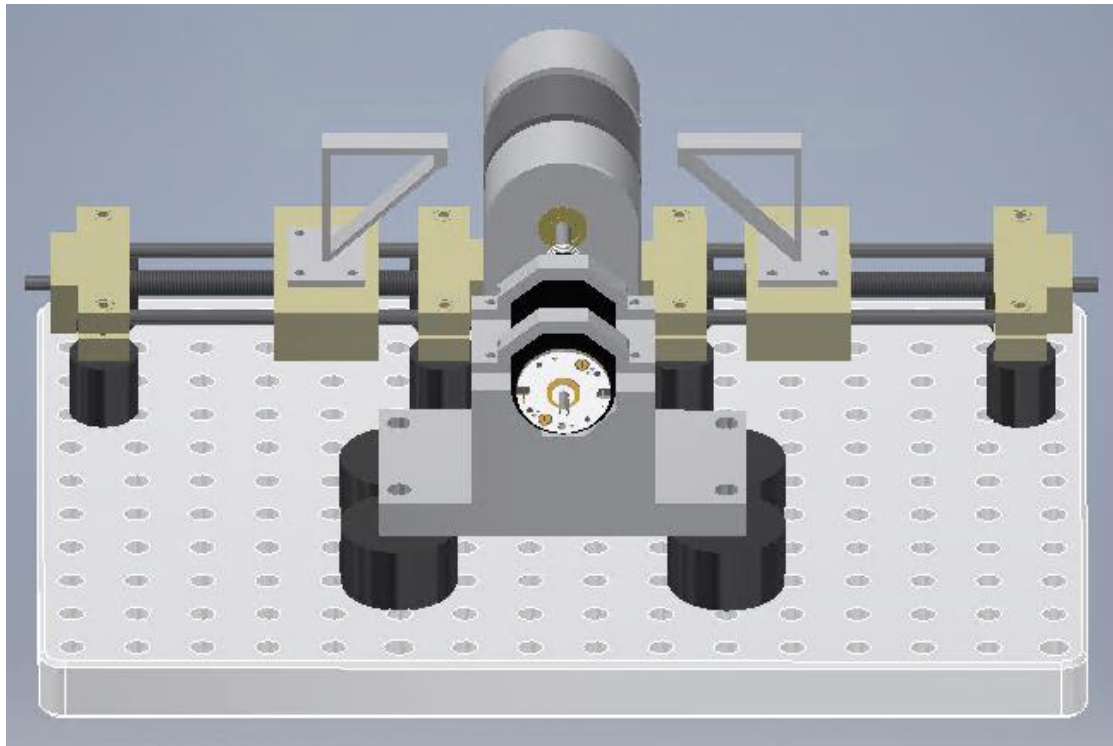
Fig 6.28 CAD model of the detector, viewing from the motor side.

An insulating breadboard can be easily produced using a CNC milling machine. Insulating bearings that are fully composed of ceramic or plastic can be used. These can be made of comparable quality to traditional metal ball bearings, though would require testing. As we have shown that the system has a low tolerance to any misalignment of the detection coils ($[\mu m]$ scale), the bearings should provide a minimum amount of wobble. To minimise any coupling between the vibrations of the motor and the detection coils, vibration dampening feet should be used on the motor holder stage and the carriage assembly.

The detector cannot avoid conducting materials entirely. A motor will be constructed of conducting materials but is positioned such that fields produced by the motor, or any other eddy current generation from the conducting materials (housing, etc), has a field small enough to be considered negligible at the detection coils. The motor is coupled to the drive magnet shaft using a flexible shaft coupling, which also will be made of metal. Shaft couplers are usually metallic to ensure that a minimum backlash and slack is produced. In this detector, the shaft coupler rotates in the same reference frame as the drive magnet, meaning that it should produce no eddy currents as it experiences no change in field.

The drive magnet would be produced from NdFeB that has been turned in a lathe. We have seen that our detection scheme is dependent on the effective nullification of the drive field. For this

reason, we must ensure that the drive magnet is machined well, with the inner bore within $\pm 2 \, [\mu m]$ of the true centre. NdFeB is a difficult material to turn as it chips, so all efforts must be made to fabricate this as well as possible.

The detection coil holders can be produced by additive manufacturing. We advise that Selective Laser Sintering (SLS) or Stereo-Lithography (SLA) 3D printing is used to create more accurate and repeatable piece parts. The holders that have been shown cannot be produced by traditional manufacturing methods (lathe, mill, etc), but the design could be adapted to be produced with these tools. Note that all piece parts can be constrained to one another using insulating components such as Nylon bolts.

We initially proposed a circular coil, which we assumed to be a single turn. The signal can be increased linearly by increasing the number of turns, but the average field will vary through each turn as the sample to coil distance increases. We propose that this can be overcome by using a spiralling coil that is produced using standard PCB production techniques. This would maintain a constant magnet to coil distance for all coils but increases the path length of the coil. This has been done in practice and is used in many RFID applications [6]–[8].

6.5. Viability and expectations

In this chapter, we have calculated the expected signal from a collection of ~ 1000 particles and compared this with the noise generated from detection coil misalignment. We have seen that a signal would have a peak magnitude of $\sim 3 \, [nV]$ for a 20 $[Hz]$ drive magnet speed. This value is small but can be detected with a low-bandwidth amplifier ($\sim 0.01 \, [Hz]$). However, we observe that the background due to misalignment is larger than the signal for displacements of $\Delta X \geq 230 \, [\mu m]$, $\Delta Y \geq 300 \, [\mu m]$, $\Delta Z \geq 2 \, [\mu m]$ and $\Delta R_{coil} \geq 50 \, [\mu m]$. This provides a tolerance for these values, which must be considered in the construction of a device.

Of most concern is the ΔZ tolerance. All other values can be constrained with relative ease through correct design, manufacturing, and calibration. However, a Z tolerance of $\pm 2 \, [\mu m]$ would be unachievable without extremely precise instrumentation. At this level of accuracy, the thermal expansion of the piece parts must be considered. An acetal piece part of 7.5 $[mm]$ length would experience a 2 $[\mu m]$ change in length for a 2.74 $[K]$ temperature change. This would only be achievable with optical instrumentation. In chapter 5, we showed that the possible number of channels η can be increased dramatically by using a changing coil separation throughout the measurement. The alignment in each measurement would need to be accurate to $\Delta Z \leq \pm 2 \, [\mu m]$.

The background due to misalignment is sinusoidal, and therefore could be reduced with digital post-processing. We propose that the detector is not viable in its current form as the build tolerance for the ΔZ of the coil sets is too stringent. If the detector was to be constructed, insulating materials should be used where possible to limit the generation of eddy currents. The system should also be vibration isolated where possible. It would be advised to first attempt to obtain a signal from a single channel, with static and precisely calibrated detection coils. This will help to obtain the true order of magnitude of ε_{bg} from combined sources, and test whether the subtraction of a pure sinusoid is beneficial.

[1]   J.-P. Akoun, G.; Yonnet, "3D analytical calculation of the forces exerced between two cuboidal magnets," *Magn. IEEE Trans.*, vol. MAG-20, no. 5, pp. 1962–1964, 1984, doi: 10.1109/TMAG.1984.1063554.

[2]   J. L. G. Janssen, *Extended Analytical Charge Modeling for Permanent-Magnet Based Devices Practical Application to the Interactions in a Vibration Isolation System*, no. december. 2011.

[3]   K. F. Eid, M. Panth, and A. D. Sommers, "The physics of water droplets on surfaces: exploring the effects of roughness and surface chemistry," European Journal of Physics, 2018, doi: 10.1088/1361-6404/aa9cba.

[4]   W. Hampshire, "Acetal datasheet." https://www.wshampshire.com/wp-content/uploads/acetal_grades.pdf (accessed Jun. 24, 2021).

[5]   H. Zijilstra, *Experimental Methods in Magnetism: Measurement of magnetic quantities - H. Zijlstra - Google Books*. North-Holland Pub. Co., 1967.

[6]   H. Jiang *et al.*, "Miniaturizing RFID for magnamosis," in *2014 36th Annual International Conference of the IEEE Engineering in Medicine and Biology Society, EMBC 2014*, Nov. 2014, pp. 638–641, doi: 10.1109/EMBC.2014.6943672.

[7]   K. Fotopoulou and B. Flynn, "Optimum antenna coil structure for inductive powering of passive RFID tags," in *2007 IEEE International Conference on RFID, IEEE RFID 2007*, 2007, pp. 71–77, doi: 10.1109/RFID.2007.346152.

[8]   N. Gvozdenovic, R. Prestros, and C. F. Mecklenbrauker, "HF RFID spiral inductor synthesis and optimization," in *International Symposium on Wireless Personal Multimedia Communications, WPMC*, Jan. 2015, vol. 2015-January, pp. 53–59, doi: 10.1109/WPMC.2014.7014790.

Chapter 7.

Conclusion

Aims of this thesis

This work aimed to design a covert, encodable tag that utilises novel magnetic information carriers. The project requires that these be invisible to the naked eye (to avoid mechanical tampering), be able to be suspended in solution and be distinguishable with modulation of a magnetic property. We proposed that these would consist of perpendicularly magnetised synthetic antiferromagnetic microparticles, which could be lifted off of a substate and into a solution for reapplication onto a tagging surface. SAF particles are made of two nominally identical magnetic layers whose magnetisation is antiferromagnetically coupled through a non-magnetic spacer layer. These have an antiparallel magnetisation configuration when no field is applied, with zero net moment. The particles should maintain the zero net moment until transitioning to a parallel magnetisation at a field equal to the coupling field between the two layers. We control the coupling field by management of the particle architecture, allowing for transitions at differing field values.

The transitions at differing field values would form the basis of our encryption scheme. Each particle could be identified by the presence or absence of a transition at a particular field strength, giving a 1, or 0. Particle solutions of n distinct coupling strengths could be produced and mixed in 2^n combinations to create an n-bit code. This would be comparable to a barcode of length n identifiers.

The project also requires a suitable detector. Current technology to characterise magnetic nano/microparticles is lab-based, usually large/static, expensive and highly technical. We looked into a potential detection scheme that could be used in an industrial setting, which would be more compact, less expensive and could be used off the shelf. We assess the viability of such a detector using computational simulation, aimed to present a detector virtually through Computer-Aided Design (CAD).

Particle fabrication

To ensure that the encryption scheme was viable, we needed to ensure that the particles could be effectively synthesised. Firstly, we confirmed the presence of strong PMA, with large anisotropy fields H_K. We demonstrated that the magnetic layers are effectively insensitive to in-plane field components through the measurement of rotating switching astroids. This means that drive fields with non-zero IP field components, such as a rotating permanent magnet, could be used with these particles.

We next demonstrated that the magnetic layers could be indirectly coupled, producing PMA SAF thin films. We confirmed the ability to control coupling strength through modulation of the Pt spacer layer thickness in a $CoFeB(1)/Pt(\mathbf{t_{Pt}})/Ru(0.8)/Pt(\mathbf{t_{Pt}})/CoFeB(1)$ magnetic stack with a Ta seed layer and Ta/Pt capping layers. Sharp switching was observed at clearly defined field values dependent on the spacer layer thickness. The films showed zero susceptibility at fields below the coupling field, allowing for an 'off' or 0 state below this and an 'on' or 1 state above this, with a sharp transition between both states, as expected. The transitions were modelled using a logistical sigmoid to quantify their location and sharpness, showing a decay of coupling strength that is consistent with literature values.

To miniaturise the particles, top-down lithography techniques were employed. We confirmed that the patterning process did not significantly affect the magnetic properties, with only a small reduction in transition sharpness. In these studies, no bleaching was seen between channels, confirming that we can effectively distinguish between neighbours. This was again confirmed for particles grown on a Ge release layer, which could be used to lift the particles into solution.

To further confirm that our particles were suitable for use with rotating field systems, we measured the transitions for a collection of ~40000 particles (on-chip) for both linear and rotating field systems. These results showed a benefit to measuring the AP-P transition as opposed to the P-AP. To try to understand why the P-AP transition is disproportionately affected by patterning, we obtained information about the inter-particle variation through analysis of distributions of many individual MOKE measurements. This difference was found to be less affected by variation in transition width for single particles (a) but by the location of the transition (c), which had a much larger variance in the P-AP transition than in the AP to P. The variation was stark and showed a minimum of 250% increase in variation between the AP-P and P-AP average transition widths.

We lastly measured the rotational switching astroids for SAF films and particles. These followed the expected order of transitions, evidence that our SAF films and particles are also insensitive to IP field components and compatible with rotating field sources. From these, we can confirm that rotating

fields provide a viable method to distinguish different channels, with transitions being separated by more than their transition widths for many films in a series with differing Pt thicknesses.

We displayed results for 8 functional channels, but this is by no means the physical limit. This could be improved with a finer Pt growth resolution, so long as the interfacial properties are maintained.

Modelling of a detector

The proposed device consists of a rotating drive field from a rotating cylindrical permanent magnet, and inductive pick-up coils. To understand how our particles may interact with the drive field, we first modelled the field from the permanent magnet and correlated this to an ideal particle set. These calculated drive fields were used to simulate the switching of an assembly of SAF particles distributed over a sample area as a function of permanent magnet angle. The Normalised Switched Area (NSA) was defined, which allowed the characterisation of the transition, and in particular its width ($W_{0.3-0.7}$). We then assessed the progression of switching fields for an ideal parameter set, given a separation relative to their $W_{0.3-0.7}$. The number of possible channels η provides a figure of merit that allowed us to assess the efficacy of our device for different input geometries and different detection methods.

Using our figure of merit η, we were able to compare different measurement styles as well as assess the ideal detector parameters, such as magnet length, magnet outer diameter, sample radius, start field, etc. We initially tested the measurement scheme, comparing the number of possible detectable channels when measuring all channels in a single measurement in a single rotation of the magnet, and comparing this with a measurement using changing magnet to sample distance.

Next, we assessed the figure of merit η for various changes to the input geometry. We suggested that any changes to the device that increased homogeneity, or the angular variation in the field would lead to smaller transition widths ($W_{0.3-0.7}$) and higher η. This was first tested for a simulation using simple constraints, with no working range limit or minimum separation but using a 25 [Oe] minimum channel field. In these simulations, larger magnet diameters or magnet lengths produced larger η values, with improved average homogeneity throughout the series. These series had an unachievably small separation between channels. For this reason, we repeated the simulations with the addition of practical constraints consisting of a minimum separation between channels of $50\ [Oe]$, and a stop condition when a working range for the detector was exceeded ($p = 10\ [cm]$). In these simulations, increasing OD produced more homogenous fields, monotonically increasing η, whereas increasing L showed a parabolic relationship with η, first increasing the number of channels and then falling. Changes in OD had a much more pronounced effect on η than changes in L, though the optimum L for a given OD was presented.

We next observed an increasing channel number as the sample radius decreases. This was expected, as a smaller, more homogenous region of the field profile is sampled for smaller s_{rad}. For changing start field, we observed increasing η with increasing start channel value B_0 up to $B_0 = 0.3\ [T]$. This suggests that a starting channel $B_0 = 0.3\ [T]$ is sufficient, though there is no detrimental effect of higher values which allow for easier particle fabrication.

We next introduced non-ideal particles. Zadeh's fuzzy logic was employed, representing the transitions with logistical sigmoid membership functions. In this section, only simulations with practical constraints were performed. We observed similar findings to the ideal particle study, though with much smaller η values.

Field calculations were also used to estimate the expected signal from a collection of ~ 1000 particles. This could be used to compare with the noise generated from detection coil misalignment. We have seen that the signal would have a peak magnitude of $\sim 3\ [nV]$ for a 20 $[Hz]$ drive magnet rotating frequency. This value is small but can be detected with a low-bandwidth amplifier ($\sim 0.01\ [Hz]$). This value can also be increased by increasing the magnetic moment of each particle. Each SAF must maintain magnetic layer thicknesses of $\sim 1\ [nm]$ to maintain the PMA, but the magnetic volume can be increased using larger particles (lateral dimensions) or by growing multiple stacks on top of one another (multilayering).

We observed that the background due to misalignment is larger than the signal for displacements of $\Delta X \geq 230\ [\mu m]$, $\Delta Y \geq 300\ [\mu m]$, $\Delta Z \geq 2\ [\mu m]$ and $\Delta R_{coil} \geq 50\ [\mu m]$. This provides a tolerance for these values, which must be considered in the construction of a device. Of most concern was the ΔZ tolerance. All other values can be constrained with relative ease through correct design, manufacturing, and calibration. However, a Z tolerance of $\pm 2\ [\mu m]$ would be unachievable without extremely precise instrumentation. At this level of accuracy, the thermal expansion of the piece parts must be considered. An acetal piece part of 7.5 $[mm]$ length would experience a 2 $[\mu m]$ change in length for a 2.74 $[K]$ temperature change. This would only be achievable with optical instrumentation. This is especially problematic as we have already noted that we hoped to make multiple measurements at different drive-magnet to sample heights to obtain higher η. The alignment in each measurement would need to be accurate to $\Delta Z \leq \pm 2\ [\mu m]$.

The background due to misalignment should be sinusoidal, which could be reduced with digital post-processing. We propose that the detector is not viable in its current form as the build tolerance for the Δz of the coil sets is too stringent. If the detector was to be constructed, insulating materials should be used where possible to limit the generation of eddy currents. The system should also be vibration isolated where possible. It would be advised to first attempt to obtain a signal from a single

channel, with static and precisely calibrated detection coils. This will help to obtain the true order of magnitude of ε_{bg} from combined sources, and test whether the subtraction of a pure sinusoid is beneficial.

We expect that with an improvement to the control of Pt interlayer growth, we can expect to be able to produce close to 20 channels. Using a presence/absence detection scheme, this allows for 2^{20} ($\sim 10^6$) possible combinations. This could be improved by using a volumetric detection scheme, but the efficacy of the system would need empirically testing before this can be considered.

Future work

This thesis presents an encryption technology, as well as a study of its suitability for use in a rotating field environment. We observe distinct transitions from 8 different channels within this thesis, though this is certainly not an upper limit. Further channels could be introduced if the growth resolution of Pt is improved. The ability to create channels using the second AF RKKY peak also presents an interesting area of research, as more channels could be introduced at low fields [1].

The next stage for the project is the prototyping of a detector – whether employing the design outlined in this work or a new design. In this work, we have outlined the potential benefits of the use of a permanent magnet-based drive field but seen that the tight spatial requirements may introduce large backgrounds, leading to low signal to noise ratios.

Additionally, measurements of an ensemble of particles with different switching values should be completed. By measuring all of the particles at once using a method such as VSM, we can also obtain further information on the distribution of switching parameters within a particle set. This should be complemented with rotational switching astroids of the patterned particle ensembles, which would be more representative of the results seen in our proposed detector.

In conclusion, we have presented an effective system to encode information in a liquid suspension using magnetic microparticles. These are distinct from one another and found to be suitable for use in rotating field environments. A potential detection scheme has been simulated, followed by a virtual build process. We consider the particles to be highly successful, but with room for improvement. The particles shown in this work could have applications that extend further than their intended usage. such as security tagging and multi-assay bio-sensing technology which is a field of high interest.

[1]   E. N. Welbourne, "Antiferromagnetic nanodiscs with perpendicular magnetic anisotropy for

biological applications," PhD thesis, University of Cambridge, December 2020.

Appendix

Caciagli equations, from [1]

In chapter 3, we briefly introduced the equations used to calculate the magnetic field from a uniformly magnetised cylinder, deduced by Caciagli, et al.

$$\Phi = \frac{MRcos(\varphi)}{\pi}[\beta_+ P_4(k_+) - \beta_- P_4(k_-)]$$

A.1

Using the relationship $H = -\nabla\Phi$, the field components for pure transverse magnetisation are found to be:

$$H_\rho = \frac{\partial\Phi}{\partial\rho} = \frac{MRcos(\varphi)}{2\pi\rho}[\beta_+ P_4(k_+) - \beta_- P_4(k_-)]$$

A.2

$$H_\varphi = -\frac{1}{\rho}\frac{\partial\Phi}{\partial\varphi} = \frac{MRsin(\varphi)}{\pi\rho}[\beta_+ P_3(k_+) - \beta_- P_3(k_-)]$$

A.3

$$H_z = -\frac{\partial\Phi}{\partial z} = \frac{MRcos(\varphi)}{\pi}[\alpha_+ P_1(k_+) - \alpha_- P_1(k_-)]$$

A.4

These use the auxiliary functions

$$P_1(k) = \kappa - \frac{2}{1-k^2}(\kappa - \varepsilon)$$

A.5

$$P_4(k) = \frac{\gamma}{1-\gamma^2}(P - \kappa) - \frac{\gamma}{1-\gamma^2}(\gamma^2 P - \kappa) - P_1(k)$$

A.6

$$P_3(k) = \frac{1}{1-k^2}(\kappa - \varepsilon) - \frac{\gamma^2}{1-\gamma^2}(P - \kappa)$$

A.7

$$P_4(k) = \frac{\gamma}{1-\gamma^2}(P - \kappa) + \frac{\gamma}{1-\gamma^2}(\gamma^2 P - \kappa) - P_1(k)$$

A.8

where,

$$\zeta_\pm = z \pm L$$

A.9

$$\alpha_\pm = \frac{1}{\sqrt{\xi_\pm^2 + (\rho + R)^2}}$$

A.10

$$\beta_\pm = \zeta_\pm \alpha_\pm$$

A.11

$$\gamma = \frac{\rho - R}{\rho + R}$$

A.12

$$k_\pm^2 = \frac{\xi_\pm^2 + (\rho - R)^2}{\xi_\pm^2 + (\rho + R)^2} \qquad \text{A.13}$$

and the symbols κ, ε and P represent the evaluation of the complete elliptical integrals of the first, second and third kind, as

$$\kappa = \mathrm{K}\left(\sqrt{1 - k^2}\right) \qquad = \int_0^{\frac{\pi}{2}} \frac{d\theta}{\sqrt{1 - (1 - k^2)\sin^2(\theta)}} \qquad \text{A.14}$$

$$\varepsilon = \mathrm{E}\left(\sqrt{1 - k^2}\right) \qquad = \int_0^{\frac{\pi}{2}} d\theta \sqrt{1 - (1 - k^2)\sin^2(\theta)} \qquad \text{A.15}$$

$$\mathrm{P} = \Pi\left(1 - \gamma^2, \sqrt{1 - k^2}\right) = \int_0^{\frac{\pi}{2}} \frac{d\theta}{(1 - (1 - \gamma^2)\sin^2(\theta)\sqrt{1 - (1 - k^2)\sin^2(\theta)}} \qquad \text{A.16}$$

These equations are all written as functions, with the appropriate caveats to ensure that division by zero is not possible.

Rewriting the generalised elliptical integral, from [1]

In Caciagli's paper, the derivation uses the complete elliptical integrals of the first, second and third kinds, to replace the expression given by Derby and Olbert for the field from a longitudinally magnetised cylinder [2]. In their work, Derby and Olbert present the generalised complete elliptic integral (k_c, p, c, s), with

$$C(k_c, p, c, s) = \int_0^{\frac{\pi}{2}} d\varphi \frac{c \cos^2(\varphi) + s \sin^2(\varphi)}{\sqrt{\cos^2(\varphi) + k_c^2 \sin^2(\varphi)} \left(\cos^2(\varphi) + p \, \sin^2(\varphi)\right)} \qquad \text{A.17}$$

For the evaluation of β_ρ, $C(k_\pm, 1, 1, -1)$ is required, simplifying to

$$\int_0^{\frac{\pi}{2}} d\varphi \frac{\cos^2(\varphi) - \sin^2(\varphi)}{\sqrt{\cos^2(\varphi) + k_\pm^2 \sin^2(\varphi)} \left(\cos^2(\varphi) + \sin^2(\varphi)\right)} \qquad \text{A.18}$$

A change in the variable is made using $\sin(\varphi) = x$, leading to

$$\int_0^1 \frac{dx}{\sqrt{1 - x^2}} \frac{(1 - x^2) - x^2}{\sqrt{(1 - x^2) + k_\pm^2 x^2} \left((1 - x^2) + x^2\right)} \qquad \text{A.19}$$

$$\int_0^1 \frac{dx}{\sqrt{1-x^2}} \frac{(1-x^2) - x^2}{\sqrt{(1-x^2) + k_\pm^2 x^2} \left((1-x^2) + x^2\right)}$$

A.20

$$= \int_0^1 dx \frac{1}{\sqrt{(1-x^2)\left(1 - \left(1 - k_\pm^2\right) x^2\right)}}$$

$$- 2 \int_0^1 dx \frac{x^2}{\sqrt{(1-x^2)\left(1 - \left(1 - k_\pm^2\right) x^2\right)}}$$

A.21

These integrals can be solved immediately using tabulated functions, giving,

$$C(k_\pm, 1, 1, -1) = \mathrm{K} - 2\left(1 - k_\pm^2\right)^{-1}(\mathrm{K} - \mathrm{E})$$

A.22

Where the substitutions given in chapter 3 are made. This is used as $P_1(k)$.

To evaluate B_z, $C(k_\pm, \gamma^2, 1, \gamma)$ is required, resulting in

$$\int_0^{\frac{\pi}{2}} d\varphi \frac{\cos^2(\varphi) + \gamma \sin^2(\varphi)}{\sqrt{\cos^2(\varphi) + k_\pm^2 \sin^2(\varphi)} \left(\cos^2(\varphi) + \gamma \sin^2(\varphi)\right)}$$

A.23

Again, a change in the variable is made using $\sin(\varphi) = x$, leading to

$$\int_0^1 \frac{dx}{\sqrt{1-x^2}} \frac{(1-x^2) - \gamma x^2}{\sqrt{(1-x^2) + k_\pm^2 x^2} \left((1-x^2) + \gamma^2 x^2\right)}$$

A.24

$$= \int_0^1 dx \frac{1}{\sqrt{(1-x^2)\left(1 - \left(1 - k_\pm^2\right) x^2\right)(1 - (1 - \gamma^2) x^2)}}$$

$$- 2 \int_0^1 dx \frac{x^2}{\sqrt{(1-x^2)\left(1 - \left(1 - k_\pm^2\right) x^2\right)(1 - (1 - \gamma^2) x^2)}}$$

A.25

Evaluating these integrals leads to the final result, which is used as $P_2(k)$.

$$C(k_{\pm}, \gamma^2, 1, \gamma) = P - (1 + \gamma) \frac{1}{1 - \gamma^2} (P - K)$$

$$= \frac{1 - \gamma^2}{1 - \gamma^2} P - \frac{1}{1 - \gamma^2} (P - K) - \frac{\gamma}{1 - \gamma^2} (P - K) \qquad \text{A.26}$$

$$= \frac{1}{1 - \gamma^2} (\gamma^2 P - K) - \frac{\gamma}{1 - \gamma^2} (P - K)$$

Note, that in all cases, the evaluation of the integral at $\gamma = \pm 1$, i.e. where $\rho = R$, leads to a division by zero. This means that fields on the surface of the cylinder cannot be probed using these equations.

Rotation matrices, from [3]

Cartesian coordinates were converted to cylindrical using

$$\rho = \sqrt{x^2 + z^2} \qquad \text{B.1}$$

$$\phi = \tan^{-1} \left(\frac{x}{z} \right) \qquad \text{B.2}$$

$$y = y \qquad \text{B.3}$$

With unit vector conversion using

$$\begin{bmatrix} \hat{\rho} \\ \hat{\phi} \\ \hat{y} \end{bmatrix} = \begin{bmatrix} sin(\phi) & 0 & cos(\phi) \\ cos(\phi) & 0 & -sin(\phi) \\ 0 & 1 & 0 \end{bmatrix} \begin{bmatrix} \hat{x} \\ \hat{y} \\ \hat{z} \end{bmatrix} \qquad \text{B.4}$$

and 3D vector field components in cylindrical co-ordinates converted to Cartesian using

$$\begin{bmatrix} B_x \\ B_y \\ B_z \end{bmatrix} = \begin{bmatrix} sin(\phi) & cos(\phi) & 0 \\ 0 & 0 & 1 \\ cos(\phi) & -sin(\phi) & 0 \end{bmatrix} \begin{bmatrix} B_\rho \\ B_\phi \\ B_y \end{bmatrix} \qquad \text{B.5}$$

[1]   A. Caciagli, R. J. Baars, A. P. Philipse, and B. W. M. Kuipers, "Exact expression for the magnetic field of a finite cylinder with arbitrary uniform magnetization," *J. Magn. Magn. Mater.*, vol. 456, pp. 423–432, Jun. 2018, doi: 10.1016/j.jmmm.2018.02.003.

[2]   N. Derby and S. Olbert, "Cylindrical Magnets and Ideal Solenoids," *Am. J. Phys.*, vol. 78, no. 3, pp. 229–235, Sep. 2009, doi: 10.1119/1.3256157.

[3]   D. Fleisch, *A Student's Guide to Maxwell's Equations*. Cambridge University Press, 2008.

Particle sizes and separation

a)

b)

c)

d)

e)

f)
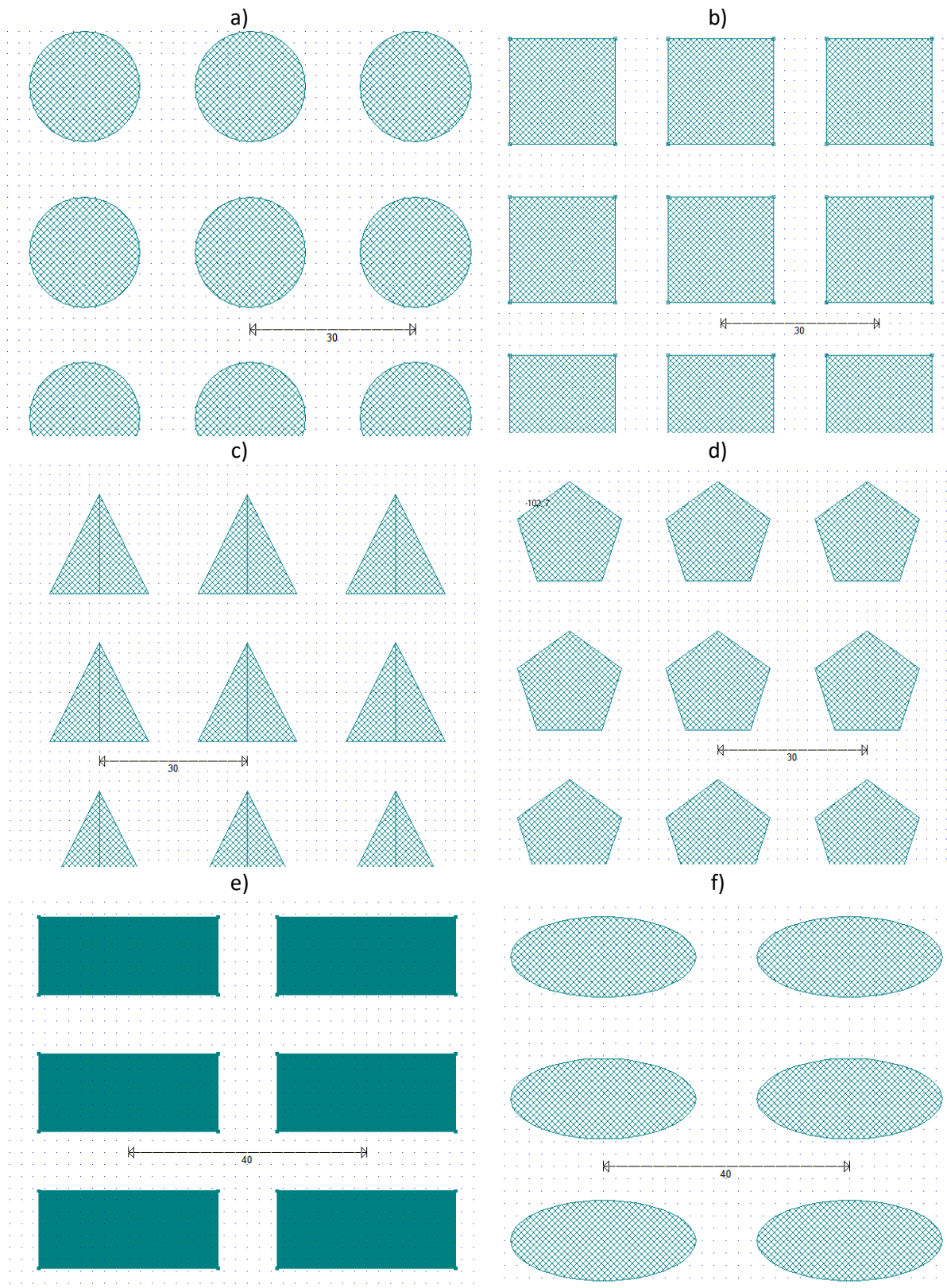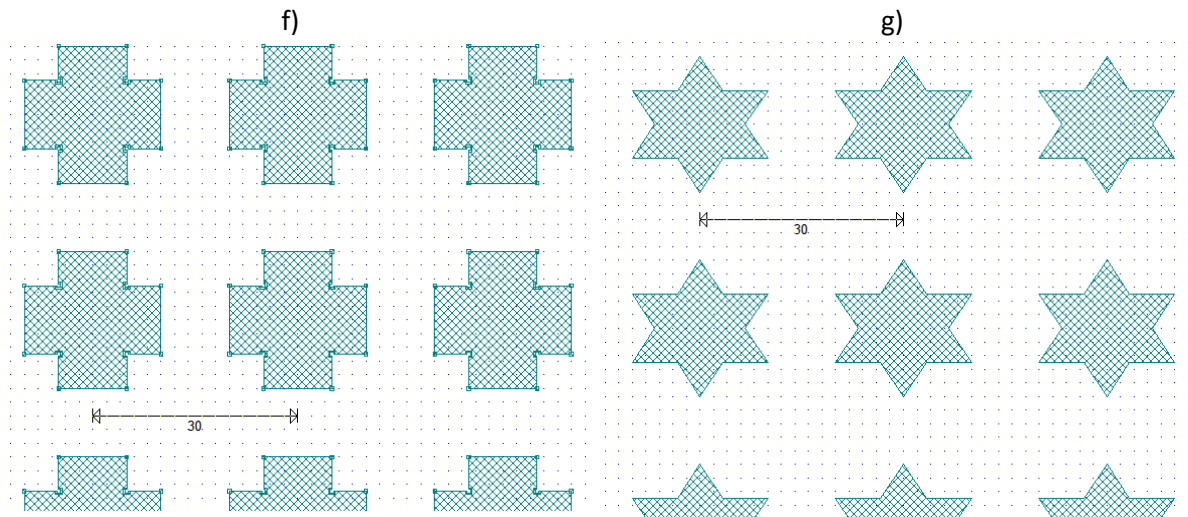
Clewin files for each particle in the series, with increasing platinum thickness.

Toroidal validation, at an angle of magnetisation.
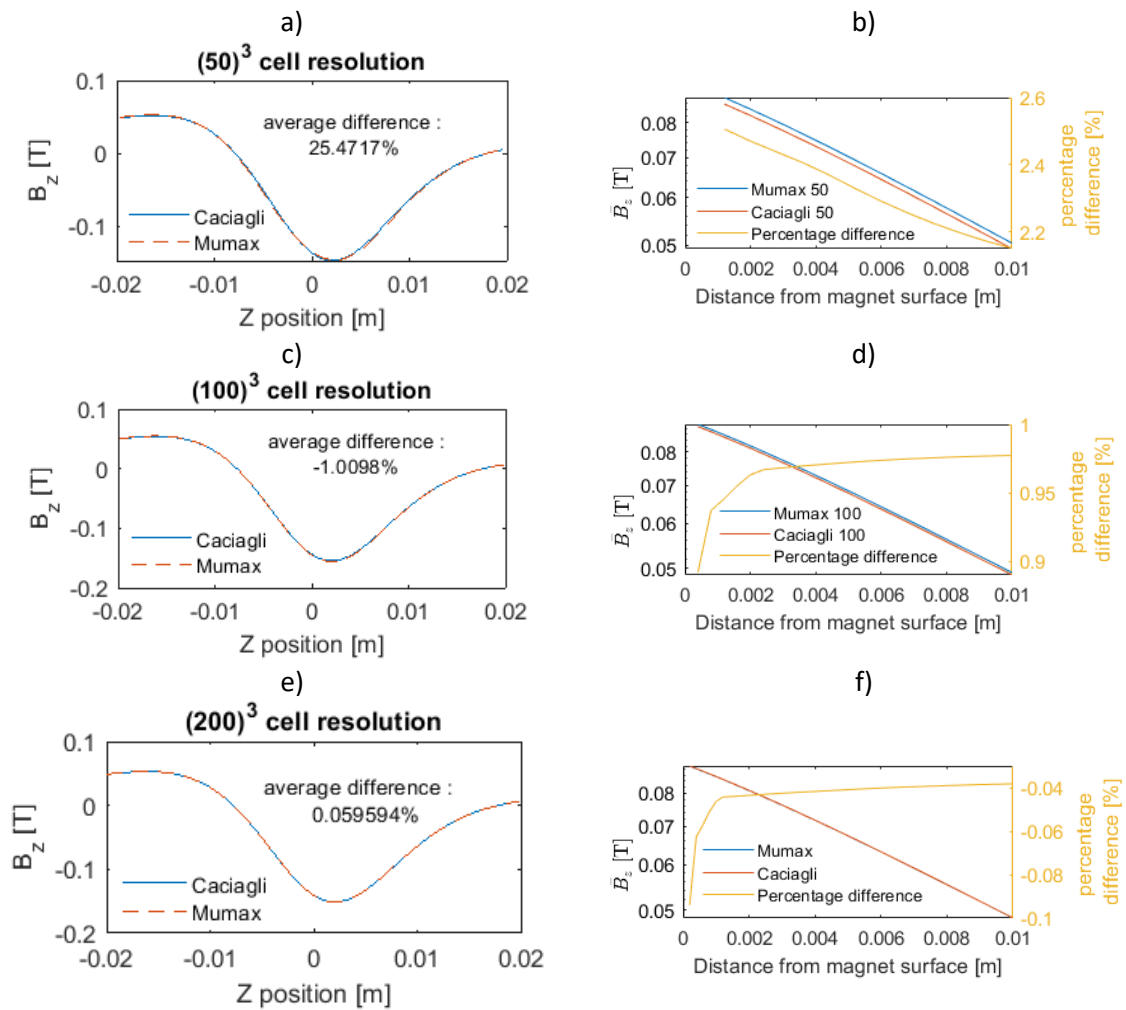
Linescan comparisons (a,c,e) and planar average field values $\overline{B_z}(x,y,p)$ (b,d,f) for differing world cell numbers and a magnetisation angle of 23[deg] for a toroidal geometry. The linescan comparisons were taken at a value (5.6,0.8)[mm] above the magnet surface in X and Y respectively. The mean fields are taken as an average in the XY plane, for changing magnet to surface distance in Z.
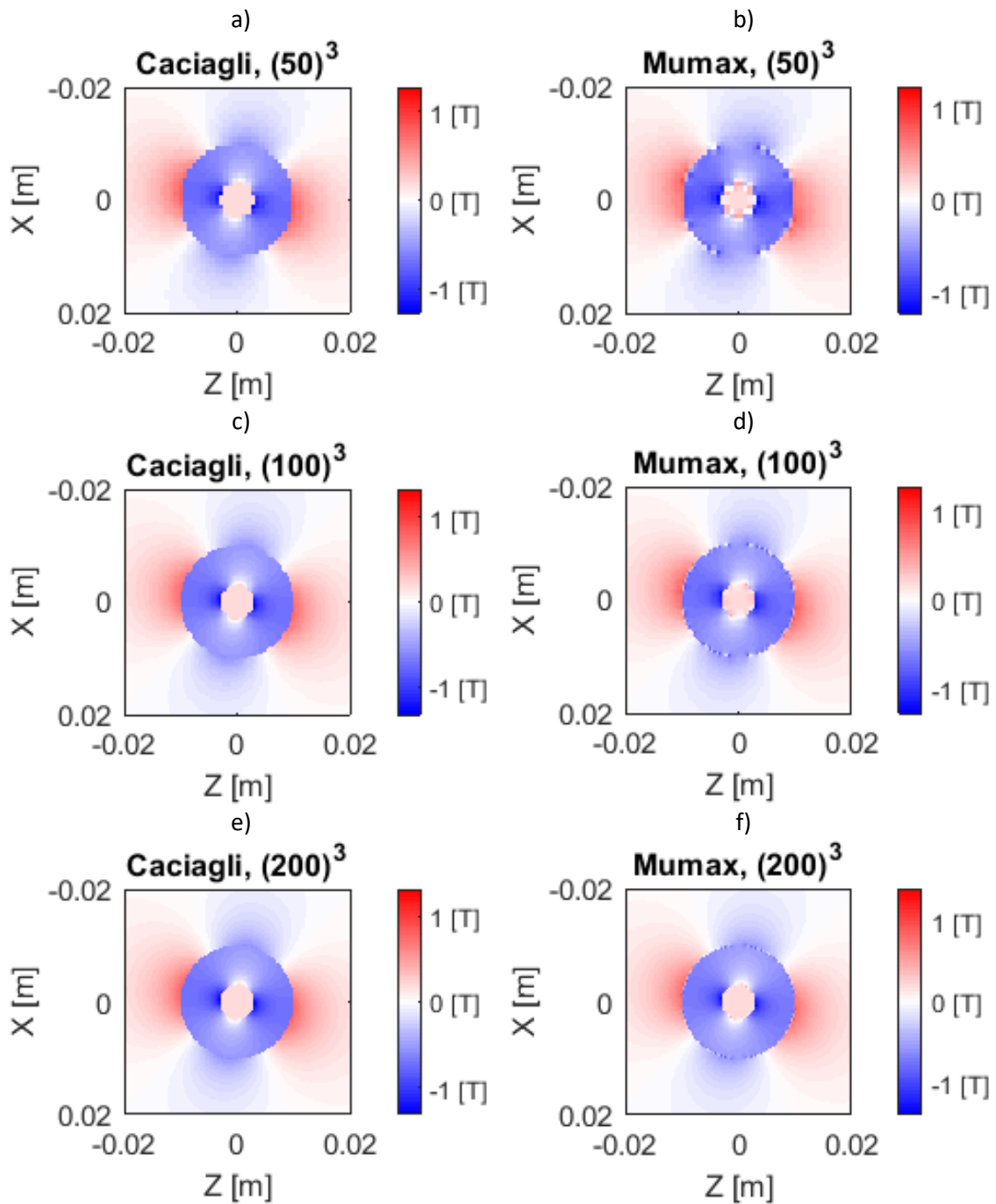
A close up of the differences in the magnet boundaries between both models for an angular magnetisation rotation of 23[deg] for toroidal geometries. These take an XZ cross-section through the magnet for various cell numbers

Detector piece part drawings

Plane A

300.00
37.50
12.50
37.50
12.50
300.00
25.00

144 6mm holes through
- 2mm C-sink one side
- 10mm deep 10.5mm OD C-bore on other
- 25mm spacing in X and Y
- starting 12.5mm from edge

4 corner 6.6mm through holes
- 10mm deep 11mm OD C-bore
- opposite face to above holes

Plane A

Plane B

Ø11.00 ⊽ 10.00
Ø6.60 ⊽ 25.00
Plane B
Ø10.50 ⊽ 10.00
Ø6.00 ⊽ 25.00

25.00

3mm fillet on corners

25.00

1mm chamfer on all outer edges
3mm fillet on 4 corners

DRAWN Jake	01/08/2019				
CHECKED		TITLE			
QA					
MFG					
APPROVED					
		SIZE A4	DWG NO Acetal_Breadboard_30x30		REV
		SCALE 1 / 4		SHEET 1 OF 1	

DRAWN Jake	23/10/2019				
CHECKED		TITLE			
QA					
MFG					
APPROVED					
		SIZE A4	DWG NO new_translation_assy_V1		REV
		SCALE 1 /1.2		SHEET 1 OF 1	

TOP VIEW

10.00
7.50
42.50
60.00
15.00
7.50
7.50

M4x0.7 - 6H
Ø4.00 ↧ 10.00
Ø9.00 ↧ 5.00
Ø5.00 ↧ 15.00

SIDE VIEW
TOP VIEW
BOTTOM VIEW

SIDE VIEW

50.00
61.72
78.28
64.60
15.00
7.50
16.57
44.60
56.32
64.60
35.00
105.00
140.00

70.00
140.00

Model has a four fold symmetry.

Enlarged side view on sheet 2.

DRAWN		
Jake	01/08/2019	
CHECKED		
QA		TITLE
MFG		
APPROVED		
	SIZE A4	DWG NO motor holder base V4	REV
	SCALE 1 / 2	SHEET 1 OF 2

PLANE A

Ø19.00 ↧ 30.00
R30.00
120.00
90.00

PLANE B

Ø19.00 ↧ 30.00
Ø19.00 ↧ 30.00
120.00
90.00
20.00
12.50
30.00
70.00
100.00

PLANE A
PLANE B
PLANE C

Outer edges with 1mm chamfer

Object is four fold symmetric

PLANE C

M6x1 - 6H
Ø6.00 ↧ 25.00 X4
17.50
12.50

All same distances from edges

DRAWN		
Jake	01/08/2019	
CHECKED		
QA		TITLE
MFG		
APPROVED		
	SIZE A4	DWG NO U_shaped_bearing_holder_V2	REV
	SCALE 1 / 2	SHEET 1 OF 1

Ø=1.00
45.4°
50.00
53.00
3.00
14.00
25.00
5.00
2.50
26.00
5.00
40.00
Ø=4.00
13.50
61.00
30.00

DRAWN Jake	21/06/2021				
CHECKED		TITLE			
QA					
MFG					
APPROVED					
		SIZE **A4**	DWG NO **coil holder**		REV
		SCALE 1 : 1		SHEET 1 OF 1	

80.00
74.00
65.00
40.00
15.00
6.00
Ø12.00 ⊽ THRU
9.50
10.50
11.50
21.00
5.00
Ø19.00 ⊽ 6.00
R3.00 ⊽THRU
30.00
20.00
Ø5.00 ⊽ 25.00
⌴ Ø8.00 ⊽ 5.00
10.00
20.00
60.00
80.00
10.00
30.00

DRAWN Jake	18/10/2019				
CHECKED		TITLE			
QA					
MFG					
APPROVED					
		SIZE **A4**	DWG NO **End Block**		REV
		SCALE 1 : 1		SHEET 1 OF 1	

Runners

DRAWN		
Jake	18/10/2019	
CHECKED		TITLE
QA		
MFG		
APPROVED		
		SIZE A4	DWG NO Runners	REV
		SCALE 1 : 1	SHEET 1 OF 1

M10x1.5 - 6H
Ø10.00 ▼ THRU
Ø6.00 ▼ THRU
10.50
21.00
15.00
65.00
80.00
40.00
40.00
10.50
21.00

Mid Block

Ø19.00 ▼ 6.00
Ø12.00 ▼ 110.00
R3.00 ▼ THRU
Ø5.00 ▼ 25.00
Ø8.00 ▼ 5.00
M5x0.8 - 6H
9.50
10.50
11.50
21.00
6.00
15.00
40.00
65.00
74.00
80.00
6.00
10.00
20.00
90.00
100.00
110.00

DRAWN		
Jake	18/10/2019	
CHECKED		TITLE
QA		
MFG		
APPROVED		
		SIZE A4	DWG NO Mid Block	REV
		SCALE 1 : 1	SHEET 1 OF 2